Institute of High Frequency Technology

RWTH AACHEN UNIVERSITY

Polarimetric Radar for Self-Localization in Automotive Environments

Von der Fakultät für Elektrotechnik und Informationstechnik der Rheinisch-Westfälischen Technischen Hochschule Aachen zur Erlangung des akademischen Grades eines Doktors der Ingenieurwissenschaften genehmigte Dissertation

vorgelegt von

Fabio Weishaupt, M.Sc. RWTH

aus Oberhausen

Berichtende: Univ.-Professor Dr.-Ing. Dirk Heberling
Univ.-Professor Dr.-Ing. Christian Waldschmidt, Universität Ulm

Tag der mündlichen Prüfung: 03.03.2026

Diese Dissertation ist auf den Internetseiten der Universitätsbibliothek online verfügbar.

Dissertation

Kurzfassung

Während bei früheren Fahrerassistenzsystemen die Erkennung von anderen Verkehrsteilnehmern im Fokus stand, so wird die Erfassung der statischen Umgebung mit höheren Automatisierungsstufen immer wichtiger. Um eine sichere Navigation in komplexen Fahrmanövern zu gewährleisten, muss das Fahrzeug zuverlässig seine eigene Position und Orientierung relativ zu seiner Umgebung kennen. Dafür sind charakteristische Elemente der Umgebung, so genannte Landmarken, zu erkennen und dann mit einer Karte zur Positionsbestimmung abzugleichen. Trotz einiger Forschungsarbeiten zu Radarsensoren zur Selbstlokalisierung, existiert bislang keine detaillierte Untersuchung von polarimetrischen Sensoren in diesem Kontext.
Daher werden in dieser Arbeit verschiedene Aspekte der Polarimetrie für die Modellierung der statischen Umgebung sowie eine anschließende Selbstlokalisierung adressiert. Eine Grundvoraussetzung für die Ausnutzung von Polarimetrie ist die Sicherstellung von Polarisationsstabilität über den gesamten Erfassungsbereichs des Radars, insbesondere über den Winkel und die Doppler-Geschwindigkeit. Dazu wird eine speziell angepasste Kalibriermethode entwickelt, welche Grundlage für die Experimente mit einem neu aufgebauten Versuchsträger ist.
Eine polarimetrische Analyse von Streumechanismen, die an typischen Landmarken auftreten, gibt Hinweise, welche Repräsentation von polarimetrischer Informationen im Umgebungsmodells geeignet ist. Neben der Analyse einer Beispielmessung aus einer realen Fahrzeugumgebung ermöglichen ungestörte Absorberkammermessungen die detaillierte Untersuchung von Streueffekten sowie deren räumliche Verteilung. Beide Analysen ergeben, dass typische Landmarken überwiegend anisotropes Verhalten zeigen, was folglich im Umgebungsmodell zu berücksichtigen ist.
Zusätzlich zu diesem neu konzeptionierten polarimetrischen Teil innerhalb des vorgeschlagenen Rasterkarten-Ansatzes wird ein Verfahren zur Integration von rohen Spektraldaten entwickelt. Beide Erweiterungsvorschläge zusammen sind Grundlage für robustere Algorithmen zur Landmarkenextraktion, was anhand umfangreicher Aufnahmen aus dem realen Straßenverkehr belegt wird. Es wird demonstriert, wie die polarimetrische Information die Extraktion von punktförmigen Landmarken robuster macht und die Nutzung von roheren Datenebenen einen Vorteil für die zuverlässige Erkennung von linienförmigen Landmarken bietet.
Auf Basis dieser vorbereitendenden Untersuchung wird ein Selbstlokalisierungssystem vorgestellt, das rein auf Radardaten basiert. Das System nutzt eine Graph-basierte Implementierung für Effizienz und wird anhand mehrstündiger Aufnahmen in verschiedenen realen Umgebungen evaluiert. Neben den generell vielversprechend genauen Lokalisierungsergebnisse wird der Einfluss von Polarimetrie im Detail untersucht. Dabei zeigt sich, dass durch polarimetrische Mehrinformationen keine Verbesserung der Genauigkeit in Umgebungen mit einer ausreichend hohen Landmarkendichte erzielt wird. In herausfordernden Umgebungen mit wenigen Landmarken hingegen kann eine klare Korrelation zwischen der Lokalisierungsgenauigkeit und dem polarimetrischen Informationsgehalt festgestellt werden, wodurch der Vorteil von Polarimetrie für die Selbstlokalisierung belegt wird.

II

Abstract

As automotive vehicles advance towards higher levels of automation, the static environment is becoming increasingly more important after the focus was primarily on the perception of other road users in earlier driver-assistance systems. For safely navigating through complex driving maneuvers, the vehicle must reliably know its own position and orientation with respect to its surroundings. Therefore, characteristic elements in the environment, known as landmarks, must be detected and aligned to a map for deriving the desired position. While some research on utilizing radar for this is available, no extensive study on leveraging polarimetric radar in a self-localization context is published to date.
Therefore, several aspects of polarimetry for perceiving the static environment and subsequently localizing against it are addressed in this thesis. One important prerequisite for exploiting polarimetric information in a practical application is ensuring the stability of a polarimetric response over the radar's field of view, especially in angular and speed dimensions. Thus, a tailored method for a polarimetric calibration is developed and builds the basis for public road experiments with a newly setup experimental vehicle.
A polarimetric analysis of the scattering mechanisms occurring at typical automotive landmarks provides insights into the requirements for properly representing and leveraging this information for static environment perception. Apart from an analysis of an exemplary real-world outdoor measurement, undisturbed anechoic chamber measurements enable a detailed investigation of scattering effects and their spatial allocation. Both analyses reveal that anisotropic behavior is prevalent for typical landmarks and a tailored handling in the environment representation is advisable.
In addition to this newly suggested polarimetric part in the proposed gridmapping approach, a technique for incorporating low-level spectral data is developed. Both extensions are the basis for more robust landmark extraction algorithms, demonstrated through extensive real-world data recordings in public road traffic. It is shown that the polarimetric information makes the extraction of point-shaped landmarks more robust, whereas the low-level data incorporation is advantageous for reliably detecting line-shaped landmarks.
Based on this preliminary work, a self-localization framework functioning solely on radar data is presented. The framework employs a factor graph formulation for an efficient implementation and is evaluated using several hours of real-world recordings in diverse environments. In addition to generally promising accuracy of the results, the influence of the polarimetric information is investigated in detail. While in environments with an abundance of landmarks, the localization accuracy does not improve with a higher polarimetric data level, a clear correlation between localization performance and polarimetric information content is observed in challenging environments. This proves the benefit of polarimetry for self-localization.

Acknowledgements

This thesis was written as an external Ph.D. student of RWTH Aachen at Mercedes-Benz AG. Therefore, I am extremely grateful for getting this opportunity by my supervisor Prof. Dr.-Ing. Dirk Heberling. His support and trust placed in me made this thesis possible in the first place. I would also like to express my special thanks to Prof. Dr.-Ing. Christian Waldschmidt for taking on the second opinion of the dissertation.

I am especially grateful to my team leader Dr.-Ing. Jürgen Dickmann for providing the best possible working environment despite adverse external circumstances such as multiple department relocations during the course of this thesis. Accordingly, my gratitude goes to the above-average number of the company's supervisors for each giving their best support, namely: Klaudius Werber, Dr. rer. nat. Jens Klappstein, Dr.-Ing. Hans-Ludwig Blöcher, Nils Appenrodt. In addition, special thanks are due to Dr.-Ing. Ulrich Kreßel for organizing the publicly funded project @CITY, whose funding made this work possible.

For the fruitful discussions and the acquisition of the anechoic chamber measurements, I like to express my gratitude to RWTH's Institute of High Frequency Technology and specially to Roland Moch. Likewise, I would like to thank my R&D colleagues within Mercedes-Benz including the supervised students for providing a friendly work environment. In particular, the uncomplicated assistance from our workshop colleagues, Cihan Oeztoprak and Kevin Seidel, helped tremendously to get the experimental vehicle on the road. The technical and scientific discussions with my colleagues Dr.-Ing. Amir Laribi, Dr.-Ing. Nicolas Scheiner, Dr. rer. nat. Ole Schumann, and Dr.-Ing. Julius Tilly played a important role for this work, for which I am grateful. The various adventures outside of work with the latter two including an indispensable ice cream tradition, brought the necessary welcome diversion and will always be remembered. Julius Tilly deserves to be mentioned once more in appreciation of the extensive joint efforts on the shared vehicle platform and the many hours spent collaboratively developing the partially shared code base.

Last but not least, the greatest thanks go to my family, especially my parents Andrea and Michael Weishaupt, for their unconditional support in every respect and for sparking my interest in the field of engineering at an early age.

Contents

1 Introduction **1**
- 1.1 Research objectives . . . 4
- 1.2 Structure of the thesis . . . 5

2 Fundamentals **7**
- 2.1 Spatial processing . . . 7
  - 2.1.1 FMCW-based range estimation . . . 7
  - 2.1.2 Chirp sequence-based range and velocity estimation . . . 10
  - 2.1.3 Angle estimation . . . 15
- 2.2 Polarization . . . 18
  - 2.2.1 Propagation of electromagnetic waves . . . 18
  - 2.2.2 Jones vector . . . 19
  - 2.2.3 Common polarization bases . . . 20
  - 2.2.4 Jones vector basis transformation . . . 20
- 2.3 Polarimetry . . . 21
  - 2.3.1 Electromagnetic scattering in radar . . . 22
  - 2.3.2 Radar cross-section . . . 22
  - 2.3.3 Radar equation . . . 24
  - 2.3.4 Scattering matrix . . . 24
  - 2.3.5 Scattering matrix basis transformation . . . 27
  - 2.3.6 Polarimetric covariance matrix . . . 28
  - 2.3.7 Canonical scatterers . . . 29
  - 2.3.8 Coherent decompositions . . . 31
  - 2.3.9 Incoherent decompositions . . . 33
  - 2.3.10 Virtual polarimetric array . . . 36

3 Measurement setup **41**
- 3.1 Vehicle setup . . . 41
- 3.2 Polarimetric radar sensors . . . 43
  - 3.2.1 State of the art . . . 43
  - 3.2.2 Utilized radar sensor . . . 46

4 Polarimetric calibration & signal processing **49**
- 4.1 State of the art . . . 50
- 4.2 Approach . . . 51
- 4.3 Calibration measurements . . . 53
- 4.4 Calibration techniques, signal processing & results . . . 55
  - 4.4.1 Deinterleaving & reordering . . . 55
  - 4.4.2 Electrical path length equalization . . . 56
  - 4.4.3 Range-Doppler FFT . . . 59
  - 4.4.4 PreDBF calibration . . . 59
  - 4.4.5 Angle estimation . . . 63

4.4.6 Polarimetric antenna pattern correction . . . 64
4.4.7 Range-dependent RCS correction & spatial calibration . . . 65
4.5 Radome influence . . . 67
4.6 Summary . . . 70

5 Static environment 71
5.1 Landmark scattering analysis . . . 72
5.1.1 State of the art . . . 72
5.1.2 Anechoic chamber measurement setup . . . 73
5.1.3 Drift compensation . . . 75
5.1.4 Scattering analysis by incident angle . . . 79
5.1.5 Spatial analysis by ISAR imaging . . . 83
5.1.6 Real-world measurements . . . 86
5.1.7 Summary . . . 89
5.2 Grid-based environment representations . . . 90
5.2.1 State of the art . . . 90
5.2.2 PreCFAR Gridmaps . . . 91
5.2.3 Polarimetric PreCFAR Gridmaps . . . 96
5.3 Landmark detection . . . 102
5.3.1 State of the art . . . 102
5.3.2 Point-shaped landmark detection . . . 103
5.3.3 Line-shaped landmark detection . . . 111
5.4 Summary . . . 114

6 Self-Localization 115
6.1 State of the Art . . . 116
6.2 Approach . . . 118
6.2.1 Mapping . . . 119
6.2.2 Ego-motion estimation . . . 120
6.2.3 Map matching . . . 122
6.2.4 Factor graph optimization . . . 123
6.3 Experimental evaluation . . . 126
6.3.1 Data set . . . 126
6.3.2 Implementation . . . 127
6.3.3 Fully polarimetric results . . . 129
6.3.4 Impact of polarimetric information . . . 130
6.4 Summary . . . 136

7 Conclusion 137

A Approximation of the FMCW signal model for a moving object 141

B Partial ISAR images 143

C High turn rate PreCFAR maps 147

D Point-shaped landmark detection in other environments 149

List of Figures **153**

List of Tables **157**

List of Abbreviations **159**

List of Symbols **161**

Bibliography **171**

List of Publications **185**

Curriculum vitae **187**

Chapter 1

Introduction

Advanced driver-assistance systems (ADASs) have attracted increased public interest in recent years. They have already made a significant contribution to road safety. Recent studies show that using an ADAS can potentially prevent or mitigate more than 60 % of passenger vehicle crashes in the United States of America [1]. With the expected widespread market penetration of automated driving systems over the next few years, the way of traveling shall change fundamentally with users regaining time as they are relieved of the driving task.

Therefore, exteroceptive sensors must perceive an increasingly accurate image of the vehicle's surroundings. Typical sensor modalities include ultrasonic sensors, cameras, radar sensors (originally an abbreviation for **ra**dio **d**etection **a**nd **r**anging but used as an anacronym today), and lidar sensors (same etymology for **li**ght **d**etection **a**nd **r**anging). They complement each other with their specific advantages and disadvantages. Radar has been used for decades and continues to be part of many ADAS sensor setups. While early experiments with radars for automotive applications date back half a century, the commercial market introduction of a 76 GHz radar in a passenger car for adaptive cruise control (ACC) by Mercedes-Benz marked a breakthrough around the turn of the millennium [2].

Compared to camera and lidar, radar has the drawback of a lower angular separability. However, the advantages are so significant that radar is still an indispensable sensor in many modern ADAS. Due to its comparatively long wavelength, radar is more robust than the competing modalities in inclement weather conditions such as rain, fog, or snow [3]. Compared to cameras, another radar advantage is the ability to directly measure exact distances to surrounding objects. Finally, radar is unique to this day in measuring the relative velocity towards all scatterers of the environment by exploiting the Doppler effect [3]. Although initial lidar prototypes in development aim to adopt Doppler-based velocity estimation, it is not yet a proven mass-produced technology [4]. These unique characteristics have led to a growing demand, resulting in the functions initially reserved for luxury vehicles becoming increasingly affordable due to economies of scale. Thus, radars are now also widespread in the mid-range segment. The cost of a radar sensor is low, especially compared to a lidar sensor.

Based on the growing number of radar sensors per vehicle for more advanced driving functions and the increasing penetration of the low-range segment, the automotive radar market is predicted to continue growing at 19 % compound annual growth rate with an estimated market revenue of $9 billion in 2025, outpacing the automotive camera market [5]. With this economic interest, the competition for innovation is strong and a lot of research is conducted with different objectives.

One direction of research deals with bringing higher levels of automation to a wider operational design domain (ODD). While the focus for radar in an ADAS up to partial automation levels has been on other road users, this changes for higher levels of automation. For these, it is also necessary to accurately perceive the immobile surroundings, such as the road infrastructure. This is not only required for safely avoiding obstacles, but also for obtaining reliable and highly available information about the ego vehicle's pose (position and orientation) relative to its environment. Estimating it is called self-localization. Having exact knowledge about the pose is the basic prerequisite for subsequent path planning modules, which attempt to find a trajectory that will bring the vehicle closer to the driving task destination. In addition, self-localization can also be used together with map information to make the driving strategy safer, e.g., by reacting appropriately and early on to map-based knowledge of upcoming hazardous road locations such as crosswalks, which might only be perceived as such at a later point in time due to occlusion.

A global navigation satellite system (GNSS) commonly used for vehicle navigation has several inadequacies. On the one hand, the accuracy at the meter level is too low. On the other hand, such a system is only available in scenarios with an unobstructed satellite view, which is not the case in various environments, such as in tunnels or between high-rise buildings. For the first shortcoming, differential GNSS provides a technical solution based on correction data for satellite ephemeris errors as well as iono- and tropospheric distortions, so that results in the centimeter range can be achieved. However, unobstructed reception remains necessary for any satellite-based system. Therefore, there is no way around additional means to achieve a wide ODD. Typical mitigation strategies involve using the already available perception sensors to create a representation of the surroundings. This representation can then be compared to a map for deriving the ego-vehicle's pose. For each sensor modality, accurate and robust self-localization approaches are subject of current research [6]. Radar is particularly suitable due to some of the above-mentioned advantages: The velocity measurement allows excluding other moving road users during landmark extraction, and the exact spatial positioning helps with the map association.

The data levels of such maps can vary considerably depending on the intended application and scale. It ranges from the collection of all raw measurements from the mapping pass, over dense grid representations, to sparse characteristic features called landmarks. Any characteristic, stationary feature of the road environment, which is robustly recognizable, can serve as such a landmark. Because the focus of self-localization is still on pose estimation in the horizontal plane, the bird's-eye view (BEV) is the most common perspective. That is why point- and line-shaped landmarks are the two main classes of abstract landmarks. In the former case, the structure in this perspective collapses to a point-shaped area, and typical examples include traffic sign and street lamp poles, tree trunks as well as guide posts. On the contrary, line-shaped landmarks still cover an extended area in BEV with curbstones, fences and buildings being common occurrences [7]. Only abstract landmark-based approaches are considered feasible for any large-scale deployment due to the comparatively compact required storage size. Furthermore, it is the closest to modality-independent maps, which are regarded as a goal [8]. Without the need to adapt the maps to the different sensors, large-scale maintainability is plausible.

Apart from the algorithmic advances and the application of available sensors for further use cases, another area of research in automotive radar concerns the improvements that are possible through progress in hardware. A sub-field of this area is polarimetry, which once again gains increasing popularity in automotive applications. This technique takes advantage of a polarization-dependent backscattering subject to the object geometry. By adjusting the sent polarization and/or distinguishing the received polarization, a polarimetric radar can draw conclusions about the scattering event and, consequently, the scattering object. Polarimetry is a proven and widely used technique in other radar domains for several decades now. One well-known application is terrain classification in space- and airborne synthetic aperture radar (SAR) systems by means of polarimetric information [9]. Another typical use case for polarimetry is weather radar, where it helps to distinguish different precipitation types [10]. Since cost sensitivity and strict size constraints play only a minor role in both above-mentioned applications, polarimetric systems have already been state of the art for some time in these fields.

In contrast, sensor size, system complexity, and cost are significant factors for automotive use. These factors are also good for differentiating between two phases of publications in automotive polarimetry research: The polarimetric radar systems of the first phase around the turn of the millennium were relatively bulky, aiming to verify the basic phenomenon of polarimetry in automotive environments. The published systems included both – laboratory setups that were not intended for vehicle integration [11, 12, 13] and an experimental mounting on a moving platform [14, 15]. However, the physical sizes of the systems were several orders of magnitude too large for a customer suitable integration into passenger vehicles. Apart from system design, one of the main research goals at that time was proving the theoretical models of typical automotive scatterers by means of comparison to real-world measurements, including guardrails [16], potholes, bricks, bolts, and metal scrap [17], as well as different conditions of the road surface in terms of roughness and wetness [18].

In recent years, the number of publications regarding automotive polarimetry increased again marking the second phase. With the strong demand for improved angular separation capabilities in common, non-polarimetric automotive radar, highly integrated monolithic microwave integrated circuits (MMICs) with multiple transmit and receive channels became available. This development makes it increasingly viable to spend channels for polarimetry while still maintaining reasonable form factors for passenger car integration. Recently published systems exhibit significant differences in their polarimetric characteristics, and so far there is no commonly agreed-upon approach. A variety of polarization types are implemented in publications relevant to the typical automotive frequency band, including a circular [19, 20], a horizontal and vertical linear [21], and a diagonal linear [22] polarization. Other work deals with the question, whether partial polarimetric information is sufficient in automotive contexts [23]. With these new systems, more and more work is published about the impact of polarimetric information on higher-level applications at a larger scale. Due to the smaller form factor and the subsequent easier packaging, extensive real-world measurements are feasible to record, and a positive impact on polarimetric road user classification is reported [21, 24, 25, 26, 27, 28].

With regard to the static vehicle environment, which is of primary interest for self-localization applications, the main focus of published research is on how typical objects look like from a polarimetric view. This is implemented either by polarimetric SAR imaging of an outdoor environment [29, 30] or by polarimetric measurements of traffic signs on a turn table in an anechoic chamber [31]. All results confirm the existence of characteristic scattering behavior depending on the considered object. However, these phenomenological studies have so far only identified the underlying effects of what might potentially improve actual driving functions on public roads. Although the idea of using polarimetry for more reliably finding landmarks in a self-localization context exists already for quite some time [32, 33], the publications only show its application on a small scale in a non-public industrial environment. Therefore, to date, no systematic experimental validation of polarimetric advantages for self-localizing in real-world public road environments have been published.
This thesis is intended to close this gap. It is positioned at the intersection of both above-mentioned areas of research – on the one hand, exploiting the new opportunities of polarimetry brought by advanced radar hardware, and, on the other hand, extending the scope of application for radar in form of self-localization by tailored algorithms leveraging the available data as best as possible. The individual research objectives required for finding an answer to this overarching research question are detailed in steps in the next section.

1.1 Research objectives

The aim of this thesis is to assess the potential benefits of polarimetry in self-localization applications of automated vehicles. Accordingly, the following individual research objectives arise:

- an investigation of necessary calibration and compensation measures for the utilized sensors in order to derive a stable and accurate polarimetric response in common public road scenarios,
- a detailed scattering analysis of typical automotive environment objects, which are suitable as landmarks, for identifying potential approaches to exploit the additional polarimetric information,
- an extension of static environment representations to incorporate polarimetric information in such a way that the subsequent landmark extraction can benefit from this addition,
- an evaluation of how the addition of polarimetry affects the self-localization performance in various real-world scenarios.

1.2 Structure of the thesis

This thesis is structured as follows: Subsequent to this introduction, Chapter 2 commences with an overview of the theory that serves as the foundation for this work. The first part includes the discussion of the underlying principles of modern automotive radar for finding spatial quantities of surrounding objects. Afterwards, the mathematical description of wave propagation is outlined as the foundation for polarimetry. The scattering matrix is introduced as the fundamental tool for expressing scattering behavior. Transformations to different polarization bases and corresponding polarimetric decompositions are presented as an aid to a more intuitive understanding of scattering mechanisms. Typical canonical scatterers are discussed to illustrate the theory.
In Chapter 3, the experimental setup is presented. The practical evaluation in this work requires real-world measurement data. For this reason, an experimental vehicle was set up from scratch. The details of the vehicle setup and the used radar sensors are described in this chapter. Additionally, a review of comparable sensors published in other work is included.
From this point onward, own scientific contributions are presented in the Chapters 4 to 6. Consequently, each of these chapters begins with an overview of related publications on this topic. Moreover, the approach developed in each section is contextually summarized at the end of each chapter. As some of the approaches have been published in papers, each citation of a publication, where this thesis' author is the first author, is marked with bold numbers for easy recognition.
One of the main challenges for utilizing polarimetric information to its full potential is calibration. Due to the relative evaluation of complex values between the different channels, it is much more complex compared to regular automotive radar. Therefore, Chapter 4 discusses the effects that need to be considered and the corresponding countermeasures in form of a calibration approach. The implementation approach of the general signal processing is also included in this chapter due to the interdependence with calibration.
Chapter 5 provides a comprehensive discussion of all aspects related to the static environment perception with the intention of a subsequent self-localization. A detailed investigation of scattering mechanisms occurring at typical landmarks, which were measured both in an anechoic chamber as well as in a real-world environment, serves as the foundation for the proposed new grid mapping technique. By taking the resulting observations about polarimetry into account, an appropriate method for an enhanced robustness during landmark detection is presented.
Based on the above-mentioned techniques, Chapter 6 presents a complete radar-only self-localization framework. An evaluation of the proposed approach is carried out on several hours of real-world recordings in diverse environments. Comparing different levels of polarimetric information allows drawing conclusions about the benefit, which polarimetry could provide in terms of robustness.
The final Chapter 7 summarizes the contributions of this work and provides an outlook.

Chapter 2

Fundamentals

Understanding the concepts and implementations of the self-localization approach developed in this thesis requires theoretical fundamentals in some areas of radar. This chapter provides the necessary basics. The radar signal processing in Section 2.1 introduces how a typical automotive radar is able to derive positional quantities of surrounding objects. Section 2.2 presents the essential principles of wave propagation, including the concept of polarization. On this basis, polarimetry is discussed in Section 2.3, which is the measurement of polarization and its interpretation.

2.1 Spatial processing

As the acronym **ra**dio **d**etection **a**nd **r**anging suggests, the purpose of radar is to detect objects in the environment and derive information about its position with the help of electromagnetic waves in the radio frequency (RF) part of the spectrum. In the simplest case, this can only mean a distance (or *range*) to the object. However, modern automotive radar systems are able to estimate at least one additional angle (azimuth) and relative radial velocity of the object as well.
Even though there are many variants of radar system designs to derive the mentioned quantities, this section focuses on the dominant design in the automotive sector, which is based on the frequency-modulated continuous wave (FMCW) principle. Moreover, the section is limited to the azimuth angle since the system utilized in this work can only measure this one angle. Although the basic principles are the same for an elevation angle, there are some specifics to consider for useful results due to the inherently present ground plane. The ground surface effectively acts as a mirror plane and interferes with elevation angle finding in particular. However, it is left out as it is irrelevant for the utilized radar.

2.1.1 FMCW-based range estimation

The range measurement of a radar is typically based on the propagation delay of an electromagnetic wave. This delay is proportional to the range of the object and can be determined in different ways. For the FMCW modulation, the time of transmission is encoded in the transmitted wave by a linearly changing frequency. By comparing the frequency of the received echo to the known time of this frequency's transmission, the propagation delay and hence the range can be estimated.
Typical FMCW radars implement this as can be seen in the simplified block diagram in Fig. 2.1. By realizing the propagation delay estimation by mixing the current transmit signal s_{Tx} with the received signal s_{Rx}, the resulting signal's frequency is proportional to the searched range as will be shown in the following.

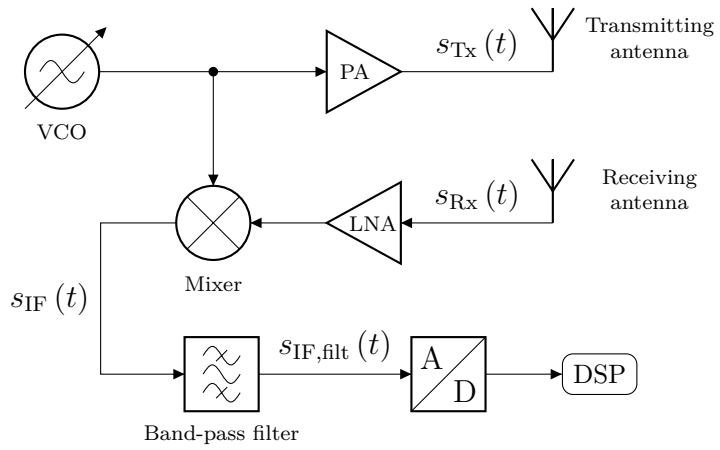


Figure 2.1: The simplified FMCW radar block diagram shows the main building blocks. The modulated signal is amplified by a power amplifier before being sent out by the transmitting antenna. The received response is amplified by a low noise amplifier before it is mixed with the current modulated signal. Subsequent filtering and analog-to-digital conversion allow digital signal processing for range estimation.

The FMCW principle is characterized by transmitting a linearly changing frequency for the duration of one chirp T_{chirp}. Starting at the start frequency f_0, a bandwidth B is swept such that the transmitted frequency is given by

$$f_{\mathrm{Tx}}(t) = f_0 + \underbrace{\frac{B}{T_{\mathrm{chirp}}}}_{\rho} t, \quad t \in [0, T_{\mathrm{chirp}}] \tag{2.1}$$

with the chirp rate ρ. Therefore, the transmitted signal can be calculated by integration of this frequency to

$$s_{\mathrm{Tx}}(t) = \gamma \cos\left(2\pi f_0 t + \pi \rho t^2\right), \quad t \in [0, T_{\mathrm{chirp}}] \tag{2.2}$$

with the arbitrary amplitude γ. In the simplified block diagram, this frequency chirp generation is shown as a voltage-controlled oscillator (VCO). Its output is amplified by the power amplifier (PA) and subsequently emitted by the transmitting antenna. The amplitude γ is neglected in the following ($\gamma = 1$), as it is not relevant for the working principle in this section. Furthermore, the complex variant of the transmit signal is chosen for simplifying calculations below, which is

$$\underline{s}_{\mathrm{Tx}}(t) = \exp\left(\mathrm{j}2\pi f_0 t + \mathrm{j}\pi \rho t^2\right) \tag{2.3}$$

with the real part $s_{\mathrm{Tx}} = \mathfrak{Re}\left(\underline{s}_{\mathrm{Tx}}\right)$ (or generally $s = \mathfrak{Re}\left(\underline{s}\right)$ for any signal). The letter j denotes the imaginary unit. In a synthetic scenario with only a single static scatterer, the received signal $\underline{s}_{\mathrm{Rx}}$ is purely a delayed version of the sent signal $\underline{s}_{\mathrm{Tx}}$ and when neglecting the amplitude again is given by

$$\underline{s}_{\mathrm{Rx}}(t) = \underline{s}_{\mathrm{Tx}}(t - \tau) \tag{2.4}$$

with propagation delay τ.

Due to the two-way traveling from the radar to the scatterer and back to the radar, the propagation delay is related to the range r by $\tau = {}^{2r}/_{c}$ with the speed of light c. This signal is received by the receiving antenna and amplified by the low noise amplifier (LNA) before being fed into the mixer. The complex intermediate frequency signal of such a single reflection can be expressed as

$$\underline{s}_{\mathrm{IF}}(t) = \underline{s}^{*}_{\mathrm{Tx}}(t)\ \underline{s}_{\mathrm{Rx}}(t) = \underbrace{\exp\left(-\mathrm{j}2\pi f_0 \tau\right)\exp\left(\mathrm{j}\pi\rho\tau^2\right)}_{\textbf{no} \text{ function of } t}\underbrace{\exp\left(-\mathrm{j}2\pi\rho\tau t\right)}_{\text{function of } t} \tag{2.5}$$

where * denotes the complex conjugate. For the real signal s_{IF}, the ideal mixer does not only produce the frequency difference between both signals but also the sum. The subsequent band-pass in the block diagram filters out the frequency sum component such that principally the same signal content will be observed for $s_{\mathrm{IF,filt}}$ as was calculated for $\underline{s}_{\mathrm{IF}}$. The only difference is that the included low-pass filter characteristic ensures that the direct coupling between the transmitting and receiving antenna is not driving the following analog-to-digital converter (ADC) into saturation.
As can be seen from (2.5), the first two terms of the intermediate frequency signal are not depending on the time and can be considered a phase constant for an arbitrary but fixed range. The third term represents a constant frequency that is proportional to the scatterer's range via the signal propagation time delay τ. Therefore, it is required to perform a frequency analysis to derive the range. This typically is performed in the digital domain by a fast Fourier transform (FFT) on the ADC-sampled signal (cf. Fig. 2.1). The desired frequency is also called beat frequency and can be derived from (2.5) to be $f_{\mathrm{b}} = \rho\tau$ such that the range r is calculated as

$$r = \frac{f_{\mathrm{b}}}{\rho}\frac{c}{2}. \tag{2.6}$$

One important parameter of a radar is its capability to separate two objects that are close to each other in one of the measurement domains. For the sake of simplicity, it is assumed that both objects have the same reflectivity and that a robust separation is possible if they are apart two times the Rayleigh resolution. This resolution is defined as the distance from the maximum to the first minimum and it is well known that for frequency estimation this spectral distance is inversely proportional to the observation time [34]. In the case of beat frequency estimation, this means the Rayleigh resolution $\delta_{f_{\mathrm{b}}}$ depends on the chirp duration T_{chirp}. It should be noted that (2.5) is only valid if $t \in [\tau, T_{\mathrm{chirp}}]$ for the presented signal model, i.e. larger ranges reduce the overlap of the transmitted and received chirp and consequently the range resolution. However, this is neglected in the following, which is justified by the fact that usually $\tau \ll T_{\mathrm{chirp}}$. Moreover, the ramp actually starts before the beginning of sampling in many common implementations to allow frequency stabilization of the chirp, such that the real bandwidth is slightly larger than the effective bandwidth. Then, the range resolution δ_r is calculated with (2.1) and (2.6) to

$$\delta_r \overset{(2.6)}{=} \delta_{f_{\mathrm{b}}}\frac{c}{2\rho} = \frac{1}{T_{\mathrm{chirp}}}\frac{c}{2\rho} \overset{(2.1)}{=} \frac{c}{2B}. \tag{2.7}$$

Equation (2.7) also applies for a pulsed radar system. Due to the different operating principle compared to FMCW systems, the bandwidth is directly determining the minimum sampling rate of the ADC [34]. As even for the least demanding use cases for automotive radar the range resolution must not exceed 1 m, a bandwidth of more than 150 MHz must be sampled in this case. Any more demanding resolution requirement common for the many use cases would directly translate into even more challenging ADC specifications. For FMCW systems, however, the sampling frequency f_s does not define the range resolution but the maximum range r_max. It can be derived by applying the Nyquist–Shannon sampling theorem to (2.6) giving

$$r_\mathrm{max} = \frac{c}{2\rho} f_\mathrm{b,max} = \frac{c}{2\rho}\frac{f_\mathrm{s}}{2}. \tag{2.8}$$

An appropriate design of the filter characteristic before analog-to-digital conversion needs to ensure that any responses from objects above the maximum range do not show as aliases at wrong ranges.
To mitigate severe aliasing effects during velocity estimation, which will be explained in the next section (especially by (2.13)), an upper limit to the chirp duration T_chirp is implied. The hardware-limited chirp rate for a desired bandwidth provides a lower limit for T_chirp. Hence, a common chirp duration is in the order of several tens of microseconds ($10\,\mu\mathrm{s} \leq T_\mathrm{chirp} \leq 50\,\mu\mathrm{s}$). Based on that, and a typical automotive maximum range requirement of 300 m, as well as the same range resolution mentioned before, the maximum beat frequency to be sampled in FMCW radar is 30 MHz in the worst case according to (2.8). Therefore, the requirements for the ADC in FMCW radars are significantly reduced compared to pulsed radars, which is one of the reasons why it has become the de facto standard in automotive applications. Additionally, FMCW radar does not require the high peak output power of pulsed radar for the same sensitivity due to the continuous mode of operation, which eases the system design.

2.1.2 Chirp sequence-based range and velocity estimation

After considering the simple static case, this section presents the theory for dynamic scenarios. It does not matter what is moving because for the radar any relative movement to itself looks the same, i.e., another moving road user observed from an ego-vehicle in standstill makes no difference to the static infrastructure observed from a moving ego-vehicle with respect to the following dynamic signal model. Furthermore, it should be noted that only the radial component of any velocity is relevant for the radar because the tangential components have no influence on the considered quantities.
For an unaccelerated, uniform relative radial velocity v_r, the range can be described by $r\,(t) = r_0 + v_\mathrm{r} t$ with the start range r_0 at $t = 0$. After some algebra (full derivation in [**35**]), the signal propagation time delay for a moving object $\tilde{\tau}$ is

$$\tilde{\tau} = \frac{2\,(r_0 + v_\mathrm{r} t)}{c + v_\mathrm{r}} \overset{v_\mathrm{r} \ll c}{\approx} \frac{2\,(r_0 + v_\mathrm{r} t)}{c} \tag{2.9}$$

where the approximation is justified for any relevant velocities in automotive applications.

Inserting (2.9) into (2.5) gives

$$\underline{s}_{\mathrm{IF}}(t) = \exp\left(\frac{\mathrm{j}4\pi}{c}\left(r_0\left(\frac{\rho r_0}{c} - f_0\right) + \left(\left(\frac{2\rho r_0}{c} - f_0\right)v_{\mathrm{r}} - \rho r_0\right)t + v_{\mathrm{r}}\rho\left(\frac{v_{\mathrm{r}}}{c} - 1\right)t^2\right)\right) \tag{2.10}$$

for the intermediate frequency signal of one object moving relatively. As derived in Appendix A, this can be simplified to

$$\underline{s}_{\mathrm{IF}}(t) \approx \exp\left(-\frac{\mathrm{j}4\pi}{c}\left(r_0 f_0 + (f_0 v_{\mathrm{r}} + \rho r_0)\,t + v_{\mathrm{r}}\rho t^2\right)\right). \tag{2.11}$$

The result is divided into three parts based on its time dependence. The first part is a constant phase term depending on the range r_0 at the start of the measurement. The second term is a constant complex frequency that depends on the range in the same way as it was the case for the static case in Section 2.1.1 and additionally on the relative radial velocity v_{r}. Using the wavelength $\lambda_c = {}^{c}/_{f}$ (with the subscript c for disambiguation with eigenvalues), this velocity-dependent frequency $f_{\mathrm{D}} = {}^{2v_{\mathrm{r}}}/_{\lambda_c}$ is caused by the well-known Doppler effect. For non-zero relative velocities the processing from before results in a distorted range estimate with a shift proportional to the relative radial velocity, which is also known as range-Doppler coupling [34]. Finally, the third part is quadratically dependent on time, i.e., it is a linearly changing frequency, and it can be interpreted as the expected beat frequency variation due to the changing range over the duration of the chirp. These three measurable quantities may seem sufficient to solve for the two unknowns (r_0, v_{r}) at first glance. However, the phase term is only unambiguous for range intervals in the order of the wavelength such that it is unusable for millimeter wave automotive radar. With the two remaining parameters, the equation system is still solvable in principle. But it is not feasible to accurately estimate the frequency variation because it is very small for typical implementations. Therefore, other approaches are required.

One possibility is to transmit multiple ramps with different slopes, e.g., by switching between up and down chirps. This way only the range-dependent proportion of the signal frequency changes, while the velocity-dependent part stays the same such that both unknowns can be calculated. For a single object, two ramps are sufficient. When more than one object has to be resolved, more ramps are required and depending on the actual implementation additional ghost object filtering must be applied.

Another approach is based on transmitting multiple ramps but with constant parameters [36, 37]. An illustration of this modulation principle, which is nowadays referred to as chirp sequence (CS) modulation, is shown in Fig. 2.2. It is characterized by using the phase progression between consecutive ramps to estimate the relative radial velocity instead of the actual Doppler frequency shift. Assuming that the velocity remains constant over all ramps, the range of the object at the start of ramp $m \in \{0, \ldots, N_{\mathrm{slow}} - 1\}$ can be described by

$$r_m = r_0 + m\,T_{\mathrm{prf}}\,v_{\mathrm{r}} \tag{2.12}$$

with ramp repetition duration T_{prf}. Replacing r_0 with r_m in (2.11) has two effects: On the one hand, the beat frequency changes per ramp according to the object's movement. Depending on the magnitude of the velocity, the range resolution and the duration of the measurement cycle, the object might touch multiple range cells. This effect is known as range migration. On the other hand, the phase progresses linearly over the ramps with a per-ramp increment of $4\pi T_{\mathrm{prf}} v_{\mathrm{r}}/\lambda_c = 2\pi f_{\mathrm{D}} T_{\mathrm{prf}}$. Thus, it can be considered as sampling the Doppler frequency f_{D} with a sample rate of $1/T_{\mathrm{prf}}$ in one specific range bin, if range migration is assumed negligible. According to the Nyquist–Shannon sampling theorem, the maximum unambiguous frequency, i.e., that no aliasing occurs, is half the sampling frequency such that $f_{\mathrm{D,max}} = 1/2T_{\mathrm{prf}}$ and, hence

$$|v_{\mathrm{r,max}}| = \left|\frac{\lambda_c}{2} f_{\mathrm{D,max}}\right| = \left|\frac{\lambda_c}{4T_{\mathrm{prf}}}\right|. \tag{2.13}$$

Accordingly, the ramp repetition duration T_{prf} and in consequence the chirp duration T_{chirp} shall be rather short to support a large unambiguous velocity domain, giving evidence to the statement about the sampling rate requirement in Section 2.1.1. Analogously to (2.7), the Rayleigh resolution of the velocity-induced frequency is inversely proportional to the observation duration, which includes all ramps of the measurement cycle, such that the relative radial velocity Rayleigh resolution $\delta_{v_{\mathrm{r}}}$ is

$$\delta_{v_{\mathrm{r}}} = \frac{\lambda_c}{2}\delta_{f_{\mathrm{D}}} = \frac{\lambda_c}{2T_{\mathrm{prf}}N_{\mathrm{slow}}}. \tag{2.14}$$

As shown in Fig. 2.2, the samples are organized in a 2D matrix format. The dimension along the samples per ramp is referred to as the fast time t_{fast} with N_{fast} samples. On the contrary, sampling over the subsequent ramps is known as the slow time dimension t_{slow} with N_{slow} samples. Organizing the samples in this matrix is beneficial for the subsequent digital signal processing (DSP) that aims to transform the time dimensions to range and velocity, respectively: As the desired quantities are represented as frequencies in the data matrix in both cases, a 2D FFT is a common and efficient processing scheme, as shown in Fig. 2.3. Transforming from the fast time domain t_{fast} to the range domain r is performed by column-wise FFTs in the chosen organization and is referred to as the range FFT. In contrast, row-wise FFTs transform from the slow time domain t_{slow} to the relative radial velocity domain v_{r}. This step is called Doppler FFT. The result is known as the range-Doppler map. Depending on the actual modulation parameters, a correction of the estimated range due to the range-Doppler coupling may be appropriate. For typical CS parameters in automotive applications, it often is considered negligible.

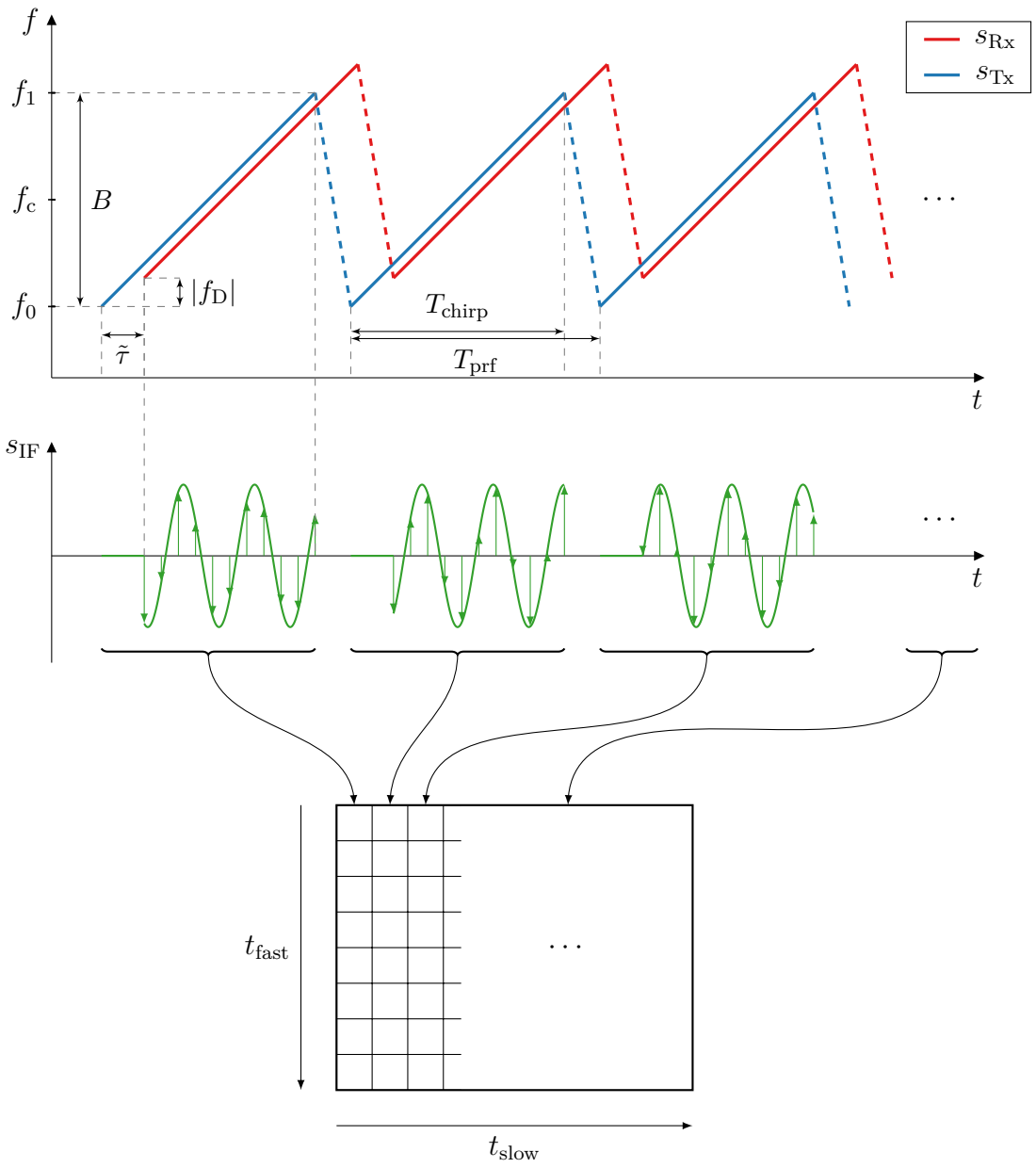


Figure 2.2: The CS modulation is characterized by repeated transmission of ramps with the same parameters. Each ramp's intermediate frequency signal is sampled as indicated by the green arrows. Samples are ordered as depicted in the bottom of the figure. It should be noted that the ratios of Doppler frequency f_D and signal propagation time delay for a moving object $\tilde{\tau}$ are not according to scale for better readability.

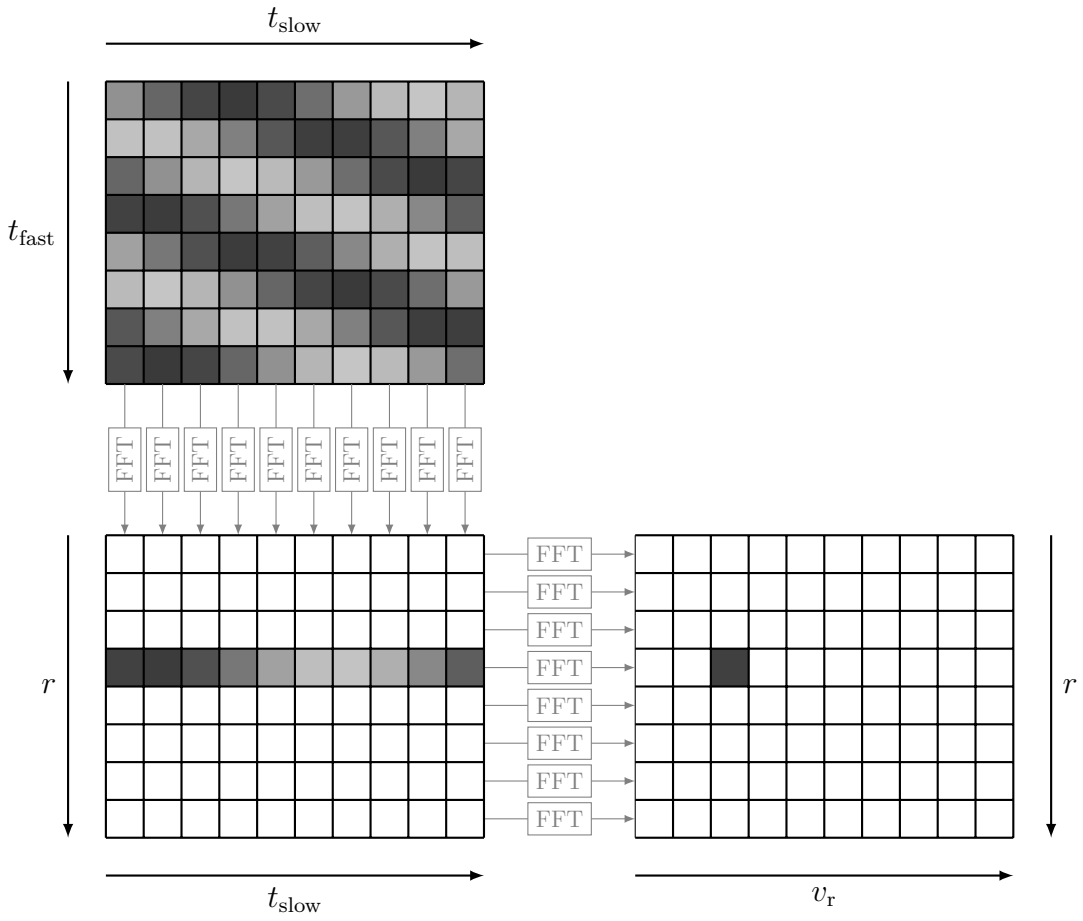


Figure 2.3: Range Doppler processing for CS modulation can be performed by applying a 2D Fourier transform. The bins are colored for an exemplary single point scatterer by the amplitude of the real part.

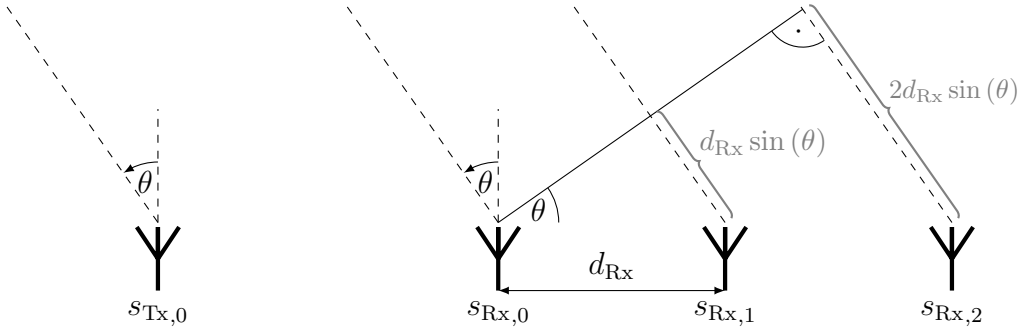


Figure 2.4: When far-field conditions are met, it can be assumed that a planar wave impinges on the receiving elements of the ULA. The difference in the received signals between the elements can be determined geometrically. For any non-broadside impingement angle, the range to the scatterer increases linearly over the receiving element.

2.1.3 Angle estimation

In addition to a scatterer's range, a complete two-dimensional spatial location also requires angular information of surrounding objects. While this work is solely focused on azimuthal angles, but the same principles apply to the elevation angle for differently designed radars. There have been various approaches to angle estimation in automotive radar in the past, including mechanical mechanisms to manipulate the antenna pattern to focus to different directions [2]. However, digital beamforming (DBF) is the state of the art in modern automotive radar [2]. This has the advantage of less susceptibility to mechanical errors typical for harsh automotive environments and eliminating the need to steer in different directions only one after the other.
To allow easy derivation, it is assumed that there is only one transmitter, and the array consists of receiving elements only, i.e., single-input multiple-output (SIMO). For DBF, each array element requires a complete receiving signal chain including the antenna, down-converter, and ADC. Only then, the beamforming can be applied in the digital domain by means of DSP algorithms. In addition, the following assumptions are made to easily understand the concept: the array is calibrated, each element has an isotropic radiation pattern, the elements are spaced uniformly along one axis in a so-called uniform linear array (ULA) configuration, the relative bandwidth is small enough to consider the narrowband case ($f_0 \ll B$), and, finally, that the scatterer is located in the far-field such that the impinging wave can be considered to be planar. The latter is widely accepted if the scatterer is in a distance larger than the far-field range r_{FF} with

$$r_{\mathrm{FF}} = \frac{2D^2}{\lambda_c} \tag{2.15}$$

where D is the maximum dimension of the antenna array [38]. With these assumptions, the signal model visualized in Fig. 2.4 is applicable. This means that for each element of the receiving array the range to the scatterer increases linearly by a range difference of $d_{\mathrm{Rx}} \sin(\theta)$ between neighboring elements with an azimuth angle θ measured from the broadside direction.

Without loss of generality, the range to the first receiving element is assumed to be r_0 such that it serves as the reference. Based on (2.11), the signal vector for a SIMO ULA can then be approximated by

$$\underline{\mathbf{s}}_{\mathrm{IF}}(t) \approx \begin{pmatrix} 1 \\ e^{-\frac{\mathrm{j}2\pi}{c}(f_0 d_{\mathrm{Rx}} \sin(\theta) + \rho d_{\mathrm{Rx}} \sin(\theta) t)} \\ \vdots \\ e^{-\frac{\mathrm{j}2\pi}{c}(N_{\mathrm{Rx}}-1)(f_0 d_{\mathrm{Rx}} \sin(\theta) + \rho d_{\mathrm{Rx}} \sin(\theta) t)} \end{pmatrix} \underline{s}_{\mathrm{IF}}(t) \tag{2.16}$$

with the number of receiving antenna N_{Rx}. Apart from the expected beat frequency shift due to the range difference, a linear phase progression over the ULA elements results. The frequency shift is usually neglected because the array aperture is typically smaller than the range resolution such that the same range bin is affected for all array elements. Using the wavenumber $k = {}^{2\pi f_0}/_{c} = {}^{2\pi}/_{\lambda}$, the phase progression can be expressed in the form of the steering vector as

$$\underline{\mathbf{a}}(\theta) = \left(1,\, e^{-\mathrm{j}kd_{\mathrm{Rx}} \sin(\theta)},\, \ldots,\, e^{-\mathrm{j}kd_{\mathrm{Rx}} \sin(\theta)(N_{\mathrm{Rx}}-1)}\right)^T. \tag{2.17}$$

Once again, a frequency estimation is required to derive the azimuth angle θ. It can be interpreted as a spatial frequency, and the same principles as before apply. Violating the Nyquist–Shannon sampling theorem by sub-sampling means the spatial sampling is too "slow" or wide, i.e., the receiving element distance d_{Rx} is too large. Critical sampling is reached when the phase increment between elements $|kd_{\mathrm{Rx}} \sin(\theta)|$ is equal to π such that the maximum unambiguous azimuth angle $\theta_{\max}$ is given by

$$|\theta_{\max}| = \arcsin\left(\frac{\lambda_c}{2d_{\mathrm{Rx}}}\right). \tag{2.18}$$

From this, it can be derived that the element spacing in an ULA must fulfill $d_{\mathrm{Rx}} \leq {}^{\lambda_c}/_{2}$ for an unambiguous azimuth angle domain of $\pm 90°$. If this is not the case, so-called grating lobes appear and the angle estimate becomes ambiguous. When the antenna radiation pattern is designed in a way that significant gain is only present in the reduced unambiguous angular domain, such a design may still be feasible.
In case of an ULA, a common approach for the spatial frequency estimation is once again the application of FFTs. For the simplified steering vector signal model in (2.17), the Fourier transform represents a matched filter. With the resolution being dependent on the observation time in temporal frequency estimation, it accordingly depends on observation aperture in spatial frequency estimation. Due to the non-linear relationship between the azimuth angle and the spatial frequency, derivation of the Rayleigh resolution is more extensive so that the approximation from [39]

$$\delta_\theta \approx \frac{\lambda_c}{(N_{\mathrm{Rx}} - 1)\, d_{\mathrm{Rx}} \,|\cos(\theta)|} \tag{2.19}$$

is used in this work. The expected dependence on the array's total aperture size $(N_{\mathrm{Rx}} - 1)\, d_{\mathrm{Rx}}$ is apparent. Furthermore, the resolution changes with the azimuth angle, which can be interpreted as a factor that describes the effective aperture. The further the azimuth angle is apart from broadside direction, the less effective aperture shows for the impinging plane wave.

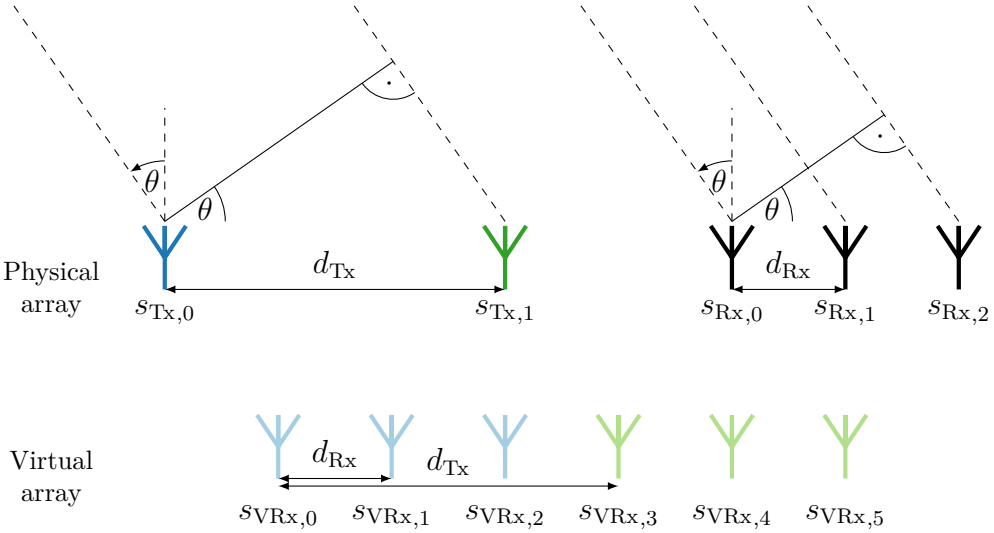


Figure 2.5: The MIMO principle allows to synthesize $N_{\mathrm{VRx}} = N_{\mathrm{Tx}} N_{\mathrm{Rx}}$ virtual antenna elements from N_{Tx} transmit and N_{Rx} receive antennas.

MIMO

From the previous section, it can be comprehended that resolution and unambiguousness are opposed to each other. For a given number of array elements, they can be used to either span a large aperture for good resolution with limited unambiguousness or no ambiguities with limited resolution. Consequently, the urge for a high number of elements in automotive applications is unabated. The multiple-input multiple-output (MIMO) principle helps to satisfy this demand. By the use of multiple spatially spread transmitting and receiving elements, so-called virtual elements can be synthesized to span a larger aperture or sample a given aperture more densely. For this, an unambiguous division of the received signal into components that are assigned to one of the transmitters must be possible. This can be achieved in various ways and will be revisited later.

If the transmitting and receiving array elements are spaced closely to each other, it is called coherent or co-located MIMO radar [40]. This is also referred to as a quasi-monostatic system, for which an equivalent SIMO array can be constructed by convolution of the spatial positions of transmitting and receiving antennas [40]. Among others, full equivalence requires that the far-field condition still holds true for the now larger antenna dimension and that no multipath propagation occurs. Fig. 2.5 demonstrates how a system of $N_{\mathrm{Tx}} = 2$ transmitting and $N_{\mathrm{Rx}} = 3$ receiving elements can achieve the performance of a $N_{\mathrm{VRx}} = N_{\mathrm{Tx}} N_{\mathrm{Rx}} = 6$ element array with double the aperture. By choosing the transmitter distance $d_{\mathrm{Tx}} = N_{\mathrm{Rx}} d_{\mathrm{Rx}}$, the resulting equivalent array is a maximum aperture ULA with no overlapping elements. Depending on the transmit-side multiplexing, overlapping elements may be desired. In order to ensure an unambiguous assignment to the individual transmitters, orthogonal signals are typically used. The most common approaches in automotive radar are time-division multiplexing (TDM) and Doppler-division multiplexing (DDM). TDM is easy to implement because the transmitters are simply activated successively, which does not require additional hardware complexity.

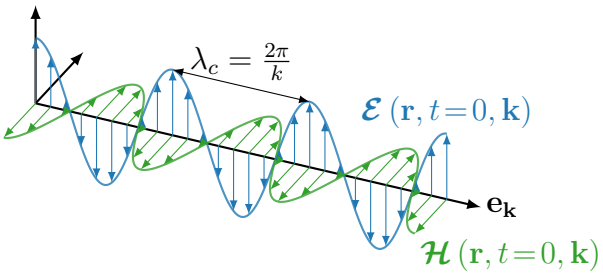


Figure 2.6: Given far-field conditions, electromagnetic propagation is described as a transverse wave, which requires the fields to be orthogonal to the direction of propagation.

However, disadvantages are a phase distortion between the virtual elements from different transmitters in dynamic scenarios as well as a reduced unambiguous relative velocity due to a slower temporal sampling of the phase for the Doppler FFT. The phase distortion has to be corrected for a correct angle estimation, which can be either achieved by compensation when the velocity is known [41] or by having virtual array positions that are sampled with multiple overlapping elements [42]. In contrast, DDM has the advantage of simultaneously active transmitters resulting in a more sensitive system. It requires phase shifters for each transmitter such that by varying each ramp's phase with a unique pattern per transmitter an assignment of the spectral repetitions in Doppler domain is possible [43]. Disadvantages of DDM arise in dense scenarios with many different velocities, when the spectral repetitions of different objects start to overlap.

2.2 Polarization

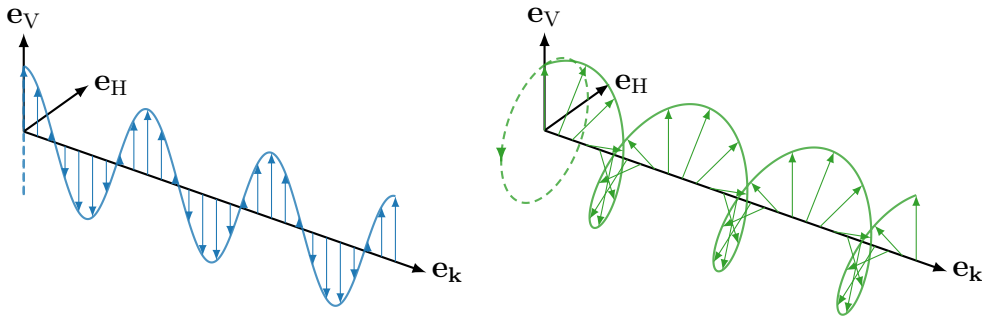
Polarization is a property of an electromagnetic wave and is fundamental to derive information about scattering mechanisms by polarimetry. Therefore, this section starts with the mathematical description of the electromagnetic fields of a propagating wave in Section 2.2.1. The Jones vector represents the polarization state, which is practical for calculus, and is introduced in Section 2.2.2. Since the basis for the vector can be different, Sections 2.2.3 to 2.2.4 describe some common bases and the transformation between them.

2.2.1 Propagation of electromagnetic waves

One solution to Maxwell's equations in a vacuum (no losses, no charges nor currents) is the harmonic monochromatic plane wave defined by its electric field

$$\boldsymbol{\mathcal{E}}(\mathbf{r}, t, \mathbf{k}) = \mathfrak{Re}\left\{\underline{\boldsymbol{\mathcal{E}}}(\mathbf{r}, t, \mathbf{k})\right\} = \mathfrak{Re}\left\{\underline{\mathbf{E}} \exp\left(\mathrm{j}\omega t - \mathrm{j}\mathbf{k} \cdot \mathbf{r}\right)\right\} \tag{2.20}$$

with $\omega = 2\pi f_0$ denoting the angular frequency, $\mathbf{r}$ describing an arbitrary point in the three-dimensional space, $\underline{\mathbf{E}}$ being a vector of the electric field's amplitude and phase considered in more detail in the following section, and the wave vector $\mathbf{k} = k\,\mathbf{e_k}$ giving the direction of propagation scaled by the wavenumber k. The notation is based on [44] and [45].



(a) linear polarization (b) circular polarization

Figure 2.7: The most common polarization state types are visualized by their spatial progression. A temporal progression at the origin is indicated by the dashed projection.

By applying Maxwell's equations, it can be shown that both the electric field $\boldsymbol{\mathcal{E}}$ and magnetic field $\boldsymbol{\mathcal{H}}$ are orthogonal to the direction of propagation and to each other [46]. The wavenumber is related to the wavelength by $k = {}^{2\pi}/_{\lambda_c}$. A visualization of the spatial field progression of an exemplary solution is given by Fig. 2.6.

2.2.2 Jones vector

When the basis vectors $\mathbf{e}_\Phi, \mathbf{e}_\Psi$ of $\underline{\mathbf{E}}$ are chosen to be in the transverse plane to the propagation direction $\mathbf{e}_\mathbf{k}$ and mutual orthogonality of the basis is ensured, $\underline{\mathbf{E}} = \underline{\boldsymbol{\mathcal{E}}}(\mathbf{r}=\mathbf{0}, t=0, \mathbf{k}) \in \mathbb{C}^2$ is called the Jones vector and almost fully describes the polarization state of the electromagnetic wave. Because this state is independent from the absolute magnitude, the Jones vector is often used in a normalized form, which will be expressed as $\hat{\underline{\mathbf{E}}} = {}^{\underline{\mathbf{E}}}/_{\|\underline{\mathbf{E}}\|}$. The interpretation of a Jones vector strongly depends on the chosen basis, such that

$$\underline{\mathbf{E}}_\mathcal{B} = \underline{E}_\Phi \mathbf{e}_\Phi + \underline{E}_\Psi \mathbf{e}_\Psi = \begin{pmatrix} \underline{E}_\Phi \\ \underline{E}_\Psi \end{pmatrix}_\mathcal{B} = \sqrt{|\underline{E}_\Phi|^2 + |\underline{E}_\Psi|^2}\, \hat{\underline{\mathbf{E}}}_\mathcal{B} \tag{2.21}$$

indicates that the arbitrary, orthonormal basis $\mathcal{B} = \{\mathbf{e}_\Phi, \mathbf{e}_\Psi\}$ is used. In principle, the temporal and spatial dependencies of the (2.20) can be easily reintroduced. However, the direction of propagation is ambiguous: the wave can be propagating in $+\mathbf{e}_\mathbf{k}$ or $-\mathbf{e}_\mathbf{k}$ direction. For a given direction, the signs for reintroducing the temporal and spatial dependencies alter, leading to $\exp(\mathrm{j}\omega t - \mathrm{j}\mathbf{k}\cdot\mathbf{r})$ or $\exp(\mathrm{j}\omega t + \mathrm{j}\mathbf{k}\cdot\mathbf{r})$, respectively. For disambiguation, the directed Jones vector notation is introduced in [44], where $\underline{\mathbf{E}}^+$ and $\underline{\mathbf{E}}^-$ stand for the $+\mathbf{e}_\mathbf{k}$ and $-\mathbf{e}_\mathbf{k}$ directions. This notation will be used in the following, whenever disambiguation is necessary. If the notation is omitted for conciseness, $\underline{\mathbf{E}}^+$ is assumed.
Three types of polarization are distinguished based on the projection of the field vector trajectory onto the transverse plane:

- linear,
- circular, and
- elliptical polarization.

The former two can be considered a special case of the general elliptical case. An example of both is given by Fig. 2.7. This work uses the handedness convention that is defined by an IEEE Standard [47], i.e., the transverse plane is looked at in the same direction of the wave's propagation. Thus, Fig. 2.7b shows a right-hand circular polarization.

2.2.3 Common polarization bases

The same physical polarization state can be described by different Jones vectors depending on the chosen polarization basis. A linear basis $\mathcal{B}_{\mathrm{HV}}$ with its basis vectors aligned to the Cartesian reference coordinate system is the most commonly used one. The horizontal basis vector $\mathbf{e}_{\mathrm{H}}$ is parallel to the ground plane, the vertical basis vector $\mathbf{e}_{\mathrm{V}}$ points upwards. Another common basis is the circular one $\mathcal{B}_{\mathrm{LR}}$ where the basis vectors $\mathbf{e}_{\mathrm{L}}$ and $\mathbf{e}_{\mathrm{R}}$ express a left- and right-hand rotation, respectively.

2.2.4 Jones vector basis transformation

Depending on the deployed radar system and the intended application, one or the other basis might be more suitable. Therefore, one has to transform the Jones vectors between different bases. A transformation from an arbitrary basis $\mathcal{B}$ to another one $\mathcal{B}'$ can be achieved by multiplying with a unitary matrix

$$\underline{\mathbf{E}}_{\mathcal{B}'} = \underline{\mathbf{U}}_{\mathcal{B}\to\mathcal{B}'}\underline{\mathbf{E}}_{\mathcal{B}} \tag{2.22}$$

where the matrix columns are the basis vectors of $\mathcal{B}$ in $\mathcal{B}'$ by design [9]. Unitary transformation matrices ensure ℓ^2-norm invariance, i.e., conservation of energy. Transforming back is achieved by matrix inversion $\underline{\mathbf{U}}_{\mathcal{B}'\to\mathcal{B}} = \underline{\mathbf{U}}_{\mathcal{B}\to\mathcal{B}'}{}^{-1}$.
Two different definitions for the right-hand circular polarization are used in literature. A difference in the phase reference can mean either $1/\sqrt{2}\begin{pmatrix}1 & -\mathrm{j}\end{pmatrix}^T$, or $1/\sqrt{2}\begin{pmatrix}\mathrm{j} & 1\end{pmatrix}^T$ is the correct representation. As a result, this definition is determining if the respective basis transformation matrix is in the special unitary group SU(2). In the former case, this is not true with $\left|\underline{\mathbf{U}}_{\mathcal{B}_{\mathrm{LR}}\to\mathcal{B}_{\mathrm{HV}}}\right| = -\mathrm{j} \neq 1$ such that $\underline{\mathbf{U}}_{\mathcal{B}_{\mathrm{LR}}\to\mathcal{B}_{\mathrm{HV}}} \in \mathrm{U}(2)$. For the second definition, $\left|\underline{\mathbf{U}}_{\mathcal{B}_{\mathrm{LR}}\to\mathcal{B}_{\mathrm{HV}}}\right| = 1$ and, hence, $\underline{\mathbf{U}}_{\mathcal{B}_{\mathrm{LR}}\to\mathcal{B}_{\mathrm{HV}}} \in \mathrm{SU}(2)$. With the latter definition, there are advantages in terms of consistency with further transformations and representations [48, p. 298f.] [9, p. 42f.]. Therefore, this definition is used in this work.
Based on this, the normalized Jones vectors of different typical polarization states are are shown in the common bases $\mathcal{B}_{\mathrm{HV}}$ and $\mathcal{B}_{\mathrm{LR}}$ in Table 2.1. Because the transformation between these bases is frequently used in this work, the corresponding matrices are provided in the following with

$$\underline{\mathbf{U}}_{\mathcal{B}_{\mathrm{LR}}\to\mathcal{B}_{\mathrm{HV}}} = \frac{1}{\sqrt{2}}\begin{pmatrix}1 & \mathrm{j}\\ \mathrm{j} & 1\end{pmatrix}, \tag{2.23}$$

and

$$\underline{\mathbf{U}}_{\mathcal{B}_{\mathrm{HV}}\to\mathcal{B}_{\mathrm{LR}}} = \frac{1}{\sqrt{2}}\begin{pmatrix}1 & -\mathrm{j}\\ -\mathrm{j} & 1\end{pmatrix}. \tag{2.24}$$

Due to the ambiguity of the propagation direction $+\mathbf{e}_{\mathbf{k}}$ of each Jones vector, the basis transformation is ambiguous as well.

Table 2.1: Jones vectors in the two most common bases for typical polarization states

Polarization state	**Type**	**Jones vector** $\hat{\underline{\mathbf{E}}}_{\mathcal{B}_{\mathrm{HV}}}$	**Jones vector** $\hat{\underline{\mathbf{E}}}_{\mathcal{B}_{\mathrm{LR}}}$
horizontal	linear	$\begin{pmatrix} 1 & 0 \end{pmatrix}^T$	$\frac{1}{\sqrt{2}}\begin{pmatrix} 1 & 1 \end{pmatrix}^T$
vertical	linear	$\begin{pmatrix} 0 & 1 \end{pmatrix}^T$	$\frac{\mathrm{j}}{\sqrt{2}}\begin{pmatrix} -1 & 1 \end{pmatrix}^T$
diagonal	linear	$\frac{1}{\sqrt{2}}\begin{pmatrix} 1 & 1 \end{pmatrix}^T$	$\frac{1}{2}\begin{pmatrix} 1-\mathrm{j} & 1+\mathrm{j} \end{pmatrix}^T$
anti-diagonal	linear	$\frac{1}{\sqrt{2}}\begin{pmatrix} 1 & -1 \end{pmatrix}^T$	$\frac{1}{2}\begin{pmatrix} 1+\mathrm{j} & 1-\mathrm{j} \end{pmatrix}^T$
left-hand	circular	$\frac{1}{\sqrt{2}}\begin{pmatrix} 1 & \mathrm{j} \end{pmatrix}^T$	$\begin{pmatrix} 1 & 0 \end{pmatrix}^T$
right-hand	circular	$\frac{1}{\sqrt{2}}\begin{pmatrix} \mathrm{j} & 1 \end{pmatrix}^T$	$\begin{pmatrix} 0 & 1 \end{pmatrix}^T$

The transformations considered so far refer to the positive propagation direction, i.e., $\underline{\mathbf{U}}_{\mathcal{B}\to\mathcal{B}'} = \underline{\mathbf{U}}^{+}_{\mathcal{B}\to\mathcal{B}'}$. If the opposite propagation direction is considered, a different transformation has to be considered referred to as $\underline{\mathbf{U}}^{-}_{\mathcal{B}\to\mathcal{B}'}$ in the following. As shown in [44], the linear basis Jones vectors of opposite directions are linked by conjugation, i.e., $\underline{\mathbf{E}}^{-}_{\mathcal{B}} = \underline{\mathbf{E}}^{+\,*}_{\mathcal{B}}$. As a consequence, the transformation can be derived by

$$\underline{\mathbf{E}}^{-}_{\mathcal{B}'} = \underline{\mathbf{E}}^{+\,*}_{\mathcal{B}'} = \left(\underline{\mathbf{U}}^{+}_{\mathcal{B}\to\mathcal{B}'}\underline{\mathbf{E}}^{+}_{\mathcal{B}}\right)^{*} = \underline{\mathbf{U}}^{+\,*}_{\mathcal{B}\to\mathcal{B}'}\underline{\mathbf{E}}^{-}_{\mathcal{B}} \tag{2.25}$$

to be

$$\underline{\mathbf{U}}^{-}_{\mathcal{B}\to\mathcal{B}'} = \underline{\mathbf{U}}^{+\,*}_{\mathcal{B}\to\mathcal{B}'}. \tag{2.26}$$

2.3 Polarimetry

In addition to the positional quantities of surrounding objects addressed in Section 2.1, a radar typically measures a spatially allocated reflection strength. Because it is an inherent characteristic of the reflecting object, unlike the previous positional ones, reflectivity can be used to draw conclusions about intrinsic properties of the object itself, as discussed in Section 2.3.1. Based on this, the definition of radar cross-section (RCS) as a scalar measure of reflectivity and the associated radar equation are introduced in Section 2.3.2 and Section 2.3.3, although non-polarimetric up to this point. However, the extension of reflectivity to a polarization-dependent quantity builds on these scalar quantities and the mathematical framework of a scattering matrix for polarimetric evaluation is described in Section 2.3.4. Any interpretation of this scattering matrix strongly depends on the employed polarization basis, such that transformation between bases is an important tool for analysis, which is derived in Section 2.3.5. A formal description of varying scattering behavior relies on a stochastic formulation by a second order moment in form of a polarimetric covariance matrix and is introduced in Section 2.3.6. For interpretation of real scattering matrices, the decomposition into basic scattering mechanisms is helpful. Typical examples of such canonical scatterers are presented in Section 2.3.7. Last, the dependence of the polarimetric configuration of virtual array elements on the realization of the antenna elements is subject of Section 2.3.10.

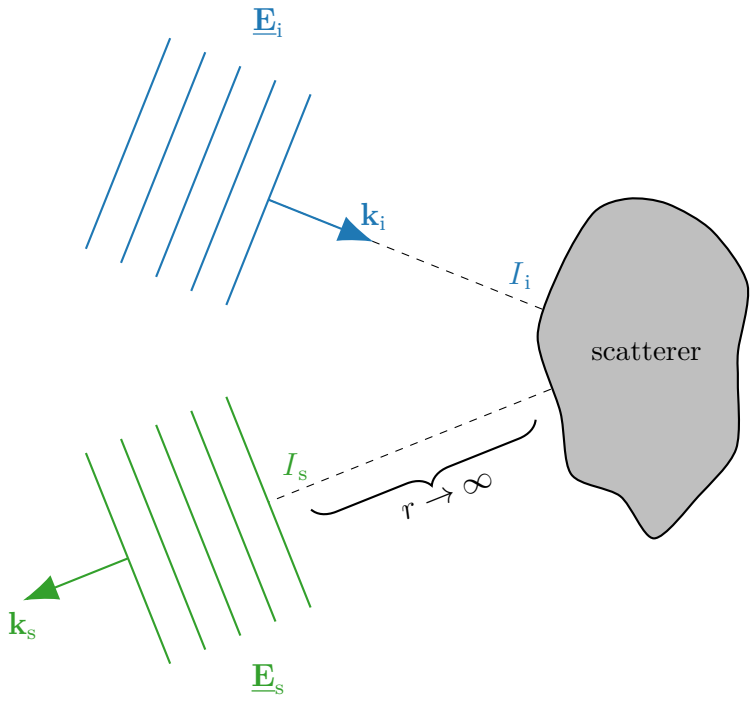


Figure 2.8: The definition of RCS is based on the ratio of incident and scattered energy flux densities measured at different positions.

2.3.1 Electromagnetic scattering in radar

When the electromagnetic properties of the propagation medium change, this transition causes scattering and is typically observed when the wave is interacting with an object after propagation through free space in radar applications. With a hypothetical exact knowledge of the medium's electrical properties and Maxwell's equations, the behavior of the re-radiated wave can be calculated. This is of interest in many radar applications. It includes, on the one hand, the reflected power for conventional radar systems but, on the other hand, also polarization for polarimetric applications [9]. The quantities to characterize objects based on these properties are introduced in the following.

2.3.2 Radar cross-section

Based on the Jones vector, the corresponding time-averaged energy flux density can be derived from the Poynting vector to be

$$I = \frac{\|\underline{\mathbf{E}}\|^2}{2Z_0} \tag{2.27}$$

where $\|\cdot\|$ is the ℓ^2-norm and Z_0 is the free space impedance [10]. For the definition of the RCS, a scattering geometry as shown in Fig. 2.8 is considered. Assuming an incident wave, which is denoted by the subscript i, is planar at the reflecting object, then the RCS σ describes an effective reflecting area such that the scattered power P_s is expressed with

$$P_\mathrm{s} = \sigma I_\mathrm{i} \tag{2.28}$$

with the subscript s denoting scattered quantities [49]. The RCS definition includes the idealization of the reflecting object to an isotropic scatterer [9, 10, 49] such that the scattered power is uniformly distributed in all directions as a spherical wave and the energy flux density can be calculated by

$$I_\mathrm{s} = \frac{P_\mathrm{s}}{4\pi {r_\mathrm{Rx}}^2} \tag{2.29}$$

with r_Rx being the range to a virtual receiving antenna [49]. In order to ensure the validity of the plane wave assumption, which is a prerequisite for (2.27) among others, the far-field has to be considered. Introduction of the limit $\lim_{r_\mathrm{Rx}\to\infty}$ ensures the latter. Together with (2.27), (2.28) and (2.29) lead to the well-known RCS definition [9, 10, 49]

$$\sigma = \lim_{r_\mathrm{Rx}\to\infty} 4\pi {r_\mathrm{Rx}}^2 \frac{I_\mathrm{s}}{I_\mathrm{i}} \overset{(2.27)}{=} \lim_{r_\mathrm{Rx}\to\infty} 4\pi {r_\mathrm{Rx}}^2 \frac{\left\|\underline{\mathbf{E}}_\mathrm{s}\right\|^2}{\left\|\underline{\mathbf{E}}_\mathrm{i}\right\|^2}. \tag{2.30}$$

The different measurement positions for the incident and scattered flux densities are illustrated in Fig. 2.8. Positioning of the flux density symbols in the drawing underlines this. Combining the quadratic dependency of the range with the square of the $1/r_\mathrm{Rx}$ loss of the scattered field amplitude in far-field, the RCS is independent of the actual range aiming to serve as a pure measure of the scatterer's reflectivity. The reflectivity of an object is influenced by its material composition and the geometrical structure, which is seen by the radar. Therefore, also parameters that are related to the measuring radar system have an impact on the apparent reflectivity. First, the frequency used is important because the geometrical properties must always be seen in relation to the wavelength. Second, the direction from which the incident wave is impinging and the direction in which the receiver is placed have a strong impact on the observed RCS. A distinction is made between setups, where transmitter and receiver are spatially distributed (bistatic) and where both are co-located (monostatic). Third, the polarization of the incident wave and the polarization of the receiving antenna can have a significant effect onto the observed RCS. While a non-polarimetric radar emits a fixed polarization and is only able to receive one particular polarization, both determined by the antenna realization, a polarimetric radar can either adaptively control the transmitted polarization or discriminate between different polarizations in the receiver or both. This allows for acquiring additional information about the scattering object.

Accordingly, there is not one single RCS for an object of interest but an entire range of possible values depending on all the mentioned factors. A mathematically sound approach to describe the polarization dependency will be given in Section 2.3.4. Considering these numerous influencing factors, it is evident that there is no simple direct dependence of the RCS on the scatterer's physical cross-section. The RCS must rather be interpreted as an effective area that typically is not physically available.

2.3.3 Radar equation

The so-called radar equation describes the power along the whole signal propagation path, starting shortly before the transmitting antenna all the way to the scatterer and back to shortly after the receiving antenna. Based on the RCS definition (2.30), the radar equation can be expressed as

$$P_{\mathrm{Rx}} = \frac{P_{\mathrm{Tx}} G_{\mathrm{Tx}} G_{\mathrm{Rx}} {\lambda_c}^2}{(4\pi)^3 {r_{\mathrm{Tx}}}^2 {r_{\mathrm{Rx}}}^2} \sigma \tag{2.31}$$

where G_{Tx} and G_{Rx} are the transmit and receive antenna gains, respectively [49]. The range from the scatterer to the transmitter r_{Tx} and to the receiver r_{Rx} are the same for a monostatic or quasi-monostatic setup, which will be considered in the following unless otherwise noted, i.e., $r = r_{\mathrm{Rx}} = r_{\mathrm{Tx}}$. For calculation of a detected object's RCS, the received power P_{Rx} has to be put in the radar equation together with a set of known parameters from calibration such as the antenna gain patterns G_{Tx} and G_{Rx} and the transmit power P_{Tx} as well as some measured quantities such as the range r and angles for correct evaluation of the antenna patterns.

2.3.4 Scattering matrix

As explained above, the polarization state of any fully polarized wave can be described by the two-dimensional Jones vector. For spanning the space of possible polarizations, two orthogonal basis vectors are required. In order to describe an arbitrary scattering event completely, a 2×2 matrix is a useful representation for the transformation of an incident Jones vector $\underline{\mathbf{E}}_{\mathrm{i}}^{+}$ expressed in a basis $\mathcal{B}_{\mathrm{i}} = \{\Phi, \Psi\}$ into a scattered Jones vector $\underline{\mathbf{E}}_{\mathrm{s}}^{-}$ in a basis $\mathcal{B}_{\mathrm{s}} = \{\Phi', \Psi'\}$ as

$$\underline{\mathbf{E}}_{\mathrm{s}}^{-} = \underline{\mathbf{S}}_{\mathcal{B}_{\mathrm{s}}\mathcal{B}_{\mathrm{i}}} \underline{\mathbf{E}}_{\mathrm{i}}^{+} = \begin{pmatrix} \underline{S}_{\Phi'\Phi} & \underline{S}_{\Phi'\Psi} \\ \underline{S}_{\Psi'\Phi} & \underline{S}_{\Psi'\Psi} \end{pmatrix} \underline{\mathbf{E}}_{\mathrm{i}}^{+}, \tag{2.32}$$

where the scattering coefficients $\underline{S}_{p'q} \in \mathbb{C}$ have a subscript order with the scattered basis first and the incident basis second ($p' \in \mathcal{B}_{\mathrm{s}}$, $q \in \mathcal{B}_{\mathrm{i}}$) such that $\underline{\mathbf{S}}_{\mathcal{B}_{\mathrm{s}}\mathcal{B}_{\mathrm{i}}} \in \mathbb{C}^{2\times 2}$ [44]. Due to the setup of the utilized radar, this work considers only the more common case of an identical basis of the incident and scattered Jones vectors. Therefore, $\mathcal{B} = \mathcal{B}_{\mathrm{i}} = \mathcal{B}_{\mathrm{s}}$ applies. A visual element interpretation of an exemplary circular basis scattering matrix is given by Fig. 2.9.

In this work, only monostatic radar setups are considered. The bistatic angle β, which is defined as shown in Fig. 2.10 to measure the difference angle between the incident wave and the direction in which the scattered wave is observed, approaches zero in these setups. Two orientation relations between the polarization basis vectors and the propagation direction are possible, which constitute two different conventions called scatter alignments. As indicated by the superscripts in (2.32), the propagation directions are defined to oppose each other in this work. Furthermore, if the polarization basis vectors for incident and scattered components are chosen to match with each other in the monostatic case ($\beta = 0$), the so-called back scatter alignment (BSA) convention is used and the scattering matrix is called Sinclair matrix [44]. It should be noted that the handedness of the incident and scattered coordinate systems is not the same in this case.

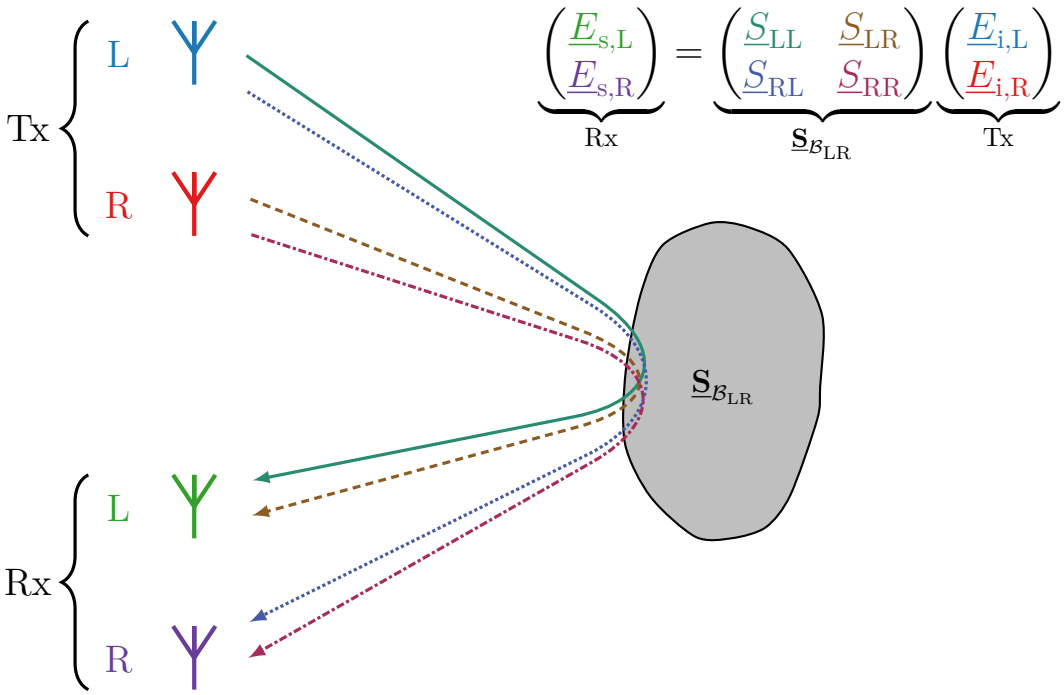


Figure 2.9: Each element of the scattering matrix can be interpreted as the scattering response for one combination of incident and scattered polarization. The element $\underline{S}_{pq}$ describes the response of an incident polarization q measured in the scattered polarization p. This example is based on a circular basis.

This convention is mainly used in radar polarimetry, and it represents a significant difference to optical polarimetry. For optical applications, the forward scatter alignment (FSA) is the more natural convention due to the fundamentally different scattering geometry [44].
Assuming that the radars in the following are at least quasi-monostatic, such that an approximation as a monostatic setup is valid for all considered detection ranges, reciprocity is valid in linear environments, i.e., $\underline{S}_{\Phi\Psi} = \underline{S}_{\Psi\Phi}$ [50]. With that, the Sinclair matrix can be decomposed according to

$$\underline{\mathbf{S}}_{\mathcal{B}} = \begin{pmatrix} \underline{S}_{\Phi\Phi} & \underline{S}_{\Phi\Psi} \\ \underline{S}_{\Psi\Phi} & \underline{S}_{\Psi\Psi} \end{pmatrix} = \underbrace{e^{\mathrm{j}\phi_{\Phi\Psi}}}_{\substack{\text{Absolute} \\ \text{phase}}} \underbrace{|\underline{S}_{\Phi\Psi}|}_{\substack{\text{Absolute} \\ \text{amplitude}}} \underbrace{\begin{pmatrix} \frac{|\underline{S}_{\Phi\Phi}|}{|\underline{S}_{\Phi\Psi}|} e^{\mathrm{j}(\phi_{\Phi\Phi}-\phi_{\Phi\Psi})} & 1 \\ 1 & \frac{|\underline{S}_{\Psi\Psi}|}{|\underline{S}_{\Phi\Psi}|} e^{\mathrm{j}(\phi_{\Psi\Psi}-\phi_{\Phi\Psi})} \end{pmatrix}}_{\text{Relative matrix}} \tag{2.33}$$

with an arbitrarily chosen element $\underline{S}_{\Phi\Psi}$ that is factored out. The absolute phase term is highly ambiguous in the considered applications and does not contain useful information. The absolute amplitude factor can be interpreted as a general measure for reflectivity, which is similar to the scalar RCS of a non-polarimetric radar with respect to the information content. Additional information of a polarimetric radar is contained in the remaining relative matrix. In case of a fully polarimetric monostatic radar, two additional independent amplitudes as well as two independent phases are available.

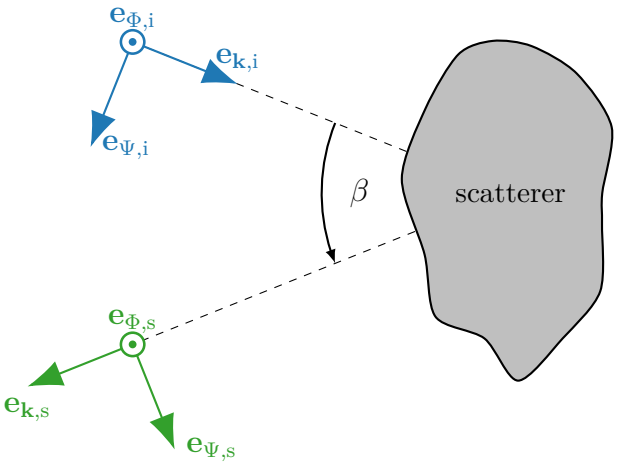


Figure 2.10: The BSA convention is commonly used for monostatic radar applications and defines the orientation of the incident and scattered wave vectors with respect to their basis vectors. This convention is chosen in this thesis and is characterized by an opposite handedness between the incident and scattered coordinate system spanned by the respective basis and wave vectors.

The RCS definition (2.30) can be extended to a polarization dependent measure, which is linked to the magnitudes of the Sinclair matrix elements. Up to four different RCS values can represent a reflectivity for each combination of incident and scattered polarization with

$$\sigma_{pq} = \lim_{r\to\infty} 4\pi r^2 \frac{\left|\underline{E}_{\mathrm{s},p}\right|^2}{\left|\underline{E}_{\mathrm{i},q}\right|^2} = \lim_{r\to\infty} 4\pi r^2 \left|\underline{S}_{pq}\right|^2, \tag{2.34}$$

where $p, q \in \mathcal{B}$. Compared to the full Sinclair matrix, the phase information is missing in this representation. In order to keep the full information including different scattering behavior encoded in the relative phases, the complex Sinclair matrix is the most common representation since polarimetric radar systems with phase measuring capability became available [9].

Statistical distribution

The typical resolution cell in most radar applications is so large that multiple scatterers have to be considered to contribute to the observed scattering coefficients. If the number of scatterers is sufficiently large, the central limit theorem applies, and each scattering coefficient can be assumed to follow a zero-mean complex Gaussian distribution denoted by $\underline{S}_{pq} \sim \mathcal{CN}\left(0, \sigma_{pq}^2\right)$. By transforming to a polar interpretation, it can be shown that the amplitude follows a Rayleigh distribution, whereas the phase is uniformly distributed [9, 51]. The latter agrees with the statement about the absolute phase term in (2.33) not containing information useful to the considered applications.

In order to describe the distribution of all elements of the scattering matrix including the correlation between its elements, the scattering matrix is vectorized. This reformulation allows interpreting the scattering vector as an observation of a multivariate random process. The vectorized scattering matrix is called the lexicographic feature vector given by

$$\underline{\mathbf{\Omega}}_{\mathcal{B}} = \mathrm{vec}\left[\underline{\mathbf{S}}_{\mathcal{B}}\right] = \mathrm{vec}\left[\begin{pmatrix} \underline{S}_{\Phi\Phi} & \underline{S}_{\Phi\Psi} \\ \underline{S}_{\Psi\Phi} & \underline{S}_{\Psi\Psi} \end{pmatrix}\right] = \begin{pmatrix} \underline{S}_{\Phi\Phi} \\ \underline{S}_{\Phi\Psi} \\ \underline{S}_{\Psi\Phi} \\ \underline{S}_{\Psi\Psi} \end{pmatrix} \tag{2.35}$$

with $\underline{\mathbf{\Omega}}_{\mathcal{B}} \in \mathbb{C}^4$ for a generalized fully polarimetric bistatic scattering matrix (full dimensionality $\nu = 4$). The basis $\mathcal{B}$ is dropped in the following for conciseness as long as it is not relevant for the discussed concept. For monostatic reciprocal setups, the feature vector can be compressed to three elements as $\underline{\mathbf{\Omega}} = \begin{pmatrix} \underline{S}_{\Phi\Phi} & \sqrt{2}\underline{S}_{\Phi\Psi} & \underline{S}_{\Psi\Psi} \end{pmatrix}^T$, where the factor $\sqrt{2}$ ensures power invariance ($\nu = 3$) [9]. Lower dimensionality extensions ($\nu < 3$), e.g., for dual-polarimetric experiments, are straightforward. Assuming a zero-mean complex Gaussian distribution for each scattering coefficient, the first order moment in form of the expected value of the feature vector is a zero vector. The statistical correlation between the elements is given by the second order moment in form of a covariance matrix $\underline{\mathbf{C}} = \mathbb{E}\left(\underline{\mathbf{\Omega}}\,\underline{\mathbf{\Omega}}^H\right), \underline{\mathbf{C}} \in \mathbb{C}^{\nu\times\nu}$, where $\cdot^H$ denotes the Hermitian transpose and $\mathbb{E}\left(\cdot\right)$ the expected value. Hence, the feature vector can be interpreted as a complex normal random vector following a multivariate complex normal distribution denoted by $\underline{\mathbf{\Omega}} \sim \mathcal{CN}\left(\mathbf{0}, \underline{\mathbf{C}}\right)$. The corresponding probability density function is defined by

$$p_{\underline{\mathbf{\Omega}}} = \frac{1}{\pi^\nu \left|\underline{\mathbf{C}}\right|} \exp\left(-\underline{\mathbf{\Omega}}^H \underline{\mathbf{C}}^{-1} \underline{\mathbf{\Omega}}\right) \tag{2.36}$$

with the covariance's determinant denoted by $|\underline{\mathbf{C}}|$ [9, 51].

2.3.5 Scattering matrix basis transformation

If a radar system is able to measure all elements of the scattering matrix including the corresponding phases, a purely mathematical transformation between different bases is possible. This allows to take advantage of the properties each basis has to offer for a specific application. With the above-mentioned definitions, the rule to perform a basis change can be derived as

$$\underline{\mathbf{E}}^-_{\mathcal{B}',\mathrm{s}} \overset{(2.22)}{=} \underline{\mathbf{U}}^-_{\mathcal{B}\to\mathcal{B}'}\, \underline{\mathbf{E}}^-_{\mathcal{B},\mathrm{s}} \overset{(2.32)}{=} \underline{\mathbf{U}}^-_{\mathcal{B}\to\mathcal{B}'}\, \underline{\mathbf{S}}_{\mathcal{B}}\, \underline{\mathbf{E}}^+_{\mathcal{B},\mathrm{i}} = \underbrace{\underline{\mathbf{U}}^-_{\mathcal{B}\to\mathcal{B}'}\, \underline{\mathbf{S}}_{\mathcal{B}}\, \underline{\mathbf{U}}^+_{\mathcal{B}\to\mathcal{B}'}{}^{-1}}_{\underline{\mathbf{S}}_{\mathcal{B}'}}\, \underline{\mathbf{E}}^+_{\mathcal{B}',\mathrm{i}}. \tag{2.37}$$

It follows that

$$\underline{\mathbf{S}}_{\mathcal{B}'} = \underline{\mathbf{U}}^-_{\mathcal{B}\to\mathcal{B}'}\, \underline{\mathbf{S}}_{\mathcal{B}}\, \underline{\mathbf{U}}^+_{\mathcal{B}\to\mathcal{B}'}{}^{-1} \overset{(2.26)}{=} \underline{\mathbf{U}}^+_{\mathcal{B}\to\mathcal{B}'}{}^{*}\, \underline{\mathbf{S}}_{\mathcal{B}}\, \underline{\mathbf{U}}^+_{\mathcal{B}\to\mathcal{B}'}{}^{-1} = \underline{\mathbf{U}}^+_{\mathcal{B}'\to\mathcal{B}}{}^{T}\, \underline{\mathbf{S}}_{\mathcal{B}}\, \underline{\mathbf{U}}^+_{\mathcal{B}'\to\mathcal{B}}, \tag{2.38}$$

which is known as a con-similarity transformation [9, 44, 51].

This is a direct consequence of the chosen BSA. A similarity transformation is resulting when using FSA [44]. For the common linear and circular bases, the transformations between both are given by

$$\begin{aligned}\underline{\mathbf{S}}_{\mathcal{B}_{\mathrm{LR}}} &= 0.5 \begin{pmatrix} 1 & \mathrm{j} \\ \mathrm{j} & 1 \end{pmatrix} \underline{\mathbf{S}}_{\mathcal{B}_{\mathrm{HV}}} \begin{pmatrix} 1 & \mathrm{j} \\ \mathrm{j} & 1 \end{pmatrix} \\ &= 0.5 \begin{pmatrix} \underline{S}_{\mathrm{HH}} + \mathrm{j}\underline{S}_{\mathrm{HV}} + \mathrm{j}\underline{S}_{\mathrm{VH}} - \underline{S}_{\mathrm{VV}} & \mathrm{j}\underline{S}_{\mathrm{HH}} + \underline{S}_{\mathrm{HV}} - \underline{S}_{\mathrm{VH}} + \mathrm{j}\underline{S}_{\mathrm{VV}} \\ \mathrm{j}\underline{S}_{\mathrm{HH}} - \underline{S}_{\mathrm{HV}} + \underline{S}_{\mathrm{VH}} + \mathrm{j}\underline{S}_{\mathrm{VV}} & -\underline{S}_{\mathrm{HH}} + \mathrm{j}\underline{S}_{\mathrm{HV}} + \mathrm{j}\underline{S}_{\mathrm{VH}} + \underline{S}_{\mathrm{VV}} \end{pmatrix}\end{aligned} \tag{2.39}$$

[52, p. 56] and

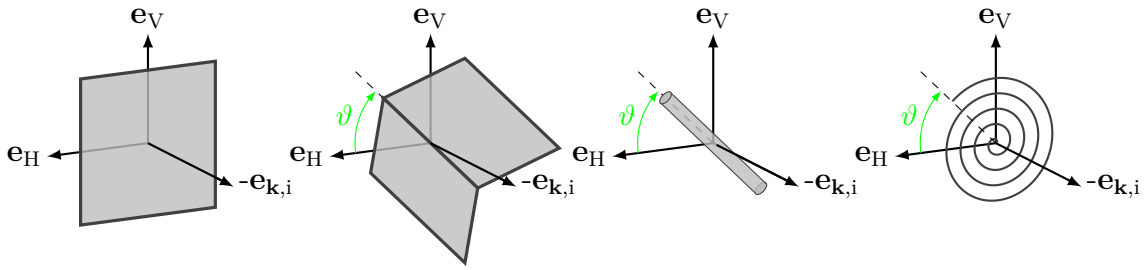
$$\begin{aligned}\underline{\mathbf{S}}_{\mathcal{B}_{\mathrm{HV}}} &= 0.5 \begin{pmatrix} 1 & -\mathrm{j} \\ -\mathrm{j} & 1 \end{pmatrix} \underline{\mathbf{S}}_{\mathcal{B}_{\mathrm{LR}}} \begin{pmatrix} 1 & -\mathrm{j} \\ -\mathrm{j} & 1 \end{pmatrix} \\ &= 0.5 \begin{pmatrix} \underline{S}_{\mathrm{LL}} - \mathrm{j}\underline{S}_{\mathrm{LR}} - \mathrm{j}\underline{S}_{\mathrm{RL}} - \underline{S}_{\mathrm{RR}} & -\mathrm{j}\underline{S}_{\mathrm{LL}} + \underline{S}_{\mathrm{LR}} - \underline{S}_{\mathrm{RL}} - \mathrm{j}\underline{S}_{\mathrm{RR}} \\ -\mathrm{j}\underline{S}_{\mathrm{LL}} - \underline{S}_{\mathrm{LR}} + \underline{S}_{\mathrm{RL}} - \mathrm{j}\underline{S}_{\mathrm{RR}} & -\underline{S}_{\mathrm{LL}} - \mathrm{j}\underline{S}_{\mathrm{LR}} - \mathrm{j}\underline{S}_{\mathrm{RL}} + \underline{S}_{\mathrm{RR}} \end{pmatrix}.\end{aligned} \tag{2.40}$$

2.3.6 Polarimetric covariance matrix

While a scattering matrix is sufficient to represent the scattering properties of a single scatterer at one instance of time, the typical scenarios considered in this work consist of multiple scatterers per resolution cell that are observed for some non-negligible duration. The observed signature of the collection of scatterers heavily depends on the phases in the coherent superposition of their individual scattering coefficients. As small spatial movements can change the phases significantly for the considered operating frequencies, the varying scattering information has to be processed by statistical methods to appropriately represent the measurements. The varying coherent superposition can be either caused by relative movements of the scatterers in one resolution cell with respect to themselves or by a change of the observation position of the radar system. Scatterers that show such behavior are called depolarizing incoherently scattering [46] or distributed targets [9] in literature.
Due to this non-stationarity, the single scattering matrix is not an appropriate representation for such targets. Instead, a statistical description via an estimation of the second order moment in form of a covariance matrix $\underline{\mathbf{C}}$ is suitable to characterize such spatially and temporally variant scattering behavior. As the observation is of finite duration, the true covariance is unknown and only an estimate can be calculated for which the expected value equals the true covariance ($\mathbb{E}(\underline{\mathbf{Z}}) = \underline{\mathbf{C}}$). Averaging all Hermitian products of the observed feature vectors $\underline{\boldsymbol{\Omega}}_i$ is such an unbiased maximum likelihood estimator, which is given by

$$\underline{\mathbf{Z}} = \frac{1}{N_{\underline{\mathbf{Z}}}} \sum_{i=1}^{N_{\underline{\mathbf{Z}}}} \underline{\boldsymbol{\Omega}}_i \, \underline{\boldsymbol{\Omega}}_i^{H} \tag{2.41}$$

with $\underline{\mathbf{Z}} \in \mathbb{C}^{\nu \times \nu}$. This matrix is also called sample or multi-look covariance matrix [51].



(a) plate (b) dihedral (c) dipole (d) helix

Figure 2.11: Canonical scatterers

Statistical distribution

Based on the knowledge of the statistical properties of the feature vector, a probability distribution for the sample covariance matrix can be found. In fact, the complex Wishart distribution is the distribution of the sum of $N_{\underline{\mathbf{Z}}}$ sample covariance matrices of zero-mean complex Gaussian random vectors and is denoted by $\mathcal{CW}_\nu\left(\underline{\mathbf{C}}, N_{\underline{\mathbf{Z}}}\right)$. Because the covariance estimator is additionally normalized by $1/N_{\underline{\mathbf{Z}}}$, the sample covariance matrix follows a scaled complex Wishart distribution $\underline{\mathbf{Z}} \sim \mathcal{CW}_\nu\left(1/N_{\underline{\mathbf{Z}}}\,\underline{\mathbf{C}}, N_{\underline{\mathbf{Z}}}\right)$. According to [9], the probability density can be expressed by

$$p_{\underline{\mathbf{Z}}} = \frac{{N_{\underline{\mathbf{Z}}}}^{\nu N_{\underline{\mathbf{Z}}}}\,|\underline{\mathbf{Z}}|^{N_{\underline{\mathbf{Z}}}-\nu}\exp\left(-N_{\underline{\mathbf{Z}}}\,\mathrm{tr}\left(\underline{\mathbf{C}}^{-1}\underline{\mathbf{Z}}\right)\right)}{|\underline{\mathbf{C}}|^{N_{\underline{\mathbf{Z}}}}\,\pi^{\frac{\nu(\nu-1)}{2}}\,\Pi_{i=1}^{\nu}\Gamma\left(N_{\underline{\mathbf{Z}}}-i+1\right)}, \tag{2.42}$$

where $\mathrm{tr}\left(\cdot\right)$ is the trace of a matrix and $\Gamma\left(\cdot\right)$ is the Gamma function.

2.3.7 Canonical scatterers

When observing a scattering matrix of a single resolution cell with an extent typical for most real-world applications, it usually is the result of a superposition of multiple elementary scattering mechanisms. Despite this circumstance, it is useful to understand the canonical scatterers for interpretation and categorization of any superposed observation. Therefore, the most common canonical objects including their normalized scattering matrices are introduced for the circular polarization basis $\mathcal{B}_\mathrm{LR}$ in the following. The canonical scatterers and the corresponding matrices are derived from the Cartesian polarization basis representations in [9], because the listed circular basis representations are inconsistent, which is mentioned in the following when applicable. Due to the less common usage of the circular polarization covariance matrix in literature, the corresponding matrices are additionally provided for scattering interpretation of its elements. Assuming a monostatic setup, a dimensionality of $\nu = 3$ is sufficient for the covariance.

Flat plate

The flat plate scattering mechanism occurs at several canonical objects. The most simple one is a planar surface, which is giving the most commonly used name "plate mechanism". In theory, an infinite surface is assumed for this model. However, an extent that is large compared to the wavelength is sufficient to use this scattering model, such that also large spheres or cylinders show this behavior. Furthermore, a trihedral corner reflector is another scatterer showing this response. Due to its retro-reflective design, the wave is reflected three times with most reflected energy being directed back in the impinging direction. Such a triple reflection cannot be distinguished from a single reflection event by polarimetry. Therefore, the odd-bounce scattering mechanism class is used, which is characterized by an odd numbers of reflections occurring on the propagation path and to which the plate mechanism belongs. A visual representation of the most simple scatterer showing the plate mechanism is given by Fig. 2.11a. The corresponding matrices are

$$\underline{\mathbf{S}}_{\mathcal{B}_{\mathrm{LR}},\mathrm{pl}} = \frac{1}{\sqrt{2}} \begin{pmatrix} 0 & \mathrm{j} \\ \mathrm{j} & 0 \end{pmatrix}, \qquad \underline{\mathbf{C}}_{\mathcal{B}_{\mathrm{LR}},\mathrm{pl}} = \begin{pmatrix} 0 & 0 & 0 \\ 0 & 1 & 0 \\ 0 & 0 & 0 \end{pmatrix} \tag{2.43}$$

in line with [9, p. 92]. Typical examples of objects that show such a scattering mechanism in automotive environments include tree trunks, walls, fences as well as poles of traffic signs, traffic lights and street lamps.

Dihedral

The dihedral scattering mechanism occurs when two plates are located orthogonally to each other. It acts as a retro-reflective object like the trihedral corner reflector, but only exhibits two reflection events due to its mechanical design. The scattering matrix structure of any even number of reflections is the same, such that the corresponding objects are called even-bounce scatterers. In contrary to the plate mechanism, the scattering response strongly depends on the rotation of the seam, which is the axis at which both parts contact each other. The rotation angle is defined in Fig. 2.11b and leads to the following matrices

$$\underline{\mathbf{S}}_{\mathcal{B}_{\mathrm{LR}},\mathrm{dih}} = \frac{1}{\sqrt{2}} \begin{pmatrix} e^{\mathrm{j}2\vartheta} & 0 \\ 0 & -e^{-\mathrm{j}2\vartheta} \end{pmatrix}, \quad \underline{\mathbf{C}}_{\mathcal{B}_{\mathrm{LR}},\mathrm{dih}} = \frac{1}{2} \begin{pmatrix} 1 & 0 & -e^{\mathrm{j}4\vartheta} \\ 0 & 0 & 0 \\ -e^{-\mathrm{j}4\vartheta} & 0 & 1 \end{pmatrix}. \tag{2.44}$$

It should be noted that the scattering matrix in reference [9, p. 95] is wrong for the special unitary circular basis [53, p. 6829] and the corrected sign is used. Typical examples of objects that show such a scattering mechanism in automotive environments include door or window recesses of buildings, fence posts, and guardrail posts.

Dipole

The dipole scattering mechanism occurs at cylindrical objects with a diameter smaller than the wavelength. Objects with such scattering behavior only reflect the projection of the incoming polarization state onto the linear polarization parallel to the orientation of the cylinder. Therefore, such objects are referred to as polarizers. An example is depicted in Fig. 2.11c. The corresponding matrices are

$$\underline{\mathbf{S}}_{\mathcal{B}_{\mathrm{LR}},\mathrm{dip}} = \frac{1}{2}\begin{pmatrix} e^{\mathrm{j}2\vartheta} & \mathrm{j} \\ \mathrm{j} & -e^{-\mathrm{j}2\vartheta} \end{pmatrix}, \quad \underline{\mathbf{C}}_{\mathcal{B}_{\mathrm{LR}},\mathrm{dip}} = \frac{1}{4}\begin{pmatrix} 1 & -\mathrm{j}\sqrt{2}e^{\mathrm{j}2\vartheta} & -e^{\mathrm{j}4\vartheta} \\ \mathrm{j}\sqrt{2}e^{-\mathrm{j}2\vartheta} & 2 & -\mathrm{j}\sqrt{2}e^{\mathrm{j}2\vartheta} \\ -e^{-\mathrm{j}4\vartheta} & \mathrm{j}\sqrt{2}e^{-\mathrm{j}2\vartheta} & 1 \end{pmatrix}. \tag{2.45}$$

It should be noted that the scattering matrix in reference [9, p. 94] is wrong for the special unitary circular basis [54, Eq. (23)] and a corrected version is used.
While for example cables of bridges show this scattering behavior for the typical frequencies used in space- and airborne SAR [9], the dipole mechanism is not observed with significant RCSs for common automotive environments and frequencies.

Helix

The helix scattering mechanism is the equivalent of what the dipole is to linear polarization for a circular polarization: a polarizer. Only one handedness of circular polarization gets reflected by such a helical structure. Depending on the handedness, one distinguishes between left- and right-hand helix mechanisms. An example is shown in Fig. 2.11d. With the orientation as defined in Fig. 2.11d and the typical handedness definition, the matrices for left and right helix are

$$\underline{\mathbf{S}}_{\mathcal{B}_{\mathrm{LR}},\mathrm{lhx}} = \begin{pmatrix} e^{\mathrm{j}2\vartheta} & 0 \\ 0 & 0 \end{pmatrix}, \qquad \underline{\mathbf{C}}_{\mathcal{B}_{\mathrm{LR}},\mathrm{lhx}} = \begin{pmatrix} 1 & 0 & 0 \\ 0 & 0 & 0 \\ 0 & 0 & 0 \end{pmatrix}, \tag{2.46}$$

$$\underline{\mathbf{S}}_{\mathcal{B}_{\mathrm{LR}},\mathrm{rhx}} = \begin{pmatrix} 0 & 0 \\ 0 & -e^{\mathrm{j}2\vartheta} \end{pmatrix}, \qquad \underline{\mathbf{C}}_{\mathcal{B}_{\mathrm{LR}},\mathrm{rhx}} = \begin{pmatrix} 0 & 0 & 0 \\ 0 & 0 & 0 \\ 0 & 0 & 1 \end{pmatrix}, \tag{2.47}$$

respectively. This scattering mechanism in its pure form is also rare in typical automotive environments and for common frequencies. However, if multiple dihedral scatterers are in one resolution cell, their superposition can appear as a helix mechanism depending on their relative poses [9].

2.3.8 Coherent decompositions

For interpreting a measured scattering matrix, the coherent decomposition technique can be utilized. It is based on decomposing the scattering matrix into components corresponding to different canonical scatterers. Thus, the scattering matrix $\underline{\mathbf{S}}$ can be interpreted as a coherently weighted superposition of known scattering behavior, which is described by basis matrices $\underline{\mathbf{S}}_i$, by

$$\underline{\mathbf{S}} = \sum_{i=0}^{N} \underline{\alpha}_i \underline{\mathbf{S}}_i \tag{2.48}$$

with the weights $\underline{\alpha}_i \in \mathbb{C}$.

Pauli decomposition

The Pauli decomposition is based on Pauli matrices, which are well-known from quantum mechanics. It is the most widely used decomposition and its application is particularly simple for measurements in the linear basis $\mathcal{B}_{\mathrm{HV}}$. While the utilized radar sensor in this work operates in the circular basis $\mathcal{B}_{\mathrm{LR}}$, some measurements in an anechoic chamber for analyzing scattering behavior were carried out in the mentioned linear basis (cf. Section 5.1) so that the Pauli decomposition is an obvious choice and, thus, relevant for this work. Moreover, circular basis measurements can be transformed according to Section 2.3.5 for application of this decomposition.
The components of the Pauli decomposition are calculated by

$$\mathcal{D}_{\mathrm{Pauli}}\left\{\underline{\mathbf{S}}\right\} = \underbrace{\begin{pmatrix} \underline{\alpha}_0 \\ \underline{\alpha}_1 \\ \underline{\alpha}_2 \\ \underline{\alpha}_3 \end{pmatrix}}_{\underline{\boldsymbol{\alpha}}_{\mathrm{Pauli}}} = \frac{1}{\sqrt{2}} \begin{pmatrix} \underline{S}_{\mathrm{HH}} + \underline{S}_{\mathrm{VV}} \\ \underline{S}_{\mathrm{HH}} - \underline{S}_{\mathrm{VV}} \\ \underline{S}_{\mathrm{HV}} + \underline{S}_{\mathrm{VH}} \\ \mathrm{j}\underline{S}_{\mathrm{HV}} - \mathrm{j}\underline{S}_{\mathrm{VH}} \end{pmatrix} \overset{(2.40)}{=} \frac{1}{\sqrt{2}} \begin{pmatrix} -\mathrm{j}\underline{S}_{\mathrm{LR}} - \mathrm{j}\underline{S}_{\mathrm{RL}} \\ \underline{S}_{\mathrm{LL}} - \underline{S}_{\mathrm{RR}} \\ -\mathrm{j}\underline{S}_{\mathrm{LL}} - \mathrm{j}\underline{S}_{\mathrm{RR}} \\ \mathrm{j}\underline{S}_{\mathrm{LR}} - \mathrm{j}\underline{S}_{\mathrm{RL}} \end{pmatrix} \tag{2.49}$$

with factor $1/\sqrt{2}$ to preserve power [9]. By comparing this to the canonical scatterers from Section 2.3.7, the components can be interpreted as amount and relative phases of the following mechanisms:

- $\underline{\alpha}_0$ characterizes plate scattering,
- $\underline{\alpha}_1$ characterizes axis-aligned dihedral scattering,
- $\underline{\alpha}_2$ characterizes 45°-aligned dihedral scattering,
- $\underline{\alpha}_3$ characterizes anti-symmetric scattering.

The component $\underline{\alpha}_3$ can be assumed to be zero in monostatic measurements due to reciprocity. While the first component $\underline{\alpha}_0$ captures all pure odd-bounce scattering, even-bounce scattering is distributed between $\underline{\alpha}_1$ and $\underline{\alpha}_2$ depending on the rotation of the dihedral axis. Dipole and helix mechanisms are distributed between multiple components as well [45].
For visualization of Pauli-decomposed data, a convention has established in the SAR community [9], which will be followed in this work. The first component $\underline{\alpha}_0$ is colored blue, matching the dominant odd-bounce scattering of the sea. Axis-aligned dihedral scattering from the second component $\underline{\alpha}_1$ is colored red, which is often observed in urban environments. Lastly, the oblique dihedral scattering of $\underline{\alpha}_2$ is colored green, which typically occurs in areas of forest canopy. Thus, a visual relation between the appearance in optical images and the Pauli images is given for these applications.

Krogager decomposition

The Krogager decomposition assumes a symmetric scattering matrix and results in three magnitude and three phase parameters. It is simple to calculate in the circular basis $\mathcal{B}_{\mathrm{LR}}$ and therefore often applied for radars operating in this basis. By comparing the proposed decomposition (adapted from [9] to match chosen basis)

$$\underline{\mathbf{S}}_{\mathcal{B}_{\mathrm{LR}}} = \underbrace{e^{\mathrm{j}\phi}e^{\mathrm{j}\phi_{\mathrm{s}}}\alpha_{\mathrm{s}}}_{\underline{\alpha}_{\mathrm{s}}} \underbrace{\begin{pmatrix} 0 & \mathrm{j} \\ \mathrm{j} & 0 \end{pmatrix}}_{\underline{\mathbf{S}}_{\mathcal{B}_{\mathrm{LR}},\mathrm{pl}}} + \underbrace{e^{\mathrm{j}\phi}\alpha_{\mathrm{d}}}_{\underline{\alpha}_{\mathrm{d}}} \underbrace{\begin{pmatrix} e^{\mathrm{j}2\vartheta} & 0 \\ 0 & -e^{-\mathrm{j}2\vartheta} \end{pmatrix}}_{\underline{\mathbf{S}}_{\mathcal{B}_{\mathrm{LR}},\mathrm{dih}}} + \underbrace{e^{\mathrm{j}\phi}\alpha_{\mathrm{h}}}_{\underline{\alpha}_{\mathrm{h}}} \underbrace{\begin{pmatrix} e^{\mathrm{j}2\vartheta} & 0 \\ 0 & 0 \end{pmatrix}}_{\underline{\mathbf{S}}_{\mathcal{B}_{\mathrm{LR}},\mathrm{lhx}}} \tag{2.50}$$

with the canonical scatterers in Section 2.3.7, the interpretation of the magnitude parameters can directly be derived:

- α_{s} characterizes plate (or sphere) scattering,
- α_{d} characterizes dihedral (or diplane) scattering
- α_{h} characterizes helix scattering.

The subscript symbols are chosen to match the original naming by Krogager, which deviates for plate and dihedral scattering as noted in parentheses [9]. Next to the overall absolute phase ϕ, which does not carry any usable scattering information, a relative displacement phase ϕ_{s} between plate and dihedral mechanism is introduced. Lastly, the angle ϑ describes the rotational orientation of the dihedral scatterer. The parameters can be derived according to

$$\alpha_{\mathrm{s}} = |\underline{S}_{\mathrm{LR}}| \qquad \alpha_{\mathrm{d}} = \min\left(|\underline{S}_{\mathrm{LL}}|, |\underline{S}_{\mathrm{RR}}|\right) \qquad \alpha_{\mathrm{h}} = ||\underline{S}_{\mathrm{LL}}| - |\underline{S}_{\mathrm{RR}}|| \tag{2.51}$$

$$\phi_{\mathrm{s}} = \phi_{\mathrm{LR}} - \tfrac{1}{2}\left(\phi_{\mathrm{LL}} + \phi_{\mathrm{RR}}\right) \qquad \vartheta = \tfrac{1}{4}\left(\phi_{\mathrm{LL}} - \phi_{\mathrm{RR}} + \pi\right) \qquad \phi = \tfrac{1}{2}\left(\phi_{\mathrm{LL}} + \phi_{\mathrm{RR}} - \pi\right) \tag{2.52}$$

with $\phi_{pq} = \sphericalangle \underline{S}_{pq}$ being the phase of the corresponding Sinclair matrix element.
Compared to the Pauli decomposition, the Krogager decomposition maps pure odd-bounce, even-bounce and helix scattering directly to its three magnitude components, which makes interpretation easier. Moreover, the angle ϑ has a direct physical meaning. Only the dipole mechanism is distributed between two magnitude components [45].

2.3.9 Incoherent decompositions

While the coherent decompositions from the previous section help interpreting the scattering behavior associated with a scattering matrix, the incoherent decompositions are the equivalent for covariance matrices. Due to the many parameters, interpretation is non-trivial. However, various tools and approaches are known from SAR literature [9, 52]. One class of decomposition approaches is based on physical scattering models derived for the typical airborne SAR imaging setups combined with specific scatterer properties, such as the Freeman-Durden decomposition [55] or the Yamaguchi decomposition [56].

However, due to the different application in this work, only the more general eigenfactorization-based decompositions are used in this work. With the covariance matrix being positive semidefinite, an eigendecomposition with real non-negative eigenvalues λ_i and orthonormal eigenvectors $\underline{\mathbf{w}}_i$ exists [52]. For a general covariance matrix $\underline{\mathbf{C}}$, it follows

$$\underline{\mathbf{C}} = \underline{\mathbf{W}} \underbrace{\begin{pmatrix} \lambda_1 & 0 & \cdots & 0 \\ 0 & \lambda_2 & & \\ \vdots & & \ddots & \\ 0 & & & \lambda_\nu \end{pmatrix}}_{\mathbf{\Lambda}} \underline{\mathbf{W}}^{-1} = \sum_{i=1}^{\nu} \lambda_i \underline{\mathbf{w}}_i \underline{\mathbf{w}}_i^H \tag{2.53}$$

with $\underline{\mathbf{W}} = \left(\underline{\mathbf{w}}_1 \ \underline{\mathbf{w}}_2 \ \cdots \ \underline{\mathbf{w}}_\nu\right) \in \mathbb{C}^{\nu \times \nu}$ and $\mathbf{\Lambda} = \operatorname{diag}(\lambda_1, \lambda_2, \cdots, \lambda_\nu) \in \mathbb{R}^{\nu \times \nu}$. The eigenvalues are ordered by a decreasing amplitude. Different approaches for interpreting the results of the eigendecomposition were proposed. The most common ones are considered in the following.

Cloude decomposition

The Cloude decomposition considers only the first eigenvector, which corresponds to the largest eigenvalue, as an estimate of the most dominant scattering mechanism [9, 57]. By comparing (2.53) with the covariance calculation in (2.41), one can derive that an equivalent corresponding feature vector to an eigenvalue-eigenvector pair is generally given by

$$\underline{\mathbf{\Omega}}_i = \sqrt{\lambda_i} \underline{\mathbf{w}}_i \tag{2.54}$$

[9, 45]. By considering only the feature vector derived from the first eigenvalue-eigenvector pair, the known coherent decomposition theorems from Section 2.3.8 can be applied for interpretation of this dominant scattering mechanism. If there is only one scattering mechanism involved and observed during covariance calculation, the dominant scattering estimate of the Cloude decomposition is reproducing this exact mechanism because only the first eigenvalue will be non-zero and the eigenvector is identical to the normalized feature vector of this mechanism. The other extreme is reached when all eigenvalues are non-zero and equal. This indicates a depolarizing mix of scatterers so that no further polarimetric interpretation is possible [9]. Consequently, the ratio of the eigenvalues is an important characteristic of a covariance matrix and leads to a decomposition, which is based on this.

Cloude-Pottier decomposition

The Cloude-Pottier decomposition considers the observed covariance as the result of a statistical Bernoulli process [58]. The occurrence probability of each scattering mechanism of the Bernoulli is given by pseudo-probabilities that are calculated from the eigenvalues λ_i according to

$$P_{\lambda_i} = \frac{\lambda_i}{\sum_{n=1}^{\nu} \lambda_n}. \tag{2.55}$$

Based on this, the polarimetric entropy H is defined as a measure of depolarization or randomness. Due to the definition

$$H = -\sum_{i=1}^{\nu} P_{\lambda_i} \log_\nu P_{\lambda_i}, \tag{2.56}$$

the range of possible values is given by $0 \leq H \leq 1$ [52]. The lower limit is reached if only one eigenvalue is non-zero, whereas the upper limit indicates equal non-zero values for a completely depolarizing scatterer.

Another parameter, which is purely based on the eigenvalues, is the polarimetric anisotropy A. It measures the dominance of the second eigenvalue in comparison to the third one as

$$A = \frac{\lambda_2 - \lambda_3}{\lambda_2 + \lambda_3} \tag{2.57}$$

and valid values are from the same range $0 \leq A \leq 1$ [52].

Because both values are calculated purely from the eigenvalues, they are independent from the chosen polarimetric basis [9]. The third important parameter of this decomposition is the average alpha angle $\overline{\alpha_\lambda}$. In order to disambiguate the use of the α symbol, the subscript λ is introduced in the context of the Cloude-Pottier decomposition. The decomposition introduces parameters to describe the eigenvectors with the magnitude of the first components being $\cos(\alpha_{\lambda_i})$, respectively. However, the original formulation is based on the eigendecomposition of the coherency matrix, which is the covariance equivalent constructed from a Pauli feature vector. Therefore, the calculated eigenvectors need to be transformed to a Pauli representation first before deriving the angles α_{λ_i}. Then, the average alpha parameter is determined by weighting with the pseudo-probabilities according to

$$\overline{\alpha_\lambda} = \sum_{i=1}^{\nu} P_{\lambda_i} \alpha_{\lambda_i}. \tag{2.58}$$

The parameter is roll-invariant [9] and describes the average scattering mechanism. It ranges from $\overline{\alpha_\lambda} = 0$ for flat plate scattering, over $\overline{\alpha_\lambda} = 45°$ for dipoles, to $\overline{\alpha_\lambda} = 90°$ for dihedral scattering.

The entropy and alpha parameters are the basis for one well-known classification approach in SAR literature. Because it is used for interpretation of some measurements later on, it is introduced here. The classes are derived from the location of the entropy and alpha parameter pair in a two-dimensional plane as shown in Fig. 2.12 [9].

While originally introduced for a $\nu = 3$ monostatic, fully polarimetric setup in [58], it also scales to the more general bistatic case ($\nu = 4$) or a restricted $\nu = 2$ variant [52], which is an advantageous property of this approach. However, the class regions and the feasible region curve change in these cases [52].

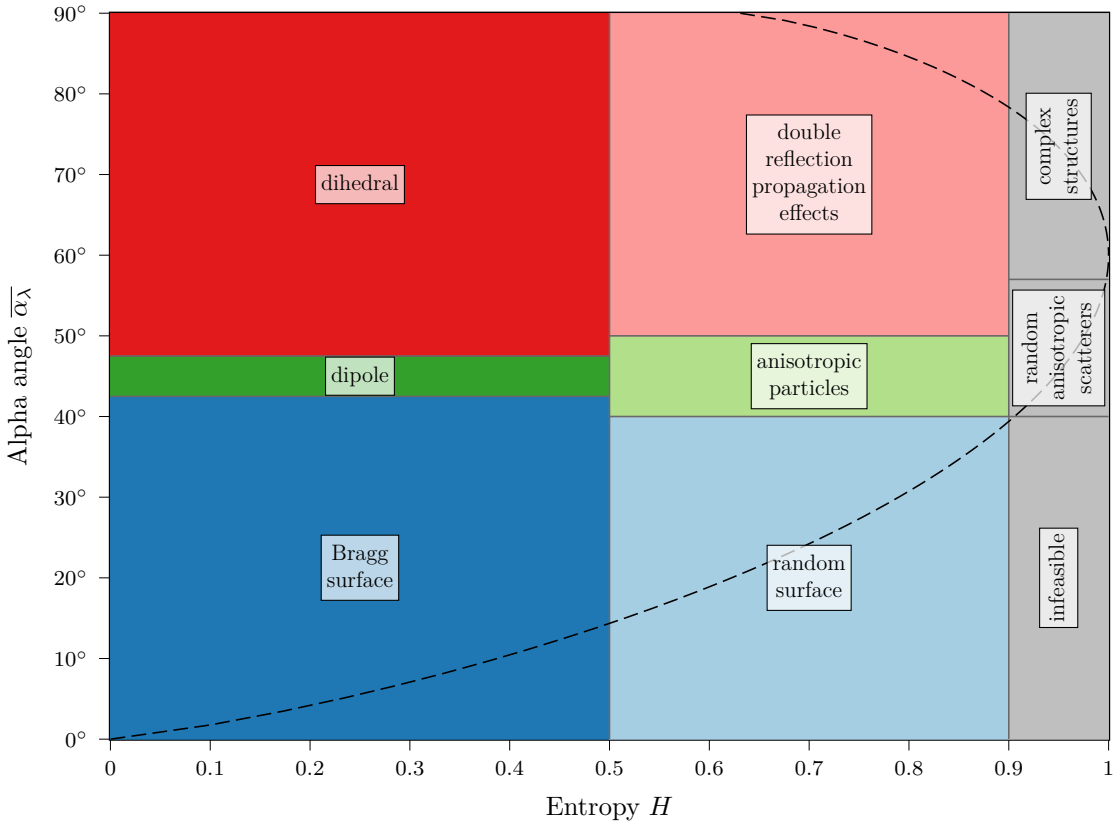


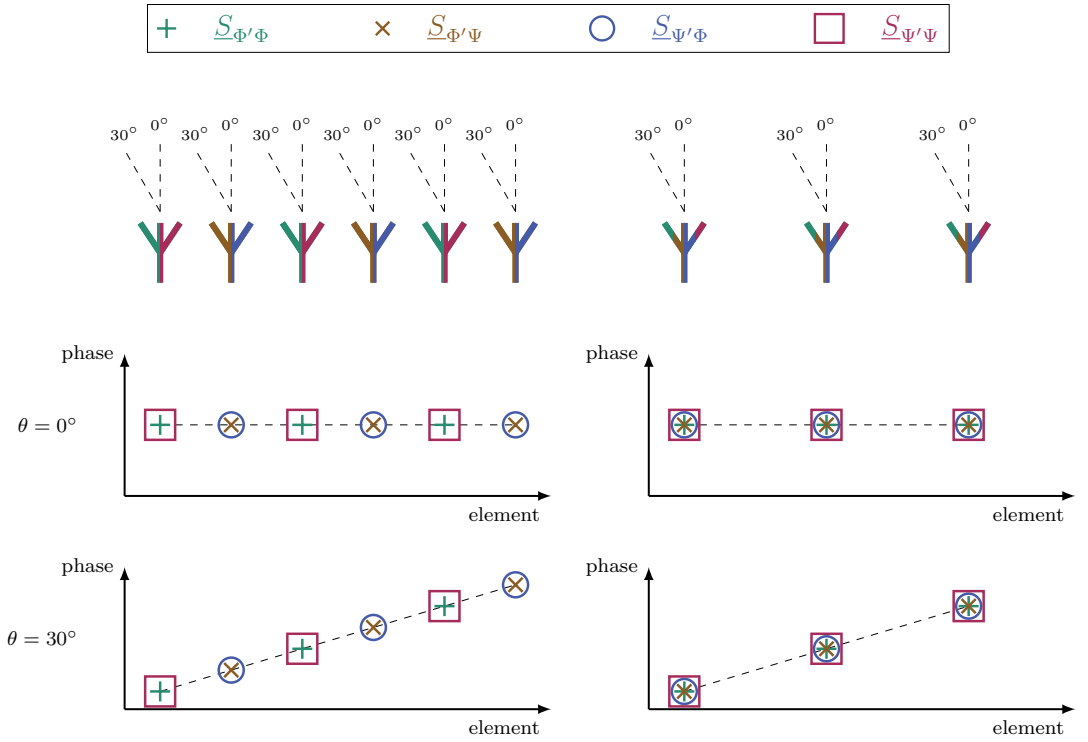
Figure 2.12: The $H/\overline{\alpha_\lambda}$ plane is used to classify scattering behavior of observed covariance matrices. The shown plane is for a monostatic setup ($\nu = 3$) with the colors for the different classes being used for visualization and interpretation of measurements in automotive environments below. The dashed line marks the area of valid values.

2.3.10 Virtual polarimetric array

In any polarimetric radar system with DBF capabilities, the array design and the approach to acquiring the scattering matrix elements are closely connected. According to the sensor used in the experimental part of this thesis, the following discussion assumes two prerequisites:

- a fully polarimetric radar system is used in a sense that all four elements of the scattering matrix are generally available (partially polarimetric systems may only suffer from some of the discussed limitation),
- the angular spectra of the polarimetric channels are processed separately as the scattering matrix information dependency on the angle is of interest (as opposed to the "polarization state as nuisance parameter" approach in [59]).

Depending on the polarizations of the transmit and receive antennas, each virtual array element is tied to one component of the polarimetric scattering matrix (see Section 2.1.3 for virtual element definition). Therefore, the virtual array of a fully polarimetric radar must include virtual elements of all scattering matrix components.

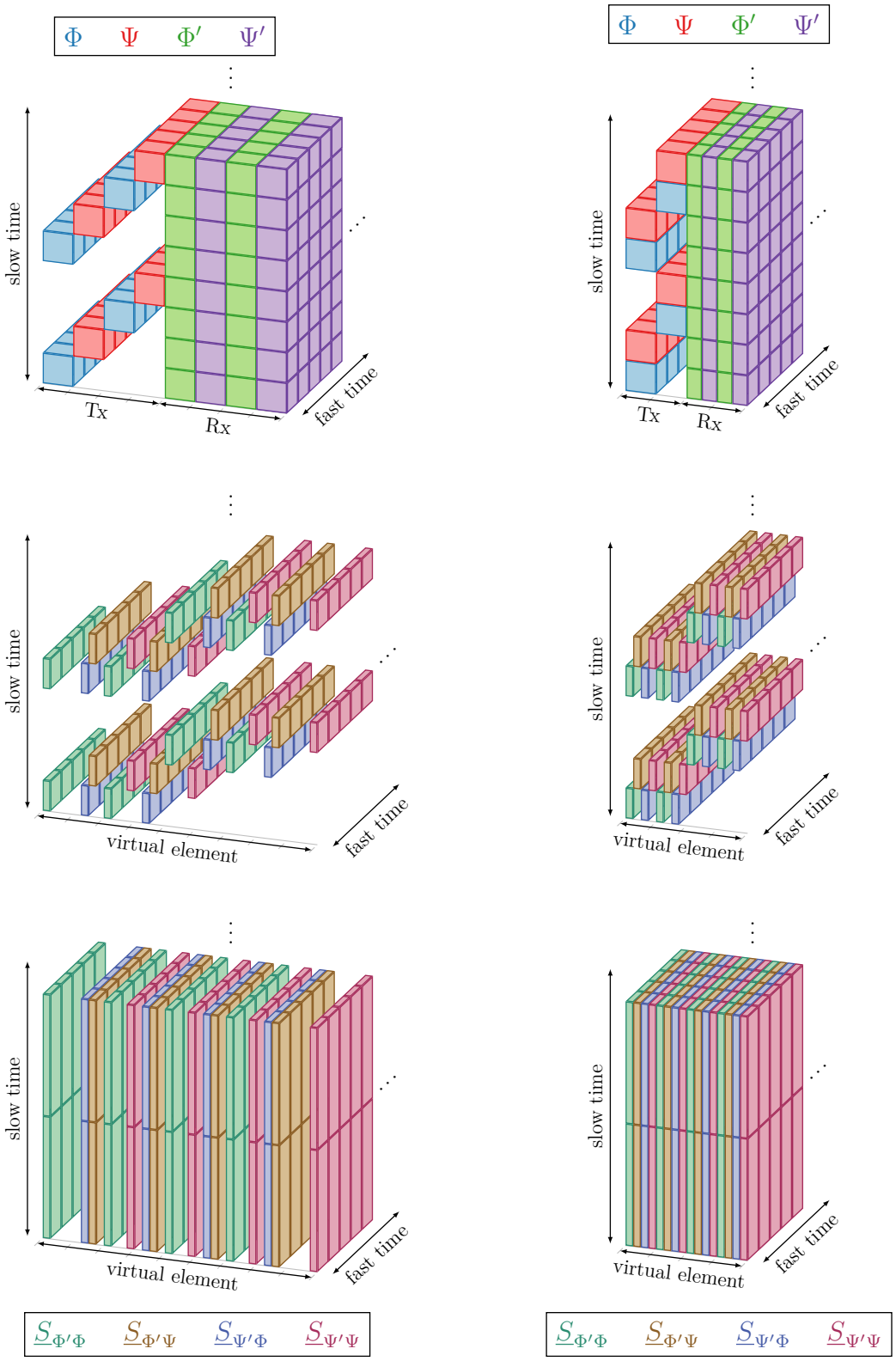


(a) virtually dual-polarimetric elements (b) virtually quad-polarimetric elements

Figure 2.13: For virtually dual-polarimetric elements in the array layout, an angle-dependent phase compensation is required. While the different spatial sampling positions are irrelevant for a broadside direction $\theta = 0°$ as shown by the upper phase plot, all other angles require the compensation to derive the full scattering matrix with correct relative phases, which is shown by example for $\theta = 30°$ in the lower part. With virtually quad-polarimetric elements, no such compensation is necessary.

It is typically desired to have multiple polarimetric channels at the same virtual array position to facilitate the correct processing of the relative phases in the scattering matrix. An example is given in Fig. 2.13. For this, the definition of an antenna's polarization multiplicity is required. For physical antennas, single- and dual-polarized elements are distinguished. The first is able to transmit or receive one polarization state and has one port, whereas the latter can transmit or receive two different polarization states based on its two ports while sharing the same aperture. The extension of this to virtual elements of an array means a virtually dual-polarimetric element is capable of measuring half of a scattering matrix, and a virtually quad-polarimetric element can estimate all elements of the scattering matrix. When the virtual array only consists of virtually dual-polarimetric elements, the full scattering matrix has to be calculated by taking multiple spatial positions into account such that an angle-dependent phase correction between the halves of the scattering matrix has to be applied (cf. Fig. 2.13a). On the contrary, there is no such compensation necessary, if the virtual elements are quad-polarimetric (cf. Fig. 2.13b).

While it is principally possible to generate virtually quad-polarimetric elements with single-polarized physical antennas, it is easier to use dual-polarized physical antennas due to fewer polarimetrically incomplete virtual elements. In fact, to the best of the author's knowledge, literature has no such radar with a virtually quad-polarimetric element but single-polarized physical antennas to offer in the 77 GHz automotive domain (cf. Section 3.2.1). Furthermore, all known systems employ a TDM scheme for activating the differently polarized transmitters due to the simplicity of implementation on the sensor hardware as well as good isolation between the different corresponding channels. This has direct impact on typical radar key performance indicators: In addition to the increased channel count requirement for a given angular performance, typical implementations of such systems bring further limitations in the Doppler domain, as is visualized in Fig. 2.14. For two example designs, the structure of the radar data cube is examined. On the one hand, the array is built based on single-polarized physical antennas (Fig. 2.14a), on the other one, both transmit and receive antennas are physically dual-polarized (Fig. 2.14b). The same number of channels is used in each case, and all receive channels are sampled simultaneously. According to the TDM principle, the transmitters are activated subsequently. The colors indicate the polarization of each cell, with the transmitted polarization basis $\mathcal{B}' = \{\Phi', \Psi'\}$ and the received polarization basis $\mathcal{B} = \{\Phi, \Psi\}$. The middle row shows when and where the different elements of the scattering matrix are measured. Due to the extent along the slow time dimension for acquiring the information of the full scattering matrix once, another compensation is necessary in non-static scenarios for correct relative phases between the polarimetric channels. After this compensation is done (for details refer to Chapter 4), the data cube structure can be interpreted as shown in the bottom row. The effective sampling frequency along the slow time dimension is quartered in both examples, i.e., also only a quartered maximum unambiguous Doppler velocity is reached.
Moreover, the last row of Fig. 2.14a shows the virtually dual-polarimetric elements as typical results from the single-polarized physical antennas. Apart from the disadvantage of the need to compensate for relative scattering matrix phase correctness mentioned in Fig. 2.13, some single-polarimetric virtual elements at the edges can be observed that are characteristic for such setups. In contrast, the virtual array for the dual-polarization antenna-based setup in Fig. 2.14b is densely populated with virtually quad-polarimetric elements avoiding the need for the angle-dependent phase compensation. On the downside, dual-polarized antennas are often more complex to design and will require more complex feeding networks.



(a) virtually dual-polarimetric elements (b) virtually quad-polarimetric elements

Figure 2.14: Typical implementations of polarimetric automotive radars employ a TDM scheme for the different transmit polarizations. Depending on the usage of single- or dual-polarized physical antenna elements, different system properties result. A detailed explanation is given in the text.

Chapter 3

Measurement setup

The developed algorithms and concepts in this thesis are evaluated on a variety of real-world recordings. Therefore, an experimental vehicle was set up that is able to record fully polarimetric data on public roads because no publicly available datasets with such data are available. The vehicle setup was carried out by the author of this thesis in collaboration with the author of another thesis on improving classification with polarimetric data [24, 25, 26, 60, 61]. Due to the different data requirements for classification tasks, the recordings are different, and the data used in this work is collected solely for this thesis.
This chapter provides details of the experimental vehicle setup in Section 3.1, as well as an in-depth introduction to the utilized radar sensors in Section 3.2, including how they compare to other systems known from literature.

3.1 Vehicle setup

The experimental vehicle is a Mercedes-Benz S-Class (V222). Relevant sensors for this work are shown in the sensor setup diagram, including simplified wiring, in Fig. 3.1. The three fully polarimetric radar sensors are mounted in the vehicle's front with mounting angles of 0° and ±60° with respect to the driving direction. They are connected to the car computer in the trunk via two Ethernet links each. The 1 Gbit/s connection is used to configure and trigger the sensor via transmission control protocol (TCP) communication. The additional 10 Gbit/s connection is used for transmitting the raw ADC data to the computer via user datagram protocol (UDP). For both the TCP and UDP connections, the corresponding software was self-written within the robot operating system (ROS) framework [62] in C++ to allow accurate timestamping and to handle the large raw data rate. Once received, the raw data can be either stored on a redundant array of independent solid-state disks or processed in real-time. Due to the large amount of data, real-time processing is implemented on the graphics processing unit (GPU) by self-written kernels in the compute unified device architecture (CUDA) language [63]. Thus, typical signal processing algorithms such as FFTs can benefit from the massive parallel architecture of GPUs enabling real-time operation. Additionally, the CUDA kernels are usable from Python via bindings written by the thesis' author for rapid prototyping.
For documentation purposes, three *Axis Communications AB* network cameras [64] are installed in the vehicle. The video data is H.264 encoded for compact recording file sizes and received within a real-time transport protocol (RTP) stream. The cameras synchronize via network time protocol (NTP) with the time master on the car computer and a mapping of the timestamps to the video frames is derived from the additional real-time control protocol (RTCP) data stream.

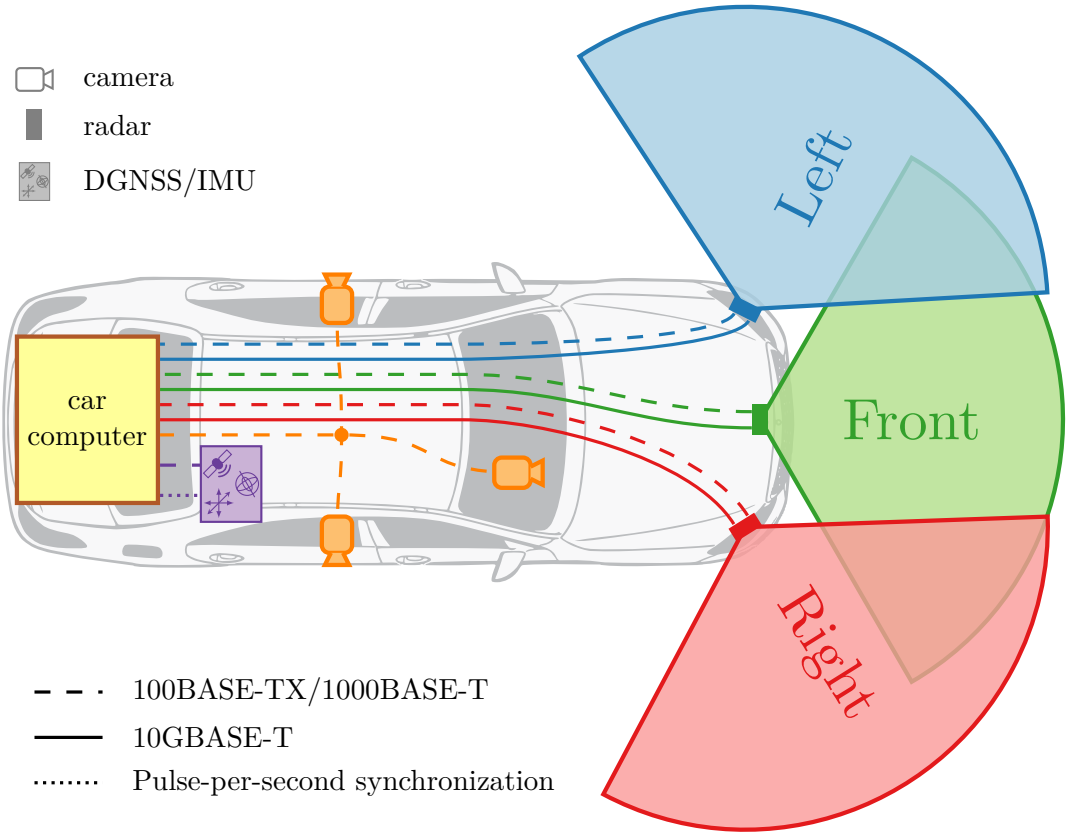


Figure 3.1: The experimental vehicle is equipped with the polarimetric radar sensors, cameras for documentation purposes as well as an integrated DGNSS/IMU device.

As a ground truth reference system, an Automotive Dynamic Motion Analyzer G PRO from *GeneSys Elektronik GmbH* [65] is installed in the vehicle's trunk. This device fuses differential global navigation satellite system (DGNSS) solution data with inertial measurement unit (IMU) data measured by fiber optic gyros and servo accelerometers. When its data serves as ground truth for the self-localization application, an additional post processing step with forward backward smoothing is carried out for reaching the most precise result without spatial jumps after GNSS outage. In this case, virtual reference station data from *AXIO-NET GmbH* [66] and *SAPOS*® [67] are used. The data from this device are internally timestamped based on the accurate GNSS time. In order to correlate this with the remaining data, the car computer time is synchronized to the GNSS time. Therefore, a pulse-per-second (PPS) signal is provided to the computer via a dedicated connection. A control line of the serial interface enables low single-digit microsecond accuracy with kernel-based timestamping support [68], which is more than sufficient for the intended application. While the PPS allows precise relative timestamping within one second, a combination of patched versions of the open-source software `gpsd` [69] and `ntpd` [70] parses the absolute time from the raw GNSS data over Ethernet.



Figure 3.2: Photograph of the experimental vehicle with the radars encircled in red (original photograph is property of @CITY consortium). The 360° roof-mounted lidar is not used in this work. Adapted from [**71**], © 2024 IEEE.

3.2 Polarimetric radar sensors

While polarimetric radar for automotive applications is still a niche, more research has been conducted in this field in the recent past. Two types of publications can be distinguished: system- or application-oriented. Because no standard approach for a polarimetric implementation exists yet, a variety of architectures and realizations are presented and discussed in the system-oriented literature. However, also the application-oriented publications typically address the polarimetry implementation briefly, given its impact on the application. Both types of research will be discussed in Section 3.2.1. Afterwards, the details of the sensors utilized in this thesis are presented in Section 3.2.2.

3.2.1 State of the art

The typical applications of radar sensors in automotive environments are detection, tracking, and classification of other road users, as well as self-localization of the ego-vehicle. Next to these applications, there are some publications on the topic of road condition monitoring [17, 23, 72, 73]. Due to the different requirements and performance figures for these systems, they are not considered further.
In addition, publications, which are limited to antenna designs only or operate in frequency bands other than 77 GHz, are not considered in detail. However, the most relevant ones are listed shortly in order to provide an overview of the automotive polarimetry research landscape and to contextualize the publications that are considered in more detail.
A series of publications covers the design of polarimetric systems by using frequency selective surfaces to rotate the polarization state in a specific frequency range in the 35 GHz band, either in a reflect- [74] or transmit-array [75] configuration including

Table 3.1: Overview of 77 GHz polarimetric radar sensors for automotive applications

Author(s)	Ref.	Year	Polarization		DBF Apert.	Band-width	Application	
			Tx	Rx			lab	real-world
Schneider et al. Daimler-Benz Research Center	[11]	1996	8× H 8× V	8× H 8× V	–	2.0 GHz		✓ Classification[11, 14, 81]
Clark et al. Sydney University	[15]	1998	1× L	1× H 1× V	–	0.6 GHz		✓ Self-Localization [32, 33]
Trummer et al. ASTYX GmbH	[19]	2016	2× L 2× R	16× L 16× R	18.2 λ_c	2.6 GHz	✓ Verification [19]	✓ Classification [28, 82]
Visentin et al. Robert Bosch GmbH	[83]	2017	4× H 4× V	4× H 4× V	4.5 λ_c	2.0 GHz	✓ Calibration [83] ✓ Classification [27, 84, 85]	
Visentin Robert Bosch GmbH	[21]	2019	4× H 4× V	4× H 4× V	8.5 λ_c	1.0 GHz		✓ Classification [21]
Nashashibi et al. University of Michigan	[86]	2020	1× H 1× V	1× H 1× V	–	2.0 GHz	✓ Calibration [87] ✓ Verification [86]	✓ Classification [88]
Tinti et al. Huawei Technologies Duesseldorf GmbH	[89]	2023	6× D 6× A	8× D 8× A	24.5 λ_c	0.5 GHz	✓ Verification [22]	
Ren et al. Chalmers University of Technology	[20]	2023	3× L	2× L 2× R	3.9 λ_c	0.5 GHz	✓ Verification [20]	✓ Classification [20]
This work Mercedes-Benz AG		since 2019	2× L 2× R	16× L 16× R	18.7 λ_c	2.0 GHz	✓ Calibration [**90**]	✓ Self-Localization [**91, 92, 93**] (✓ Classification [24, 25, 26, 60])

the necessary phase-compensating calibration [76]. This approach could facilitate the cost-effective realization of polarimetric systems by re-using existing radars without substantial changes at the cost of lower range resolution. Another publication investigates the scattering centers of vehicles with high resolution at 222 GHz showing a polarization and look angle dependency of the main scattering centers [77]. With respect to the static environment, the authors find benefits for vehicle landmark discrimination in a fully polarimetric SAR application at 5.9 GHz in [30]. Publications focusing on antenna arrays at 77 GHz instead of whole radar systems propose different implementations of dual-polarized elements either based on linear polarization by microstrip patches [78] or circular polarization by a quadrature network-fed microstrip patch [79] or slot antennas fed by ridge gap waveguides [80].

In order to put the utilized sensors into context, Table 3.1 provides an overview of publications covering generally comparable 77 GHz systems. The sorting is chronological. The very first automotive polarimetric radar system was built at *Daimler-Benz Research Center*. It was working in a linear basis and allowed fully polarimetric measurements that were used in a series of publications with the main interest in classification and tracking [11, 14, 81]. Apart from the multiple beams, the field of view was scanned mechanically. Another system was built at *Sydney University* and worked in a compact polarimetry mode, i.e., a circularly polarized wave is transmitted and the receive channels worked in a linear basis. With self-localization applications as the goal, artificial beacons with a specific polarimetric signature were designed in order to use those as landmarks that are distinguishable from the regular environment [15, 32, 33]. The angular domain was resolved by mechanical scanning as well such that this sets apart both early architectures from the later approaches.

Despite the promising results, a longer pause in publications in this field has occurred. This can be attributed to the fact that the effort and complexity to realize such a system was too high for a viable application. The cited systems have a very large physical extent. Recently, this has changed due to the advances in miniaturization of complex radio systems in a lot of application fields. Accordingly, this trend also reached radar and combined with the ever-increasing demand from the automotive industry, most components needed for a multi-channel radar system are available within a single chip nowadays. Parallel to this development, several publications about polarimetric DBF systems appeared in the last decade.
It starts with the quad-polarimetric aperture sensor from *ASTYX GmbH* [19] that works in a circular polarization basis. Fully polarimetric data is generated by transmit-side TDM with dual-polarized antennas on both sides in form of corrugated horn antennas fed by rectangular waveguides via septum polarizers. Results of this system for classification applications are published in [28, 82].
In contrast, the two sensor designs from *Robert Bosch GmbH* are based on single-polarized waveguide horn antennas in the linear polarization basis [21, 83]. By that, only dual-polarimetric channels are synthesized for the virtual aperture as discussed in Section 2.3.10. Both designs especially focus on spatially overlapping diagonal scattering matrix elements $\underline{S}_{\mathrm{HH}}$ and $\underline{S}_{\mathrm{VV}}$ for distinction between even- and odd-bounce scattering. As a consequence, the other channels were placed at a different height of the aperture such that non-zero elevation angles could introduce polarimetric distortion. After polarimetric calibration [83], both designs are used to investigate several classification-related applications [21, 27, 84].
Another approach by the *University of Michigan* involves a spatial power divider to even avoid a spatial separation of transmit and receive antenna such that one antenna aperture is serving as a dual-polarized transmit as well as dual-polarized receive element [86]. However, no DBF is realized with this single element setup and apart from a comprehensive calibration method [87] only very few real-world results are published yet [88].
A recent design by *Huawei Technologies Duesseldorf GmbH* uses a diagonal $\pm 45°$ polarization basis and focuses on an overlap of elements that helps to distinguish between even- and odd-bounce scatterers due to the single-polarized physical antennas [22, 89]. The effects of the non-overlapping channels are explicitly mentioned [22]. However, there are no real-world measurements with this system published yet.
Lastly, yet another antenna technology for generation of circular polarizations based on septum polarizers fed by gap waveguides is used by *Chalmers University of Technology* to build a polarimetric radar [20]. With dual-polarized receive and single-polarized transmit antennas, the virtual array consists of dual-polarimetric elements. Some real-world measurements of road users confirm the strong angle dependency of the RCS and dominant odd-bounce scattering.
Comparing the different designs, there is no clear favorite approach yet that has evolved as the de facto standard. The system used in this work is considered state of the art when compared to the other publications in Table 3.1. All real-world applications targeting classification of other road users are not part of this work but a parallel thesis and, therefore, are written in parenthesis in the table. The radar sensors utilized in there are the same non-commercially available prototype devices as in this thesis. A detailed explanation of the sensors follows in the next section.

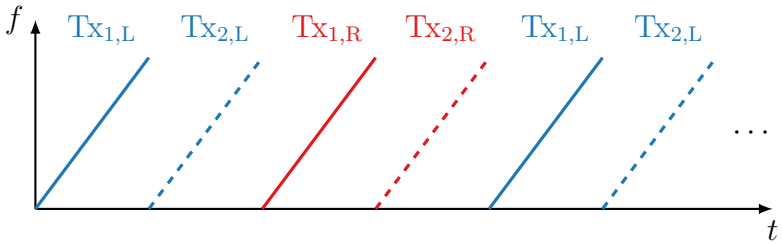


Figure 3.3: A TDM scheme is used for achieving fully polarimetric operation mode as well as the dense virtual aperture from Fig. 3.4. Adapted from [**90**], © 2022 IEEE.

3.2.2 Utilized radar sensor

The radar sensors utilized in this work are operated in CS modulation mode such that range and velocity can be calculated as described in Section 2.1.2. Each receive channel is generating 2048 12-bit samples per 2 GHz ramp resulting in a Rayleigh resolution of 7.5 cm. All physical antenna elements are dual-polarized with a left- and right-hand circular polarization. The antennas are implemented with the same horn antenna technology as published in [19]. The receive channels including the different polarizations are sampled concurrently whereas the transmit channels operate in TDM mode. In addition to the polarization switching, it is also switched between two different transmitter positions consecutively for virtually enlarging the antenna aperture. The activation scheme is depicted in Fig. 3.3. Consequently, the effective sampling frequency of the slow time domain is reduced by a factor of four, resulting in a low unambiguous radial velocity. This implementation approach was already discussed in Section 2.3.10 and the principle shown in Fig. 2.14b is applicable. With the dual-polarized physical antennas, all virtual elements of the array are quad-polarimetric as a consequence. The virtual array is shown in Fig. 3.4. Due to the shape of the azimuth gain pattern, the sensor was designed to not be fully unambiguous over the whole 180° to the advantage of a slightly better separability and more space for a single antenna element (cf. Section 2.1.3). The receiving antennas are spaced with a distance of $\Lambda_c = 1.1\lambda_c$, such that the combination with the shown transmitter spacing results in a virtual array with an unambiguous domain of approximately ±60°. Overall, a virtual aperture of $17\Lambda_c = 18.7\lambda_c$ is spanned with most elements being $\Lambda_c/2$ apart, resembling mainly an ULA. A few empty positions are generated at the edges of the array. One overlapping element is constructed, which can be used for phase compensation in non-static scenarios. The details of how the array processing is implemented will be provided in Chapter 4.

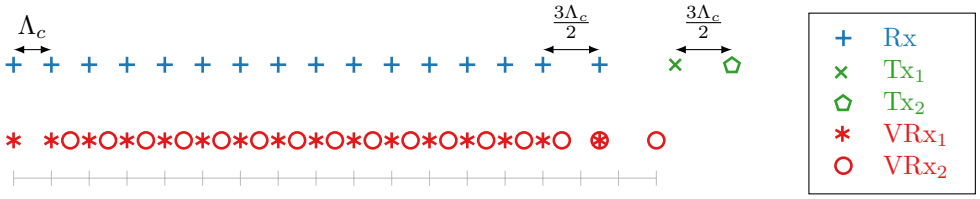


Figure 3.4: The virtual array antenna layout consists purely of quad-polarimetric elements and largely forms a ULA. It is not fully unambiguous with $\Lambda_c = 1.1\lambda_c$. Adapted from [**90**], © 2022 IEEE.

Table 3.2: Parameters of the utilized polarimetric radar sensors. Adapted from [**71**], © 2024 IEEE.

Parameter		**Value**
Start frequency	f_0	78 GHz
Maximum range	$r_{\max}$	80 m
Bandwidth	B	2 GHz
Range resolution (Rayleigh)	δ_r	7.5 cm
Azimuthal field of view	$\theta_{\max}$	±60°
Fully calibrated azimuthal field of view	$\theta_{\max,\mathrm{cal}}$	±45°
Azimuthal resolution (Rayleigh)	δ_θ	3°
Unambiguous radial velocity	$v_{\mathrm{r},\max}$	±5.15 m/s
Radial velocity resolution (Rayleigh)	δ_{v_r}	0.15 m/s
Update rate	f_{cycle}	10 Hz

With 256 ramps per measurement cycle, the net size of one raw data cube is 24 MiB. Including some headers at a cycle rate of 10 Hz, the data rate per radar is approximately 254 MB/s, which must be stored or processed. An overview of the radar parameters is given in Table 3.2. The photograph in Fig. 3.5 shows one of the side-looking sensors mounted on the vehicle.



Figure 3.5: Both radar sensors looking to the sides include a cover with rounded edges for pedestrian protection. The three connections are power, 1 Gbit/s and 10 Gbit/s Ethernet, respectively. Adapted from [**71**], © 2024 IEEE.

Chapter 4

Polarimetric calibration & signal processing

All measurement systems are subject to measurement errors. While random noise-induced errors are unavoidable, systematic errors due to an imperfect system can be counteracted by calibration. In the context of automotive radar systems, the array calibration for correct angle finding, and the RCS calibration over range and angles are most important. However, both are well-known and simple to implement so that it is usually not considered a challenge for typical systems in literature. In contrast, the application of polarimetry requires an additional dimension for the calibration approach to fully utilize its potential. For an arbitrary but fixed scattering mechanism, observed at various positions in the field of view, including both spatial and velocity dimensions, the estimated scattering matrix should remain constant. Consequently, calibration methods must be added to compensate for polarimetric channel imbalances in differential amplitude and phase values.

In this chapter, Section 4.1 provides a review of the relevant literature for the proposed calibration approach. The focus is on the calibration of polarimetric distortions in general and over a wide field of view in array system. The underlying signal model for the proposed calibration approach is derived in Section 4.2. The description of the acquisition of an extensive set of calibration measurements in an automated test facility is included in Section 4.3. Based on this, Section 4.4 presents the implementation details and results of the calibration. Since the calibration has to be applied at different stages in the signal processing chain, the description of the signal processing that forms the basis for the subsequent chapters is integrated here. Additionally, the potential influence of a radome on the estimated polarimetric properties is investigated through exemplary measurements in Section 4.5.

The contributions of this chapter are as follows:

- electrical path length equalization scheme for improving the DBF result,
- precise angular alignment of the polarimetric channels by exploiting radar-based ego-motion estimation,
- target-independent polarimetric phase compensation for Doppler distortion,
- angular domain calibration of the polarimetric phase difference,
- investigation of the influence on the polarimetric information by a radome.

This chapter includes content that is based on the own publication “Calibration and Signal Processing of Polarimetric Radar Data in Automotive Applications” [**90**].

4.1 State of the art

Only literature on monostatic and narrow band systems is considered in the following to ensure relevance to the utilized radar and the proposed calibration approach. Furthermore, the focus lies on the specific requirements for polarimetric radars in automotive applications, as array calibration for single-polarimetric DBF systems is well-established [94, 95].
A general calibration approach for non-DBF systems is the 12-term error model, which includes isolation, channel imbalance, and polarization cross-coupling terms [96]. The signal model for a measured scattering matrix $\underline{\mathbf{S}}^{\text{meas}}$ is given by

$$\underline{\mathbf{S}}^{\text{meas}} = \underline{\mathbf{I}} + \underline{\mathbf{R}}\,\underline{\mathbf{S}}^{\text{cal}}\,\underline{\mathbf{T}} \tag{4.1}$$

with the target's actual scattering matrix $\underline{\mathbf{S}}^{\text{cal}}$ and where $\underline{\mathbf{I}}, \underline{\mathbf{R}}, \underline{\mathbf{T}} \in \mathbb{C}^{2\times 2}$ represent the isolation matrix, and the receive and transmit distortion matrices, respectively. The isolation component is target-independent and models direct coupling from the transmit to the receive path. Next to such an isolation measurement, calibration requires measurements of at least three linear independent targets with exact knowledge of one of the scattering matrices [96]. The selection of suitable calibration targets is dependent on the used polarization basis. For example, an ambiguity can result if typical linear-basis standard calibration targets are chosen for a circular-basis calibration and specific non-standard targets are proposed as a solution [97].
If the isolation matrix and the polarization cross-coupling are negligible ($\underline{\mathbf{I}} = \mathbf{0}$ and $\underline{\mathbf{R}}, \underline{\mathbf{T}}$ are diagonal matrices), the calibration equation is simplified as follows by using the lexicographic feature vector form (cf. (2.35)) for the scattering matrices

$$\underline{\boldsymbol{\Omega}}^{\text{meas}} = \text{vec}\,[\underline{\mathbf{S}}^{\text{meas}}] = \underline{\mathbf{F}}\,\underline{\boldsymbol{\Omega}}^{\text{cal}} = \begin{pmatrix} \underline{R}_\Phi \underline{T}_\Phi & 0 & 0 & 0 \\ 0 & \underline{R}_\Phi \underline{T}_\Psi & 0 & 0 \\ 0 & 0 & \underline{R}_\Psi \underline{T}_\Phi & 0 \\ 0 & 0 & 0 & \underline{R}_\Psi \underline{T}_\Psi \end{pmatrix} \begin{pmatrix} \underline{S}^{\text{cal}}_{\Phi\Phi} \\ \underline{S}^{\text{cal}}_{\Phi\Psi} \\ \underline{S}^{\text{cal}}_{\Psi\Phi} \\ \underline{S}^{\text{cal}}_{\Psi\Psi} \end{pmatrix} \tag{4.2}$$

where $\underline{\mathbf{F}} \in \mathbb{C}^{4\times 4}$ represents the simplified distortion matrix [52, Chapter 9.3.3].
While in principle, a single target with a completely known scattering matrix is sufficient to calculate $\underline{\mathbf{F}}$ [76], it is often impractical to realize because either an adequate target, which reflects sufficient energy back to the radar in all 4 polarimetric channels, is not easily available, or because the sensitivity to imperfect orientations can generate large calibration errors quickly. It should be noted that this again depends on the used polarization basis. In a linear basis, two selected targets are proposed for calibration in [98], which are more easily available and do not require a major alignment effort to guarantee a perfect orientation: a sphere with no orientation sensitivity serves as the absolute RCS value reference as well as the calibrator for the co-polarized channels and any arbitrary target with a strong cross-polarized response combined with the reciprocity assumption (cf. Section 2.3.4) complements the equations. However, this is not directly transferable to circular polarization, as the inherently orientation-sensitive channels, which are the even-bounce elements $\underline{S}_{\text{LL}}$ and $\underline{S}_{\text{RR}}$, are not constrained by the reciprocity assumption in the same way that they are for linear polarizations. As a consequence, a careful orientation alignment matters for circular polarization calibration.

Calibration is of utmost importance for any polarimetric radar, and as such, different approaches and investigations in that regard are published for most of the systems mentioned in Section 3.2.1 [20, 76, 83, 87]. For polarimetric channel distortion correction, the authors of [87] use the above-mentioned approach [98] assuming negligible polarization cross-coupling. Moreover, a compensation technique to remove phase errors due to non-negligible chirp non-linearity is demonstrated. The calibration of another non-DBF system uses a fully characterized target in form of a 22.5°-rotated dihedral reflector as a single reference target with a repeated neglect of polarization cross-coupling [76, 99]. The operating principle for acquiring fully polarimetric data by a frequency-controlled polarization rotating reflector requires further calibration steps in form of electrical length equalization and phase band correction.
When it comes to polarimetric DBF systems with typical automotive radar characteristics, the calibration investigations in [21, 83] are one of the most elaborate. The simplified diagonal distortion matrix (4.2) is again used as the underlying model. The novelty here lies in the consideration of the polarimetric responses of each of the virtual elements in the array. However, the response dependency on the angular domain after beamforming is just as unaccounted for as the velocity dimension.
To the best of the author's knowledge, no comprehensive consideration of polarimetric stability over all measurement dimensions has been published in the context of automotive radar. Due to the more narrow azimuthal opening angles in typical SAR applications compared to the widely open antennas in automotive environments, stable polarimetric measurements over the whole field of view are less challenging for the former. Therefore, most relevant literature is found in the context of recent array-based weather radars that will replace the proven rotating dish-based systems. A signal model from this context is proposed in [100] and describes an overall distortion model for a polarimetric array system. Assuming a restriction to only the azimuthal angular dimension and including an adaption to the notation used in this work, this general model is given by

$$\underline{\mathbf{S}}^{\text{meas}} = \frac{\underline{\gamma}}{N_{\text{Rx}}} \left[\sum_{n_{\text{Rx}}} \underline{a}^{*}_{n_{\text{Rx}}}(\theta_{\text{s}})\, \underline{\mathbf{R}}_{n_{\text{Rx}}}\, \underline{\mathbf{G}}_{n_{\text{Rx}}}(\theta) \right] \underline{\mathbf{S}}^{\text{cal}} \frac{1}{N_{\text{Tx}}} \left[\sum_{n_{\text{Tx}}} \underline{a}^{*}_{n_{\text{Tx}}}(\theta_{\text{s}})\, \underline{\mathbf{G}}_{n_{\text{Tx}}}(\theta)\, \underline{\mathbf{T}}_{n_{\text{Tx}}} \right] \tag{4.3}$$

where $\underline{\gamma}$ is a complex term for the range-dependent propagation loss and the absolute target phase, $\underline{a}_n(\theta_{\text{s}}) \in \mathbb{C}$ represent the elements of the steering vectors, which are steered to the azimuth scan angle θ_{s}, and $\underline{\mathbf{G}}_n(\theta) \in \mathbb{C}^{2\times 2}$ are the polarimetric antenna patterns per element as a function of the target azimuth angle θ. Similarly to the element-wise antenna patterns, the distortion matrices of the transmit and receive channels $\underline{\mathbf{T}}$ and $\underline{\mathbf{R}}$ from (4.1) are introduced for each element of the array, as indicated by the corresponding index.

4.2 Approach

The calibration approach used in this work is developed based on known methods from literature by incorporating the simplified distortion model (4.2) into the array model (4.3) of the previous section. Therefore, the polarization cross-coupling is assumed to be negligible in all relevant terms. This applies to both distortion matrices $\underline{\mathbf{T}}_{n_{\text{Tx}}}$ and $\underline{\mathbf{R}}_{n_{\text{Rx}}}$ as well as to both polarimetric element patterns $\underline{\mathbf{G}}_{n_{\text{Tx}}}$ and

$\underline{\mathbf{G}}_{n_{\mathrm{Rx}}}$. Hence, they are all purely diagonal matrices. This is justified by the waveguide technology with septum polarizers in the utilized radar frontend while only a very limited field of view in elevation is covered. Measurements with a system with the same frontend technology showed good polarization cross-coupling suppression of more than 20 dB for a large part of the considered field of view [19]. As the measurements include the distortion matrices for the RF channels as well as the element patterns for the antennas, the validation of the assumption applies to both.
Furthermore, the polarimetric element patterns are assumed to only differ between the array elements by a phase shift according to the element's position, which is a typical assumption [100]. For calibration, the array is steered towards the calibration target such that the scan angle equals the target azimuth ($\theta = \theta_{\mathrm{s}}$). The polarimetric element pattern for either the transmitting or receiving antenna can then be expressed by $\underline{\mathbf{G}}_n(\theta_{\mathrm{s}}) = \underline{a}_n(\theta_{\mathrm{s}})\,\underline{\mathbf{G}}(\theta_{\mathrm{s}})$, such that the element-independent pattern $\underline{\mathbf{G}}$ can be factored out of the summation. If all of this is inserted in (4.3), the steering vector elements cancel each other out and the simplified array model is given by

$$\underline{\mathbf{S}}^{\mathrm{meas}} = \frac{\underline{\gamma}}{N_{\mathrm{Rx}}} \left[\sum_{n_{\mathrm{Rx}}} \underline{\mathbf{R}}_{n_{\mathrm{Rx}}}\right] \underline{\mathbf{G}}_{\mathrm{Rx}}(\theta_{\mathrm{s}})\ \underline{\mathbf{S}}^{\mathrm{cal}}\ \underline{\mathbf{G}}_{\mathrm{Tx}}(\theta_{\mathrm{s}})\, \frac{1}{N_{\mathrm{Tx}}} \left[\sum_{n_{\mathrm{Tx}}} \underline{\mathbf{T}}_{n_{\mathrm{Tx}}}\right]. \tag{4.4}$$

Using the vectorized formulation $\underline{\boldsymbol{\Omega}}^{\mathrm{meas}}$ instead of $\underline{\mathbf{S}}^{\mathrm{meas}}$ (cf. (2.35)) for conciseness and introducing the symbols

$$\underline{\mathbf{G}}_{\mathrm{Rx}}(\theta_{\mathrm{s}}) = \begin{pmatrix} \underline{G}_{\mathrm{Rx,L}}(\theta_{\mathrm{s}}) & 0 \\ 0 & \underline{G}_{\mathrm{Rx,R}}(\theta_{\mathrm{s}}) \end{pmatrix} \qquad \underline{\mathbf{G}}_{\mathrm{Tx}} = \begin{pmatrix} \underline{G}_{\mathrm{Tx,L}}(\theta_{\mathrm{s}}) & 0 \\ 0 & \underline{G}_{\mathrm{Tx,R}}(\theta_{\mathrm{s}}) \end{pmatrix} \tag{4.5}$$

$$\underline{\mathbf{R}}_{n_{\mathrm{Rx}}} = \begin{pmatrix} \underline{R}_{n_{\mathrm{Rx}},\mathrm{L}} & 0 \\ 0 & \underline{R}_{n_{\mathrm{Rx}},\mathrm{R}} \end{pmatrix} \qquad \underline{\mathbf{T}}_{n_{\mathrm{Tx}}} = \begin{pmatrix} \underline{T}_{n_{\mathrm{Tx}},\mathrm{L}} & 0 \\ 0 & \underline{T}_{n_{\mathrm{Tx}},\mathrm{R}} \end{pmatrix} \tag{4.6}$$

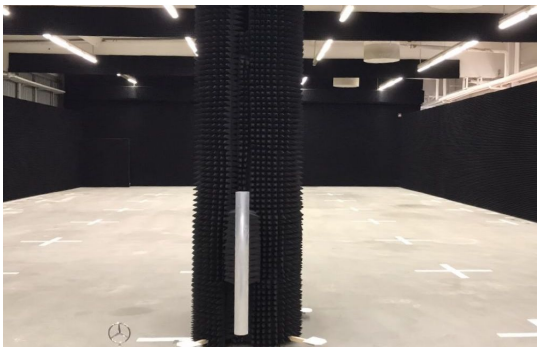
for the diagonal matrix elements in the circular basis, it follows

$$\underline{\boldsymbol{\Omega}}^{\mathrm{meas}} = \frac{\underline{\gamma}}{N_{\mathrm{Rx}} N_{\mathrm{Tx}}} \begin{pmatrix} \underline{G}_{\mathrm{Rx,L}}(\theta_{\mathrm{s}})\, \underline{G}_{\mathrm{Tx,L}}(\theta_{\mathrm{s}}) & \sum\limits_{n_{\mathrm{Rx}}} \underline{R}_{n_{\mathrm{Rx}},\mathrm{L}} \sum\limits_{n_{\mathrm{Tx}}} \underline{T}_{n_{\mathrm{Tx}},\mathrm{L}} & \underline{S}^{\mathrm{cal}}_{\mathrm{LL}} \\ \underline{G}_{\mathrm{Rx,L}}(\theta_{\mathrm{s}})\, \underline{G}_{\mathrm{Tx,R}}(\theta_{\mathrm{s}}) & \sum\limits_{n_{\mathrm{Rx}}} \underline{R}_{n_{\mathrm{Rx}},\mathrm{L}} \sum\limits_{n_{\mathrm{Tx}}} \underline{T}_{n_{\mathrm{Tx}},\mathrm{R}} & \underline{S}^{\mathrm{cal}}_{\mathrm{LR}} \\ \underline{G}_{\mathrm{Rx,R}}(\theta_{\mathrm{s}})\, \underline{G}_{\mathrm{Tx,L}}(\theta_{\mathrm{s}}) & \sum\limits_{n_{\mathrm{Rx}}} \underline{R}_{n_{\mathrm{Rx}},\mathrm{R}} \sum\limits_{n_{\mathrm{Tx}}} \underline{T}_{n_{\mathrm{Tx}},\mathrm{L}} & \underline{S}^{\mathrm{cal}}_{\mathrm{RL}} \\ \underbrace{\underline{G}_{\mathrm{Rx,R}}(\theta_{\mathrm{s}})\, \underline{G}_{\mathrm{Tx,R}}(\theta_{\mathrm{s}})}_{\text{Polarimetric antenna pattern calibration}} & \underbrace{\sum\limits_{n_{\mathrm{Rx}}} \underline{R}_{n_{\mathrm{Rx}},\mathrm{R}} \sum\limits_{n_{\mathrm{Tx}}} \underline{T}_{n_{\mathrm{Tx}},\mathrm{R}}}_{\text{Separable regular MIMO array calibration}} & \underline{S}^{\mathrm{cal}}_{\mathrm{RR}} \end{pmatrix}. \tag{4.7}$$

The distortion model can be split into different parts, which can be interpreted independently:



(a) Automated test facility setup



(b) Pole calibration target



(c) Dihedral calibration target

Figure 4.1: All three sensors are calibrated in an automated test facility with different calibration targets. The targets are mounted to a crane, which can be moved to an arbitrary position in the absorber-lined hall. Adapted from **[90]**, © 2022 IEEE.

On the one hand, the complex factors for each of the array's RF channels on both the transmitting and receiving side are well-known from regular MIMO array processing to model variances from manufacturing in the RF components and transmission lines. In the polarimetric distortion model (4.7), one can interpret the sums as the influence of deviations from four separate regular array calibrations. With appropriately chosen targets, standard techniques from literature such as [94] can be applied to each of the polarimetric channels independently, so that only the specifics to be considered for polarimetry are addressed in Section 4.4.4.

On the other hand, the polarimetric element patterns must be calibrated. In addition to the varying antenna gain over the azimuth angle, which is already well-known from non-polarimetric radars, the angle dependency of the differential phases between the polarimetric channels must be taken into account for polarimetry. In Section 4.4.6, the polarimetric phases are analyzed and a correction technique is proposed.

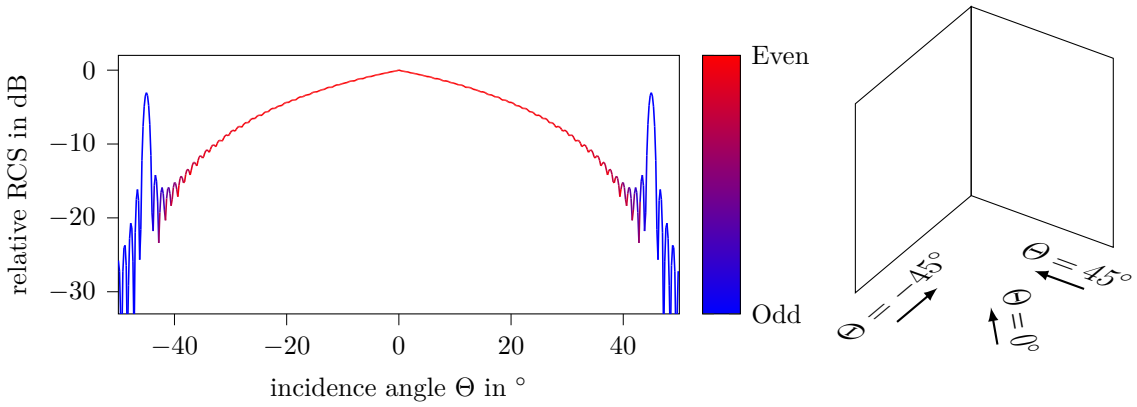
4.3 Calibration measurements

The calibration measurements are carried out in an automated test facility that is designed for radar testing. The photograph in Fig. 4.1a shows a panoramic view of the facility. An absorber-lined crane can be electrically moved by controller area network (CAN) commands to arbitrary positions in an area of 12 m×24 m. To re-

duce reflections from the building's infrastructure, additional absorber material is installed at the walls. Due to the size of the facility, the radar under test can still be mounted to a vehicle. This would allow an easy measurement of the influence of a radome or bumper. However, the calibration measurements in the test facility were all carried out without a secondary surface to exclude any additional impacts and to focus on the novel polarimetric components first. An experiment with a secondary surface in form of a radome is presented in Section 4.5 but was conducted outside due to a closure of the test facility.
Different targets were chosen for calibration in order to acquire sufficient data for all polarimetric channels. An electrically large pole is chosen for the odd-bounce channels because it provides enough reflected energy at the receiver for a good signal-to-noise ratio (SNR) while at the same time being rotationally symmetric around the vertical axis. This is beneficial as no large effort has to be spent to ensure proper alignment over the whole traversing range of the crane. Therefore, the pole is particularly suited for the antenna element pattern calibration. The photograph in Fig. 4.1b shows the crane-mounted pole. For the even-bounce channels, a vertically aligned dihedral reflector as displayed in Fig. 4.1c is used. While it also has sufficient SNR, a viewing angle dependency of the scattering response requires more attention regarding alignment. The intended incidence angle for the calibration measurements is the bisecting line of the 90° dihedral angle ($\Theta = 0°$ according to the definition in Fig. 4.2b). Fig. 4.2a shows the theoretical relative RCS of a dihedral reflector with an indication of the dominant scattering mechanism by color according to [101]. The intended incidence angle corresponds with the maximum return of power in the even-bounce channels as desired. Moreover, it can be seen that one mechanical mounting position on the crane is not sufficient to cover the traversing range because no automated rotation along the vertical axis is available. For normal incidence onto the individual halves of the dihedral ($\Theta = \pm 45°$), the second part is practically not involved in the scattering and odd-bounce behavior is observed. Due to this, manual re-alignment is carried out during traversal of the whole ±45° field of view.
The ideal lexicographic feature vectors for these two calibration targets are

$$\underline{\mathbf{\Omega}}^{\mathrm{cal}}_{\mathcal{B}_{\mathrm{LR}},\mathrm{pole}} = e^{\mathrm{j}\varphi_{\mathrm{pole}}} \sqrt{\frac{\sigma_{\mathrm{pole}}}{4\pi}} \begin{pmatrix} 0 \\ 1 \\ 1 \\ 0 \end{pmatrix} \qquad \underline{\mathbf{\Omega}}^{\mathrm{cal}}_{\mathcal{B}_{\mathrm{LR}},\mathrm{dih}} = e^{\mathrm{j}\varphi_{\mathrm{dih}}} \sqrt{\frac{\sigma_{\mathrm{dih}}}{4\pi}} \begin{pmatrix} 1 \\ 0 \\ 0 \\ -1 \end{pmatrix} \tag{4.8}$$

with $\sigma_{\mathrm{pole}}, \sigma_{\mathrm{dih}}$ representing the respective RCS values and $\varphi_{\mathrm{pole}}, \varphi_{\mathrm{dih}}$ some absolute phases.
To minimize the manual interventions for the dihedral re-alignment, the crane is programmed to follow a path constituting a star pattern. Azimuth angles from −45° to 45° with 5° increments are measured by range sweeps from 0.5 m to the farthest distance within the traversable area. To enable a static evaluation of the calibration targets, the crane is stopped for a few seconds every meter of distance traveled. The BEV of some measurement in Fig. 4.10 can be used to understand the traversed path. Due to the limited traversing velocity of the crane, the radar's frame rate was set to 2 Hz to manage the amount of data. However, each target measurement per radar still consists of more than 4000 frames.



(a) (b)

Figure 4.2: The RCS of a dihedral strongly depends on the incidence angle. While for an observation in the proximity of the bisecting line of the 90° dihedral angle the double-bounce scattering is dominant, oblique incidence into the structure can show odd-bounce behavior for the individual parts. A mixture of both scattering mechanisms is observed at the transition between the single-dominated parts. Adapted from [**91**], © 2019 IEEE.

4.4 Calibration techniques, signal processing & results

The description of the calibration steps is combined with an explanation of the general radar processing blocks in the signal path. An overview of the steps involved is depicted in Fig. 4.3. The gray blocks are part of the calibration procedure. Regular signal processing blocks (displayed in white) are included in the diagram as well and are described briefly in the following to establish the fundamental pre-processing basis for the specific algorithms for localization in subsequent chapters.

4.4.1 Deinterleaving & reordering

The raw data byte stream from the ADCs consists of densely packed 12 bit integer values. Due to the used floating-point arithmetic in all subsequent processing steps, the samples are unpacked and converted to floating-point values first. Furthermore, the positions of the samples in the memory block are changed. Analogously to the matrix organization of the measurement data in Fig. 2.2, three-dimensional tensors are constructed for each of the four polarimetric channels. Each one of the tensors has a shape of $N_{\text{fast}} \times N_{\text{VRx}} \times N_{\text{slow}} = 2048 \times 32 \times 64$ with the TDM MIMO principle already applied such that the size of the array dimension equals the number of virtual elements. The output of this block is labeled $s_{\text{IF},pq}\left(t_{\text{fast}}, n_{\text{VRx}}, t_{\text{slow}}\right)$ in the block diagram in Fig. 4.3 in accordance with the notation in Chapter 2 with the polarimetric channel designation $p, q \in \mathcal{B}_{\text{LR}}$, the fast and slow time dimensions t_{fast} and t_{slow}, and the array element index n_{VRx}. Because no quadrature mixers are used in the radar, the signal is real up to this point.

All operations of this processing step are implemented in form of CUDA kernels and this building block is thus the first part being executed on the GPU. Reception of the UDP packets and concatenation of the raw data payload is carried out on

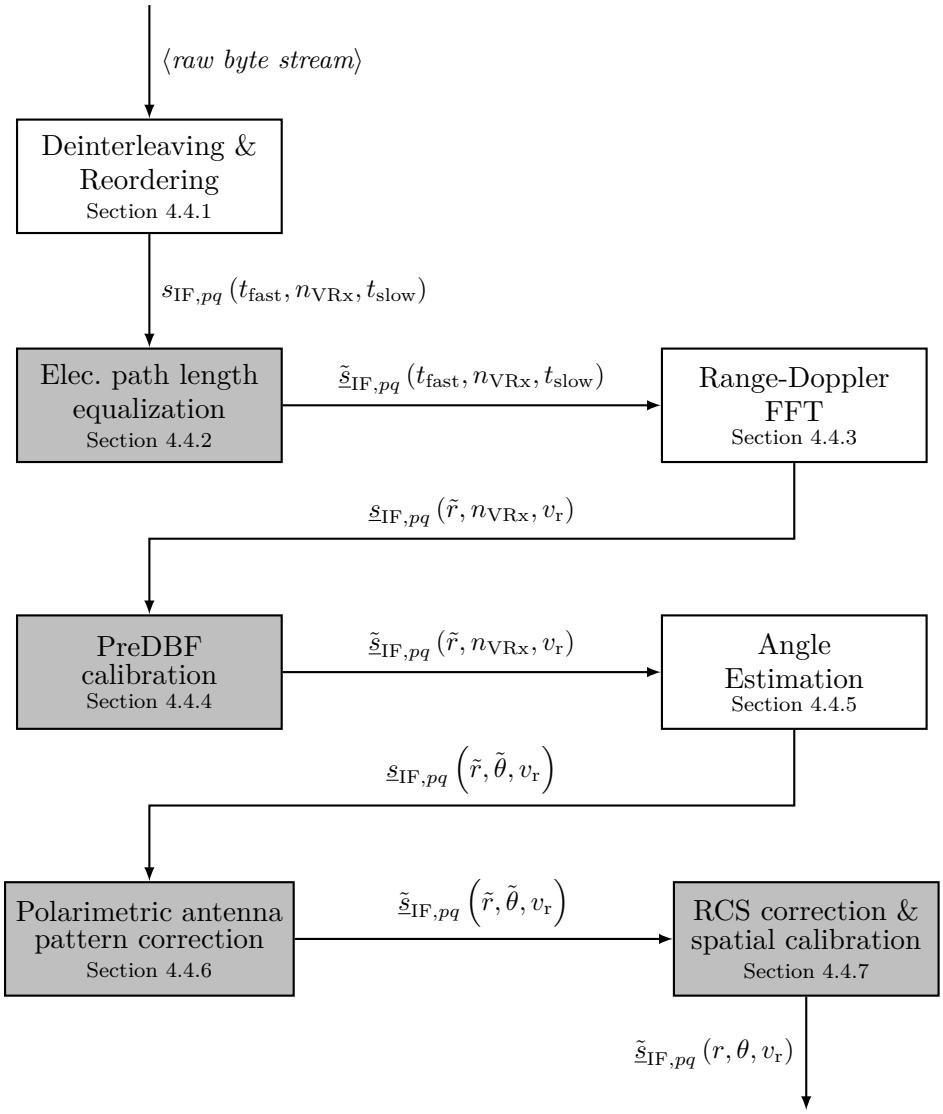


Figure 4.3: The signal processing block diagram shows where the different steps of the proposed calibration approach (gray blocks) are applied. Symbols marked with a tilde˜ stand for modified variants of the original symbol's meaning, e.g., an applied calibration function for the signal s_{IF} or uncalibrated range and azimuth variables. Adapted from [**90**], © 2022 IEEE.

the central processing unit (CPU) and the result is uploaded to the GPU thereafter to run this kernel. Most of the following calibration steps can be formulated as a multiplication of one bin value by a complex factor that could depend on the bin's position. This is easy to implement in form of GPU kernels and therefore it is not a repeated topic in the following sections. For other more complex operations, the way of implementation will be mentioned.

4.4.2 Electrical path length equalization

The electrical path length between the channels of any RF frontend can differ due to various reasons. Examples include differences in the physical layout of the channels

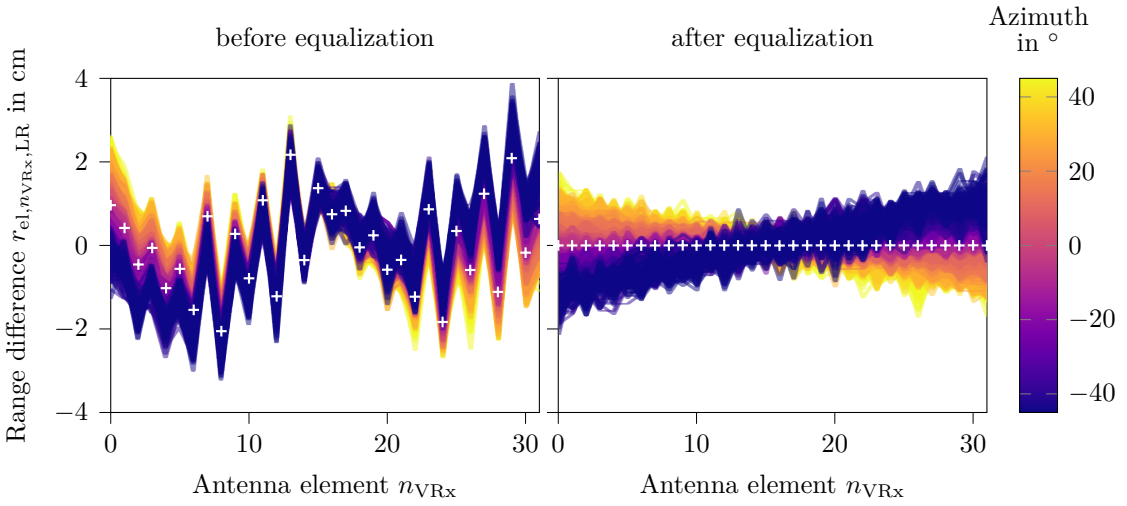


Figure 4.4: The electrical path length differences between the antenna channels is clearly visible for the LR-channel and the pole target without any equalization. The average over all measurements $\overline{r_{\mathrm{el},n_{\mathrm{VRx}},\mathrm{LR}}}$ is shown by the white cross. With application of the calibration step, only the physical range-angle coupling effect is left. Adapted from **[90]**, © 2022 IEEE.

and manufacturing tolerances of the connecting transmission lines as well as the RF components such as mixers, amplifiers, and filters. An alignment is important for two reasons. First, the beamforming would suffer if the electrical lengths are not equalized. While the complex factors in the array calibration help to mitigate the impact, the phase could only be fully compensated if a linear progression in the vicinity of the target is assumed, which is an assumption that is not always valid. Furthermore, the amplitude behaves non-linearly over frequency and a variation over the elements would occur depending on where in the range bin the target is located, which deteriorates the side-lobe level after beamforming. Second, the relative polarimetric information is also sensitive to such phase and amplitude variations in a similar way. With clean calibration measurements, it is easy to estimate the differences and derive calibration parameters to compensate this systematic error. A similar approach is reported in [76] in order to align the polarimetric channels of one virtually quad-polarimetric element, whereas all the array elements for angle finding are length-equalized in the author's publication **[90]**.

The range corresponding to the maximum amplitude and in turn corresponding to the calibration target is estimated very precisely for each antenna channel by zero-padding before calculating the range FFT. For a good SNR, the ranges for the odd-bounce channels were estimated based on the pole, for the even-bounce channels based on the dihedral. A relative range difference $r_{\mathrm{el},n_{\mathrm{VRx}},pq}$ to the average over all channels is calculated for each virtual element n_{VRx} and each polarimetric channel pq. This is done for each measurement cycle and the mean over all cycles $\overline{r_{\mathrm{el},n_{\mathrm{VRx}},pq}}$ is calculated per element for usage during calibration. An example for the LR-channel and the pole target is plotted in Fig. 4.4, where deviations up to roughly 2 cm compared to the element average can be observed. The alignment between the

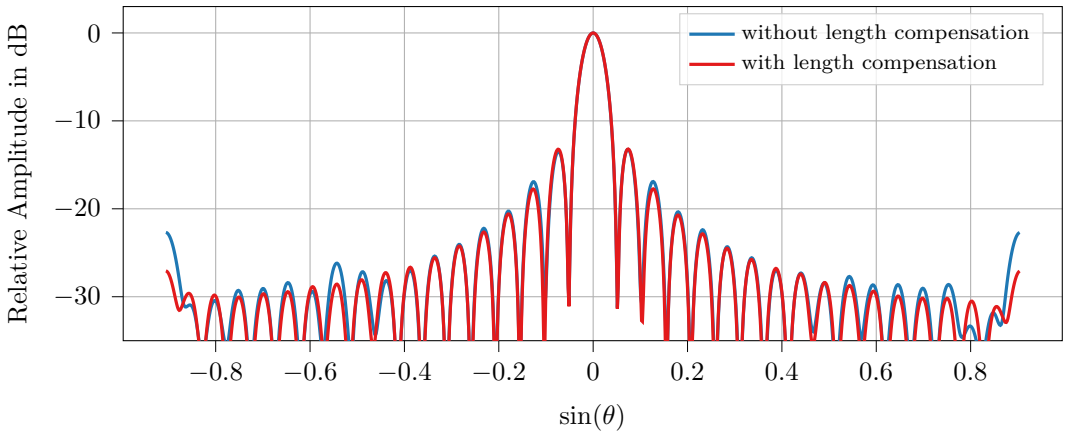


Figure 4.5: The beamforming result shows better side-lobe levels when the electrical length equalization is used. Adapted from **[90]**, © 2022 IEEE.

channels can be achieved by application of the Fourier modulation theorem according to

$$\tilde{s}_{\mathrm{IF},pq}\left(t_{\mathrm{fast}}, n_{\mathrm{VRx}}, t_{\mathrm{slow}}\right) = s_{\mathrm{IF},pq}\left(t_{\mathrm{fast}}, n_{\mathrm{VRx}}, t_{\mathrm{slow}}\right) \exp\left(\mathrm{j}\pi t_{\mathrm{fast}} \frac{\hat{\varepsilon}_{r,pq} - \overline{r_{\mathrm{el},n_{\mathrm{VRx}},pq}}}{r_{\max}}\right) \quad (4.9)$$

where $\hat{\varepsilon}_{r,pq}$ is an additional phase-center offset, which is derived in Section 4.4.7.
A successful compensation is achieved with (4.9) when no mean shift is observed for each channel, as depicted by the right diagram in Fig. 4.4. The chosen colorization of the single measurements by the target's azimuth angle illustrates another well-known effect, the so-called range-angle coupling [102]. Due to the aperture of the array, the distance from each element to the point target is different. The greater the azimuth angle, the larger the difference of distances. Thus, it matches the observation in the plot. This has also been mentioned in the array signal model (2.16) in the fundamentals chapter. While it deteriorates the beamforming result and the relative polarimetric information especially in the outer regions for the aforementioned reasons, it is not compensated for in this work due to the relatively high effort that would be necessary.
As an example for the effect of the electrical length equalization, azimuth spectra are compared in Fig. 4.5. Range and Doppler bins were chosen by searching for the maximum response amplitude of the target. To achieve statistical relevance of the evaluation, the azimuth spectra over all static pole measurements of the LR-channel are averaged. Therefore, the spectra were normalized and aligned on the directional sine domain. A rectangular window is used and zero-padding is introduced to make the result better interpretable. The array calibration is carried out as discussed in Section 4.4.4 for a signal processing chain with and without the length compensation. Comparing both resulting spectra, a considerably lower side-lobe level with a 5 dB difference can be observed at the farthest spectral distance to the main maximum. The virtual array layout in Fig. 3.4 combined with the observation of the alternating pattern between neighboring antenna elements in Fig. 4.4 serves as an explanation. The interlaced correspondence of the virtual elements to the two transmit antennas

translate into the altering range difference when there is a variation between the transmitters. As an alternating modulation between neighboring elements constitutes the maximum frequency in the array, the worse side-lobe level shows at the farthest distance to the original direction. While a purely detection-based processing could suppress the generation of detections at the increased side-lobe position, the subsequent chapters are based on the processing of dense image-like representations, so that this improvement is desired.

4.4.3 Range-Doppler FFT

Range-Doppler processing is implemented in a conventional way. The fast and slow time dimensions are transformed by FFTs to range and Doppler velocity domain, respectively. This operation can be expressed by

$$\underline{s}_{\mathrm{IF},pq}\left(\tilde{r}, n_{\mathrm{VRx}}, v_{\mathrm{r}}\right) = \mathcal{F}_{t_{\mathrm{slow}}}\left\{\mathcal{F}_{t_{\mathrm{fast}}}\left\{\underline{\tilde{s}}_{\mathrm{IF},pq}\left(t_{\mathrm{fast}}, n_{\mathrm{VRx}}, t_{\mathrm{slow}}\right)\right\}\right\} \tag{4.10}$$

with $\mathcal{F}$ being the Fourier transform. For efficient GPU execution of this operation, the library `cuFFT` is used [103].
Range-Doppler coupling is neglected in the processing as the impact for the selected modulation parameters is considered to be small enough to not interfere notably with the intended application (cf. Section 2.1.2). In contrast, range migration has a perceivable effect on the processed radar images. However, due to the required substantial processing effort for correcting the effect, the results of the intended localization application were generated without a compensation first. If the desired results had not been achieved due to range migration, a compensation would have been implemented. Empirical evidence of the following chapters shows that the compensation is not mandatory for good results. Therefore, no range migration compensation is included in the signal processing. Window functions other than the rectangular window are selected depending on the use case and usage is mentioned in the corresponding section.

4.4.4 PreDBF calibration

This step in the calibration approach combines the compensation of multiple effects. Once the individual components are described, the joint application is presented in the last part of this section.

DBF array calibration

The array calibration is carried out by well-known standard approaches [94, 95] for each polarimetric channel individually as a first step. For this purpose, the diagonal distortion matrix model in (4.6) is transformed into the equivalent single transmitter virtual receive array representation so that one complex calibration coefficient $\underline{R}_{n_{\mathrm{VRx}},pq}$ for each virtual element and per polarimetric channel is estimated. The differences to a linear phase progression and a constant amplitude distribution over the virtual elements are calculated for all target positions. After outlier rejection, the inverse of the average over all measurement serves as the calibration coefficient. The

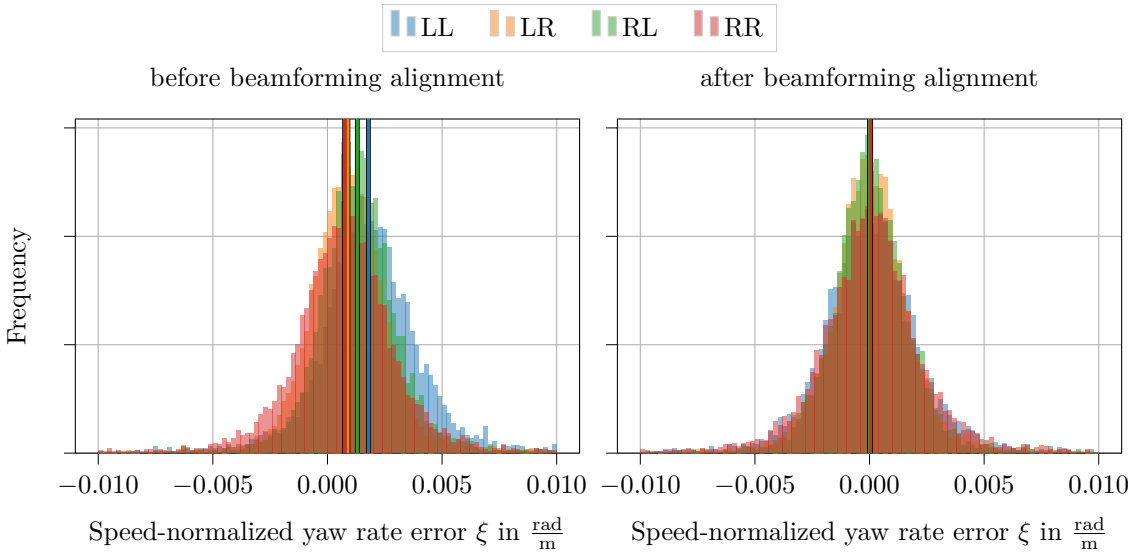


Figure 4.6: The separate application of regular array calibration approaches leaves a small misalignment between the polarimetric channels. A large-sample statistic of the speed-normalized yaw rate error from polarization-separated ego-motion estimation is an indicator for this. Vertical lines show the median error per polarization, which can be translated to a misalignment angle. The proposed beamforming alignment allows to compensate this systematic error. Adapted from **[90]**, © 2022 IEEE.

pole target is used for the odd-bounce channels and the dihedral for the even-bounce ones.

With the independent array calibration per polarimetric channel, the angular alignment between them is not ideal. Because even- and odd-bounce channels are calibrated in separate measurements, the precise alignment is hard to derive from the measurements in the test facility. Consequently, another newly proposed approach is followed. It is known that a very precise mounting angle of a non-polarimetric radar can be derived from the comparison of a radar-based ego-motion estimation and a known ground truth motion [104, 105]. Details about the ego-motion estimation and the ground truth generation are included in Chapter 6. The idea is to carry out the ego-motion estimation for each polarimetric channel separately and derive the misalignment for each subsequently. It can be shown by a first order approximation for typical driving scenarios that the yaw rate estimation error ε_{ω_z} is related to the yaw misalignment ε_ψ by

$$\xi = \frac{\varepsilon_{\omega_z}}{\|\mathbf{v}_\mathrm{s}\|} \propto \varepsilon_\psi \tag{4.11}$$

where ξ is the speed-normalized yaw rate error and $\mathbf{v}_\mathrm{s}$ represents the sensor's velocity vector [105, Chapter 6.4.6]. The histogram of this normalized error ξ calculated over a 5 km drive for the front sensor is shown in Fig. 4.6. A shift between the distributions of the channels is recognizable, especially by the marked median values of the distribution. After translating this shift to a correction angle, a corresponding phase progression can be modulated onto the array calibration factors

to steer the beamforming response. In a $\lambda_c/2$ ULA, the phase progression would follow $\exp\left(\mathrm{j}\pi \sin\left(\varepsilon_\psi\right) n_{\mathrm{VRx}}\right)$ and has to be included in $\underline{R}_{n_{\mathrm{VRx}},pq}$. For the present array, the phases need to be adapted according to the element distances. When applied correctly, the resulting histogram looks as shown on the right-hand side of Fig. 4.6. The polarimetric channels are now aligned to each other and the mounting angle of the sensor in the vehicle is also correct as can be seen by no bias of the distribution. In this case, the maximum relative difference between channels was about 0.3°.

TDM MIMO phase compensation

Without even considering the transmit polarization switching, the utilized radar sensors switch between two different transmit antennas in a TDM mode for achieving the desired virtual array layout, cf. Section 2.1.3. For sufficient gain, the receiving antennas need a certain physical space such that no denser placement than a λ_c distance is possible. The MIMO principle allowed to achieve a spacing in the order of $\lambda_c/2$ in the virtual array for a nearly unambiguous angle finding as shown in Fig. 3.4. This results in a phase shift between the two halves of the virtual array. The shift amount is dependent on the relative velocity to the reflecting object and can be calculated by the absolute phase at the two different sampling points in time. With the available array, two different approaches for compensation are possible. Both are well-known in literature and can be applied as is. One approach is based on an overlapping element in the virtual array, such that one can evaluate the phase difference at this position and use it for bringing the two halves into phase alignment [42]. The advantage of this approach is that it is independent from where the object's velocity is located in the Doppler domain in terms of the Nyquist zone. A disadvantage, however, is that the measurement uncertainty of the phases influences the quality of the phase alignment and can cause raised side-lobe levels for lower SNRs. Because the DBF array calibration from the previous step already needs to be included for calculating the difference phase, the compensation phase is calculated as

$$\varphi_{\text{TDM-MIMO},pq}\left(\tilde{r}, n_{\mathrm{VRx}}, v_{\mathrm{r}}\right) = \begin{cases} \sphericalangle\left(\dfrac{\underline{R}_{n_{\mathrm{VRx,ovl,2}},pq}\ \underline{s}_{\mathrm{IF},pq}\left(\tilde{r}, n_{\mathrm{VRx,ovl,1}}, v_{\mathrm{r}}\right)}{\underline{R}_{n_{\mathrm{VRx,ovl,1}},pq}\ \underline{s}_{\mathrm{IF},pq}\left(\tilde{r}, n_{\mathrm{VRx,ovl,2}}, v_{\mathrm{r}}\right)}\right) & \text{if } n_{\mathrm{VRx}} \text{ belongs to } \mathrm{Tx}_2 \\ 0 & \text{else} \end{cases} \tag{4.12}$$

with $n_{\mathrm{VRx,ovl,1}}$ and $n_{\mathrm{VRx,ovl,2}}$ denoting the overlapping element related to Tx_1 and Tx_2, respectively.

The second approach is based on the information in the Doppler domain. While the actual implementation can vary, the general idea is that one can calculate how much phase shift occurs with the knowledge of the Doppler velocity and compensate accordingly [41]. For the image-like representations, one could iterate over the Doppler bins and use their associated velocities to compensate the corresponding virtual elements. While this theoretical model does not suffer from low SNR, the main drawback lies in the limitation to the unambiguous Doppler domain. The cor-

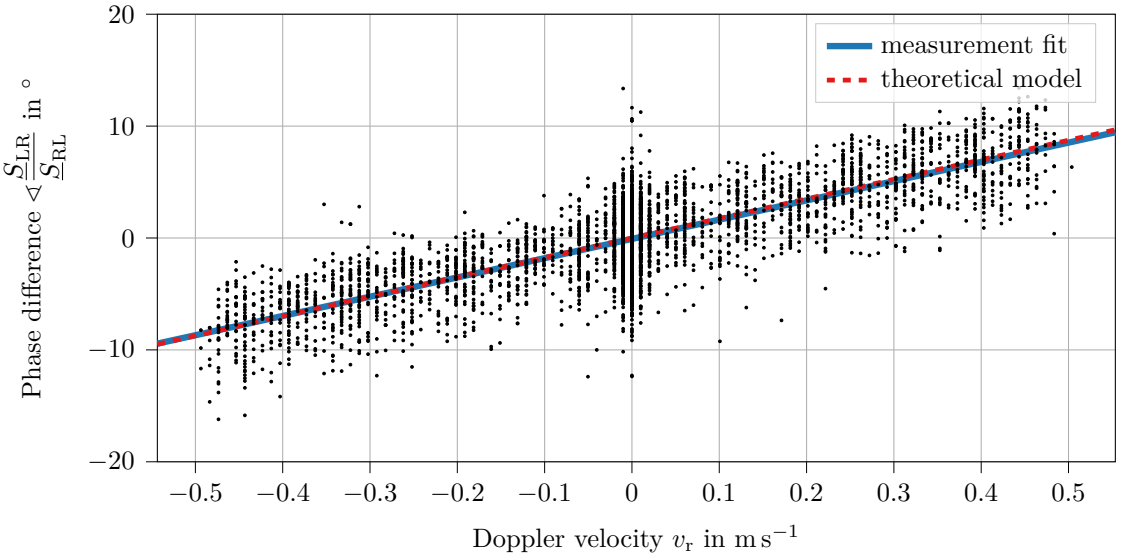


Figure 4.7: Without phase compensation, the phase difference between the odd-bounce channels for the pole target show a linear dependency on the velocity. The expected value is zero due to the quasi-monostatic measurement of a reciprocal environment. A fit of the measurement and the theoretical model from (4.14) agree with each other. Adapted from [**90**], © 2022 IEEE.

rection would fail for velocities that are wrapped from a non-zero Nyquist zone. The compensation phase is simply calculated by

$$\varphi_{\text{TDM-MIMO},pq}\left(n_{\text{VRx}}, v_{\mathrm{r}}\right) = \begin{cases} -\frac{\pi}{4}\frac{v_{\mathrm{r}}}{v_{\mathrm{r,max}}} & \text{if } n_{\text{VRx}} \text{ belongs to } \mathrm{Tx}_2 \\ 0 & \text{else} \end{cases} \tag{4.13}$$

when the modulation scheme for fully polarimetric measurements shown in Fig. 3.3 is chosen. Unless noted otherwise, using the overlapping element is set as the default method.

Transmit polarization TDM phase compensation

Analogously to the TDM-induced phase shift between elements with the same polarization associated to the two different transmit antennas for realization of the MIMO principle, the transmit polarization TDM causes a velocity-dependent phase shift. This time, the phases of the two halves of the scattering matrix are shifted. Therefore, similar approaches as in the previous section are appropriate. The purely mathematical approach based on the Doppler bin for the transmitter firing scheme in Fig. 3.3 can be formulated as

$$\varphi_{\text{TDM-polar},pq}\left(v_{\mathrm{r}}\right) = \begin{cases} -\frac{\pi}{2}\frac{v_{\mathrm{r}}}{v_{\mathrm{r,max}}} & \text{if transmit polarization is} \\ & \text{right-hand circular } (q = \mathrm{R}) \\ 0 & \text{else } (q = \mathrm{L}) \end{cases}. \tag{4.14}$$

It should be noted that this calibration was carried out after angle finding in [**90**]. Due to better efficiency, the application is now done before potentially extending

the number of samples in the angular dimension by the angle estimation (cf. Section 4.4.5). A good agreement between this theoretical model and what was measured in the test facility for the pole target is shown in Fig. 4.7. This establishes suitability of this approach. It should be noted that the depicted phase distortion is apparently rather low with maximum values of less than 20° but this is caused by the low crane velocities. For higher velocities, a substantial phase distortion occurs. The disadvantage regarding the unambiguous velocity can be counteracted by using the ego-motion estimation for unfolding the velocity. With respect to the static infrastructure required for localization, this unfolding provides the correct phase compensation. This does not work for other moving road users, but they are not within the scope of this work.
An alternative approach, equivalent to the overlapping element from before, is based on the assumption of a reciprocal environment that is illuminated by a quasi-monostatic radar. Then, the anti-diagonal elements of the scattering matrix are the same (cf. Section 2.3.4). This equality can be exploited to carry out the phase alignment because each element corresponds to one of the transmitter polarizations. As the quality would again depend on the SNR, it is advisable to perform this after beamforming to include the processing gain. However, it cannot be completely avoided to introduce polarimetric distortion in case of low SNR. Therefore, this approach is not used in this work. A circular polarization basis would actually be more suitable for such a method in typical automotive scenarios, because the anti-diagonal scattering matrix elements correspond to all odd-bounce objects. In the typical linear basis, these elements are associated with 45° double-bounce scattering, which occurs much less frequently, such that it is only applied above some threshold to avoid excessive distortion [76].

Joint calibration application

Combining all the above-mentioned correction factors, the joint calibration of this processing step is given by

$$\tilde{\underline{s}}_{\mathrm{IF},pq}\left(\tilde{r}, n_{\mathrm{VRx}}, v_{\mathrm{r}}\right) = \underline{s}_{\mathrm{IF},pq}\left(\tilde{r}, n_{\mathrm{VRx}}, v_{\mathrm{r}}\right) \underline{R}^{-1}_{n_{\mathrm{VRx}},pq}\, e^{\mathrm{j}\left(\varphi_{\text{TDM-MIMO},pq}+\varphi_{\text{TDM-polar},pq}\right)}. \quad (4.15)$$

4.4.5 Angle estimation

The selection of the angular processing method is made while taking the intended principle of subsequent algorithmic steps into account. This results in the requirement that a dense angular domain information shall be available after angular processing, i.e., no sparse single peak positions are desired. It would be advantageous if the resulting image-like representation is more focused in the angular domain than from usual beamforming utilizing only the native aperture. Moreover, the amplitudes should correspond to real power values and the phase must be part of the estimation result, i.e., pseudo-spectra from subspace-based approaches are not desired either. Lastly, the ideal approach would be able to appropriately handle the gaps in the virtual array layout shown in Fig. 3.4. As a results, many approaches are already excluded.

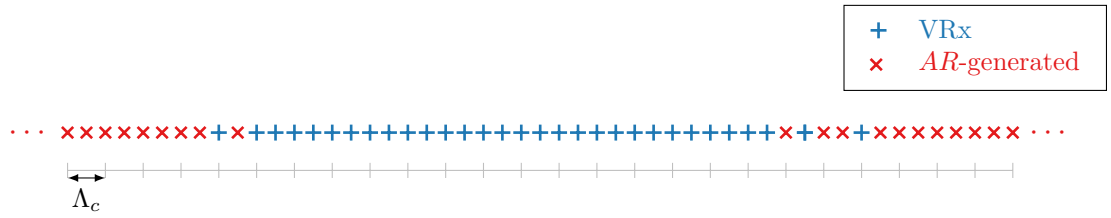


Figure 4.8: The AR model-based prediction of spatial samples is used to fill the gaps of the virtual array and to extent the overall aperture to both sides.

An approach that meets all requirements is based on array element prediction by autoregressive models (AR). After estimation of the AR model parameters on the elements of the virtual array, this allows to predict values for the gaps in the aperture and to extend the aperture by extrapolating elements left and right. A visualization of the AR predicted elements for the present array layout is given by Fig. 4.8. Regular FFT processing is applied after prediction of the extended aperture such that the spectral estimates are consistent for the polarimetric application.
For estimation of the AR parameters, different approaches exist [39]. One particularly suitable technique is the so-called Burg method [106]. The resulting AR model estimate is guaranteed to be stable, which is important for larger extrapolation sizes. Applying it in the context of automotive radar in this way was also proposed in [107]. This method is chosen for this work and the default processing includes the prediction of a 128 element $\Lambda_c/2$ ULA with a subsequent FFT. Due to the possibility to do the parameter estimation and prediction in parallel for each range-Doppler bin on the GPU, it was possible to unconditionally use a model order of 8 everywhere. Exemplary azimuth spectra of a single cycle measurement of the pole target are shown with and without aperture extension by AR prediction in Fig. 4.9. By comparing the amplitude and phase differences between both odd-bounce channels, it can be observed that no significant disagreement between the regular and AR-extended processing exits in terms of the relative polarimetric information. It should be noted that the calibration between the polarimetric channels (see Section 4.4.6) is not carried out yet such that the observed phase differences are not expected to be zero at this stage. Rather, it is about the comparison between the processing variants.

4.4.6 Polarimetric antenna pattern correction

For the antenna pattern correction, the separate transmit and receive models in (4.7) are transformed into a single two-way azimuth-dependent complex gain pattern per polarimetric channel $\underline{G}_{pq}(\theta)$. One part of it is already well-known from non-polarimetric radars, namely the real factor describing the different antenna gains for varying spatial angles. The resulting course of the amplitudes over azimuth can be seen in Fig. 4.10. A calibration can be achieved by storing some values at a few control points and applying a linearly interpolated value between them.
A new aspect is that care must also be taken of a potential imbalance of the phases in the different polarimetric channels. Fig. 4.11 shows an investigation of the differential phase of the pole's odd-bounce channels as a function of azimuth angle. It

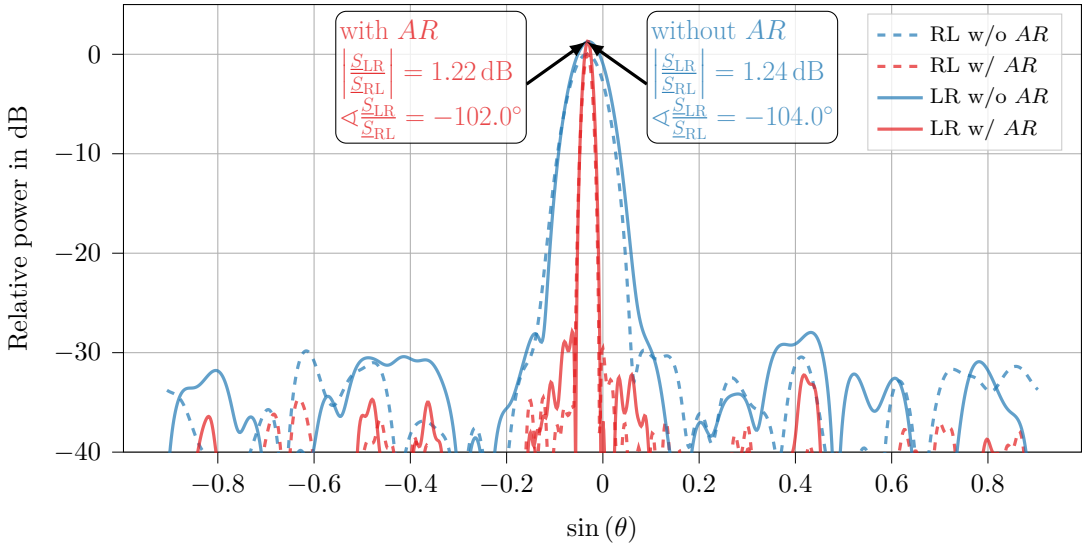


Figure 4.9: With a synthetically extended aperture by AR prediction, the angular spectrum is more focused while not distorting the relative polarimetric information. A comparison of the amplitude and phase differences of the odd-bounce channels for one pole target measurement cycle with and without AR processing confirms this. A Hamming window is used for lower side-lobes and zero-padding for more comprehensible courses.

should be noted that the average azimuth-independent phase difference is already compensated beforehand to make the figure more easy to read. One can clearly identify a systematic error because a value of zero is expected. Control points are introduced with a distance of 5° each and medians of the corresponding measurements serve as the basis for a piecewise linear interpolation as visualized in red in Fig. 4.11. After correction, the standard deviation of this phase difference is reduced from 5.3° to 2.8°. Due to the characteristic of the two selected calibration targets, no phase alignment between the even- and odd-bounce channels is possible. Therefore, the complex gain pattern $\underline{G}_{pq}$ consists of the real gain characteristic measured independently for all polarimetric channels and the phase corrections only for the channels corresponding to a right-hand circular sent polarization, which is derived from the pole measurement for $\underline{S}_{\mathrm{LR}}$ and from the dihedral measurement for $\underline{S}_{\mathrm{RR}}$. This calibration step is applied according to

$$\tilde{\underline{s}}_{\mathrm{IF},pq}\left(\tilde{r},\tilde{\theta},v_{\mathrm{r}}\right) = \underline{G}_{pq}^{-1}(\tilde{\theta})\;\underline{s}_{\mathrm{IF},pq}\left(\tilde{r},\tilde{\theta},v_{\mathrm{r}}\right). \tag{4.16}$$

4.4.7 Range-dependent RCS correction & spatial calibration

The following calibration steps are not specific to a polarimetric system, and therefore this section is kept short. Next to the azimuth dependency of the RCS, the range dimension also needs to be calibrated for a constant RCS as can be seen in Fig. 4.10: The combination of the radar's band-pass characteristic and the theoretical r^{-4} dependency causes a range-dependent change of amplitude without compensation. The calibration is achieved through piecewise linear interpolation as well.

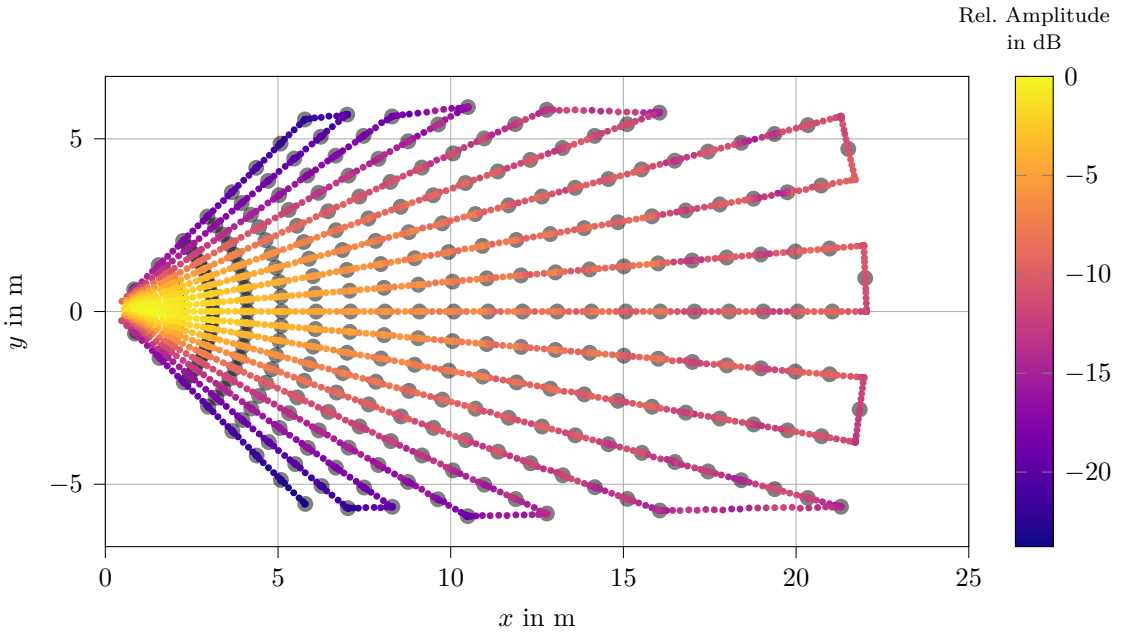


Figure 4.10: The colored scatter points show all estimated spatial positions of the pole target in the LR-channel by a partially calibrated radar. The programmed star pattern is clearly recognizable. Gray scatter points show positions where the crane was stationary for a moment. The color-coded amplitude values show the antenna gain pattern characteristic as well as the range dependency as a combination of the theoretical r^{-4} function and the radar's band-pass. Adapted from [**90**], © 2022 IEEE.

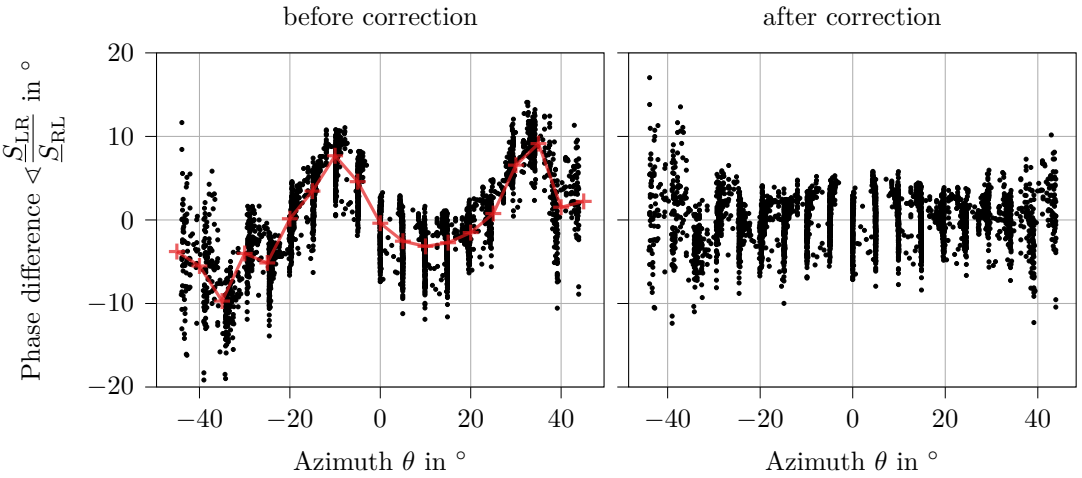


Figure 4.11: The odd-bounce phase difference shows a systematic error as a function of the azimuth angle. A simple correction approach by piecewise linear interpolation (red) allows to improve it. Adapted from [**90**], © 2022 IEEE.

With localization being an application that is dependent on spatial accuracy, the precise ground truth data of the crane position is used to calibrate range and azimuth. Both dimension estimates $\tilde{r}$ and $\tilde{\theta}$ up to this point are calculated based on the theoretical modulation parameters. Deviations of the actual chirp bandwidth or element spacing relative to the wavelength might require a re-scaling of the dimensions, which is model by the factors κ_r and κ_θ for range and azimuth, respectively. Furthermore, the radar might not be perfectly angle aligned with the test facility and the actual antenna array phase center may not be known exactly, such that the bias terms $\varepsilon_{r,pq}$ and ε_ψ for the range and yaw mounting angle domains are allowed. Compared to the per-channel value in Section 4.4.4, the yaw angle error ε_ψ is one universal value to allow an additional degree of freedom. However, the result after optimization is not used. Lastly, the origin of the ground truth coordinate system might be shifted by Cartesian coordinates x and y. This model is used for formulation of the least squares optimization

$$\underset{x,y,\kappa_r,\kappa_\theta,\varepsilon_{r,pq},\varepsilon_\psi}{\arg\min} \sum_i \left(\frac{1}{r_{\mathrm{gt}}} \left\| \begin{pmatrix} r_{\mathrm{gt}} \cos(\theta_{\mathrm{gt}}) + x \\ r_{\mathrm{gt}} \sin(\theta_{\mathrm{gt}}) + y \end{pmatrix} - (\kappa_r \tilde{r}_i + \varepsilon_{r,pq}) \begin{pmatrix} \cos(\kappa_\theta \tilde{\theta}_i + \varepsilon_\psi) \\ \sin(\kappa_\theta \tilde{\theta}_i + \varepsilon_\psi) \end{pmatrix} \right\| \right)^2 \tag{4.17}$$

where r_{gt} and θ_{gt} are the ground truth parameters known from the crane positioning. The Euclidean length of the error vector is normalized by the ground truth range r_{gt} to take the increasing error for larger ranges despite a constant angular error into account. From the resulting parameter vector, the optimal phase center range offset $\hat{\varepsilon}_{r,pq}$ is used in (4.9) and the optimal scaling parameters are applied according to

$$r = \hat{\kappa}_r \, \tilde{r} \qquad\qquad \theta = \hat{\kappa}_\theta \, \tilde{\theta} \tag{4.18}$$

for finding the final spatial estimates.
The remaining errors for the pole target are depicted in Fig. 4.12. Low root mean square errors (RMSEs) of 6 mm for range and 0.07° for azimuth indicate a successful calibration, as they lie in the same order of magnitude as the crane positioning accuracy. Besides, the larger errors are observed for the very close ranges below 5 m only, which is expected due to disregard of tailored processing when the typical far-field beamforming assumptions are violated.

4.5 Radome influence

A front radar sensor in series vehicles is usually mounted behind a radome, which serves as a protective cover from environmental factors. If this secondary surface severely distorts the polarimetric information, it could imply the need for a different calibration strategy compared to today's typical setup. An intrinsic calibration independent from the radome at the radar supplier's plant with a purely extrinsic calibration of the radome-mounted radar during vehicle production could become insufficient. In order to provide an initial assessment, measurements were taken and differential polarimetric information is evaluated. Due to the closure of the automated test facility, the measurements were recorded outside with the targets

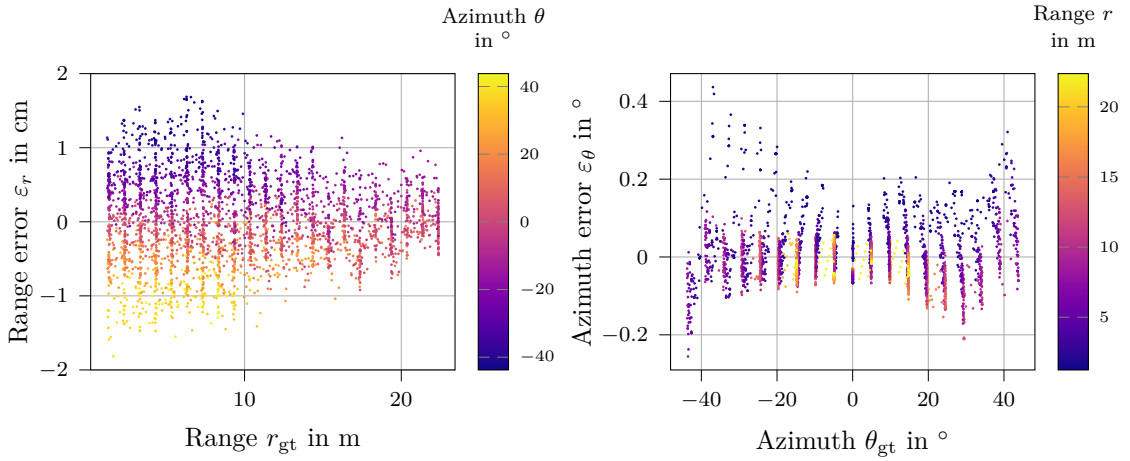


Figure 4.12: After applying the spatial calibration, the remaining errors in range and azimuth are small. The positioning accuracy of the crane is in the same order of magnitude. This figure is best viewed on a screen.



(a) (b)

Figure 4.13: A series-production radome is temporarily mounted in front of the front radar (a) and a dihedral reflector is placed under various azimuth angles successively as shown in the composite photograph (b). Adapted from **[90]**, © 2022 IEEE.

mounted on a low reflectivity tripod as shown in Fig. 4.13. As the radome measurements were performed after all other experiments including the recordings for localization in the subsequent chapters, the potential impact of the radome was not known for the experiments such that no secondary surface was present in these as a precaution. The radome is a series-production part with a composite structure. Due to the temporary installation of the radome, the mounting angle along the axis lateral to the driving direction is not controlled precisely. The emitted waves do not impinge orthogonal to the radome's backside but at a slightly rotated one by a few degrees.

The measurements include a sphere and a dihedral target. Due to the low SNR for the sphere and the associated partial evaluation difficulties, the results for the dihedral target are shown in Fig. 4.14. Analyzing the phase difference distribution for the measurement without the radome, some variation can be observed that amounts to an RMSE of 7°. This could be attributed either to an imperfect calibration or a

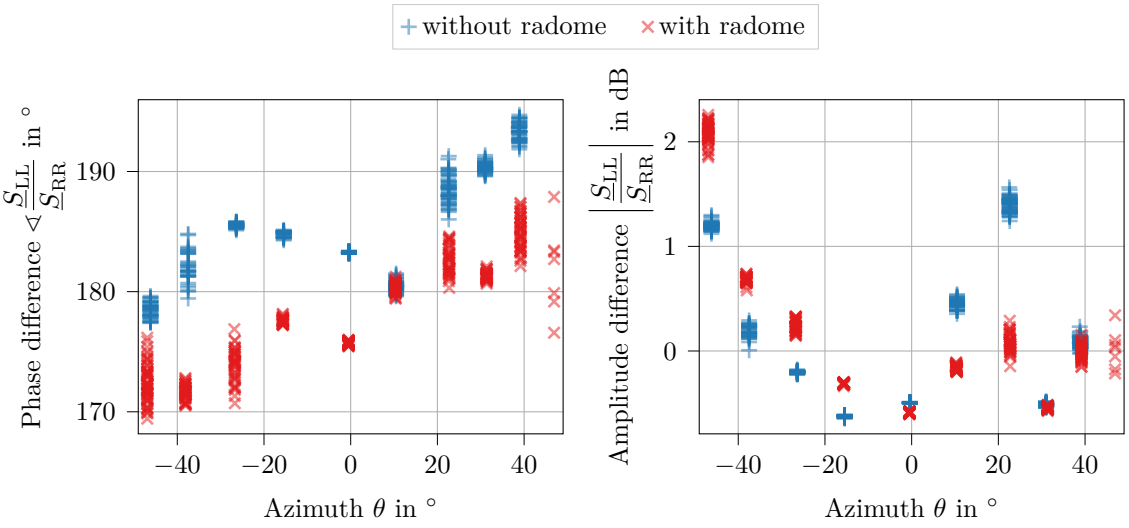


Figure 4.14: A comparison of the relative polarimetric information of the even-bounce channels for the dihedral target shows the difference between presence and absence of the radome. Adapted from **[90]**, © 2022 IEEE.

misalignment of the dihedral. Rotating the dihedral results in a proportional change of the even-bounce phase difference as described in Section 2.3.7. The observed errors are in the same order of magnitude as one would expect from non-ideal alignment due to the manual setup. Comparing the result for the measurement with the radome, an RMSE of 5° is calculated. Therefore, an equal order of magnitude is observed and phases do not give an indication for needing a completely new calibration. The same holds true for the amplitude ratio also shown in Fig. 4.14. RMSEs of 0.20 dB and 0.14 dB are calculated for absence and presence of the radome, respectively. When not limited by SNR, orders of magnitude comparable to those observed for the sphere target can be identified.

The presented results do not indicate the immediate demand for a full re-calibration after installation behind an RF-optimized radome. However, it should be noted that the limited number of measurements in a not precisely controlled measurement setup only serves as a starting point for such investigations. Comparing the results with more precise measurements and evaluations available in literature, a confirmation of a consistent amplitude and phase behavior along the extent in the relevant central area of the radome is found [108]. Next to the shown same-bounce evaluation, the polarimetric cross-coupling is expected to deteriorate for azimuth angles close to the field of view borders depending on the realization of the radome [109]. Moreover, for mounting positions at the vehicle corners, the impact of an installation behind the non-flat bumper is not included in this study but remains open. The available bumper did not offer enough space for an integration of the sensor with its given size.

4.6 Summary

In this chapter, new challenges of exploiting the full potential of polarimetry in automotive applications were highlighted. The polarimetric information should be determined as distortion-free as possible regardless of where the object is located in the radar's field of view, including both the spatial as well as velocity dimensions. Extensive measurements were taken in an automated test facility and appropriate calibration approaches were developed based on a combination of a theoretical model and the observations made by evaluating the measurements. In particular, this included the idea to use extrinsic mounting angle correction algorithms separately per polarimetric channel for a precise intrinsic beamforming alignment, the adaption of phase compensation techniques from TDM MIMO processing to TDM polarimetry acquisition and the investigation of phase distortion over the azimuth angle. Because there is a strong interdependency between the general radar signal processing approach and the necessary calibration steps, the entirety of the involved processing was covered for comprehensibility to the reader. Additionally, measurements with a secondary surface in form of an RF-optimized series-production radome were carried out. The intention was to investigate if a fundamentally different approach to state of the art series production calibration has to be pursued for enabling polarimetry. Evaluation of these measurements did not indicate that.

Chapter 5

Static environment

For higher levels of automated driving, increasing attention must be paid to the static surroundings of an automated vehicle. Safe navigation is only possible with reliable and accurate knowledge about the vehicle's pose within an environment. Therefore, characteristic elements of the environment serve as points of orientation. Such *landmarks* are crucial parts of the localization process and their detailed analysis facilitates developing tailored approaches. In particular, the newly applied polarimetry in this work requires a detailed investigation of the resulting opportunities and challenges.

For this purpose, typical automotive environment objects are investigated with regard to their scattering behavior and a potential to serve as robust landmarks in Section 5.1. This includes an analysis of the scattering behavior in dependence of the incident angle as well as spatially resolved images by using the inverse SAR (ISAR) principle to examine which parts are the origin of different scattering. The results of this analysis suggest the necessity for a specific algorithmic representation of the polarimetric data from static environments within the perception stack. A technique that attempts to fulfill these requirements in a practicable way is proposed in Section 5.2. This new approach takes advantage of incorporating low-level data for mapping the environment as complete as possible. On the basis of the novel representation technique, suitable landmark candidate detectors that utilize the new properties are introduced in Section 5.3.

Summarizing, this chapter includes the following contributions:

- a detailed analysis of the scattering behavior of typical automotive landmarks,
- the introduction of a novel grid map representation suitable for storing polarimetric information,
- a point-shaped landmark detector exploiting polarimetric scattering differences for increased robustness,
- a comparison of recognition performance of point-shaped landmark candidates with different levels of polarimetric information, and
- an evaluation of line-shaped landmark extraction quality for detection- and low-level data.

5.1 Landmark scattering analysis

In order to develop a suitable framework for representing the static environment and to design an associated detector for landmarks, it is desirable to know what scattering to expect from a typical automotive environment. Therefore, available literature in that regard is summarized in Section 5.1.1. For the remaining subsections of Section 5.1, an own two-fold scattering analysis is carried out to fill in the gaps in current literature. First, undisturbed measurements of individual point-shaped landmarks in an anechoic chamber are calibrated and evaluated in Sections 5.1.2 to 5.1.5 with respect to their scattering behavior both in dependence of the incident angle as well as the spatial position of the scattering centers. This investigation is based on the own publication "Polarimetric Scattering Mechanism Analysis of Automotive Landmarks" [**110**] and the supervised thesis "Polarimetric Evaluation of Scattering Mechanisms of Automotive Landmarks" [111]. Second, scattering behavior in a typical real-world measurement is evaluated and discussed in Section 5.1.6. Some parts have been published beforehand by this thesis' author in the paper "Polarimetric Radar for Automotive Self-Localization" [**91**].

5.1.1 State of the art

An early publication of scattering behavior of localization-suitable road infrastructure in the 77 GHz automotive radar frequency band deals with the RCS's strong dependence on the incident angle for most objects [112]. The objects examined are different traffic signs and a guide post, all showing a wide range of RCS values over the incident angle with variations as large as 60 dB in the most prominent cases. A single vertical polarization is used for the transmitter and receiver, and no polarimetric data is acquired. Local maxima are observed for normal incidence to the fronts of the signs or the guide post. For oblique incidence, in which the sign face still covers a part of its mounting pole, local RCS minima result because the incident energy is mostly deflected away from the receiver. If the back side of the traffic sign is observed, higher values than the minima are observed, which is explained by a combination of the visibility of a larger part of the pole and a dihedral corner-like structure formed between sign face and mounting pole.

The latter publication is extended by [31] to include a polarimetric assessment in a similar setup. Due to the large physical extent of typical traffic signs, usual measuring distances in a real-world application may not be in the far-field region for 77 GHz. This was also not the case in the publication's measurements and the consequential broadening of the local RCS maximum is discussed and proven. A linear basis is used for the polarimetric evaluation, but only the absolute values of the scattering matrix elements are analyzed such that no even- and odd-bounce distinction for the co-polarized response is possible. Except for a small offset between $|\underline{S}_{\mathrm{HH}}|$ and $|\underline{S}_{\mathrm{VV}}|$, the patterns are very similar for all objects. The cross-polarized channel is reported to be about 15 dB below the co-polarized channels, which is attributed to edge scattering.

Another non-polarimetric publication [113] confirms that a large range of RCS values for typical road infrastructure objects has to be expected depending on the incident angle. With respect to line-shaped landmarks, guardrails are observed to primarily backscatter from their posts both by simulation [114] and measurement [115], when typical forward-looking setups, i.e., the vehicle-parallel guardrail is detected by a front sensor, are considered. No significant difference is identified between both co-polarized channels in a linear basis for the frequency of interest [115]. When incidence is close to normal in the horizontal plane, a significant RCS is measured also from the guardrail beam itself and not only the posts. The w-shaped profile of a guardrail beam is the reason for reflecting non-negligible power not only in a specular manner but at different observation heights [115].
In a setup similar to the one used for this thesis' analysis, the distribution of scattering centers on typical automotive landmarks along the height dimension is investigated [116]. The polarimetric information is used for calculating a sample covariance matrix for resolving the height dimension, i.e., no scattering mechanism analysis is performed. A successful discrimination of plate and pole in the generated height profiles of the measured traffic signs is demonstrated and the derived estimates for the target dimensions closely match the actual ones.

5.1.2 Anechoic chamber measurement setup

For a detailed analysis of the scattering mechanisms including their spatial allocation, common automotive environment objects were measured on a turntable in the compact antenna test range (CATR) at the Institute of High Frequency Technology, RWTH Aachen [117]. A visualization of the setup is shown in Fig. 5.1. The reflector design in this anechoic chamber ensures that the spherical wave from the feed is transformed to a plane wave before impinging on the object of interest in the so-called quiet zone, where a the wave's phase ripple is below a specific threshold. With an inverse transformation of any reflected power, this effectively is equivalent to a far-field measurement in total. Contrary to the partial near-field measurements in [31, 112], no measurement distance-dependent propagation effects have to be considered during evaluation in this work.
The three objects measured are shown in Fig. 5.2. Two different traffic signs are mounted on a steel pole with a diameter of 60 mm. All signs are made from 2 mm thick aluminum plates. A circular speed limit sign with a 600 mm diameter and a rectangular supplementary sign is measured first. As a second object, the custom-made octagonal stop sign is used. It is 600 mm wide and high. The reflective cover for optical frequencies does not influence the response at 77 GHz [112] and is omitted. The guide post dimensions are standard as required by the German authorities (bounding box of approx. 120 mm × 100 mm). It is made from polyethylene.
The turntable with the objects is revolved by a full 360° rotation to assess the scattering for each incident angle. One full revolution is repeated four times per object to measure all elements of the scattering matrix, which requires a manual rotation of the linearly polarized transmitting and receiving antennas between the repetitions. The range dimension is resolved by operating a vector network analyzer with external frequency converters as a stepped-frequency continuous wave (SFCW) radar. An overview of the operating parameters is given by Table 5.1.

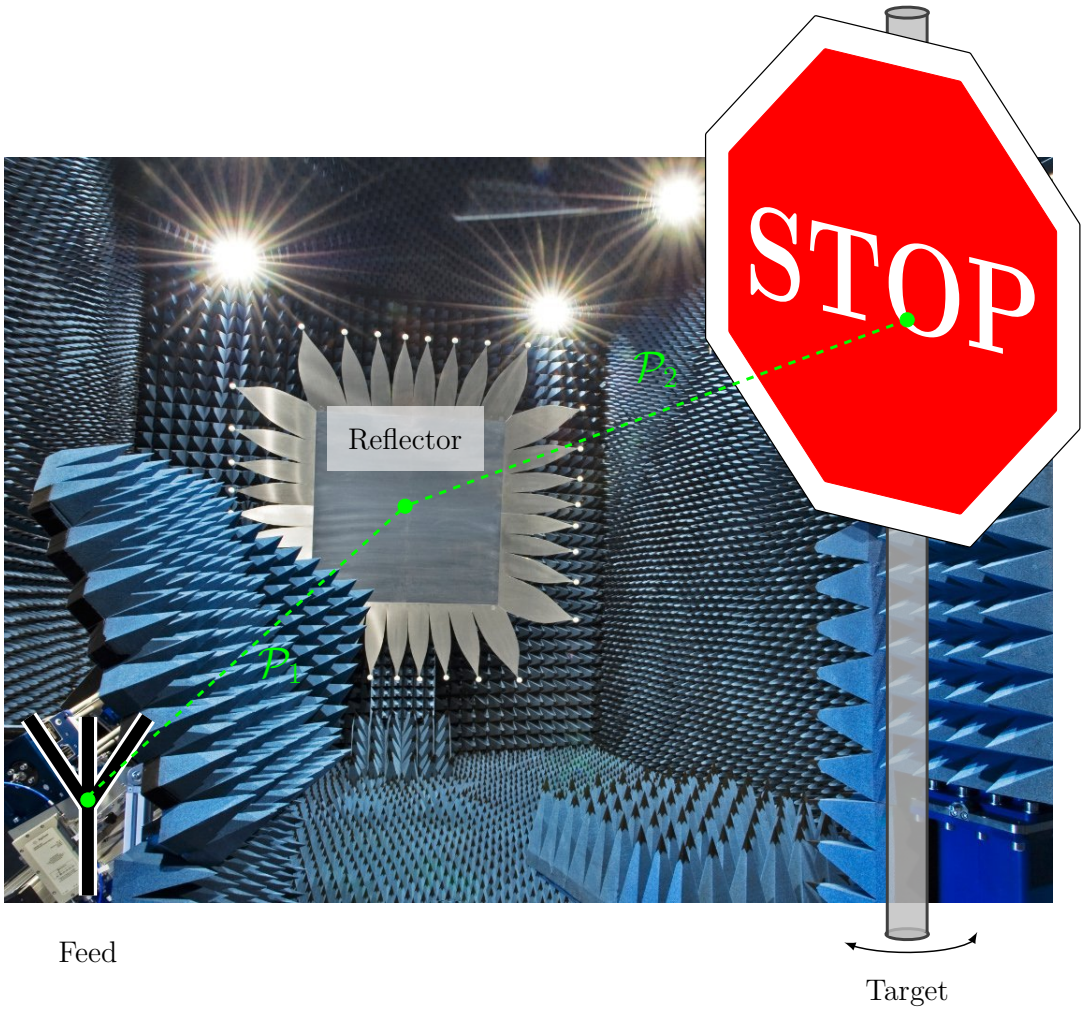
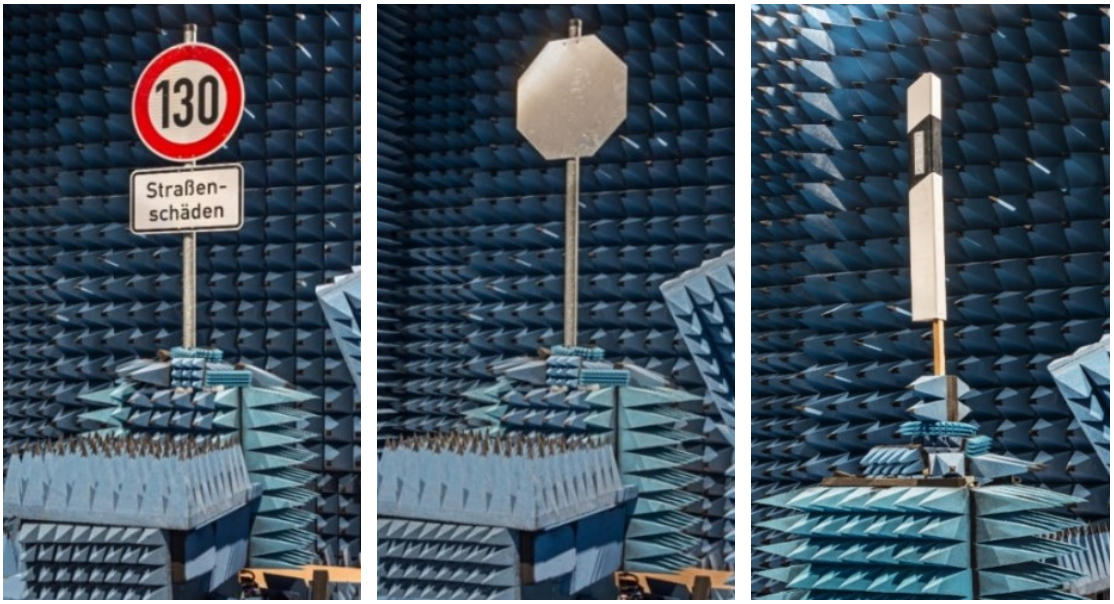


Figure 5.1: The landmarks are mounted on a turntable in an anechoic CATR to measure the scattering response from varying incident angles. Underlying photograph is a courtesy of Institute of High Frequency Technology, RWTH Aachen [117].

Table 5.1: Parameters for the landmark scattering analysis

Parameter		**Value**
Center frequency	f_c	75 GHz
Frequency step size	Δ_f	10 MHz
Bandwidth	B	15 GHz
Range resolution (Rayleigh)	δ_r	1 cm
Incident angle step size		
speed limit sign, stop sign	Δ_Θ	0.15°
guide post	Δ_Θ	0.2°
Incident angle range	Θ	0° - 360°
Polarization basis	$\mathcal{B}$	$\mathcal{B}_{\mathrm{HV}}$



(a) Speed limit sign (b) Stop sign (c) Guide post

Figure 5.2: Three typical automotive objects suitable as landmarks are measured on a turntable in an anechoic chamber. Adapted from **[110]**, © 2020 IEEE.

To allow a high-resolution evaluation, a bandwidth of 15 GHz is sampled with a step size of 10 MHz. Thus, a native range resolution of 10 mm is reached, and the unambiguous range is larger than the longest expected path in the CATR. A center frequency of 75 GHz is chosen, where the frequency band of interest for automotive radar is close. The maximum angular step size is dictated by the desired unambiguous cross-range for the ISAR processing. Due to the different physical extents, this results in step sizes of 0.15° for the traffic sign objects and 0.2° for the guide post including some safety margin. As no reference target calibration is carried out, no absolute RCS values are resulting. Instead, the relative behavior is analyzed in the following.

5.1.3 Drift compensation

The intended scattering mechanism analysis based on linear polarization basis measurements makes a stable phase information next to the amplitude values important because discriminating between even- and odd-bounce scattering requires the phase difference of the co-polarized channels. Due to the selected measurement parameters, the acquisition duration per object amounts to a low double-digit number of hours. Consequently, drift effects must be taken into account. An investigation for the same CATR setup at 2.4 GHz showed a phase drift of 0.3° over a course of 24 h, which is attributed to a temperature change of 0.3 °C [118, Ch. 6.3.8]. Assuming that a linear translation to 75 GHz is justified due to an attribution to pure linear thermal expansion effects, this equals to a phase drift of up to 31 °/°C. As the measurements were carried out during very warm summer days and comparatively cooler nights, a non-negligible phase drift has to be expected.

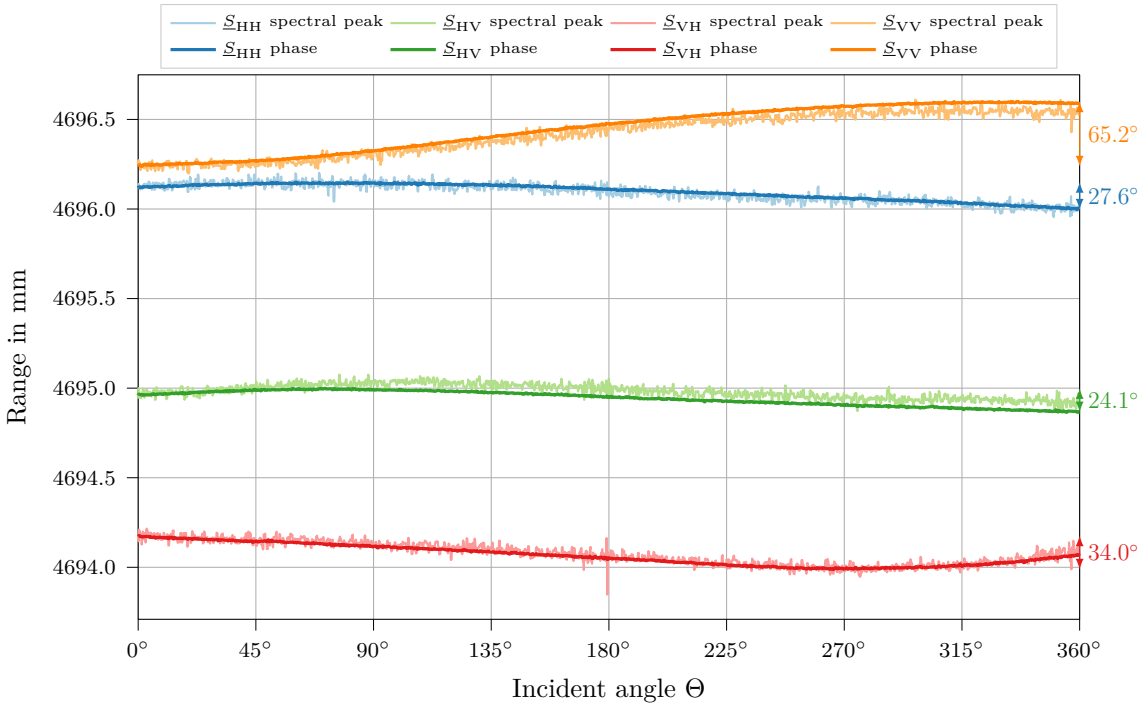


Figure 5.3: The spatial position of the reflector and the range-translated and -aligned phase show a non-negligible drift over the course of the stop sign measurement. The span of the phase drift is given on the right. The profiles of the range and phase curves per polarization channel are very similar.

For investigating the long-term phase stability of the measurement setup, reflections originating from the CATR reflector are assessed. For this, the spatial position of the local maximum in the range spectrum belonging to the reflector is estimated precisely, e.g., by using a large zero-padding factor for transforming to the range domain. Additionally, the phase of this maximum is determined. Both are plotted in Fig. 5.3 for all polarimetric channels of the stop sign measurement. The phase is transformed into an equivalent range by multiplying with $\lambda_c/4\pi$ and its start is aligned to the spatial peak position in order to allow a better comparison between range and phase. This comparison shows that both are drifting almost identically, which supports the assumption of thermal expansion effects as the cause. It is expected that such effects become visible as actual distance changes between the different components of the setup, so that phase and frequency would drift together, which matches with the observation.

Additionally to the phase compensation approach in **[110]**, a range compensation of the drift per polarimetric channel as well as an alignment between the channels is carried out for this thesis. The same principle and method as introduced in Section 4.4.2 for the electrical path length equalization applies. The average range difference to the reflector between the polarimetric channels is assumed to be caused by the manual rotation procedure, which is necessary when changing the polarization of the transmit and receive antennas. Therefore, this difference is compensated with a factor of one. The drift over the course of the measurement, however, is attributed to thermal effects of the measurement setup. Because the information is derived from the reflector, only the drift from path $\mathcal{P}_1$ (cf. Fig. 5.1) is considered.

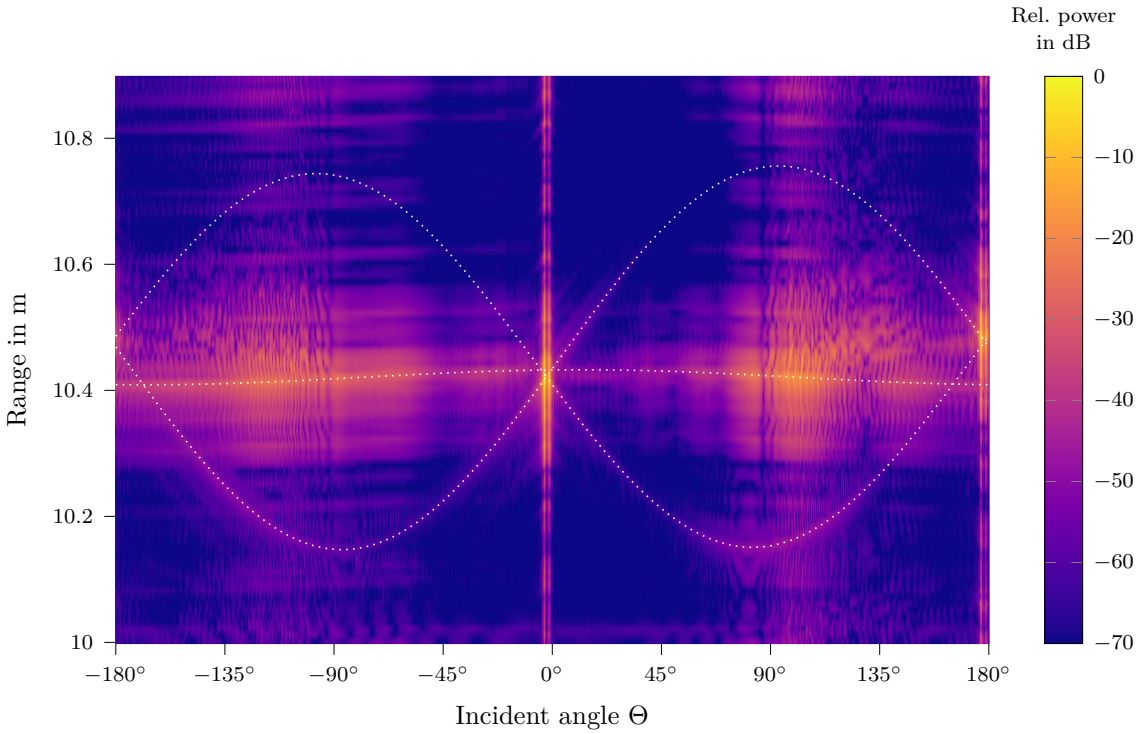


Figure 5.4: All $\underline{S}_{\mathrm{VV}}$ range profiles of the stop sign measurement are shown as a normalized power map. Three distinctive scatterer positions are identified by robustly fitting a model function to the position of local reflection maxima.

In order to compensate for a target scattering analysis, a factor of two is used as an approximation for also taking path $\mathcal{P}_2$ into account. Due to the close spatial proximity of feed and target, comparable contributions of drift are expected per path. The combined compensation curve is applied to both, range and phase, according to a SFCW signal model. Subsequently, an additional purely phase-based compensation is applied by assuming an equal phase of the co- and cross-polarized channels at the reflector. While the range-based compensation is novel in this work, the last phase-based step was previously published in [**110**].

The reflector-based approach is the only reliable source available in the measurement for range compensation, which entails a corresponding use in this work. However, when observing the target phases for a scattering mechanism analysis, they are not in accordance with the expectations for scattering centers with known scattering behavior, e.g., from simulation, as will be shown in the following. This observation can be explained by additional phase drifts not yet compensated, e.g., due to deviations from previously made assumptions. Therefore, an additional phase compensation based on the target itself is carried out. While the idea was already published in the paper [**110**], a refined version is used in this work. For this, three distinctive scattering centers with known scattering behavior are chosen and tracked in the range profiles over all incident angles: the pole, to which the traffic sign plates are attached, and the edges of the traffic sign plates on the left and on the right. By precisely searching for local maxima in the vicinity of the expected scattering center positions over all incident angles Θ, the parameters of the position model are estimated robustly via a random sample consensus (RANSAC) algorithm [119].

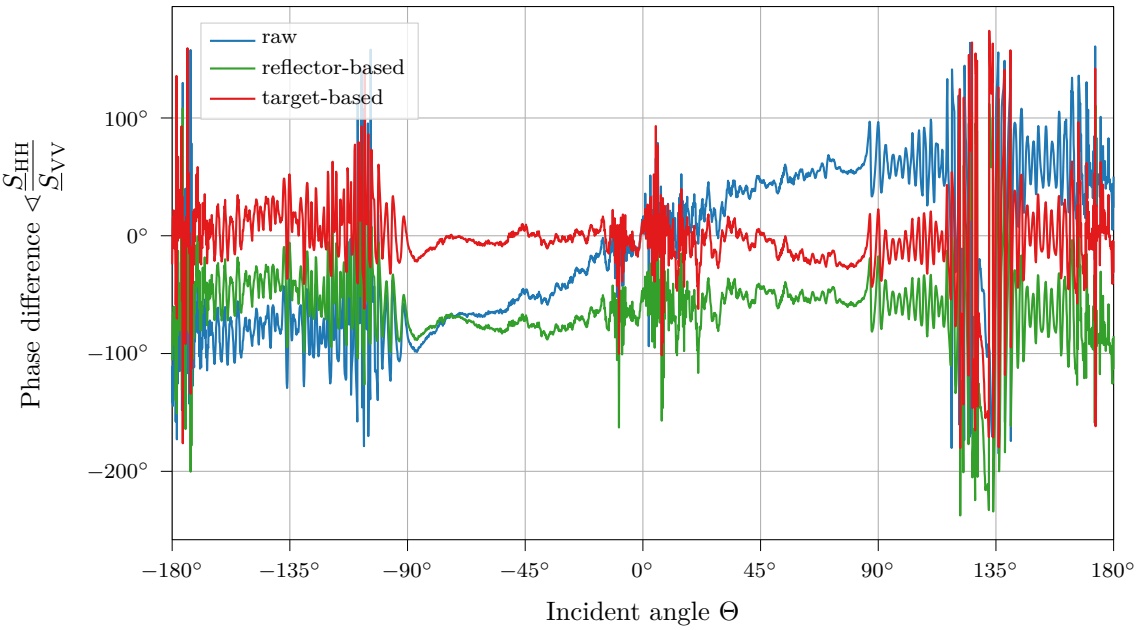


Figure 5.5: The phase difference between the co-polarized channels for the pole scattering shows a significant drift without compensation. Applying the reflector-based compensation with a factor of two clearly improves the drift. A meaningful scattering mechanism analysis requires the additional target-based phase compensation.

For the edges, the model is $r_{\mathrm{rc}} + x_0 \sin(\Theta) + y_0 \cos(\Theta)$, and for the pole $r_{\mathrm{rc}} - r_{\mathrm{pole}} + y_0 \cos(\Theta)$ is chosen with the rotation center distance r_{rc} and the radius of the traffic sign pole r_{pole}. The result of such an estimation for the stop sign target is shown in Fig. 5.4. The positions of the three scattering centers are shown by white dots. By comparing them to the underlying power map, a good agreement between local power maxima and the estimated models can be observed. In addition to the below-mentioned phase compensation, the estimated parameters are used to determine the rotation center distances used for the subsequent ISAR image formation.

For the target-based phase compensation, a priori knowledge about the scattering mechanisms for the distinctive scattering centers is exploited: all three are expected to be dominated by odd-bounce scattering (this hypothesis is confirmed below by an analysis of a simulation in Section 5.1.5). Thus, zero phase difference between both co-polarized channels is assumed for the corresponding range cells. Fig. 5.5 shows the phase difference of the pole scattering for different steps in the proposed compensation chain for the stop sign target. It is extracted by matched filtering using the ranges from the model parameters estimated before. In general, the phase differences can be separated into two characteristic regions: For incident angles $|\Theta| < 90°$, a lower frequency component is dominant and makes identifying the drift easy. Outside of this region, a higher frequency variation occurs that will be attributed to scattering other than odd-bounce later on. Quantifying a drift component in this region is more challenging.

For the uncompensated raw data, a phase drift of more than 150° can be observed. With the first compensation step using reflector information, a significant improvement is achieved with respect to the drift, which justifies the assumptions about the

paths $\mathcal{P}_1$ and $\mathcal{P}_2$ from above. However, the improved phase difference after this step still shows an overall offset and a minor remaining drift component. Therefore, a compensation based on the observed phase difference of the three distinctive scatterers is carried out in a secondary step. Apart from the pole values shown in green in Fig. 5.5, equivalent information is derived from the two edges. After outlier rejection and consensus finding between the three scatterers by averaging, a polynomial is fitted in order to smoothly model the remaining drift and offset. The resulting polynomial is used for phase compensation and data of the pole scattering calibrated by this is shown in Fig. 5.5 as well. A successful suppression of the slow drift with a preservation of the scattering-related higher frequency variation can be observed. This calibration approach works well for the two traffic sign targets. On the contrary, the guide post does not possess such distinctive scatterers with known dominant mechanisms and a visibility over a large range of incident angles. Therefore, range bins, which exceed a power threshold after incoherent summation over all incident angles, were chosen as an alternative to provide the data for target-based compensation. For calibration of the cross-polarized channels, the phase difference is assumed to be zero, too, due to a quasi-monostatic setup. Thus, the same calibration steps as for the co-polarized channels is carried out, although the scattering intensity is expected to be much lower in comparison due the geometrical target structures.

5.1.4 Scattering analysis by incident angle

Given that the preceding compensation approach allows an interpretation of actual scattering mechanisms, the first analysis is intended to investigate an incident angle dependencies. Therefore, the measurements are decomposed into Pauli components (cf. Section 2.3.8). The measured ranges to the different scatterers are only taken into account in this analysis to the extent that a scattering origin of a reflection is located at the target of interest. For this, the calibrated and decomposed data is transformed into a range-angle map by applying an inverse Fourier transform to the wavenumber dimension k as in regular SFCW processing according to

$$\underline{\boldsymbol{\alpha}}_{\text{Pauli}}(r,\Theta) = \mathcal{F}_k^{-1}\left\{\mathcal{D}_{\text{Pauli}}\left\{\underline{\mathbf{S}}_{\mathcal{B}_{\text{HV}}}(k,\Theta)\right\}\right\}. \tag{5.1}$$

Scattering originating from the target of interest is assumed to stem from a 1 m window around the rotation center so that the angle-dependent scattering power, expressed as a pseudo-RCS $\tilde{\sigma}$, is calculated by incoherently integrating along the range domain with

$$\tilde{\sigma}_i(\Theta) = \sum_{r=r_{\text{rc}}-0.5\,\text{m}}^{r_{\text{rc}}+0.5\,\text{m}} \left|\underline{\alpha}_i(r,\Theta)\right|^2 \tag{5.2}$$

for each Pauli component $\underline{\alpha}_i$.

The resulting contributions of the different scattering types for the speed limit sign are shown in Fig. 5.6. A polar plot is chosen to illustrate the incident angle dependency. While an absolute comparison with the results from [31, 112] is not suitable due to the different setups (near- vs. far-field and partial vs. full vertical illumination), the general behavior of overall reflectivity is comparable. For normal incidence to the plates of the sign ($\Theta \in \{0°, -180°\}$), the maximum back-scattered power is

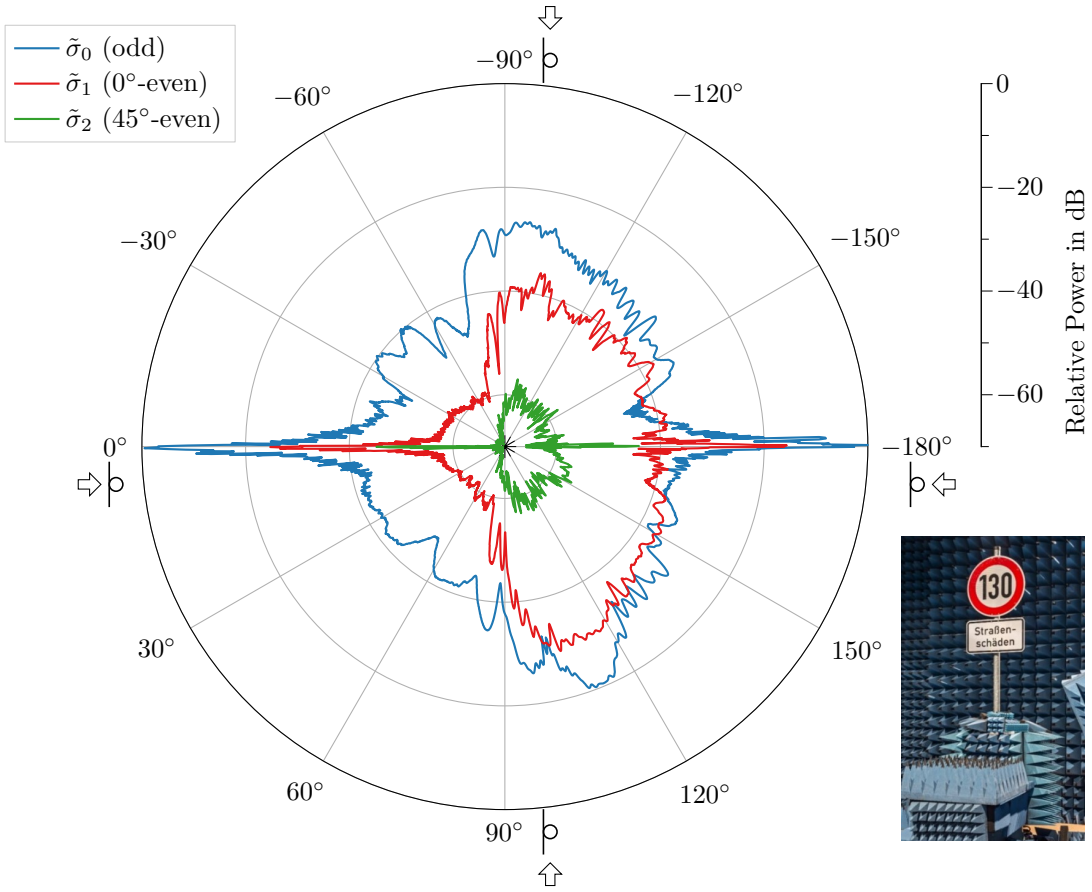


Figure 5.6: Pauli-decomposed relative back-scattered power for the speed limit sign. Adapted from **[110]**, © 2020 IEEE.

observed. Due to the odd-bounce nature of this specular scattering, the first Pauli component (blue) has the largest contribution. Owing to the calibration approach from Section 5.1.3, the discrimination between odd and 0°-even-bounce scattering is limited such that the approximately 20 dB lower 0°-even-bounce (red) component for these incident angles is not necessarily stemming from such actual scattering but an imperfect calibration. Furthermore, the more than 35 dB lower 45°-even-bounce component (green) is related to a limited cross polarization discrimination (XPD) inherent to any real measurement setup. This high rejection value indicates a high quality setup. The anti-symmetric scattering component of the decomposition is not shown because it provides no additional information in a monostatic setup.

For oblique incidence, a categorization of the back-scattered power into two regions can be made. When the pole is partially occluded from the sign plates ($0° < |\Theta| < 90°$), odd-bounce scattering remains the dominant mechanism with an on average 45 dB lower back-scattered power compared to the overall maximum. Possible sources for this scattering are the non-occluded part of the pole and the edges of the plates due to the knife-edge diffraction effect (cf. Fig. 5.4). The 0°-even-bounce component is additional 15 dB lower and might not be unambiguously attributed to a real scatterer of this type but can be caused by the imperfect calibration. When backside incidence is considered ($90° < |\Theta| < 180°$), an increase in all Pauli components can be observed. The previous publications attributed the increased

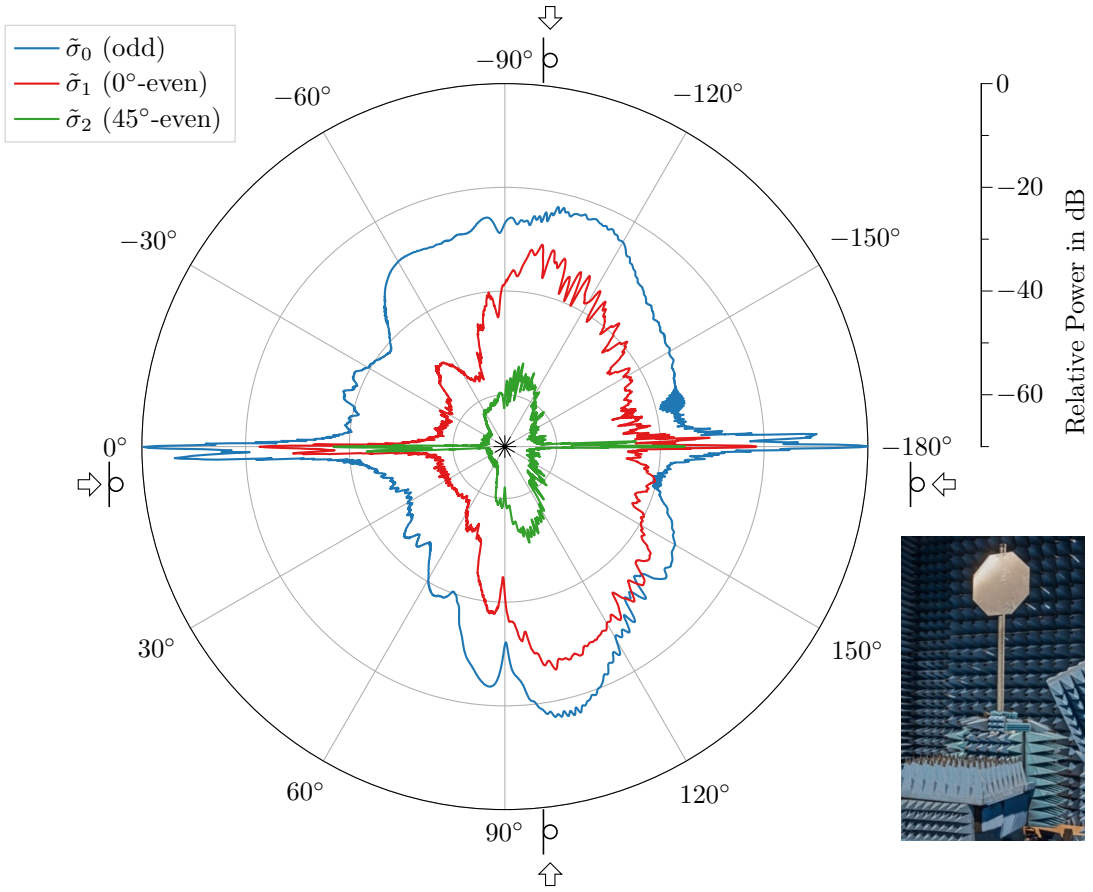


Figure 5.7: Pauli-decomposed relative back-scattered power for the stop sign. Adapted from **[110]**, © 2020 IEEE.

overall reflectivity to a dihedral structure formed by the pole and plate [31, 112], which matches to the 0°-even-bounce component rise in this work. However, the additional increase of the odd-bounce scattering can not be explained by a dihedral structure. One possible explanation would be the absence of the partial occlusion of the pole by the sign's plate in case of backside incidence. While this can explain the observation, another additional effect is part of the reason as will be proven in Section 5.1.5. Assuming a constant XPD over the course of the measurement, the observed 45°-even-bounce component can be attributed to two causes for oblique angles. On the one hand, the limited XPD determines the observed values for some incident angles. On the other hand, the dihedral structure between pole and plate can also contribute to this component due to an imperfect alignment, which can be observed for example for $\Theta = 150°$ with a difference of approximately 20 dB to the other components being significantly less than the assumed XPD.

A similar result is observed for the second measured target, which is depicted in Fig. 5.7. While the quantitative values for the stop sign are different, the overall course of the scattering mechanisms is qualitatively very similar to the speed limit sign. Again, a very strong anisotropy of the reflectivity spanning multiple orders of magnitude is observed in general. One visible difference between both targets is the shape of the specular reflection maxima for normal incidence. The stop sign measurement exhibits two distinctive local maxima in this angular region. It was

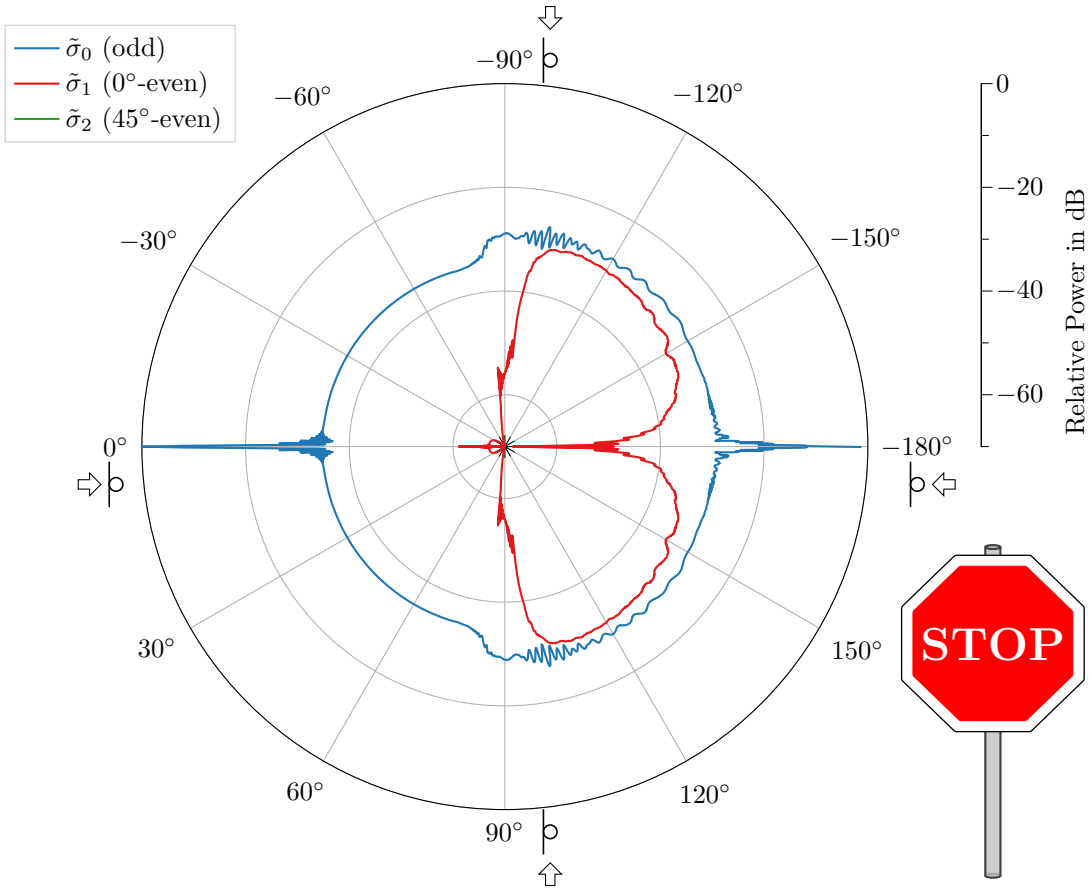


Figure 5.8: Pauli-decomposed relative back-scattered power for a simulated stop sign.

identified to be caused by a slightly bent shape of the self-constructed stop sign plate.

In addition to the evaluation of the anechoic CATR chamber measurements, the same analysis principle is applied to a simulation of the stop sign measurement. Therefore, the physical shape of the stop sign target is modeled by a perfect electric conductor for simulation in *CST Microwave Studio* ® [120]. The result is shown in Fig. 5.8. Due to the ideal simulation environment without any constraints due to a limited XPD and alignment, no 45°-even-bounce scattering is observed within the displayed dynamic range. Moreover, a better discrimination between odd- and even-bounce scattering is possible because no phase drift must be compensated. Considering these differences for a comparison with the real chamber measurements, a very good agreement of the qualitative statements about the scattering behavior is found. Both the formed dihedral structure causing even-bounce scattering and the increased odd-bounce scattering are recognizable again. Therefore, the assumptions for the proposed calibration procedure can be regarded as valid.

The analysis for the guide post target is presented in Fig. 5.9. In general, the reflectivity change for small incident angle changes is less smooth compared to the two previous objects. However, the overall dynamic range is smaller because no large highly reflective metal surfaces are involved, so that only a range of 40 dB is shown. The local maxima of the odd-bounce scattering occur when normal incidence to the

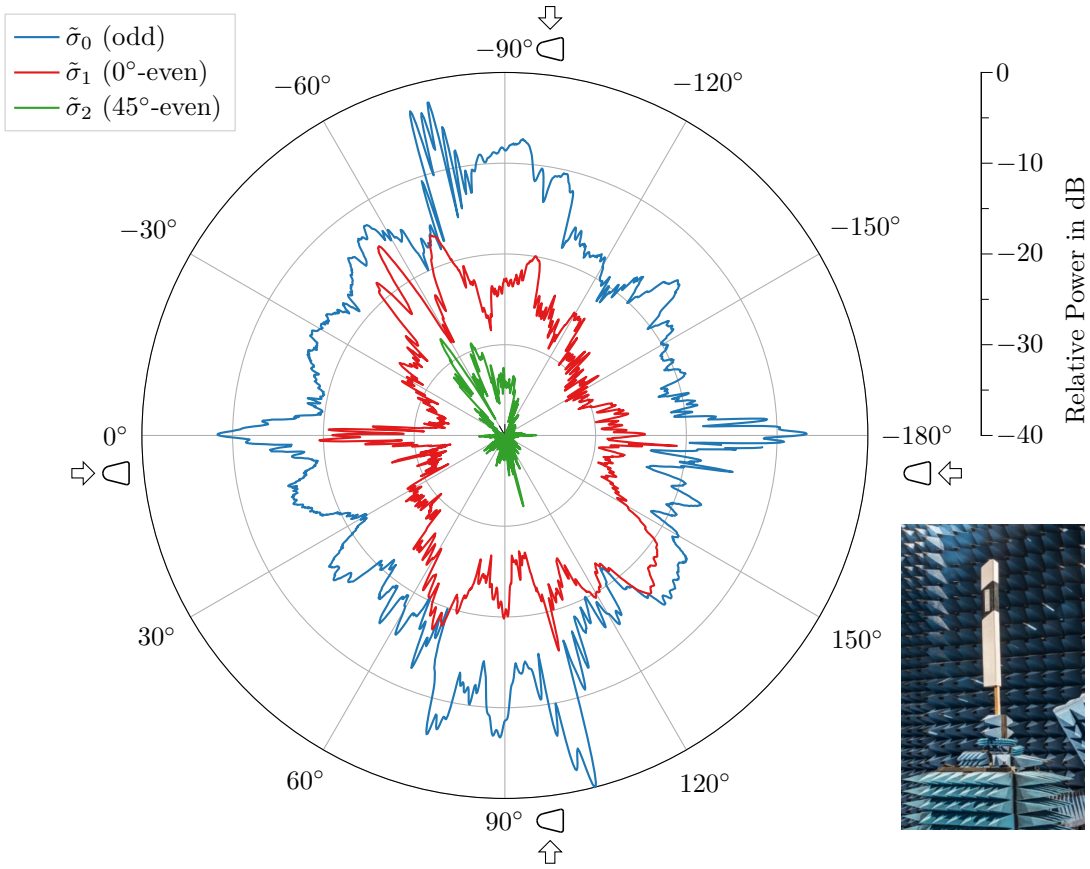


Figure 5.9: Pauli-decomposed relative back-scattered power for the guide post. Adapted from [**110**], © 2020 IEEE.

flat plastic surfaces is given ($|\Theta| \in \{0°, 75°, 180°\}$). Due to the less simple scatterer distribution compared to the traffic sign objects, the more challenging calibration is potentially causing worse discrimination between odd- and even-bounce scattering. In conjunction with the penetrable polyethylene material, this makes an unambiguous allocation of the scattering source impossible. Potential sources for even-bounce scattering are the optical retro-reflectors, which are framed in a recess, or the wooden pole used for mounting the guide post to the turn table. Further analysis is carried out in the next section.

5.1.5 Spatial analysis by ISAR imaging

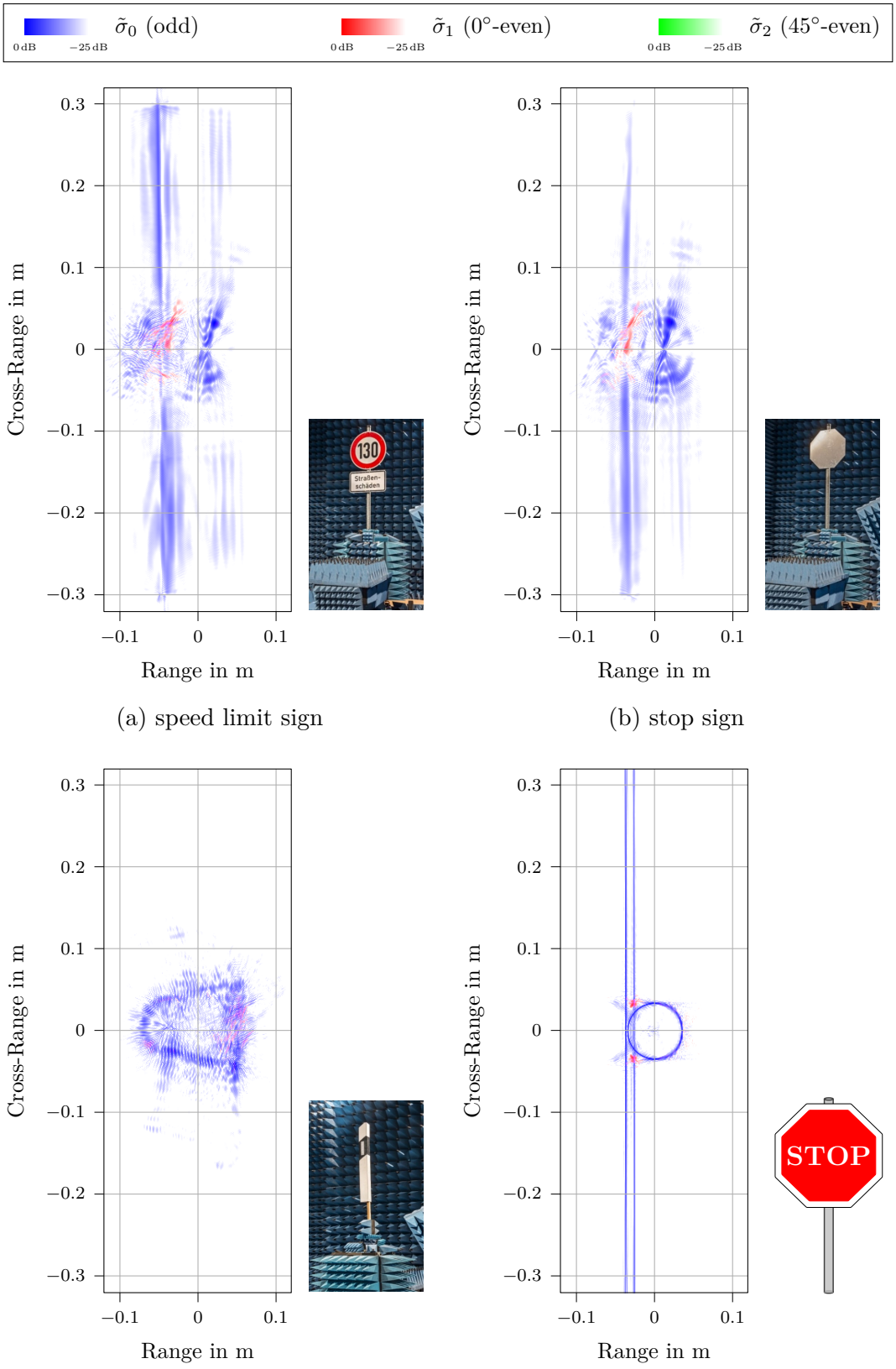
For confirmation of the previously made assumptions about the origin of the observed scattering behavior, a spatially resolved analysis of the reflectivities is enabled by ISAR imaging. The large bandwidth during measurement acquisition allows locating the scattering centers precisely along the range dimension, while the different incident angles can be used to locate and separate different scatterers in the cross-range direction. One can show that the matched filter for an isotropic scatterer on a turntable in far-field is calculated by the so-called direction integration approach as

$$\underline{\Pi}_{pq}(x,y) \propto \sum_{k} \sum_{\Theta} \underline{S}_{pq}(k,\Theta)\; e^{\mathrm{j}2k(\cos(\Theta)x+\sin(\Theta)y)} \tag{5.3}$$

where $\underline{\Pi}_{pq}(x,y)$ is the complex ISAR image reflecting the spatial allocation of reflectivity for one polarimetric channel pq at the Cartesian turntable coordinates x and y [121]. The rotation center is the origin of this coordinate system. Although the scattering centers in the landmark measurements are not expected to be isotropic, (5.3) is used without any modifications. As a result, the effective illumination aperture of a specific scatterer is limited, so theoretically, extreme cross-range separability for extensive intervals of incident angle integration is not practically reached. Furthermore, the theoretically required viewpoint correction [122] is neglected in the following analysis. An experimental implementation showed no relevant change for the present scattering mechanisms.
Due to the simplicity and easy parallelizability of the direction integration approach, no polar reformatting algorithm is employed for imaging. An interpolation of the measurement data onto a rectangular grid is carried out for reformatting algorithms to be able to use highly efficient FFT algorithms. Conversely, a custom CUDA kernel can easily perform the direct integration in parallel for each pixel of the resulting ISAR image. Even a not fully optimized implementation is adequate for fully polarimetric processing of the traffic sign images with 1 cm pixel width in less than 2 min, which is negligible compared to the acquisition time of the measurements and, hence, is sufficient for an offline analysis. Therefore, the calibrated measurement data is range-gated to the turntable region first and then down-sampled to cover an unambiguous range, which is sufficient to cover the extent of the analyzed object. A subsequent extension of the wavenumber domain k by AR processing (cf. Section 4.4.5) allows to reduce the peak width and side-lobes in the range domain. This additional step was not used for the results in the corresponding paper **[110]**, but is newly applied within this work. Due to linearity of the imaging algorithm with respect to the scattering information, the decomposition is applied after image formation in the Cartesian domain, and a relative power-related pseudo-RCS is chosen for analysis:

$$\tilde{\boldsymbol{\sigma}} = \left|\mathcal{D}_{\mathrm{Pauli}}\left\{\underline{\boldsymbol{\Pi}}(x,y)\right\}\right|^2 . \tag{5.4}$$

The resulting images for all objects are shown in Fig. 5.10 with a color mapping according to the standard convention for a Pauli decomposition, cf. Section 2.3.8. A 25 dB dynamic range referred to Pauli component maximum per object is chosen.
The resulting image for the combined speed limit sign is shown in Fig. 5.10a. Overall, odd-bounce scattering from the sign plates and the pole is dominant. The observed physical extents of both structures match well with the actual sizes. Analyzing the spatial position of the 0°-even-bounce component, the hypothesis of a dihedral structure formed by the pole and plate can be confirmed due to the matching location. Further reasons for the increase of odd-bounce scattering for backside incidence can be found by spatial analysis. It seems as if additional odd-bounce scattering occurs close to the pole region but on the other side of the sign plates. However, no physical object is located there. Thus, the most plausible cause is a triple-bounce mechanism, where the sign plates act as a mirror for the pole, so that a propagation path “plate



(a) speed limit sign

(b) stop sign

(c) guide post

(d) simulated stop sign

Figure 5.10: The Pauli-decomposed spatial allocation of the relative back-scattered power by ISAR imaging allows understanding of the sources of observed scattering behavior. A dynamic range of 25 dB is shown. Adapted from **[110]**, © 2020 IEEE.

– pole – plate" arises. Additional evidence for this hypothesis is found in the stop sign results from the measurement in Fig. 5.10b and the simulation in Fig. 5.10d, as well as in partial ISAR images in Appendix B. Comparing the overall result for the measurement of the stop sign in Fig. 5.10b with the speed limit sign one, the general similarity of the scattering mechanisms can be identified, which is expected due to their comparable physical properties. The less clear plate representation for the combined speed limit sign including side-lobes can be attributed to the two different plates, which, compared to the wavelength, have a sizable difference in mounting orientation and position. The doubled number of mounting clamps and screws at the side could also be the reason for the stronger scattering at the pole's maximum cross-range positions, when comparing the speed limit sign with to the stop sign.
The ISAR image for the guide post measurement is shown in Fig. 5.10c. Its cross-section shape can be clearly recognized with a dominant odd-bounce scattering. Significant even-bounce scattering is only observed at the flat backside face. While from the guide post material and geometry no such scattering is expected, the inserted wooden pole for mounting might cause it by interaction with the polyethylene of the guide post. Contrary to the metal objects, it has to be considered that the polyethylene is penetrable. To analyze this, Fig. 5.11 uses 20° integration intervals for smaller aperture ISAR images to still allow assessing the spatial two-dimensional position with sufficient accuracy despite a potentially lower cross-range resolution compared to the coherent integration over all incident angles. The incidence direction is visualized by an arc, which symbolizes the angular incidence interval with start and end angles given by additional arrows.
For a multitude of angular intervals, significant reflectivity is located at positions on the backside with respect to the incident waves, thus proving the penetrability hypothesis. When evaluating the scattering mechanisms, odd-bounce scattering is dominant at the guide post's contour. This is very similar to the scattering occurring after penetration of the material, which indicates a polarization-preserving behavior of the material for normal incidence. The only other relevant mechanism is 0°-even-bounce scattering. Again, the latter is mostly observed at the flat backside close to the wooden mounting pole supporting the assumption of a potential interaction.
Processing and analyzing partial ISAR images enabled further insight for understanding scattering at the guide post. Therefore, Appendix B includes the results of this technique for the other two objects.

5.1.6 Real-world measurements

In the next step, the previously obtained anechoic chamber results, shall be confirmed in a real-world environment study. Therefore, the experimental vehicle equipped with the experimental sensors introduced in Section 3.2.2 is driven in the scenario shown in Fig. 5.12. It passes a straight road section with a fence and some street lamps in the vicinity. The photograph was taken in a closer distance to the objects of interest. The exact position is visualized by the camera symbol in the sketch in Fig. 5.12b. Three posts are selected and their scattering behavior as seen from the front radar is evaluated over time. For this measurement only, the radar is operated in a longer range mode compared to the parameters given in Table 3.2. Due to the utilized circular polarization basis, the two components

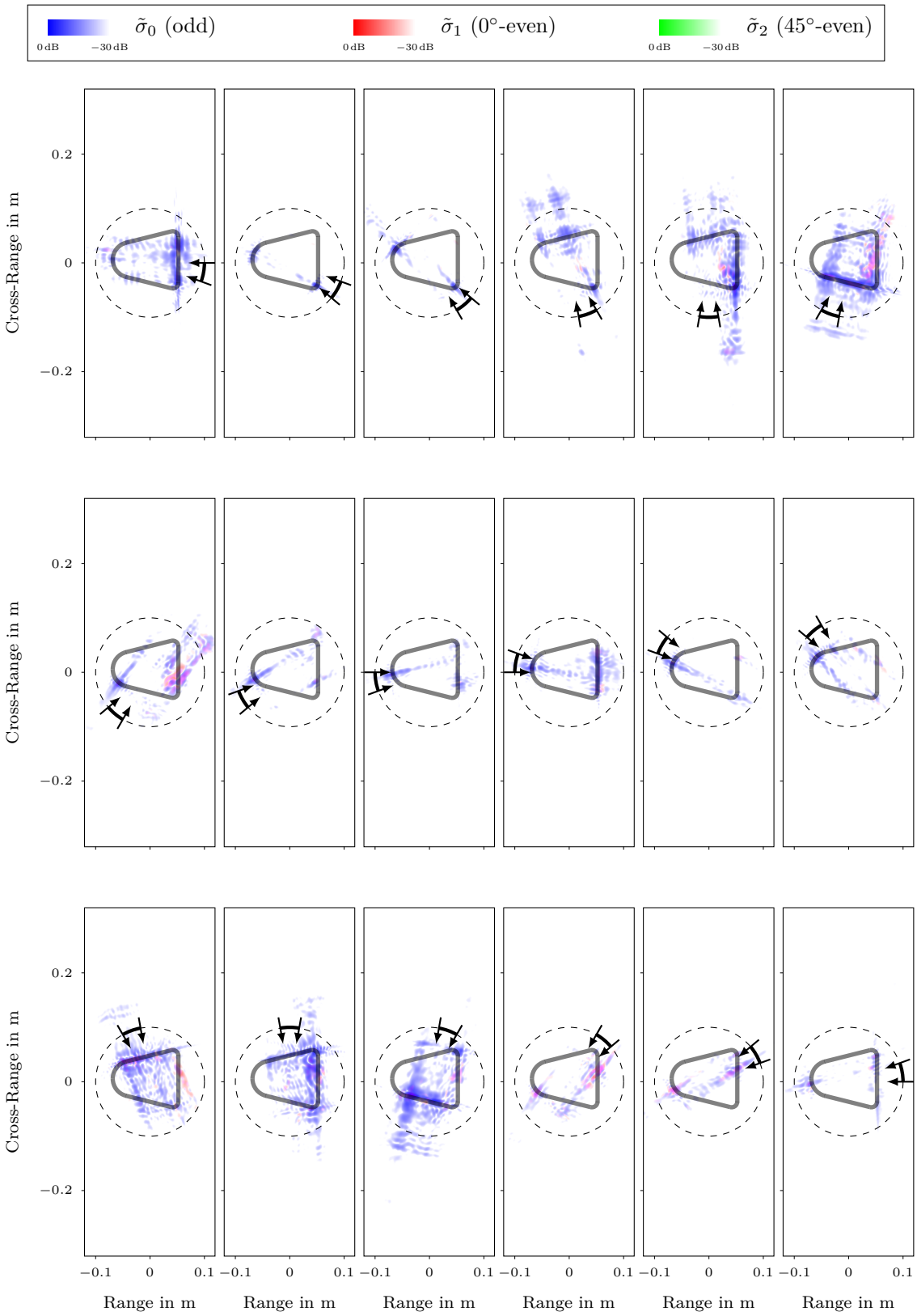
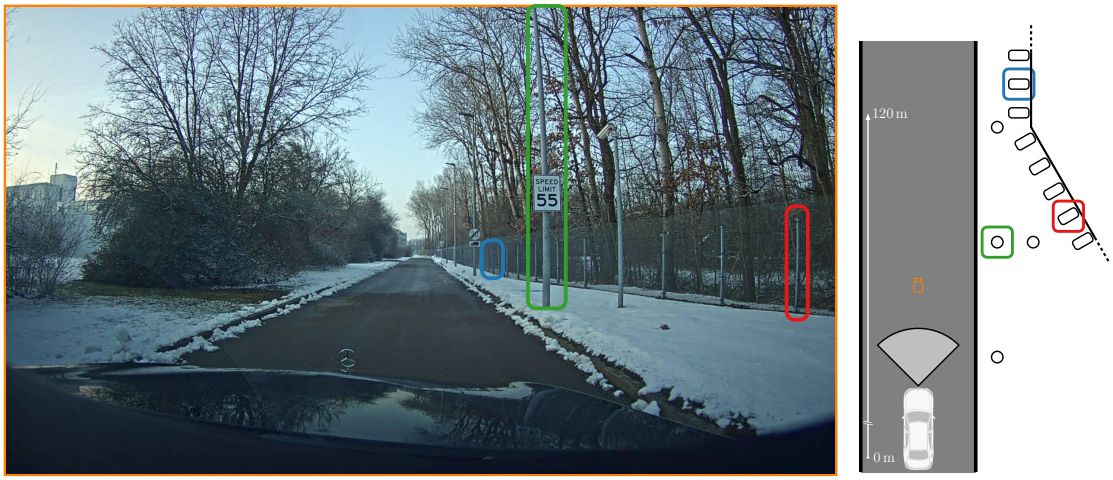


Figure 5.11: By performing the ISAR imaging with 20° partial incident angle intervals only (shown by the arcs and arrows on the dashed circle), the origin of specific scattering can be related to physical structures in dependence of the incident angle. A Pauli decomposition with a 30 dB dynamic range of the guide post is shown.



(a) Photograph (b) BEV sketch

Figure 5.12: The analysis of the scattering behavior of typical landmarks is carried out in the environment shown in the photograph in (a). The position from where the photograph was taken is marked by the orange camera symbol in (b). The vehicle drives the shown path to observe the three exemplary landmarks from different angles. Two fence posts and one street lamp post are selected. Adapted from **[91]**, © 2019 IEEE.

$$S_{\text{odd}} = |\underline{S}_{\text{LR}}| + |\underline{S}_{\text{RL}}| \qquad S_{\text{even}} = |\underline{S}_{\text{LL}}| + |\underline{S}_{\text{RR}}| \tag{5.5}$$

are used as indicators for the odd- and even-bounce scattering. Their ratio over the course of the approach is visualized in Fig. 5.13 for the three selected landmarks. Next to the raw ratios, a rolling average is shown as an overall trend indicator.
One selected object is the street lamp post, which is visualized in green in the respective figures. As expected from the previous anechoic chamber measurements, the metallic structure of the post itself as well as the front side of the traffic sign plate are showing odd-bounce scattering as the dominant mechanism. This holds true for the whole approach with a ratio of approximately 15 dB and fits with the front side incidence overall.
For the fence posts, the different fence parts must be distinguished. The posts themselves are on the fence side that is facing the vehicle as sketched in Fig. 5.12b. The post marked in blue is located at the fence section that is parallel to the road. Its observed scattering behavior changes from odd-bounce to even-bounce dominated over the course of the approach. The mechanically identical fence post marked in red is from the oblique part of the fence, and, on the contrary, mostly shows a balanced ratio between odd- and even-bounce scattering. A temporary shift towards an even-bounce dominated region is an exception.
Both observations can be explained under the assumption that the fence posts form a dihedral structure together with the wire mesh. Then, the different incident angles to this structure are expected to cause a scattering behavior depending on the considered fence section similar to the observation. An incidence close to the bisecting line of the ideal dihedral structure causes a dominating even-bounce scattering,

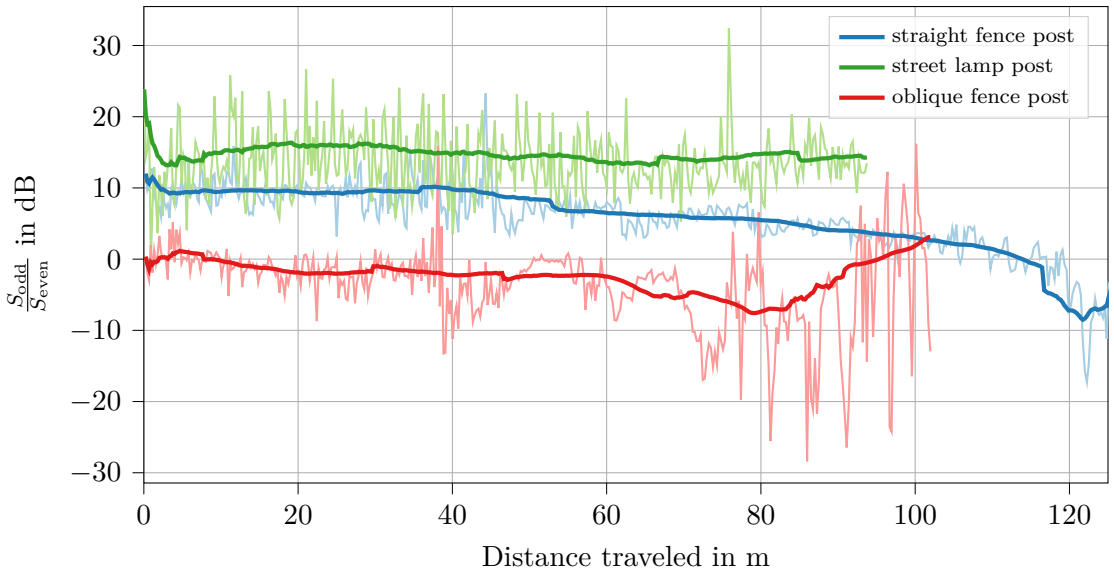


Figure 5.13: The ratio of the odd- and even-bounce component changes during the approach, which results in changing incident angles to the landmarks. The thicker, bold-colored lines are smoothed by applying a rolling average with a window size of 71 to the raw measurements shown by the thinner, faint lines.

while more normal incidence to the individual parts of the structure shows mainly as odd-bounce scattering, cf. Fig. 4.2. The more complex shape of the real object is the reason that this could only serve as an approximation. The continuous decrease of the odd-even ratio for the fence post marked in blue fits with the theory of moving from almost normal incidence to the post's face to an incidence along the bisecting line over time. The temporary even-bounce bias for the fence post marked in red is congruent to the bisecting incident angle, and, therefore, supports the hypothesis. This principle scattering behavior change was previously demonstrated in [**91**].

It should be noted that there is a significant difference of the variation in the plotted odd-even ratio. While the street lamp post with the traffic sign plate shows a deviation of up to 10 dB from the local average regularly, it is approximately only one third of that for the fence post located on the parallel section. A potential explanation for the observed phenomenon is a alternately constructive and destructive interference of either the lamp on top and the sign, or a multipath propagation with the ground acting a mirror for one of the concentrated scatterers.

5.1.7 Summary

The scattering behavior of typical automotive landmarks was analyzed in a clean anechoic chamber environment as well as in a real-world scenario. Both evaluations showed a strong dependency on the incident angle so that an anisotropic behavior must be assumed to be common in automotive environments. The anisotropy shows in the reflection amplitude and in the scattering mechanism. Therefore, incorporating polarimetric data into grid representations requires a tailored approach to exploit the full potential of polarimetry. This is considered in the following section.

5.2 Grid-based environment representations

Grid-based representations divide the surrounding space into a grid of cells as an efficient data structure for different tasks. The technique is well-established in robotics and has been used for a long time following its initial introduction for sonar measurements [123]. Nowadays, such representations are also used for all kind of different sensor modalities in an automotive context. The different approaches for radar are introduced in the following section.

5.2.1 State of the art

With the self-localization application as the intent of this work, the focus is on gridmaps for the static surroundings only. It should be noted that plenty of literature is also available for additionally incorporating other dynamic road users in gridmap representations, e.g. [124]. Radar is especially suited for both approaches due to its capability to instantaneously classify between static and moving surroundings based on the directly measured Doppler information. Within radar-based gridmapping of the static surroundings, the type of information in the grid cells can vary. The two main, widely used variants are amplitude and occupancy maps [125]. Modified variants exist in more niche applications: in environments with changing visibility of the static surroundings, the occupancy probability is stored in different layers of the gridmap depending on the viewing angle [126]. For the task of landmark detection, the occurrence count of detections per grid cell is another type of utilized information [127].
The common objective of all these gridmapping approaches is to reduce some uncertainty inherent in any single measurement by accumulating a sufficient number of measurements, originating either from a temporal or spatial distribution of measuring points. For an occupancy gridmap, the focus is on improving the spatial uncertainty in order to allow a clear distinction between occupied and free cells for an appropriate path planning [125]. In case of amplitude gridmaps, the objective is typically to derive a more stable estimate for the reflectivity [125], which, among other applications, could be used to improve classification and object detection [128].
Another distinctive feature for categorizing radar gridmapping approaches is the data level used during construction. In the past, typical automotive interfaces to radar sensors, such as CAN, were rather limited in bandwidth. Consequently, most communication interface implementations were based on object-level data. Even if lower-level data is transferred over low bandwidth interfaces, it remains a limited detection-level interface resulting from a constant false alarm rate (CFAR) detector [7, 125]. Such implementations are categorized as target-list gridmaps by [129]. On the contrary, the utilization of lower-level raw data for constructing grid-like representations in an automotive context is only published in more recent publications, given the availability of higher bandwidth interfaces. Automotive SAR can be classified to fall into the category of raw data gridmapping. Several publications examine the feasibility of SAR approaches in automotive environments [130, 131, 132, 133]. The majority of SAR approaches yield amplitude information, although [129] proposes a SAR-based occupancy estimation. Moreover, some investigations using polarimetric information in different frequency bands are available with [29, 30]. How-

ever, general feasibility and scattering phenomenon analysis are the main objectives rather than exploiting improved imaging characteristics for functional applications. Principally, SAR techniques fulfill the formulated gridmapping objective of reducing uncertainty two-fold: one the one hand, the synthetic aperture allows localizing scatterers in cross-range direction precisely due to a large synthetic aperture causing lower uncertainty in the spatial information. On the other hand, multiple amplitude observations are considered, which causes less amplitude uncertainty and a generally better sensitivity due to a coherent integration in this domain. While both desired properties could be demonstrated by the mentioned publications, the commonly known challenges of automotive SAR imaging remain: the sensor's position must be known very precisely (sub-wavelength accuracy) for each measurement, a maximum ego-vehicle speed must not be exceeded for an aliasing-free sampling to avoid ambiguous imaging results, and it is very demanding in terms of computational resources.

5.2.2 PreCFAR Gridmaps

The technique for constructing gridmaps from low level data without the above-mentioned challenges inherent to SAR approaches was introduced in the course of this thesis' work and previously published in [**134**]. For conciseness, it is presented in this section for non-polarimetric data before being extended to the polarimetric case in Section 5.2.3.

The main motivation for the proposed PreCFAR approach is to overcome the limitations that are inextricably linked with detection-based techniques. On the one hand, the false positive rate of detection lists must be kept reasonable due to the limited bandwidth and due to requirements originating from other applications that depend on the same data. Thus, low-reflectivity surroundings, which would only stand out after the accumulation of multiple measurements, are typically not mapped entirely. On the other hand, detectors generally cause some loss of information in case of extended objects, because some cells can raise the noise estimate for other neighboring cells, which all are occupied by different parts of the same physical object.

As the designation "PreCFAR" for the proposed technique suggests, the data used for accumulation is extracted prior to the detector stage in a classical radar processing chain. Therefore, the information loss is kept minimal. In fact, all information about the static environment, which is available in the raw spectral data, shall be used for the grid accumulation. This can be achieved by slicing along a sinusoidal surface in the radar data cube to extract a dense, image-like representation of the area of interest in polar coordinates. This concept is visualized in Fig. 5.14. After extracting this polar representation, a transformation to Cartesian world-fixed coordinates is necessary for a meaningful accumulation.

For extraction of this "static surface", the motion state of the radar sensor must be known. Then, the anticipated Doppler velocities for stationary objects under various azimuth angles θ can be determined. Due to the underlying principle of the Doppler measurement, only the radial projection of any velocity vector can be estimated. Thus, the expected scalar velocity $v_{\mathrm{r,stat}_{si}}$ of static surroundings observed by one of the radars sensors si can be calculated by a dot product:

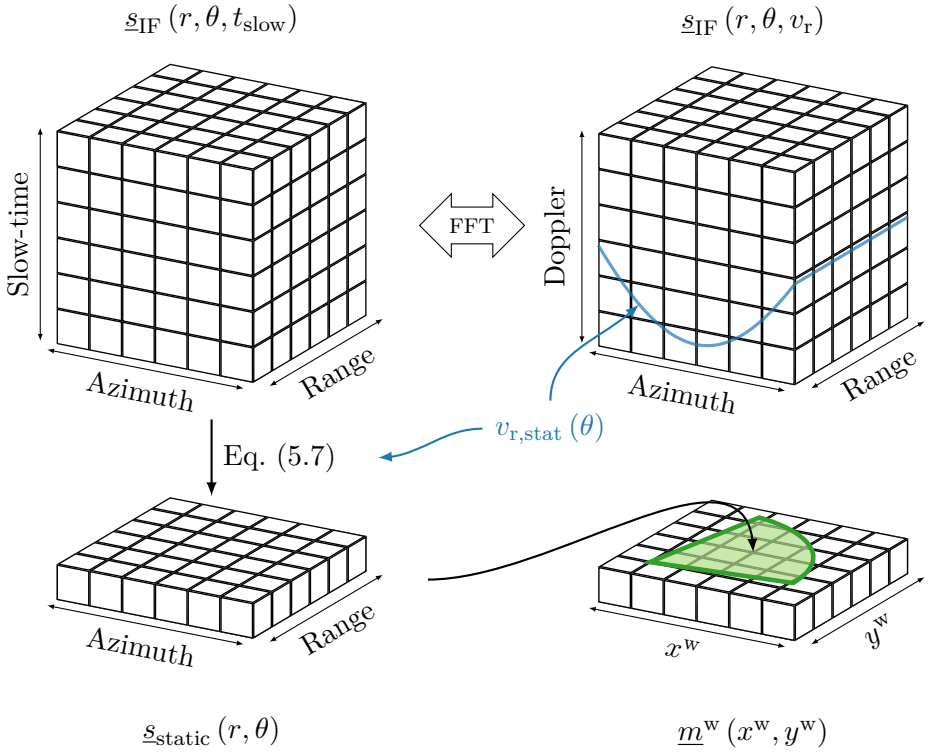


Figure 5.14: The PreCFAR gridmapping approach is based on cutting out the slice of the data cube that contains the information about the static surroundings. The resulting static map must be transformed from a polar coordinate to a Cartesian representation for accumulation. Adapted from [**134**], © 2021 IEEE.

$$v_{\mathrm{r,stat}_{si}}(\theta) = -\begin{pmatrix}\cos(\theta)\\ \sin(\theta)\\ 0\end{pmatrix} \cdot \underbrace{(\mathbf{v}^{\mathrm{c}} + \boldsymbol{\omega}^{\mathrm{c}} \times \mathbf{p}^{\mathrm{c}}_{\mathrm{s}i})}_{\mathbf{v}_{si}}, \tag{5.6}$$

where $\mathbf{v}^{\mathrm{c}}$ is the ego-motion velocity vector measured at the origin of the car coordinate system (typically the rear axle center), $\boldsymbol{\omega}^{\mathrm{c}}$ is the angular rate vector and $\mathbf{p}^{\mathrm{c}}_{\mathrm{s}i}$ the mounting position of the considered sensor si, both with respect to the car coordinate system. The cross-product between the angular rate and the mounting position, which is effectively acting as a lever arm, gives an additional velocity component at the sensor position, so that the overall sensor velocity $\mathbf{v}_{\mathrm{s}i}$ results. Fig. 5.15 provides an overview of the involved coordinate systems. In general, superscripts indicate the coordinate system in which a quantity is measured. While the formulation in (5.6) is restricted to a radar with only one angular measurement domain, the extension to the full three-dimensional case is straight forward.

When knowing the expected velocity, the corresponding closest cells can be extracted from the radar data cube to get the desired PreCFAR image. However, the most accurate amplitude representation is gained when the relative position within one cell is considered correctly. Therefore, it is proposed to apply the Fourier modulation theorem in the slow-time domain in order to warp the static surface from a sinusoidal shape in the Fourier-transformed Doppler domain to a flat surface in the (zero-

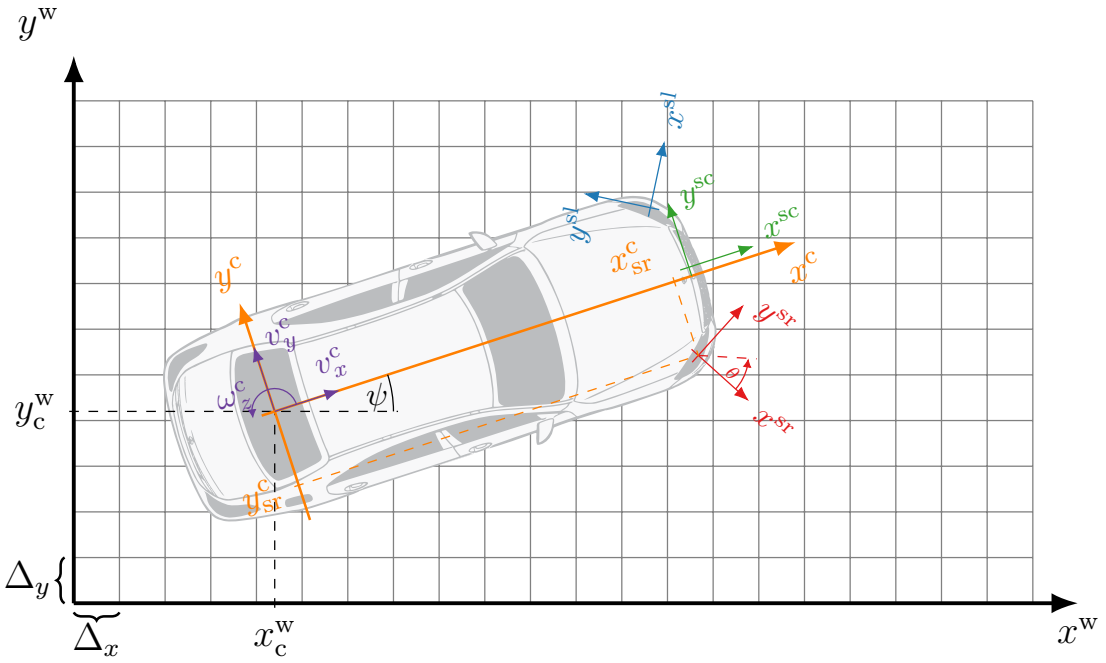


Figure 5.15: For any coordinate that is not unambiguously attached to a specific coordinate system, a superscript indicates the corresponding coordinate system. The superscripts $\cdot^{\mathrm{w}}$, $\cdot^{\mathrm{c}}$, $\cdot^{\mathrm{sl}}$, $\cdot^{\mathrm{sr}}$ and $\cdot^{\mathrm{sc}}$ stand for world, car and left, right and center sensor coordinates, respectively. Adapted from **[92]**, © 2020 IEEE.

frequency) DC bin. The extraction is then equivalent to a summation along the slow-time domain of the distorted radar data cube. Depending on the specific signal processing implementation, the slow-time domain can be made accessible either by maintaining an intermediate representation of an incompletely processed data cube or by an inverse FFT on a fully processed data cube. The extraction operation can be interpreted as a reduction operation and is mathematically formulated as

$$\underline{s}_{\mathrm{static}}\left(r,\theta\right)=\sum_{t_{\mathrm{slow}}}\underline{s}_{\mathrm{IF}}\left(r,\theta,t_{\mathrm{slow}}\right)\exp\left(-\mathrm{j}2\pi\frac{v_{\mathrm{r,stat}}\left(\theta\right)}{2v_{\mathrm{r,max}}}\frac{t_{\mathrm{slow}}}{T_{\mathrm{chirp}}}\right), \tag{5.7}$$

where $\underline{s}_{\mathrm{static}}$ is the polar PreCFAR image. The subsequent transformation to Cartesian coordinates is carried out by nearest-neighbor interpolation due to simplicity and a correct preservation of the scattering information in the polarimetric extension later on.

For demonstrating the advantages of the PreCFAR approach compared to a CFAR detection-based one, real-world experiments were carried out. The two side-looking radars from the vehicle setup in Fig. 3.1 are used to accumulate the measurements acquired during traversal of two different environments. For the correct extraction and accumulation, ego-motion information is required. The first derivatives of the pose in form of translatory and angular velocities are used for the static reduction operation, while the pose itself is needed for map incorporation at the correct positions. For this purpose, the ground truth motion information form the coupled DGNSS/IMU device is utilized.

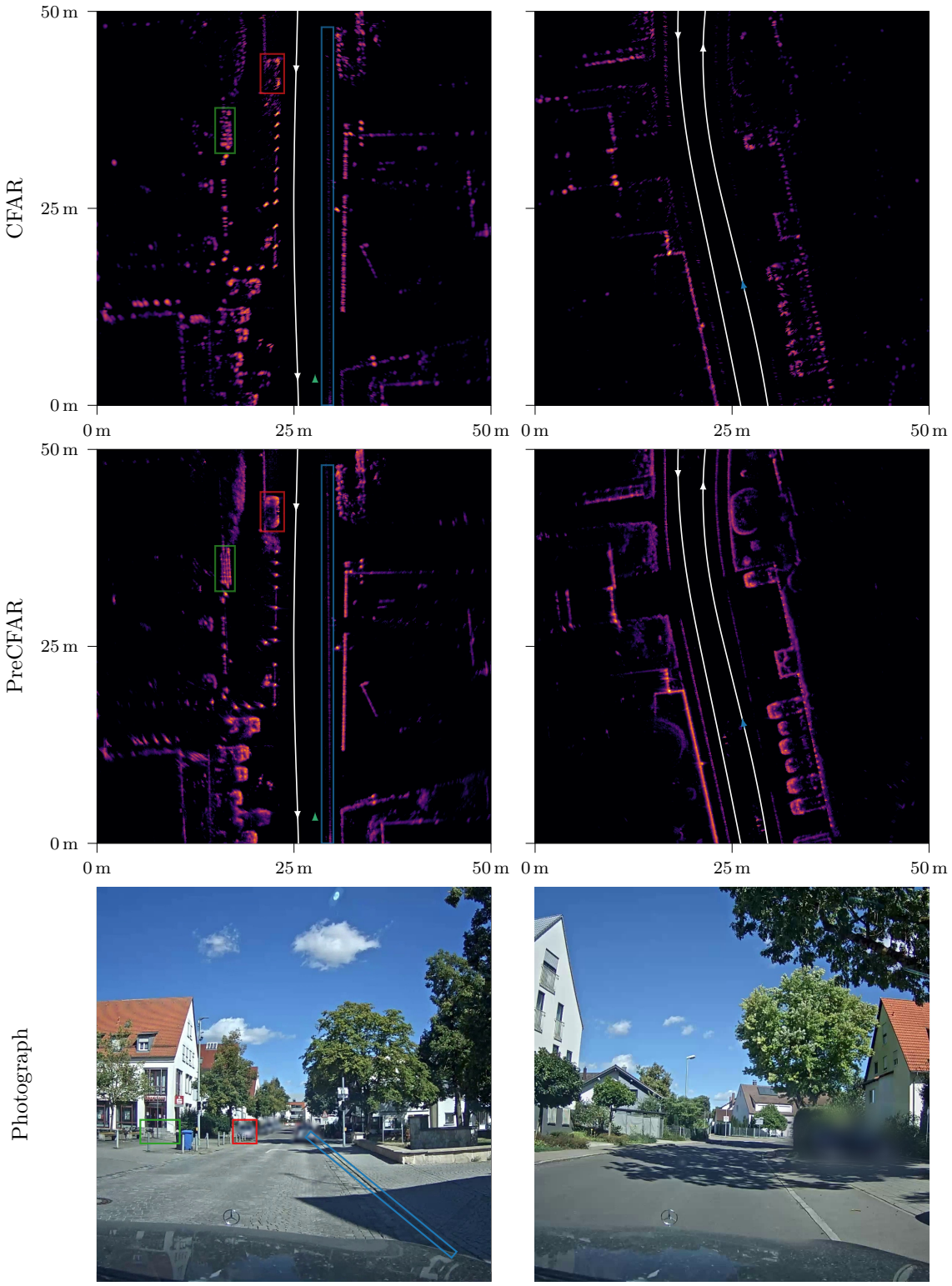


Figure 5.16: The qualitative comparison (best viewed on screen) between exemplary two CFAR and PreCFAR gridmaps shows the advantage of avoiding masking on extended objects (stairs with green box, car with red box) and of a more complete mapping of low-reflectivity objects (lowered curbstone with blue box). Adapted from **[134]**, © 2021 IEEE.

Table 5.2: Comparison of gird-based static environment representations

	CFAR	**PreCFAR**	**SAR**
Sensitivity	-	+	++
Separability	+	+	++
Extended object masking	-	++	++
Computational demand	+	+	-
Arbitrary motion	+	+	-
Allowed pose uncertainty	+	+	-
Interface data rate	+	-	-

Two exemplary scenarios are qualitatively compared in Fig. 5.16. The same underlying raw data are used with the method of processing being the only difference. For the CFAR variant, the threshold is chosen in a way to be comparable to current series production sensors (an average of 350 detections per radar and frame). For the left scenario, two objects are marked by bounding boxes as examples for the masking drawback on extended objects in detection-based approaches: stairs in a green box and a car in a red box. In the PreCFAR variant, each single step of the stairs can be clearly identified and the contour of the car is continuous. Neither holds true for the CFAR case. Moreover, a lowered curbstone is marked by a blue box as an example for a weakly reflecting object. It is only sparsely populated with detections in the CFAR map. For PreCFAR mapping, a much denser representation of the curbstone can be observed. This thinning-out to the point of disappearance can also be seen clearly for low-reflectivity objects in the right scenario of Fig. 5.16. Some vegetation in the upper right corner of the plot is much clearer in the PreCFAR map. While these are not suitable as landmarks due to their temporal variability, the generally increased continuity of line-shaped objects in PreCFAR maps is an advantage for their robust extraction when searching for landmark candidates. A quantitative analysis for confirming this qualitative observation is provided in Section 5.3.3 after introduction of the landmark detectors.

Summarizing the conceptual differences between the approaches, PreCFAR gridmapping is a favorable compromise between CFAR and SAR approaches. Table 5.2 provides a comparison of the main properties of the different concepts. It was demonstrated by the above examples that PreCFAR maps are more sensitive to low-reflectivity objects and they do not suffer from extended object masking. SAR approaches can potentially reach even better sensitivity and cross-range separability. However, the main goal for the intended self-localization application is the generation and recognition of robust landmarks, for which SAR's sensitivity and separability benefits might not be worth the challenges involved. The proposed PreCFAR technique is much less demanding in terms of necessary computational power and with respect to an allowed pose uncertainty. Moreover, specific algorithmic adoptions might be required for some SAR methods in driving scenarios with high angular rates. As demonstrated in Fig. C.1 in Appendix C, the PreCFAR method does sup-

port such scenarios without any modifications by nature. Requiring a high data rate interface for both low data level approaches is a potential disadvantage. However, the need for central processing in the experimental vehicle setup in this work has already required a corresponding interface. Accordingly, the PreCFAR approach will be pursued in this work and the incorporation of polarimetric information is discussed next.

5.2.3 Polarimetric PreCFAR Gridmaps

While scalar amplitude accumulation as considered in the previous section is simple and provides meaningful results by straightforward magnitude averaging, this is not appropriate for polarimetric measurements. As described in Section 2.3.4, the scattering information is contained not only in magnitude but also differential phase values. Depending on the selected polarization basis, originally differentiable scatterers would not be distinguishable anymore when only magnitudes are considered. In a linear basis, an odd-bounce object would result in the same scattering contribution as an axis-aligned dihedral structure. In a circular basis, the information on the orientation angle of a dihedral structure would be lost. Averaging of the complex scattering matrix or feature vector on the other hand would also not obtain meaningful results because the absolute phase has to be considered as random.
Therefore, in the course of this thesis, the concept of polarimetric covariance matrices from SAR imaging was adapt to the gridmapping technique in automotive contexts. First results were previously published in [**92**]. After this publication's CFAR detection-based processing, the extension to low level PreCFAR data was published in [**71**].
The main application of covariance matrices in SAR imaging is spatial averaging for speckle reduction, i.e., neighboring cells are combined to reduce the reflectivity fluctuation [9]. In this work, however, the multiple samples per cell result from either different radar sensors, when inside an overlapping part of the field of view, or from consecutive samples of a single sensor. The sample covariance is calculated according to (2.41). Contrary to [29, 30], the real aperture radars in this work allow an association of a scattering matrix to each cell for every measurement cycle and not only after a synthetic aperture created over the whole trajectory provides a cross-range resolution. Accordingly, this enables an adequate handling of the anisotropy of typical landmarks, cf. Section 5.1. The covariance representation is able to model a superposition of different scattering mechanisms as explained in the following section. Moreover, the polarimetric covariance formulation is the second order moment known from statistics, so that the probability distribution of the matrix is well-defined (cf. Section 2.3.6). Thus, a practical distance measure can be derived [135], which will be utilized for the robust extraction of point-shaped landmarks in Section 5.3.2. Although this Wishart distance for measuring similarity between two covariance matrices does not fulfill all requirements to be considered a metric, it proved valuable in a lot of classification applications [136].
The implementation block diagram for generation the polarimetric PreCFAR covariance gridmaps from low level data is shown in Fig. 5.18. To simplify the notation, a monostatic configuration and reciprocal media are assumed so that a $\nu = 3$ channel configuration is sufficient for fully polarimetric information. An extension to a

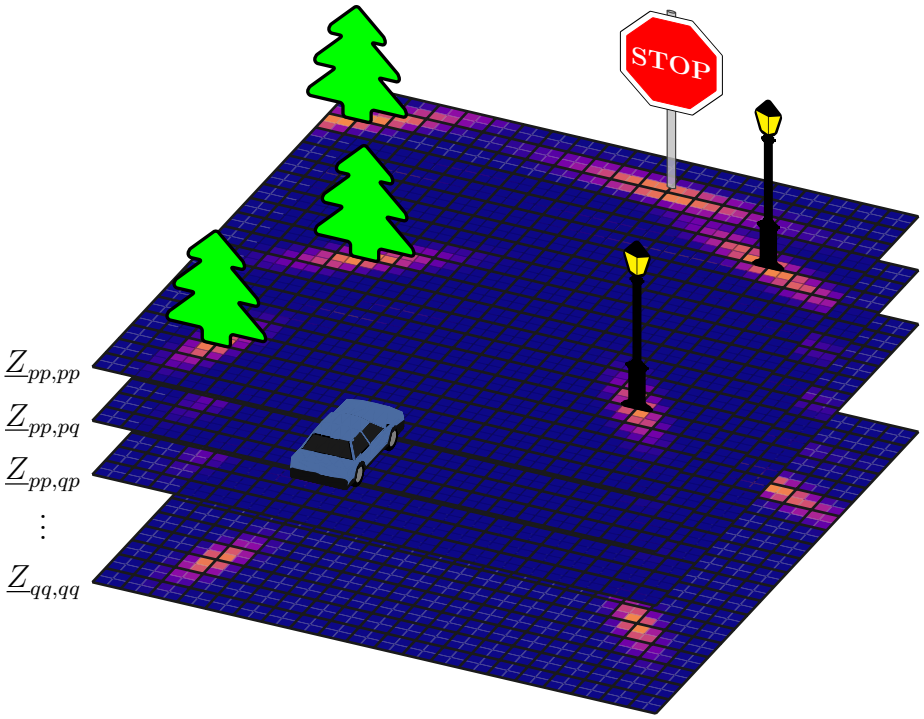


Figure 5.17: The proposed polarimetric gridmaps are constructed from multiple layers, which contain the elements of the polarimetric sample covariance matrix, so that the cells at one spatial position contain one such matrix. Adapted from [**92**], © 2020 IEEE.

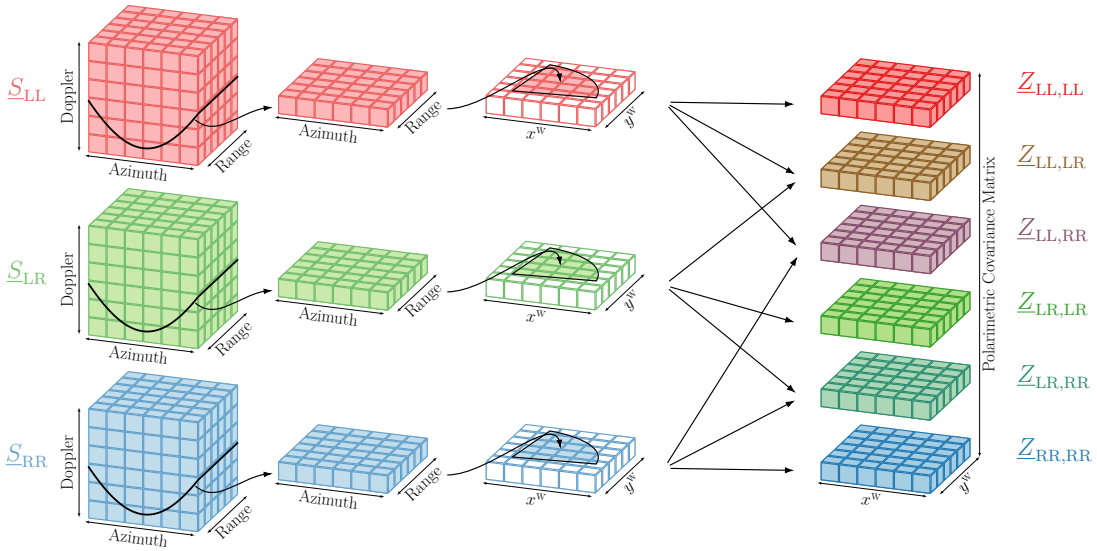


Figure 5.18: PreCFAR covariance gridmaps combine a low-level radar data utilization with a meaningful accumulation of polarimetric information for incorporation into a gridmap. By this, extended objects and scattering mechanism superpositions are well represented. Adapted from [**71**], © 2024 IEEE.

four-channel formulation is straightforward. First, the PreCFAR image is created for each channel separately. The covariance is calculated only subsequently for computational efficiency reasons. In order to avoid unobserved polarimetric scattering values to end up in the grid due to interpolation to Cartesian coordinates, a nearest neighbor mapping strategy is used. Due to the Hermitian property of the covariance, a compressed representation only including the main diagonal and one of the triangles can be used to save processing time and memory. The number of layers is reduced from ν^2 to $\frac{\nu(\nu+1)}{2}$.

Interpretation

The interpretation and visualization of a polarimetric covariance matrix per grid cell is not trivial [137]. One approach is closely related to the Cloude decomposition introduced as the first incoherent decomposition in Section 2.3.9. Instead of only considering the first eigenvalue-eigenvector pair, one of the coherent decompositions can apply to any of the pairs. This was shown for a detection-based gridmap in [**92**] with a direct mapping of the lexicographic elements to the color vector. A PreCFAR variant of the same recording with a Krogager decomposition is shown in Fig. 5.19. Again, relative pseudo-RCS values as the absolute square of the decomposition components are shown ($\tilde{\sigma}_i = |\underline{\alpha}_i|^2$). The colors for the Krogager components are chosen to best match with the previously used coloring scheme for Pauli components and thus allow an easier interpretation (odd-bounce mechanisms stay blue; all even-bounce scattering is represented by red compared to only the more relevant 0°-even-bounce scattering for a Pauli decomposition). A dynamic range of 60 dB is visualized with a normalization to the overall largest eigenvalue.
Focusing on the eigenmap corresponding to the largest eigenvalue λ_1 first, the dominant scattering mechanism can be identified. Odd-bounce scattering is dominating on fences, e.g. on the right side in Fig. 5.19a, building walls, for example on the left in Fig. 5.19b, traffic signs and street lamps, e.g. in Fig. 5.19c, and curbstones throughout the whole recording (blue bounding boxes). On the contrary, even-bounce mechanisms are the dominant ones for some parts of the scaffolds on the left in Fig. 5.19a, the steel beams of the car park on the right side in Fig. 5.19b, and the window and door reveals of the building in Fig. 5.19d (red bounding boxes). Compared to the CFAR-based result in [**92**], more helix-like scattering can be observed in general. This is the result of various changes. With the increased dynamic range for this study, lower amplitude features show up in general, as can be seen by more continuous curbstones. Furthermore, by omitting the CFAR detector, more energy from extended objects (cf. Section 5.2.2) and potentially side-lobes might be incorporated into the gridmap. Finally, it should be noted that the diplane and helix components are not independent in Krogager decompositions, such that a helix component might also result from the superposition of two or more diplane scatterers within one resolution cell [9].
Another example for the relevance of strongly anisotropic scattering behavior in automotive environments is the barrier shown as an additional overlay in Fig. 5.19a. It is observed with completely different scattering mechanisms for the two physically identical parts. The only difference is the incident angle with respect to the barrier halves causing either strong even-bounce or odd-bounce scattering.

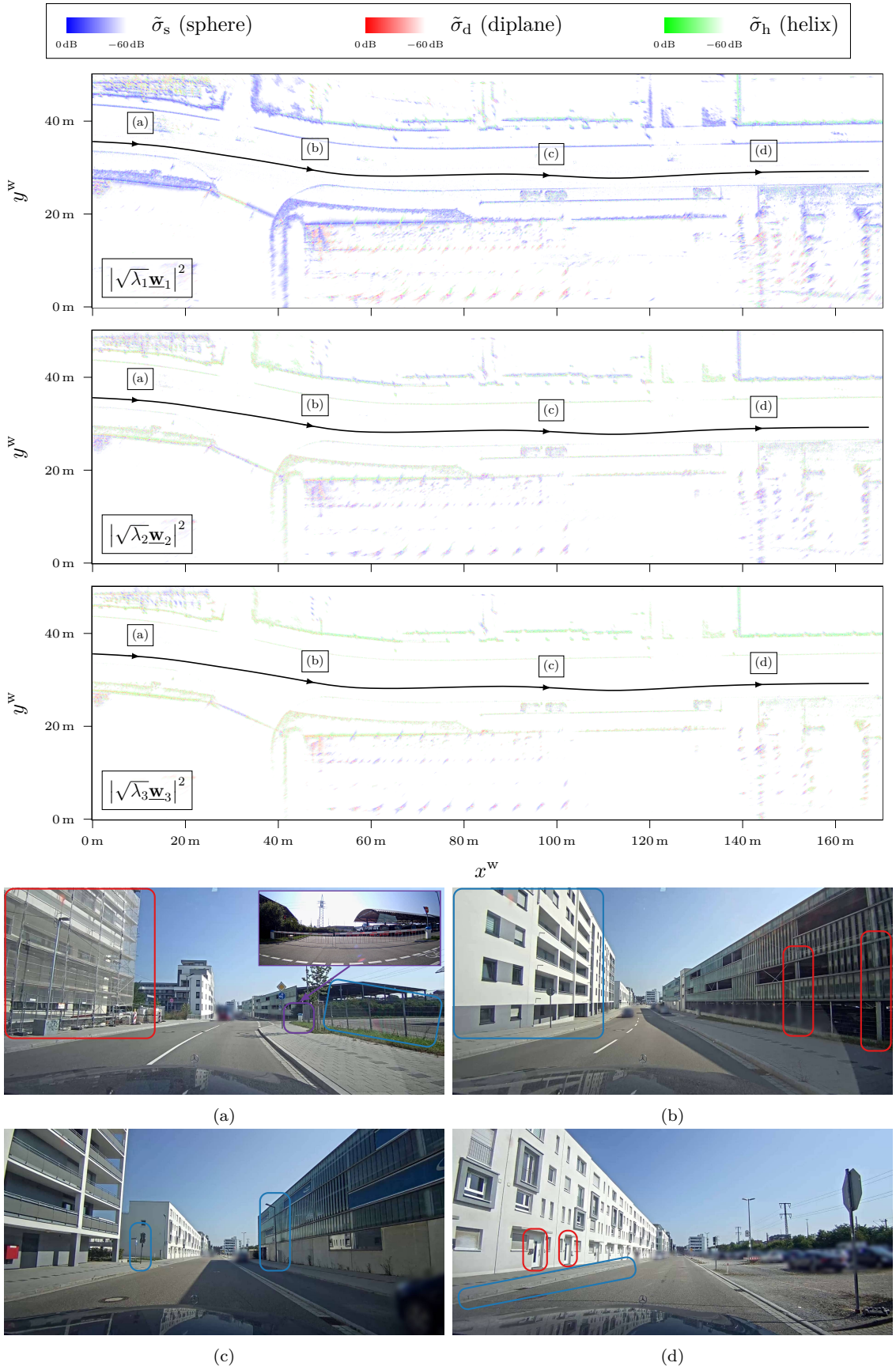


Figure 5.19: Each eigenvalue-eigenvector pair can be interpreted separately by a coherent Krogager decomposition. The ego-trajectory is shown with some photographs.

The eigenmaps associated to the second and third eigenvalues show non-negligible amplitudes indicating that multiple scattering mechanisms are observed in many cells. This is evidence that the covariance approach is justified due to the frequent observation of a superposition of scattering behavior per cell by non-zero second and third eigenmaps. Moreover, the inherent orthogonality of the mechanisms between each layer is apparent from the example given. If the dominant mechanism in the first layer is odd-bounce, the corresponding mechanism in the second layer is showing as an even-bounce or helix-like behavior. As a result, a perfect reconstruction of the superposition of multiple individual mechanisms is only possible if they are orthogonal themselves. With this limitation, another interpretation looking only for the presence and distribution of such mechanism superpositions is useful and will be discussed in the following.
The Cloude-Pottier decomposition introduced in Section 2.3.9 quantifies the contribution of multiple scattering mechanisms by analyzing the distribution of the eigenvalues in its first two parameters, entropy H and anisotropy A. A third angle parameter $\overline{\alpha_\lambda}$ represents the type of the dominant scattering mechanism. All three parameters of the generated covariance gridmap are shown in Fig. 5.20. Furthermore, a classification of the scatterer types according to the $H - \overline{\alpha_\lambda}$ scheme shown in Fig. 2.12 is depicted. In accordance with the classification limits, grid cells with high entropies $H \geq 0.9$ are blanked in the three parameter maps because no useful scattering information other than being almost completely random can be derived. Additionally, all cells with a power lower than 60 dB below the maximum in this scenario are filtered out in the parameter maps. As can be seen by comparison with the classification result without such filter at the bottom of Fig. 5.20, most of the near-range ground clutter is removed. Thus, the focus is directed to the regions with meaningful scattering information.
Given that none of the Cloude-Pottier parameters is scaled according to a power equivalent, as shown in the Krogager eigenmaps, some lower reflectivity artifacts are more noticeable using that decomposition. Some oncoming vehicles in the opposite lane show up more pronounced. Vehicles that are directly next to the ego-vehicle can have some scatterers with a radial velocity component identical to the one expected from the static environment so that these scatterers occur in the gridmap due to the extraction principle of the static surface from the data cube (cf. Section 5.2.2). The first vehicle is a larger truck causing a larger artifact then the two following passenger cars. While a more elaborate filtering of such contributions by leveraging tracker results is possible, it does not impede the intended localization and is therefore not implemented in this work. Further objects in the opposite lane are attributed to manhole covers, such as the two close to the trajectory position (c).
Lower entropy values are mainly observed for fences, curbstones and some parts of buildings. Vegetation, gravel and other building parts show higher entropy values. Areas with no significant reflection back to the radar look like noise to the sensor, so that such areas with resulting high entropies are filtered out and appear in white. For the anisotropy parameter, no clear assignment of typical values per object type is possible. The mean alpha angle confirms the observations of the dominant scattering mechanisms already made with the Krogager eigenmaps. With the classification map being a combination of entropy and alpha angle, the general scattering mechanism assignment is confirmed again. It should be noted, however, that many of the

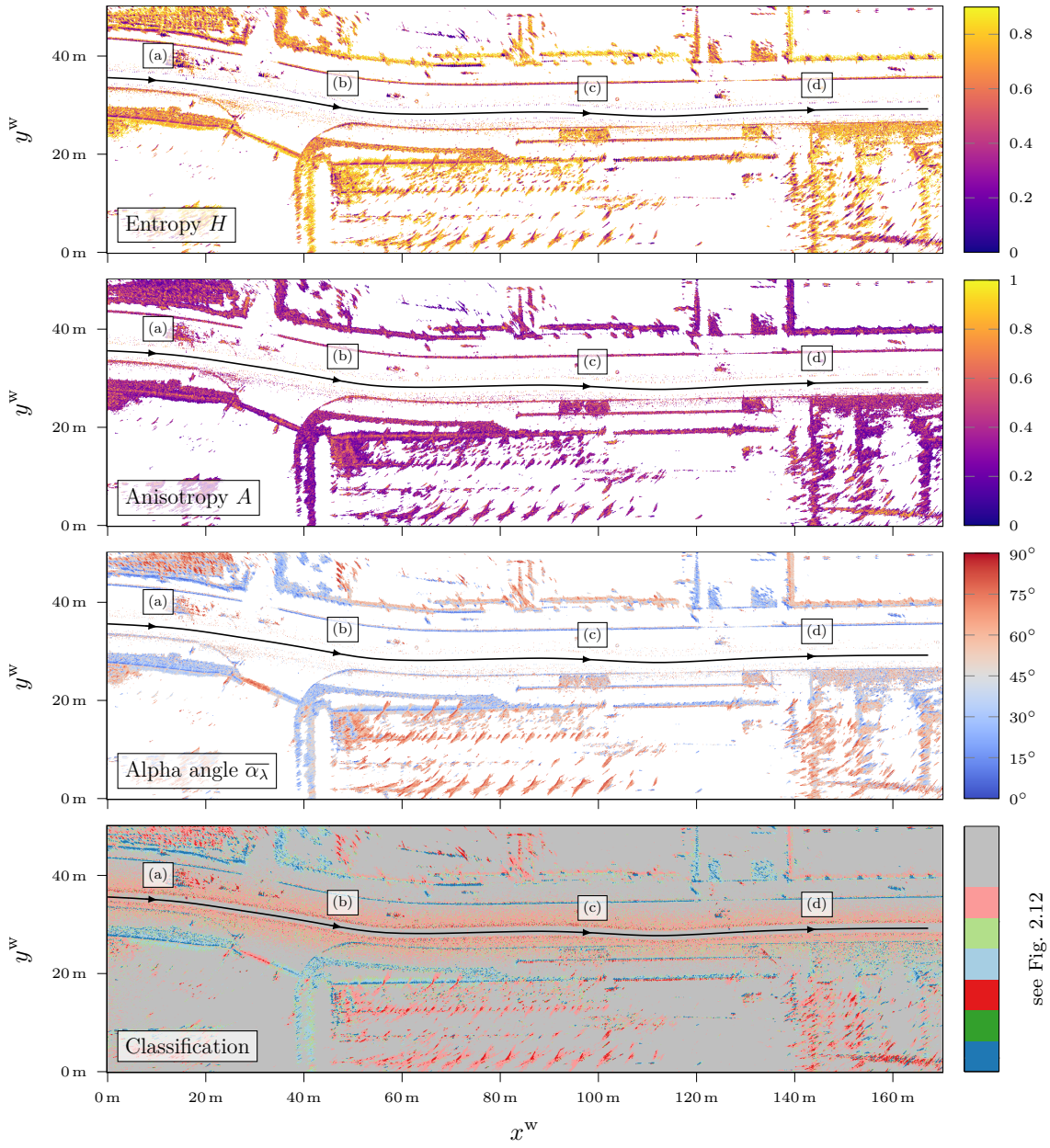


Figure 5.20: The Cloude-Pottier decomposition allows interpretation of the scattering behavior by its different parameters. An entropy filter rejecting anything above 0.9 and a power filter for 60 dB dynamic range were applied to the parameter maps. Classification is based on the scheme shown in Fig. 2.12. The ego-vehicle trajectory is shown by the black line with references to the photographs in Fig. 5.19.

helix-like mechanisms at the buildings in Fig. 5.19 are classified as double reflection propagation effects now, which supports the previous hypothesis. As mentioned before, no power limit is considered for estimating the classification map causing the near-range clutter to show up. While the PreCFAR approach allows to decompose in all cells including low-reflectivity objects but also the noise-covered cells, a combined consideration of the scattering mechanism derived from the decomposition and a general reflection power is usually advisable instead of only one of them.

5.3 Landmark detection

Large-scale self-localization benefits from the compact map size of landmark-based approaches. While this will be detailed in Chapter 6, the need for robust landmark detectors, which exploit the advantages of the rich environment representation of covariance PreCFAR gridmaps introduced above, arises. For this application, robustness is defined as a frequent re-extraction of some landmark in multiple traversals of the same environment. The detectors are needed for map creation as well as during the localizing phase in the proposed localization framework. It should be noted that landmarks intentionally consist only of their spatial positions without any descriptor functionality in this study, which is explained in Section 6.2.1. While the scattering information is internally used for identifying the landmark positions in the most robust way, the detectors output just geometrical information.
Two generic types of landmarks are considered and used in this work: point- and line-shaped landmarks. An observation and correct map association of a point-shaped landmark constrains the ego-vehicle position to a circle. The same condition for a line-shaped landmark leads to a line of possible ego-vehicle positions because they can typically be observed only partially without reliable start and end points.
The detector for point-shaped landmarks presented in Section 5.3.2 takes advantage of a cell's scattering mechanism difference to its immediate environment added by the polarimetric information. This section is based on the own publication "Robust Point-shaped Landmark Detection Using Polarimetric Radar" [**93**] and the supervised thesis "Investigation of polarimetric landmarks for self-localization in automated driving" [138]. An analysis of the impact of different levels of polarimetric information is carried out, and the characteristics of various point-shaped landmark types are investigated by correlation with a high-definition (HD) map.
A line-shaped landmark detector is presented in Section 5.3.3 and exploits the improved incorporation of extended, low-reflectivity objects due to the PreCFAR approach. A comparison between the extracted landmarks from a CFAR and a PreCFAR processing path using the same raw data provides an quantitative insight into this improvement. Additionally, the HD map correlation again enables an assessment of the suitability of different types of line-shaped landmarks.

5.3.1 State of the art

The available literature on the subject of arbitrary landmark detection on radar data in automotive environments is limited. In this context, only approaches for non-polarimetric sensors are published. However, one related early study considered the installation of artificial landmarks with a specific polarimetric response in an industrial environment due to the unique identifiability and the good distinguishability from other surroundings [33]. Although the unambiguously detected landmarks were used for a successful localization, it was only evaluated on a very small scale for a single drive in only one environment.
In an automotive, non-polarimetric context, the clustering of detection lists from multiple frames is the most common approach for extracting point-shaped landmarks. If the number of detections forming the cluster exceed some threshold, it is considered to be a suitable landmark. This could either be based on classical clus-

tering algorithms [139, 140] or an occurrence counting in a grid-like approach [127]. Another technique is closer to the introduced grid representation by leveraging amplitude grid maps for landmark extraction [7]: considering the assessment criteria of repeatability, completeness, and computational effort, a connected-component analysis algorithm is regarded as the optimal compromise in this work. Additionally, this approach provides not only point- but also line-shaped landmark candidates. In a continuation of the work, geometric and radar-specific feature distance measures between line-shaped landmark candidates are proposed [141]. Furthermore, this work analyzed the impact of both different feature types onto a varying pose uncertainty. It is demonstrated that for low uncertainties, the geometric features are sufficient. The radar-specific features improve the results mainly for larger pose uncertainties.

5.3.2 Point-shaped landmark detection

A point-shaped landmark detector is desirable if landmark candidates are re-observed at similar positions for multiple traversals of the same environment. In this case, they contribute to a reliable and precise self-localization. Characteristic regions that stand out from their immediate neighborhood are best suited for this. Previously, the variable used for characterization of uniqueness in the neighborhood was limited to an amplitude information as a measure for reflectivity. The new covariance gridmap approach allows including scattering mechanism information as a criterion for uniqueness. Accordingly, one objective for the detector is its ability to reliably detect the position of a characteristic scatterer, which only shows a different scattering mechanism compared to its environment while being similar in reflectivity. This requires a measure that quantifies the similarity between different regions in the gridmap, ideally based on the covariance matrix, which is the basis in the developed gridmap representation.
In the context of landmass classification in polarimetric SAR applications, a technique was developed that assigns a sample covariance matrix to one of several classes of landmasses based on a distance to the class centroid's covariance. By using the Wishart distribution as the statistical model for the covariance's probability density as introduced in Section 2.3.6 and by applying Bayes maximum likelihood classification theorems, the Wishart distance measure can be derived [142]. It is calculated as

$$d_{\text{wishart}}\left(\underline{\mathbf{Z}},\underline{\mathbf{\Sigma}}\right) = \ln\left|\underline{\mathbf{\Sigma}}\right| + \operatorname{tr}\left(\underline{\mathbf{\Sigma}}^{-1}\underline{\mathbf{Z}}\right), \tag{5.8}$$

with the class centroid's covariance $\underline{\mathbf{\Sigma}}$ and the sample covariance $\underline{\mathbf{Z}}$ ($\operatorname{tr}(\cdot)$ and $|\cdot|$ as trace and determinant of matrices as introduced in Chapter 2). The use of this distance measures is relatively widespread in SAR applications due to empirically good results, even though many conditions for a general metric, such as symmetry and triangle inequality, are not fulfilled [136]. In addition to the original classification use, the Wishart distance also proofed useful in further applications such as the automatic detection of weakly reflecting ships [143]. While only very small amplitude differences of such ships in comparison to the surrounding sea surface exist, significantly different scattering mechanisms are exploited for successful detection. Moreover, the distance measure is also advantageous if only partial polarimetric data is available because the calculation method scales without change to dual and

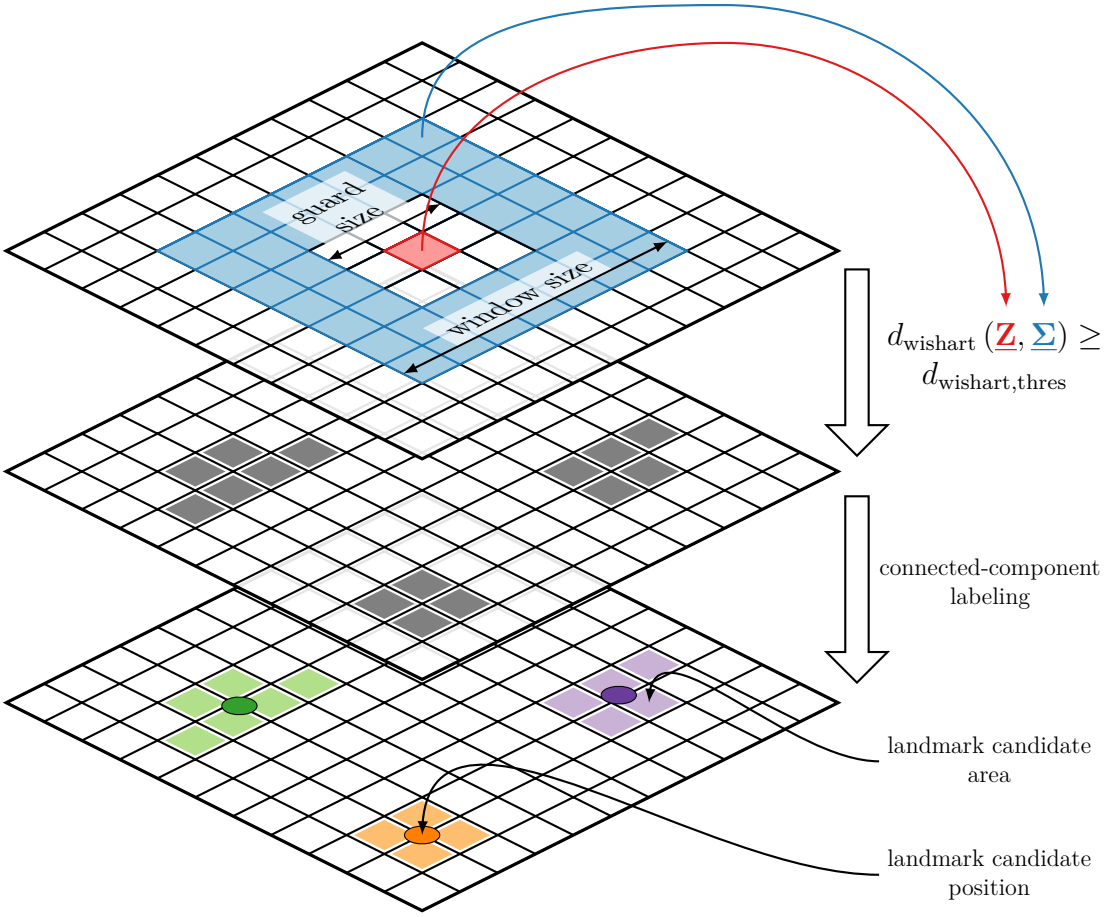


Figure 5.21: Comparing the cell under test with its spatial neighborhood in terms of amplitude and scattering mechanism is performed by the Wishart distance measure. If a threshold is exceeded, a binary map with characteristic regions is obtained. Landmark candidate positions are defined as the centroid of each characteristic area found by a connected-component labeling. Adapted from [138].

even down to single-polarimetric data [144]. While other distance measures, either based on the same complex Wishart distribution [145] derived from a hypothesis test or a more general matrix distance [146], exist, the Wishart distance showed best empirical results for the detector application [138].

Applied to the landmark detection use case, using the Wishart distance can be interpreted as a binary classification. Instead of comparing to multiple classes, a cell under test is only compared to a local neighborhood class. If a difference to the neighborhood either in amplitude or scattering mechanism is indicated by exceeding a distance measure threshold, a landmark candidate is detected. The chosen technique for calculating a neighborhood covariance is conceptually similar to a cell-averaging CFAR detector. A visualization is given in Fig. 5.21. The kernel parameters shape, size and weights for the neighborhood average have been chosen according to an empirical study. While a rotational symmetric kernel is preferred functionally, a rectangular one is significantly more effective to calculate by leveraging summed area tables [147], which can be calculated very efficiently on the GPU [148]. A non-zero

guard area around the cell under test should be introduced to avoid the inclusion of the spectral leakage into the neighborhood average calculation.
The procedure of the subsequent steps after calculating the Wishart distance map are depicted by the lower layers in Fig. 5.21. After binarizing the distance map with the threshold $d_{\text{wishart,thres}}$, a connected-component labeling [149] identifies the regions of different landmark candidates and each centroid of such regions is considered as the spatial position. A confirmation that landmark candidates as an output from the extractor are actual landmarks is given by reobservation from multiple traversals and will be addressed in Section 6.2.1.

Qualitative evaluation

In order to demonstrate the advantage of leveraging also scattering uniqueness for landmark detection, the proposed technique is applied to a real-world recording. A fence serves as the test object and the landmark candidate detection performance between a fully polarimetric extraction based on a covariance PreCFAR gridmap is compared with a non-polarimetric amplitude-only one. By comparing landmark candidates of multiple drives along this fence, conclusions about the detector's quality can be drawn. The result is shown in Fig. 5.22. In both cases, the Wishart distance with the dimensionality matched to the respective available data according to (5.8) is used as a distance measure. Due to the comparable amplitudes of the fence and its posts, the non-polarimetric detector had no chance to reliably extract the posts as landmark candidates, which can be seen by an irregular spacing and low amount of matching candidate positions between both drives. On the contrary, if the polarimetric information is available, the detector reliably extracts the fence posts as can be seen from the high overlap between the two drives. A closer look reveals a small additional even-bounce component at the fence post positions. This difference in scattering allows the polarimetric detector to identify these positions as characteristic. Therefore, the fence can only serve as a line-shaped landmark in the non-polarimetric case for a lateral localization. For fully polarimetric data, however, the additionally detected fence posts also support a longitudinal relative positioning.

Quantitative evaluation

In order to quantify the robustness improvement with the addition of more polarimetric information on a larger statistical scale, different environments are traversed multiple times with the measurement setup introduced in Chapter 3. Due to the integrated DGNSS/IMU device, the ground truth ego-vehicle pose is always known so that georeferenced PreCFAR covariance gridmaps can be calculated. For each drive, the point-shaped landmark candidate detector is applied and the resulting candidate positions are analyzed. When candidate centroid from multiple drives are spatially close in an Euclidean distance sense, the probability is high that a stable and characteristic landmark is detected. A landmark is established in such cases. In this study, distances below 0.3 m are considered sufficiently close. An efficient implementation is achieved by creating a k-d tree [150] representation for all candidates per drive and by querying for spatially close groups via a graph-based connected-component analysis. While a landmark is already established from two observed

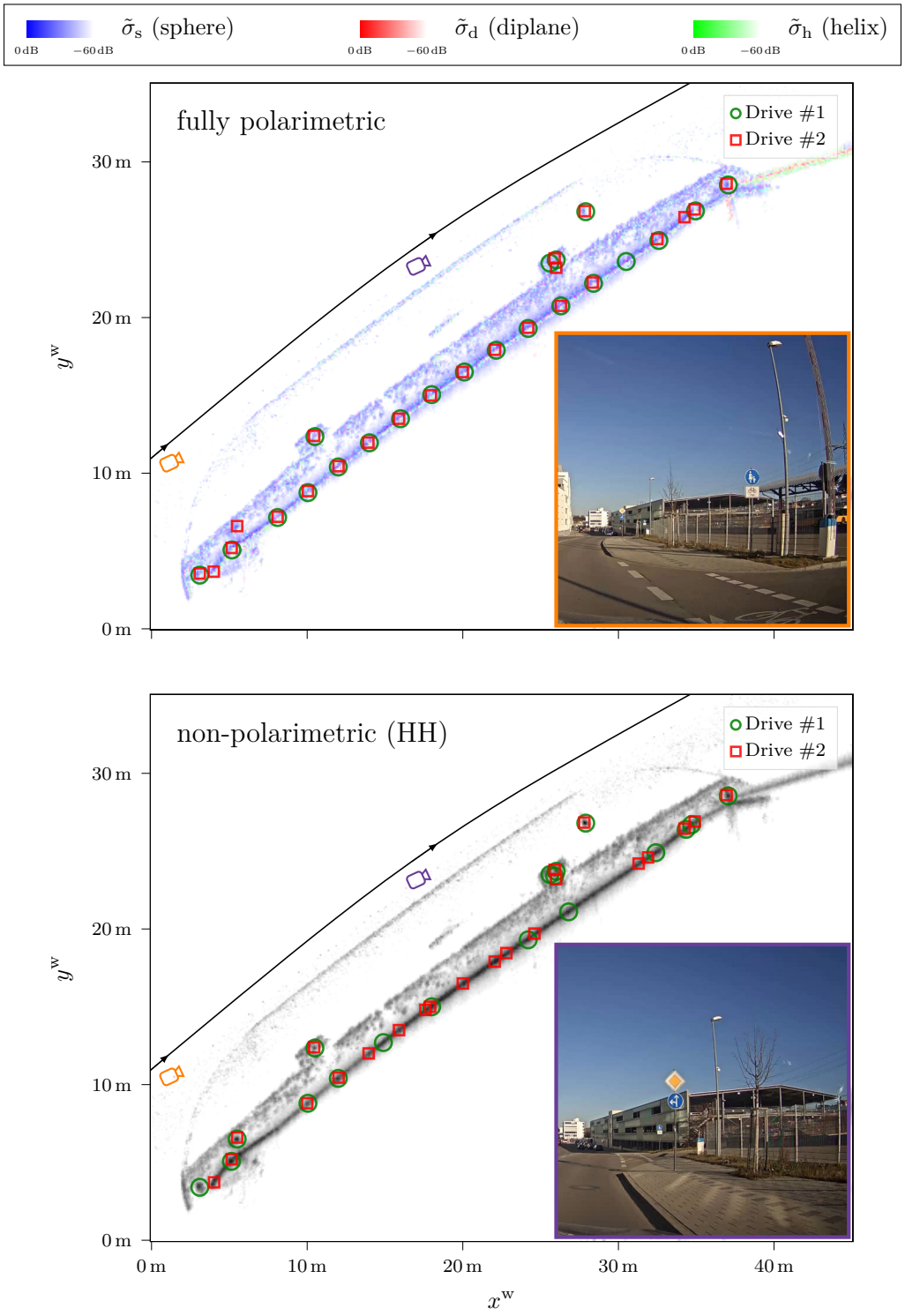


Figure 5.22: Comparing the extracted point-shaped landmark candidates from two drives along the same fence show a good detector quality if next to the amplitude also scattering information from polarimetry is leveraged. The colored camera symbols indicate the position where the photographs with matching color frame are taken from. Adapted from [**71**], © 2024 IEEE.

and close candidates, the robustness quality grows with an increasing number of re-observations. This is the basis for comparing the detector qualities of different levels of polarimetric information.
The gridmaps are calculated with a regular cell size of 0.1 m. Analogously to the window parameter optimization by a random grid search for detection-based gridmaps in [138], an empirical evaluation was basis for the quadratic window sizes with a two-sided width of 5 bins for the guard area and a 31 bin width for the averaging. For a fair comparison, the polarimetric combination with the lowest number of detected candidates in one of the drives specified the allowed candidate counts for all other combinations. Thus, the detector's ability to allocate the most unique candidates with the highest re-observation number within a given count limit is probed. The experimental validation is carried out in a variety of environments, which are described in Section 6.3.1 in more detail due to the significance for self-localization. However, the abbreviations for designating the environments are already introduced in this section for clarity: the environment of a route is indicated by the subscript abbreviation for the area, e.g., $\mathcal{R}_{\mathrm{Fra}}$ for the route in the Frankfurt area. The resulting distributions of landmark re-observations for the Ulm area $\mathcal{R}_{\mathrm{Ulm}}$ are shown in Fig. 5.23.
The first observation is that the overall established landmark count between the different polarimetric combinations deviate only slightly and approximately 2000 landmarks are detected. This differs from the results in **[93]**, where the landmark count rose noticeably with an increasing level of polarimetry. But it can be attributed to the fact that the PreCFAR implementation used in this work helps by providing a more populated local neighborhood for the lower polarimetric data levels (contrary to the detection-based gridmapping in the paper). However, both studies agree with respect to the distributions of re-observations. A general correlation exists between an increasing amount of polarimetric scattering information (by adding more channels) and a better landmark detection quality measured by a higher number of re-observations. Both, the share of landmarks observed in all drives and the average re-observation count in Fig. 5.23 confirm this. Comparing the non-polarimetric odd-bounce results with the fully polarimetric one as an example, an increase of 10 % of landmark observations is found. An additional evaluation for another route in the localization dataset shows comparable results and can be found in Appendix D.

HD map correlation

The experiments from the previous section are carried out in environments, which are mapped and labeled by a third party using another custom mapping vehicle. These HD maps are part of the cooperative project @CITY – Automated Cars and Intelligent Traffic in the City [151]. Due to the georeferencing of the gridmaps and all subsequent landmarks, a spatial correlation with the HD map allows classifying some of the landmarks. It was assumed that a landmark and HD map feature belong together if they are closer than 0.5 m (larger tolerance than for radar-only mapping due to a potential additional offset between the different data sources). While most map features are point-shaped entries such as poles and streetlamps, fences and guardrails are line-shaped map elements without specific entries for their posts. In these cases, the spatial distance is calculated as the smallest point-line distance of

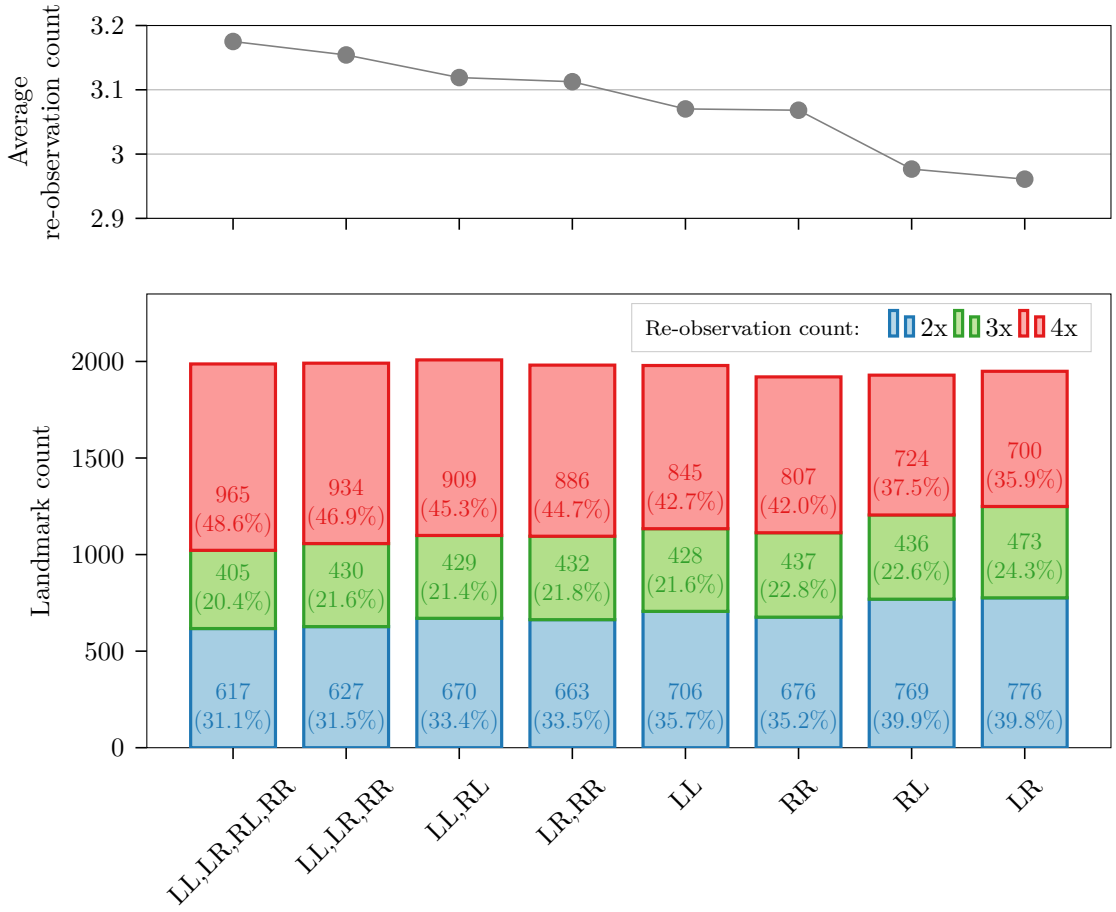


Figure 5.23: While a comparable overall number of landmarks is established for all levels of polarimetric information for $\mathcal{R}_{\text{Ulm}}$, the quality of detected landmarks differs based on the number of re-observations per landmark. The upper graph provides the average number of re-observations over all established landmarks, which served as a sorting criterion. The lower graph shows the absolute and relative values for the different numbers of re-observations per polarimetric combination.

all relevant line segments. However, other point-shaped map elements have priority. Only if a landmark could not be assigned to such while being sufficiently close to one of the line-shaped elements, is it assumed to be a post of fence or guardrail as the best guess in the automated approach. All following evaluations in this section are performed for fully polarimetric data.

The distribution of re-observation counts per landmark type and the respective overall number of associated landmarks for $\mathcal{R}_{\text{Ulm}}$ are shown in Fig. 5.24. Streetlamps represent the best landmark type by the re-observation metric. With their metallic nature and a cylindrical shape with a larger diameter, they show an isotropical and relatively large reflectivity and typically stand alone, all of which causes a good recognizability. Additional presence of a traffic sign plate does not result in a noticeable impact. The group of poles is the next best landmark type and generally includes traffic sign posts, traffic light posts, and bollards in the utilized map. If a traffic sign plate is mounted to the pole, a higher average number of re-observations

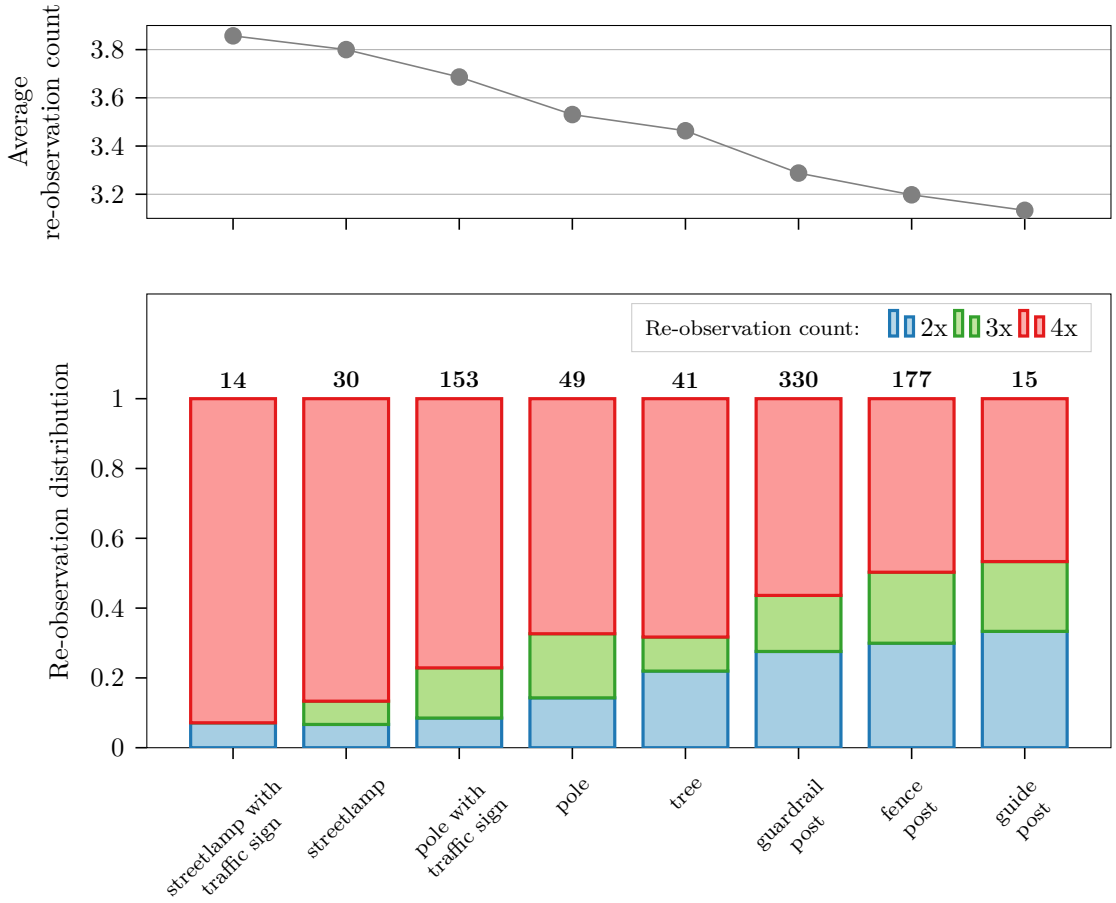


Figure 5.24: The distribution of re-observation counts and the overall landmark number for $\mathcal{R}_{\text{Ulm}}$ allows assessing the suitability of the different landmark types. Based on the sorting according to the average re-observations, free standing metallic objects are most frequently recognized.

occurs, which might be attributed to the strongly increased reflectivity for aspect angles with orthogonality to the plate surface (cf. Section 5.1.4). Trees are typically not such strong reflectors and often are located in a vegetation area, such that reflectivity is further dampened and less contrast to the local neighborhood exists. Accordingly, the sorting behind the pole group is expected. The guide posts are the least often re-observed point-shaped map elements for the same reasons as for the tree, but with even less reflectivity. For the landmark classes derived from the line-shaped map elements, i.e., the guardrail and fence posts, the average re-observation is only slightly better than for the guide post. However, they are still extremely useful for a successful localization because they occur very frequently in typical driving environments, such as $\mathcal{R}_{\text{Ulm}}$, cf. Fig. 5.24. As the evaluation in another environment results in the same order for the mentioned groups of landmark types, it does not offer any further insight but only serves as an additional confirmation. Therefore, the result is included only in Appendix D.

By associating all extracted landmark candidates separately from each drive with the HD map (and not only established landmarks as a consensus over multiple drives),

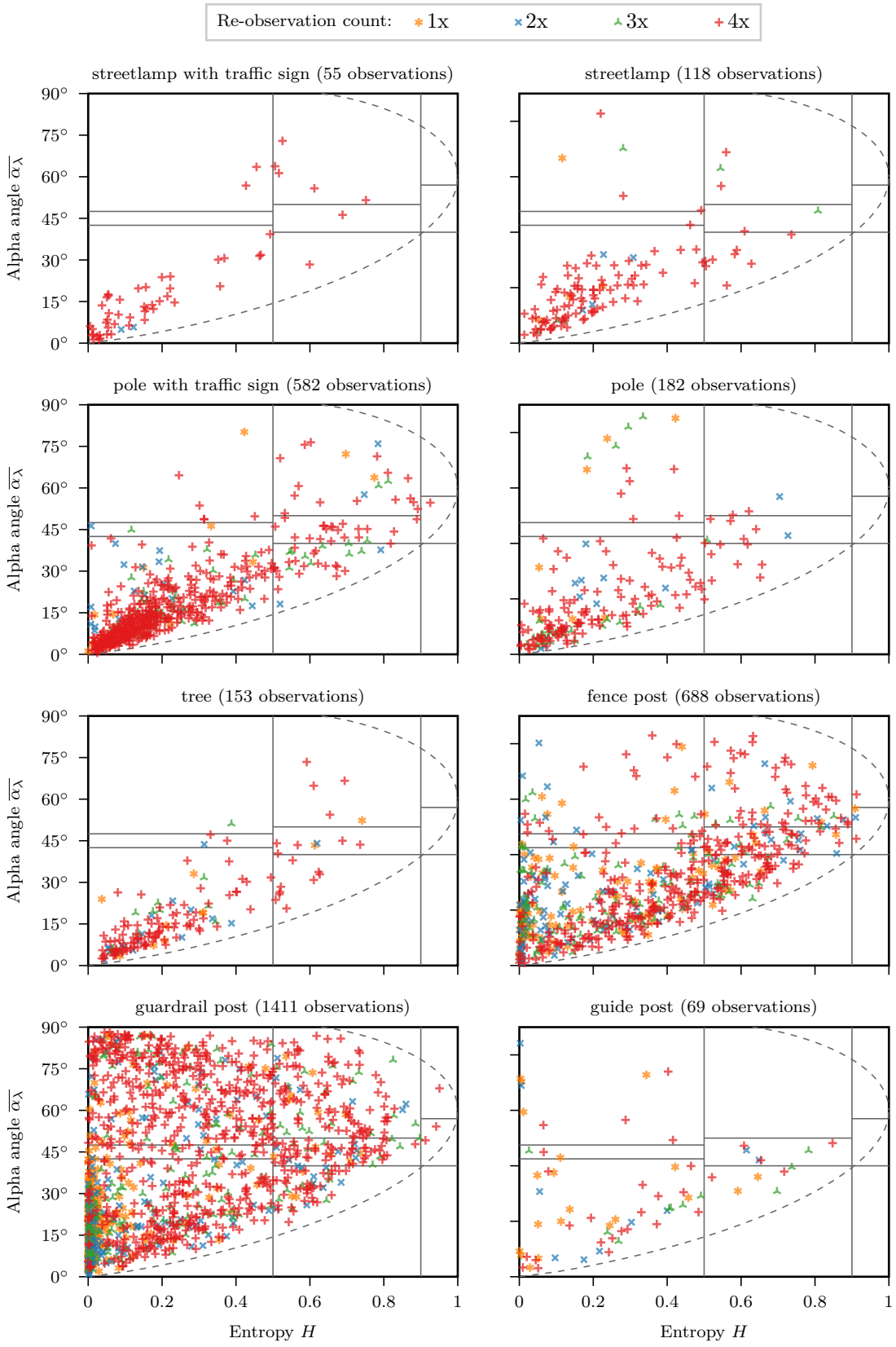


Figure 5.25: A spatial association of landmark candidates with map elements allows a landmark type-based scattering analysis via the Cloude-Pottier approach according to Fig. 2.12. Furthermore, the symbols and colors of samples indicate if a candidate is part of an established landmark in case of at least 2 re-observations. $\mathcal{R}_{\text{Ulm}}$ is the basis of this evaluation.

the observed scattering mechanisms per landmark type can be analyzed respectively. Therefore, the polarimetric covariance matrix at the spatial position with the largest Wishart distance of the corresponding candidate area is decomposed according to Cloude-Pottier. The resulting positions in the entropy-alpha plane are shown in Fig. 5.25. Because all extracted candidates are considered and the decomposition result is visualized per drive, also single observations in only one drive are included. A group of landmark types can be identified that is characterized by clearly having the most occurrences in the area of lower entropy odd-bounce scattering (Bragg surface according to original classification scheme, cf. Fig. 2.12): streetlamps and poles, both with and without additional traffic sign plates, trees, and guide posts belong to this group. A clustering of certain re-observations counts at specific locations in the Cloude-Pottier plane can not be observed for this group. The second group is formed by the fence and guardrail posts, for which a wider distribution over multiple scattering classes is observed. For the guardrail posts, a sizeable number of observations are dominantly even-bounce scattering. This is expected due to the dihedral structures forming at the posts due to their typical I-beam shape [115]. Moreover, a concentration of objects with lower re-observation counts is found in an area of low entropy (below 0.05). They result from short visibility due to occlusion or very few samples with a significantly increased reflectivity due to anisotropic scattering. Therefore, such detector results with very low entropy are not advantageous, but some variation leading to slightly higher entropies indicates an extended observation period, which is helpful for a robust recognition.

5.3.3 Line-shaped landmark detection

The polarimetric scattering information is not exploited for the detection of line-shaped landmark candidates. An empirical study showed that scattering arrangements, in which a potential benefit can be expected, do not occur in the considered environments. Analogously to the observation for point-shaped landmarks, such an arrangement would require an object, which itself is observed as extended in the gridmap, to be located within another extended scatterer of similar amplitude but a different scattering mechanism. Hence, only one scalar reflection power is used for the line-shaped landmark detection. For the polarimetric measurements, the trace of the covariance matrix describes such an overall reflectivity.
Typical line-shaped landmarks in automotive contexts are curbstones, fences, guardrails or walls of buildings. Considering the appearance in a gridmap, these objects are characterized by a line of locally maximal reflectivity, which is thin along the minor axis. Contrary to the common edge detection approaches in optical image processing, an amplitude ridge rather than an edge is the topology of interest. Therefore, the scalar map is transformed into a map of ridgeness scores by evaluating the eigenvalues of the Hessian matrix [152]. After thresholding of these scores, a topological skeleton [153] is calculated for thinning a potential multi-pixel thickness of a ridge region. Thereby, the subsequent Hough transform [154] for extraction of line segment candidates has a chance to generate more reproducible lateral positions. Given the emphasis on the advantages of the PreCFAR approach particularly for line-shaped landmarks, a qualitative and quantitative evaluation in comparison to a CFAR detection-based implementation is conducted. The CFAR threshold is chosen

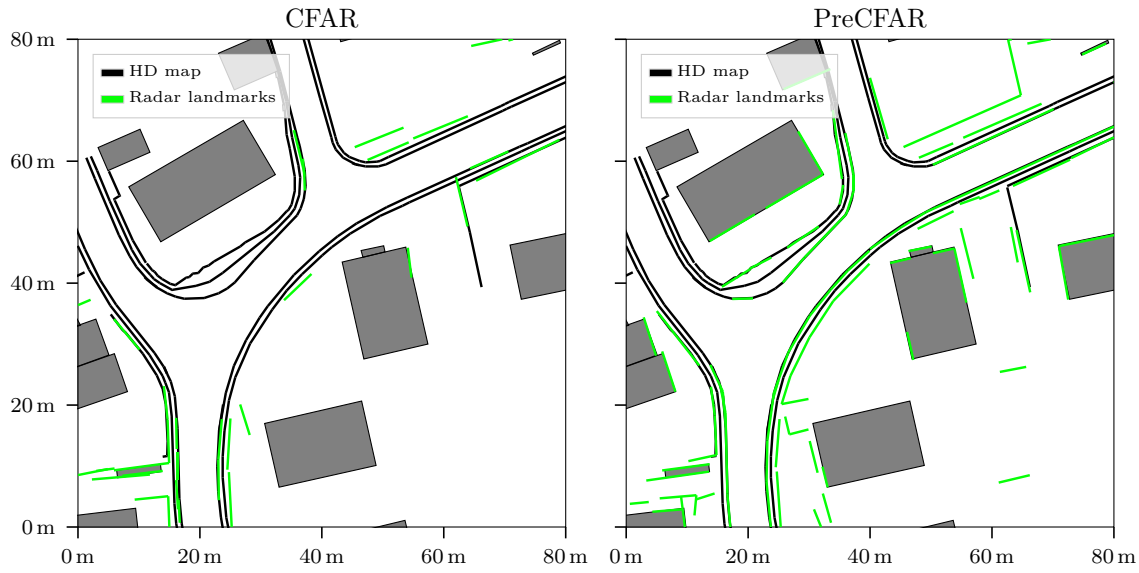


Figure 5.26: For a qualitative comparison of the line-shaped landmark extraction between a CFAR and a PreCFAR gridmap as the data basis, the established landmarks (green) after re-observing candidates during multiple traversals are considered. Additional HD map elements (black) serve as an orientation.

such that the number of detections matches a modern series sensor with an average of approximately 400 detections in typical environments. Each resulting gridmap is fed to the introduced line segment extraction algorithm with the same parameters. Analogously to point-shaped landmarks, a line-shaped landmark is established when matching candidates are observed multiple times in different drives. The method for associating line segments and creating an optimal joint line segment from such associations is the same as will be introduced below for constructing the landmark map (cf. Section 6.2.1). This landmark-focused approach enables an indirect but concise evaluation of the quality of the extracted landmark candidates and, consequently, the extraction approach including the corresponding data basis. Especially for the qualitative comparison between the CFAR and PreCFAR data bases, a simple and clear result interpretation is possible, whereas a visualization of all the candidates from the four drives is incomprehensible.

The exemplary map extract in Fig. 5.26 shows such a comparison for a section of $\mathcal{R}_{\text{Ulm}}$. A substantial increase in both the number of elements and the total length is evident for the PreCFAR case when compared to the CFAR variant. Accordingly, it can be concluded that the more consistent and complete PreCFAR representation ensures the extraction of more robust candidates. In addition to the established radar-based landmarks, some HD map elements, which can be perceived as line-shaped objects, accompany the map extracts. The high degree of congruence between both map types indicates that the established landmarks correspond to real-world object in meaningful way and that the proposed approach is suitable.

With availability of the HD map, information about the types of extracted landmarks can be derived. This enables to quantitatively demonstrate the superiority

Table 5.3: Overall lengths of extracted line-shaped landmarks, which are matched to and classified by HD map elements, for $\mathcal{R}_{\mathrm{Ulm}}$. The secondary "share" columns indicate the share of the matched lengths to the overall available length in the HD map.

Type	**HD map**	**CFAR**		**PreCFAR**	
		Length	Share	Length	Share
barrier	558.4 m	102.3 m	18.3 %	274.4 m	49.1 %
building	8976.0 m	338.3 m	3.8 %	1201.2 m	13.4 %
curbstone	12 396.0 m	502.2 m	4.1 %	3736.8 m	30.1 %
fence	1905.9 m	355.8 m	18.7 %	1093.7 m	57.4 %
guardrail	2927.5 m	473.0 m	16.2 %	1398.3 m	47.8 %
shoulder	7372.2 m	61.4 m	0.8 %	144.3 m	2.0 %
sidewalk	6091.6 m	104.8 m	1.7 %	138.6 m	2.3 %

of the PreCFAR data basis and to determine the suitability of different line-shaped landmark types for self-localization. Therefore, Table 5.3 provides the accumulated lengths of extracted line-shaped landmarks, which are matched to HD map elements. Due to the labeling in the HD map, matched landmarks can be classified. When comparing the data bases, a strong advantage of the PreCFAR-based approach is confirmed: for all types of landmarks, a noticeable amount of landmark lengths is added when choosing the lower data level. Moreover, comparing overall matched lengths and percentages of matched length relative to the available HD map lengths, the following landmark types appear to be particularly suitable for self-localization: barriers, buildings, curbstones, fences and guardrails. Less suitable, however, are objects labeled as shoulder and sidewalk lines in the HD map.

5.4 Summary

This chapter explored necessary building blocks for a successful self-localization with a polarimetric radar. For this, characteristic environmental elements, or landmarks, are vital, which is why landmarks were analyzed in detail as a first step in this chapter. It included undisturbed measurements of individual landmarks, which are expected to frequently occur in typical automotive environments, in an anechoic chamber. An analysis of the scattering mechanisms by incident angle showed that they exhibit strong anisotropy in both reflectivity and scattering mechanism. Additionally, ISAR imaging for a spatially resolved analysis of reflection centers confirmed assumptions about scattering origins. Further real-world measurements validated these findings, showing significant variations in scattering behavior depending on the incident angle.

For a robust detection of such landmarks, an accumulation of multiple measurement frames is required. While this is state of the art in literature and the approach to carry out such an accumulation is well-known in form of gridmaps, novel techniques were introduced to incorporate low-level polarimetric data. The concept of PreCFAR gridmaps, which are constructed from low-level data, was discussed and shown to overcome limitations of common detection-based techniques by providing more complete and continuous representations of extended, lower reflectivity objects. It is extended to polarimetric data usage in form of polarimetric PreCFAR gridmaps. By incorporating polarimetric covariance matrices, different types of scattering information in one grid cell can be preserved to account for the discussed anisotropy. The proposed polarimetric PreCFAR representation was designed with landmark detection as the target from the beginning. For the point-shaped candidate extraction, the Wishart distance measure characterizes the scattering difference between covariance matrices in order to also detect landmarks that do not distinguish from their neighborhood by amplitude but only by scattering mechanism. This allowed to more reliably detect fence posts in an example scenario. A larger-scale statistical analysis further demonstrated that the number of re-observations as a robustness measure grew when the level of polarimetric information was increased. On the contrary, only a non-polarimetric scalar reflection power was used for the line-shaped landmark detection. For these, in particular, the clear advantage of using lower data levels for a higher recognition performance was demonstrated.

In summary, this chapter provided a comprehensive analysis of static environment landmarks, introduced advanced grid representations, and developed robust landmark detection methods, forming the foundation for the actual implementation of self-localization in the next chapter.

Chapter 6

Self-Localization

With the robust extraction techniques for point- and line-shaped landmarks developed in the previous chapter, the application of these in the context of self-localization is the next step and subject of this chapter. While an advantage in terms of re-observations has already been demonstrated when leveraging the polarimetric information, the main objective of this section is investigating the effect on self-localization. This will be answered by means of the first application of polarimetry for self-localization in real-world public road traffic.

Therefore, the available literature on the topic of radar-based self-localization in automotive environments is discussed in Section 6.1 as an introduction. In order to successfully self-localize globally, a map with georeferenced elements must be accessible. A simple method to create such a map, which is required for the subsequent localization performance evaluation, is presented in Section 6.2.1. For the self-localization phase, a radar-only technique is proposed in Sections 6.2.2 to 6.2.4. The information required for a spatially correct incorporation of consecutive measurements into the polarimetric PreCFAR gridmap is derived instantaneously by a radar-only ego-motion estimator. With landmark candidates derived from this accumulation in a robust way as demonstrated in Section 5.3, a map matching is carried out for constructing a factor graph. A graph optimization then yields the best ego-vehicle pose estimate. The performance of this approach in various real-world environments and the dependency on the polarimetric information level is evaluated in Section 6.3, before Section 6.4 summarizes this chapter.

Hence, this chapter contributes

- an extension of a known radar-based ego-motion estimation technique to overcome the challenge of a low unambiguous Doppler velocity due to a fully polarimetric acquisition,
- a graph-based radar-only self-localization framework built on point- and line-shaped landmarks,
- an extensive real-world evaluation of self-localization in diverse environments including a comparison of different levels of polarimetric information.

This chapter is mainly based on the own publication “Landmark-based Vehicle Self-Localization Using Automotive Polarimetric Radars” [**71**] using a factor graph implementation with some preliminary work from the supervised thesis “Automotive Self-Localization using Polarimetric Radar” [155], which utilizes a particle filter.

6.1 State of the Art

Despite the abundance of literature on vehicle self-localization based on exteroceptive sensors due to the recent hype around autonomous driving, the subject of radar-based approaches remains limited in comparison to the other common modalities, such as lidar and camera [6]. The two research areas place recognition and simultaneous localization and mapping (SLAM) are connected to this study due to the inherent search for the ego-vehicle's pose, but it is evident that their purpose and the associated localization accuracy, which is accepted as a success, differ considerably. Results in the range of meters are state of the art for these applications [156, 157, 158, 159], but this neither is intended for nor enables correct positioning within a lane. Therefore, only the directly connected research topics of ego-motion estimation and map-based self-localization are considered in detail in the following.

Radar-based ego-motion estimation seeks to ascertain the motion parameters of the ego-vehicle indirectly as accurately as possible by analyzing the reflections of static surroundings. A complete state for describing motion in a plane includes one angular and two translational velocities. While an integration of motion states over time enables the calculation of a time series of relative poses, the resulting accuracy is subject to a drift degradation as integration time increases. However, ego-motion estimation frequently constitutes a component of a more complex localization system, wherein the drift error is addressed by correlation with a map. Thus, locally smooth trajectory estimates aligned to a global frame can be calculated. For radar sensors without the capability to measure Doppler velocities, two consecutive scans must be matched based on an association of static reflectors. This is typically applied to data from 360° *mechanically scanning* radars due to a missing instantaneous velocity measurement in both classical [160, 161] and learned [162, 163] fashions. Regular automotive-suitable *beamforming* radars provide instantaneous angle and velocity estimates, so that the motion state can be derived from a single measurement cycle [164, 165]. These approaches exploit the fact that the velocities of static objects vary with angle because the velocity measuring capability is inherently radial.

The literature on complete radar-based self-localization frameworks with known maps can also be differentiated on the basis of the utilized sensor types. Besides the two types introduced in the ego-motion estimation context, one additional type of radar is proposed for self-localization: *ground-penetrating* radar (GPR) [166, 167]. Compared to the other two sensor technologies for perceiving the above-ground environment, GPR's vertical scanning plane limits it to record sub-surface features and, therefore, is only suitable for self-localization in the context of automated driving. The group of above-ground radar types with horizontal scanning planes are integrated into vehicles in the first place for detecting surrounding obstacles in order to plan a safe, collision-free vehicle trajectory. An additional use of these for self-localization is therefore a beneficial multi-purpose capability. This factor and further ones such as cost, packaging constraints, durability, customer-friendly design and power consumption have led to beamforming radars becoming the de facto standard in series-produced vehicles. The radar type is one criterion for classifying the approaches available in literature, for which Table 6.2 provides an overview. Different radar types are depicted by symbols that can be translated by Table 6.1.

Table 6.1: Symbolic abbreviations for sensor and map types

Sensor Types		Map Types
Above-ground beamforming radar	Gyroscope	cross-modal
Above-ground scanning radar	Accelerometer	mono-modal
Ground-penetrating radar	Speedometer	sparse
Polarimetric capability	Steering angle	quasi-dense
Lidar	GNSS	dense
Camera	Magnetometer	

Table 6.2: Literature overview on the topic of map-based self-localization using radar sensors. Resulting localization errors are given as RMSE values unless otherwise noted. The symbol † indicates that 68 % of errors were below the given value. The symbol * denotes MAE values, # marks indirect values, e.g. estimates from graphs.

Author	Ref.	Year	Sensor Set		Route	Map		Error (m)	
			Radar	additional		Modality	Sparsity	longitudinal	lateral
Clark et al.	[32]	1998	1x		0.2 km			–	–
Lundgren et al.	[140]	2014	1x		5 km			$\approx 0.50^{\#}$	$\approx 0.50^{\#}$
Rapp et al.	[168]	2015	4x		0.1 km			$0.16^{\dagger,\#}$	
Cornick et al.	[166]	2016	1x		1.6 km			0.06	0.04
Schuster et al.	[169]	2016	4x		0.4 km			$> 1.0^{\#}$	
Ward et al.	[170]	2016	2x		5.4 km			0.38	0.07
Yoneda et al.	[171]	2018	9x		2.2 km			0.19	0.26
Li et al.	[172]	2019	1x	–	0.2 km			0.65	
Iannucci et al.	[173]	2020	3x		1.5 h			$\approx 0.3^{\dagger,\#}$	
Jürgens et al.	[174]	2020	6x	–	2 km			$0.20^{\dagger,\#}$	$0.25^{\dagger}$
Narula et al.	[175]	2020	3x		1.5 h			$\approx 0.3^{\dagger,\#}$	
Ort et al.	[167]	2020	1x		7 km			0.17*	0.26*
Pishehvari et al.	[176]	2020	1x		0.2 km			0.16	
Yin et al.	[177]	2020	1x	–	9 km			> 6.0	
Engel et al.	[139]	2021	2x		6 km			0.18	0.16
Otake	[178]	2021	5x		1.4 km			0.07	0.07
Burnett et al.	[179]	2022	1x	–	8 km			0.13	0.12
Yanase et al.	[180]	2022	9x		4.6 km			0.16	0.14
Yin et al.	[181]	2022	1x	–	9 km			≈ 1.0	
This work			3x	–	10 km			0.11	0.06

Another differentiating factor is the necessity of supplementary sensors for a successful self-localization and when applicable their type. While most studies rely on proprioceptive data sources such as wheel tick and gyroscope sensors, some approaches get by with radar-only data as the input. Only one of them uses the Doppler information for deriving an a priori motion state [174], while the remaining approaches rely on a matching of consecutive cycles [172, 177, 179, 181].

In case a reference compares results from different sensor sets, the table always refers to the experiments with the minimal set including radar. Due to varying research objectives, the quantity of validation data differs significantly and, thus, is presented in the table for orientation. The stated values reflect the respective longest, unique routes each.
A further categorization can be established based on the properties of the map. On the one hand, the map might be created from data of another sensor modality than the one used during the self-localization. This is referred to as *cross-modal* below. On the opposite, *mono-modal* designates approaches that use the same sensor modality for both mapping and self-localization. In addition, the table also categorizes the data level present in the map. *Sparse* maps store an abstracted representation of the environment in a memory-saving way by focusing on landmark-like objects. This can include cross-modal positions of artificial beacons [32] and pole-like objects commonly found in HD maps [174, 176], or mono-modal results of landmark extractors [139, 140]. On the contrary, *dense* maps are characterized by a high density of information requiring comparatively large spaces of memory. The advantages are a an easier and less ambiguous association of map elements with actual observations in the self-localization phase. The occurring data levels range from simple unfiltered accumulations of point cloud data [170, 175] to planar [171, 177, 178, 180] and volumetric grids [166, 167]. As an intermediate classification, the *quasi-dense* approaches rely on filtered and partially compressed data levels such as filtered [179] or clustered [169] point clouds, and visual scale-invariant feature transform keypoints [173].
As an approximate order of magnitude of the self-localization quality, the table also contains longitudinal and lateral errors. If available, the RMSE is reported, whereas † indicates the 68 % threshold in a cumulative distribution function and * marks a mean absolute error (MAE) value. The joint horizontal plane error is stated in case no separate axis-referred values are available. Due to the vast difference in the utilized sensors and the environment conditions, absolute comparability between the results is impossible.

6.2 Approach

The following sections describe the remaining components required for implementing the self-localization. An overview over the components of the proposed approach is given by Fig. 6.1 in form of a block diagram. The figure is divided into the processing sequence for the mapping phase in the upper half and the localization phase in the lower half. Each processing block provides a reference to the corresponding sections. For creating the map, multiple passes through the same environment with ground truth poses from an integrated DGNSS/IMU device are required. The processing block copies in lighter color symbolize the multiple passes. After finding a consensus, the desired map results. During the localization phase, only the polarimetric radar data and this map are needed to derive the pose estimates, which is indicated by the darker colored boxes.

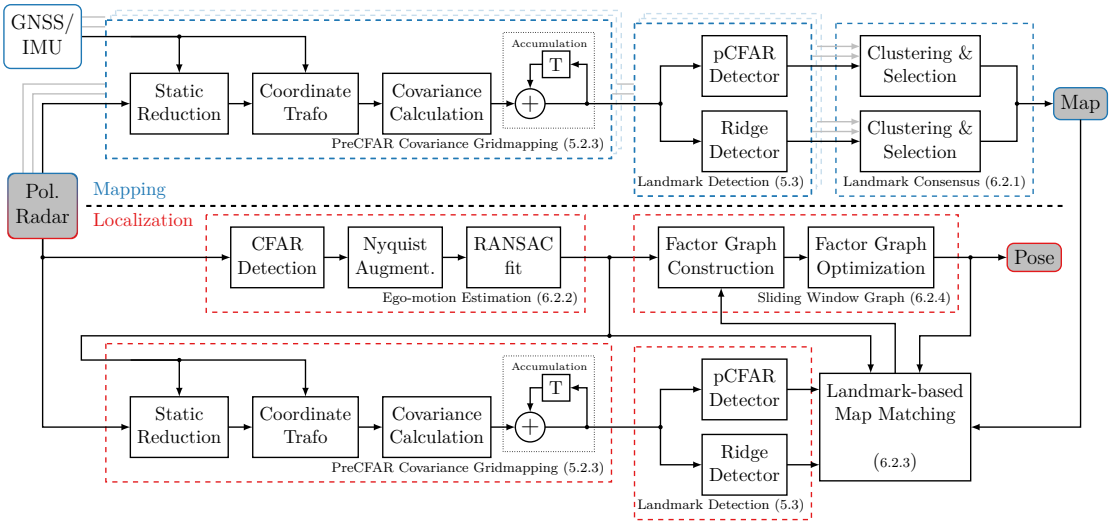


Figure 6.1: The block diagram provides an overview of all components involved in the proposed self-localization approach. It includes both the mapping and localization processing blocks. Adapted from [**71**], © 2024 IEEE.

6.2.1 Mapping

The map data level in this study is chosen to only include spatial positions of point- and line-shaped landmarks. This abstracted representation allows compact storage sizes and is generic in the sense that, in principle, it is applicable to other sensor modalities as well. Furthermore, a perspective use of maps generated purely from non-radar data is possible with such an approach. For instance, the majority of HD map creation procedures does not build upon radar data. However, the most significant part of landmark types relevant for radar can also be detected by camera or lidar. For the same reason, no radar specific or even polarimetric descriptors are used as landmark features because of the implications that would have for a large-scale mapping. The principal possibility of using such descriptors, which is supported by the chosen mapping approach, is intentionally not employed.

The mono-modal mapping pipeline in Fig. 6.1 consists largely of components known from the previous chapter. For each pass, point- and line-shaped landmark candidates are extracted based on the polarimetric PreCFAR gridmap data. The new processing step is finding consensus over landmark candidates for establishing actual landmarks, which will be included in the map. Sufficient spatial closeness of the landmark candidates from different passes serves as a criterion to assume a re-observation of the same physical object. In such a re-observation case, the landmark is considered robust and easily recognizable, which justifies the map incorporation. Moreover, only temporarily static objects, such as trash bins or parked vehicles, will automatically be excluded from the map due to the lack of re-observations, which is desired. For this mapping approach, an accurate ground truth pose must be available during the multiple passes. Therefore, the outage of GNSS signal reception must remain short. However, it should be noted that this does not impede the self-localization phase itself, which would be most beneficial in scenarios without an unobstructed satellite view. Just a more sophisticated map creation process, which leverages SLAM approaches or further sensors, is necessary then.

The set of all L landmarks $\mathbf{l}$ is enumerated by the landmark index l ($l \in \{0, \dots, L-1\}$). Individual point-shaped landmarks are defined by their spatial position in form of a two dimensional Cartesian coordinate and are denoted by $\mathbf{l}_l^{\mathrm{p}} \in \mathbb{R}^2$. The associated group of landmark candidates is formed when the Euclidean distance between them is lower than the threshold $d_{\mathrm{thres}}^{\mathbf{l}^{\mathrm{p}}}$ and the re-observation spans at least $N_{\mathrm{thres}}^{\mathbf{l}^{\mathrm{p}}}$ separate passes. The resulting position is set to the spatial average over all candidates forming an associated group together. Querying for spatial neighbors via a k-d tree [150] for each pass is an efficient method for finding the groups.
Line-shaped landmarks are defined as line segments by a start and end point, so that $\mathbf{l}_l^{\mathrm{l}} \in \mathbb{R}^{2\times 2}$. For these, multiple observations from different passes are precondition for creation too. A re-observation association is established when two line segment distance measures are below a threshold. The convex hull and projection distance measures from [141] are used with the thresholds $d_{\mathrm{ch,thres}}^{\mathbf{l}^{\mathrm{l}}}$ and $d_{\mathrm{prj,thres}}^{\mathbf{l}^{\mathrm{l}}}$, respectively. As these line segment distances in [141] are proposed for a similar purpose, they are well suited. In order to match sequences of associated line segment pairs, a connected-component analysis allows establishing larger contiguous groups. The start and end point of the landmark are calculated by searching all mutual candidate projection points for the pair with the longest distance. For contiguous sequences, these points might be a shortcut to an originally curved shape. Thus, an approximative reconstruction via the Ramer-Douglas-Peucker algorithm [182] is carried out to model the original shape with the least amount of supporting points. Furthermore, if start or end points of neighboring line segments are spatially close within some tolerance, a common supporting point is calculated and the separate segments are combined to a line string.

6.2.2 Ego-motion estimation

The ego-vehicle's instantaneous motion information is a key element during the self-localization phase. Multiple processing components require it as an input as shown in Fig. 6.1: for the PreCFAR gridmap construction, on the one hand, the parameters for describing the static surface in the data cube depends on translational and rotational motion parameters. On the other hand, subsequent measurements have to be accumulated spatially correct by taking the difference in acquisition poses into account. Integration of the motion parameters provides such a pose sequence, which is also used in the map matching and factor graph modules.
The advantage of radar sensors in this context is given by their Doppler measuring capability, thereby enabling the estimation of the required motion information without the necessity for further sensors. By identifying the reflections originating from static surroundings and using the associated velocities as an input to a model-based estimator, the instantaneous motion state of the ego-vehicle can be derived. This is well-known in literature and a well-working RANSAC-based technique [164] is the basis for the implementation in this work. The most recent scans from each sensor are aggregated and used for a joint estimation. Because a basic prerequisite for accurate results is the precise knowledge of the mounting angle, the alignment of the polarimetric channels in Section 4.4.4 is an important calibration step.
For an increased accuracy and robustness, additional adaptions to the original paper are introduced. Considering an acceleration as a first order derivative of consecutive

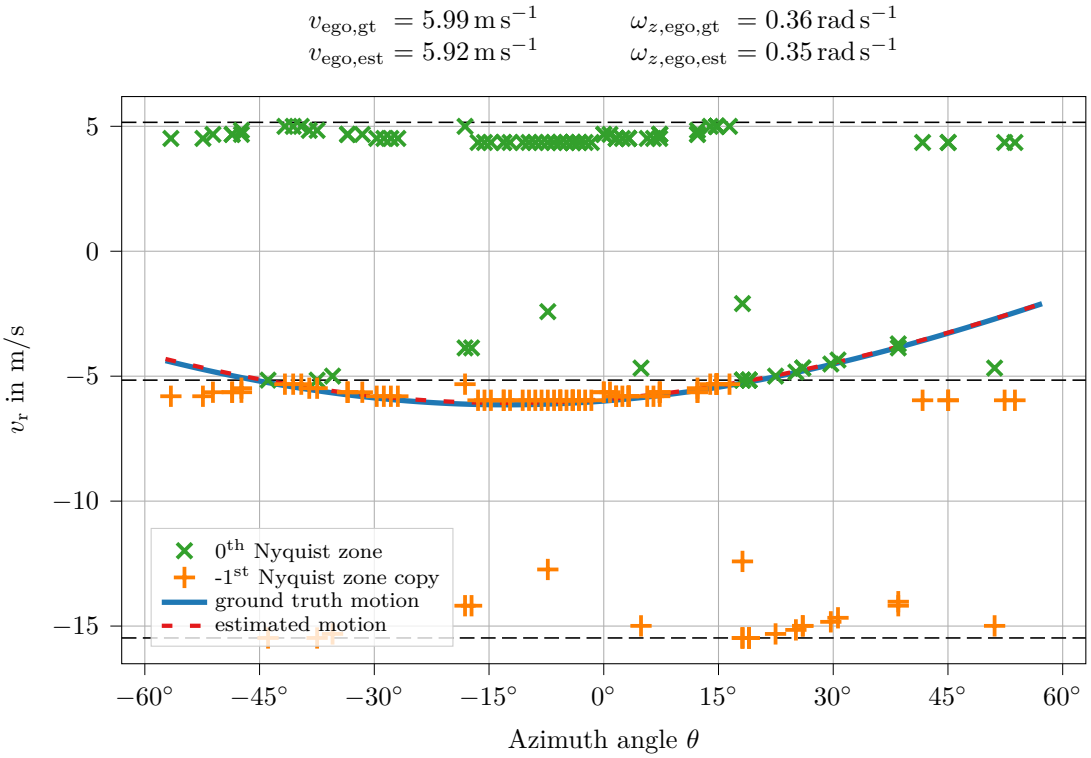


Figure 6.2: The Nyquist zone augmentation allows estimating a correct ego-motion also in cases of ego-velocities above the radar's unambiguous Doppler domain. Adapted from [**71**], © 2024 IEEE.

measurements enabled the following measures: On the one hand, an outlier rejection for unreasonable apparent accelerations is implemented to avoid wrong estimates in cases where reflectors other than the static surrounding are wrongly selected, such as in dense traffic. On the other hand, the consecutive measurement times for each sensor, introduced in order to avoid intra-vehicle interference, can lead to distorted results in actual acceleration scenarios. Therefore, the difference in the measurement times is compensated with the help of previous acceleration estimates as in [174].

Typical fully polarimetric radars acquire the two scattering matrix halves by sequentially activating the transmitters with the different polarizations (cf. Section 2.3.10). Thus, the sampling rate for the Doppler velocity estimation and consequently the unambiguous domain is halved. Since the ego-motion estimation is an integral component of the self-localization, a simple yet effective technique to deal with the small unambiguous velocity domain is proposed. Instead of carrying out all calculations in the unambiguous domain including the tracking of all possible unfolding hypotheses, the measurements are augmented by copies in the different Nyquist zones. With the RANSAC algorithm scoring a high number of inliers positively, the correct solution is still found even with a potentially higher apparent false alarm rate. The number of copies must be chosen according to the expected velocity range. A visualization of a simple example for only the front sensor of the vehicle setup in Section 3.1 is presented in Fig. 6.2. Only one copy of the detections is sufficient to correctly estimate the ego-vehicle velocity, which is slightly above the unambiguous Doppler velocity for the utilized sensors (cf. Table 3.2).

6.2.3 Map matching

The overall success of the self-localization strongly depends on the performance of the map matching. If a landmark observation is wrongly associated with a map landmark, the ego-pose estimate might quickly diverge. Therefore, it is of great importance to keep the misassociation rate as low as possible while at the same time not suppressing some correct associations. Accordingly, one important requirement is robustness in a sense that a temporary, inevitable misassociation does not directly lead to a divergence. Since this data association problem is challenging not only for a radar-based self-localization but relevant to a wider body of research, more literature is available on this topic. A robust modality-independent method is proposed in the excellent work [8]. This multistage matching approach serves as a basis for this study with only some minor adaptions.

In the first stage, landmark observations from a fixed temporal window are transformed into a local coordinate system purely according to the integration of the ego-motion information. If some observations are spatially close in this local frame, they are considered to originate from the same landmark and a cluster is established. Such clusters are the counterparts for the map landmarks in the second association stage. By using the clusters instead of individual observations, also measurement cycles with a temporarily very low observation count can be correctly associated with the corresponding map landmarks. An adaption compared to the original implementation [8] is given by a clustering via a connected-component analysis in a distance-weighted sparse graph derived from a k-d tree. This tolerates more ego-motion drift and, hence, allows longer temporal windows.

The second stage involves the association the landmark clusters to map landmarks in an optimal way. This is achieved if a high percentage of clusters is matched and the overall distances between associations is small. Therefore, a joint cost function considering both the distances but also the number of matches is evaluated for all possible ego-poses. The set of possible poses is generated from all combinations of point-shaped landmark pair associations. Both point- and line-shaped landmarks contribute to the cost function by Euclidean coordinate distances, and convex hull and projection line segment distances, respectively.

A final temporal smoothing stage is implemented for robustness against outlier matches. By counting how often a landmark cluster is association with which map landmark, potential temporarily wrong associations can be identified and subsequently rejected. Due to the drift-tolerant clustering of the first stage, landmark clusters from one landmark typically do not split. As a result, an injective mapping between clusters and map landmarks is targeted, which is different from the approach in [8]. If a landmark cluster is wrongly association with another map landmark for some cycles while there is no corresponding correct one, the wrong association would still be additional to the correct one after this stage. By finding the maximum weight matching of a bipartite graph with the association counts serving as the weights, only the correct association, which was predicted more often, will result.

The map matching result is called association graph in this study and an example is given by Fig. 6.3a. It helps to understand which map landmarks are observed from which pose. This is translated into a factor graph in the following section, making it possible to determine an optimum solution for the given observations.

6.2.4 Factor graph optimization

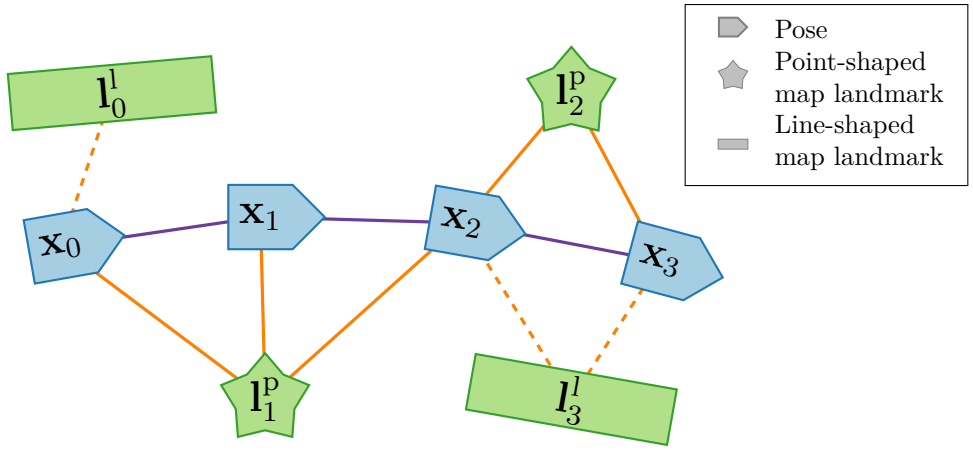
A wide range of approaches for estimating the ego-pose after determining the ego-motion and landmark associations is available in literature. Due to this step's independence from sensor specifics and its consistency of the problem formulation with a vast number of robotic applications, the insights from numerous research in the area of SLAM can be utilized. In SLAM literature, this processing step is part of what is known as the back-end. Apart from filtering techniques such as an extended Kalman filter or a particle filter, the modern class of graph-based optimization frameworks are becoming increasingly popular. The latter have various advantages such as being deterministic and being less prone to linearization and association errors, reducing the risk of divergence [183]. In typical scenarios, the sparsity of the associations allows an efficient optimization of all graph variables.
In such a factor graph representation, the ego-poses and the landmarks compose the variable vertices $\mathbf{\Theta}$, which shall be optimized. Besides the apparent interest in the pose estimates for a self-localization, the design choice of landmarks as additional variables allows deriving information for a potential map update. However, this is not within the scope of this work. With the entirety of X poses being denoted as $\mathbf{x} \in \mathrm{SE}(2)^X$ in the sliding time window, the optimization objective is finding the optimal variable values $\hat{\mathbf{\Theta}}$ as the maximum a posteriori probability

$$\hat{\mathbf{\Theta}} = \arg\max_{\mathbf{\Theta}} p\left(\mathbf{\Theta} \,|\, \mathbf{z}\right) \qquad \text{with} \quad \mathbf{\Theta} = \begin{pmatrix} \mathbf{x} \\ \mathbf{l} \end{pmatrix} \tag{6.1}$$

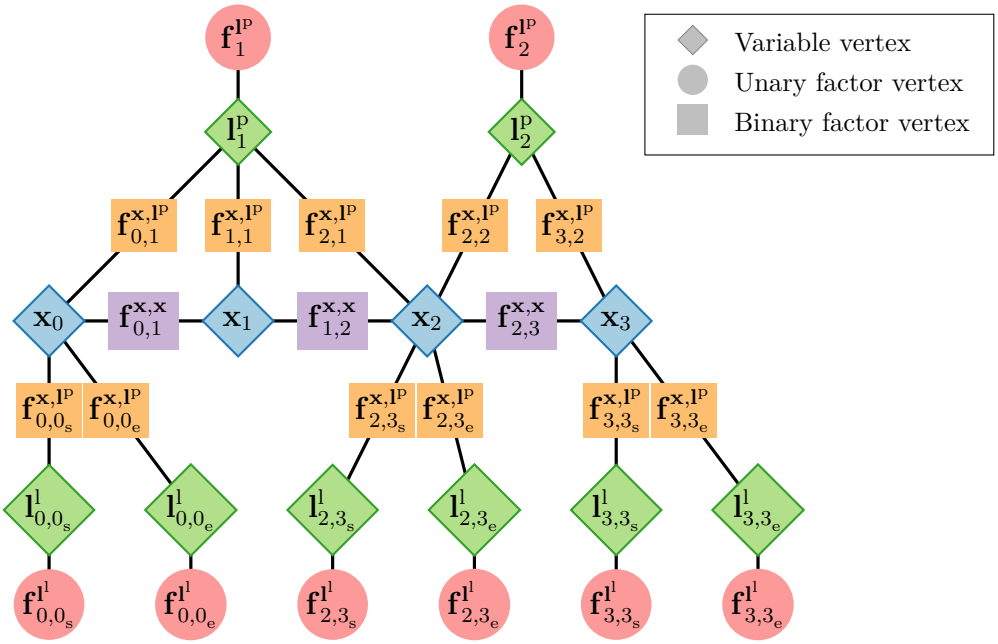
for the given measurements $\mathbf{z}$ [183, 184]. Using the Bayes theorem and assuming multivariate Gaussian distributions for priors and measurements, this can be transformed to a minimization of a sum of non-linear least-squares

$$\hat{\mathbf{\Theta}} = \arg\min_{\mathbf{\Theta}} \sum_i \left(\mathbf{z}_i - \mathbf{h}_i\left(\mathbf{\Theta}_i\right)\right)^T \mathbf{P}_i \left(\mathbf{z}_i - \mathbf{h}_i\left(\mathbf{\Theta}_i\right)\right) \tag{6.2}$$

with the measurement function $\mathbf{h}$ and the information matrix $\mathbf{P}$, which is the inverse of the covariance matrix [183, 184]. In the factor graph, this is represented by the second type of vertices: factors. Thus, the graph is bipartite. A factor vertex is denoted by $\mathbf{f}_i$ and includes the corresponding measurement $\mathbf{z}_i$, measurement function $\mathbf{h}_i$, and information matrix $\mathbf{P}_i$. The generic index i identifies one arbitrary factor so that the sum in (6.2) considers all available factors. Factors can be unary and therefore only constrain one variable vertex, which is denoted by $\mathbf{f}_i^u$ where $u \in \{\mathbf{x}, \mathbf{l}^\mathrm{p}, \mathbf{l}^\mathrm{l}\}$ is indicating the constrained variable type. Binary factors $\mathbf{f}_i^{u,v}$ on the contrary constrain the relation between two variable vertices with $v \in \{\mathbf{x}, \mathbf{l}^\mathrm{p}, \mathbf{l}^\mathrm{l}\}$.
The translation of the exemplary association graph in Fig. 6.3a into the corresponding factor graph in Fig. 6.3b helps in understanding the factor types relevant for the self-localization. The odometry factors $\mathbf{f}^{\mathbf{x},\mathbf{x}}$ are binary and constrain consecutive poses. The ego-motion estimation provides the factor's measurements $\mathbf{z}^{\mathbf{x},\mathbf{x}}$ by integrating the velocity estimates to position and heading deltas. Because the measurement function $\mathbf{h}^{\mathbf{x},\mathbf{x}}$ maps the poses from a special Euclidean group to the measurement space ($\mathbf{h}^{\mathbf{x},\mathbf{x}} : \mathrm{SE}(2)^2 \mapsto \mathbb{R}^3$), the optimization is not straight forward but must be carried out by using a Lie algebra to ensure staying within the Lie group after optimization [184].



(a) Association graph



(b) Factor graph

Figure 6.3: The map matching result is an association graph, exemplarily shown in (a), which connects point-(—) and line-shaped (- - -) landmark observations with their corresponding map landmarks. The corresponding factor graph is shown in (b) and is basis for the ego-pose optimization. Adapted from [**71**], © 2024 IEEE.

The second factor type $\mathbf{f}^{\mathbf{x},\mathrm{l^p}}$ models the observation of landmarks and, thus, is binary by constraining a pose and a landmark variable. This factor is used for both point- and line-shaped landmark observations. Details for the specific implementation necessary for line-shaped landmarks will follow. In order to ensure that this factor's model takes the radar measurement principle into account in the best possible way, the least-square calculation is carried out in polar coordinates. Thus, the noise model for the information matrix $\mathbf{P}^{\mathbf{x},\mathrm{l^p}}$ can be constructed from range and azimuth angle variances, which directly correspond to radar parameters, which are easy to quantify.

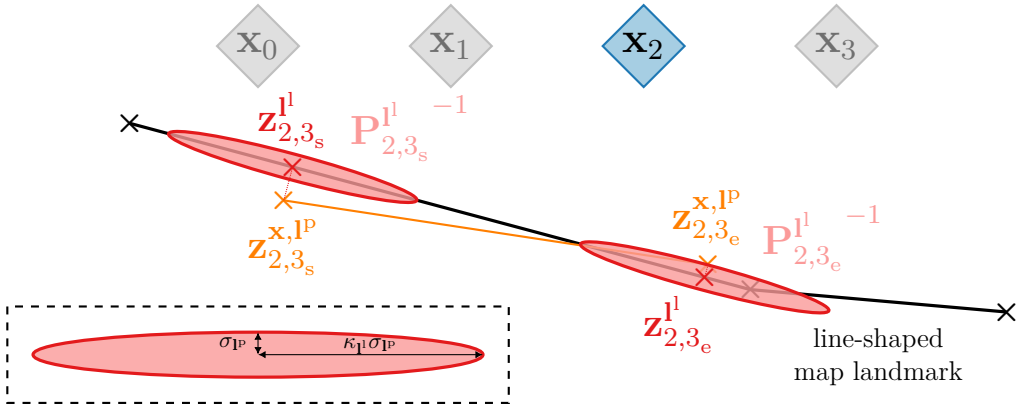


Figure 6.4: Line-shaped landmark associations are considered by two point-shaped landmark factors $\mathbf{f}^{\mathbf{x},\mathrm{l^p}}$ at the projection points of the segment's start and end onto the map landmarks. Due to highly anisotropic covariance matrices for both, it mainly constraints the orthogonal distance to the map landmark. Adapted from [**71**], © 2024 IEEE.

Line-shaped landmark associations are split into independent start and end point observations, including a separate variable vertex and an associated factor $\mathbf{f}^{\mathbf{x},\mathrm{l^p}}$ each. This is indicated by the subscripts s and e for start and end points so that

$$\mathbf{l}^{\mathrm{l}}_l = \begin{pmatrix} \mathbf{l}^{\mathrm{p}}_{l_\mathrm{s}} \\ \mathbf{l}^{\mathrm{p}}_{l_\mathrm{e}} \end{pmatrix}. \tag{6.3}$$

In addition, the split is done separately for each pose, from which an observation occurred, because different parts of a line-shaped landmark may have been observed, e.g., due to occlusion. For example, the line-shaped landmark $\mathbf{l}^{\mathrm{l}}_3$ in Fig. 6.3 is observed from both ego-poses $\mathbf{x}_2$ and $\mathbf{x}_3$ resulting in four variable vertices. While this is more costly compared to the implementation in [8], it allows a map update.

The final type of factors is unary and introduces the global map positions as priors into the optimization. The point-shaped landmark priors directly include the landmark positions as the measurements $\mathbf{z}^{\mathrm{l^p}}_l$ with an identity measurement function $\mathbf{h}^{\mathrm{l^p}}$ and an overall circular map uncertainty $\mathbf{P}^{\mathrm{l^p}}$.

For line-shaped landmarks, the two prior factors for start and end point are introduced in such a way that they essentially only constrain the pose in its orthogonal distance to the line segment. Therefore, the start and end point of an observed line-shaped landmark are transformed to global positions by the unoptimized ego-pose in a first step. Subsequently, these positions are projected onto the map line segment, which then serve as the prior positions. Fig. 6.4 illustrates this with an example. This approach is appropriate even though the ego-pose might be inaccurate at this point because a high uncertainty in the direction of the line segment (a factor of $\kappa_{\mathrm{l^l}}$ compared to the orthogonal direction) is assumed by choosing a strongly directional covariance matrix, which is also depicted in Fig. 6.4. Due to this special treatment of the information matrix compared to the common one for actual point-shaped landmark priors, the factors $\mathbf{f}^{\mathrm{l^l}}$ keep the line-shaped landmark designation in their superscripts. Data dependent information matrices $\mathbf{P}^{\mathrm{l^l}}_l$ result in this case.

For an actual implementation, the factor graph must be limited in size. In this work, this is achieved by limiting to a certain window of time. This window is sliding in such a way that always the last T_{graph} seconds of poses and the corresponding landmark observations are included, similar to [8]. Graph vertices to be dropped are removed by simple truncation to avoid fill-in, which would result from proper marginalization [185]. Therefore, it can occur that the graph is underconstrained for optimization due to too few associations, e.g., in an environment with very few landmarks. In this case, another prior type $\mathbf{f}^{\mathbf{x}}$ for the oldest pose is introduced to loosely constrain the graph.

6.3 Experimental evaluation

For answering one of the main research objectives of this study, the proposed approach is implemented and the real-world self-localization performance in various environments is experimentally evaluated. The data set used for this purpose is described in Section 6.3.1. This is followed by details of the implementation in Section 6.3.2. The results are presented in two parts: first, Section 6.3.3 is an analysis of the self-localization quality achievable with fully polarimetric information. After this, the impact of different levels of polarimetric data is assessed in Section 6.3.4.

6.3.1 Data set

Table 6.3: Overview of routes for the self-localization experiments

Route	Single-Pass Route Length	Evaluated Ride Duration	Environment Type	Point-shaped Landmarks	Line-shaped Landmarks
$\mathcal{R}_{\text{Fra}}$ / Frankfurt	7 km	45 min	urban, industrial	6762	39 km
$\mathcal{R}_{\text{Ing}}$ / Ingolstadt	10 km	75 min	urban, industrial	4202	37 km
$\mathcal{R}_{\text{Ulm}}$ / Ulm	5 km	35 min	village, rural	1545	16 km

Three different routes in Germany were traveled multiple times with the vehicle described in Section 3.1. One work package of the cooperative project @CITY [151] was the creation of HD maps for some specified environments. Therefore, the routes are chosen to lie within these environments allowing the radar landmark correlation in Section 5.3. For each route, three passes are used for the experiments. The self-localization performance is evaluated for each of the passes with a radar landmark map created from the two remaining passes in a cross-validation fashion. All passes were driven in the same direction to avoid any influence from occlusion, e.g., due to partially widely spaced separations of opposite lanes. An overview of the routes is provided in Table 6.3. The metric route length is given for a single pass, whereas the duration includes all three passes. A variety of environment types including urban, industrial and rural areas are present in the data set. For reference, the number of point-shaped landmarks and the overall length of line-shaped landmarks calculated from the fully polarimetric data are provided. In both cases, the given order of routes correlates with a decreasing landmark density per route length unit.

The ground truth position data from the coupled DGNSS/IMU device was not able to acquire a full-precision differential carrier phase solution everywhere. The availability of expected standard deviations for positional quantities from its internal Kalman filter allows estimating the ego-pose quality. The average of 0.086 m for the horizontal standard deviation over all utilized passes in case of lower quality solutions is non-negligible with respect to the self-localization performance, as will be shown below. Therefore, only the route parts with high quality carrier phase solutions are considered to possess ground truth information. A horizontal standard deviation average of 0.014 m is observed in this case. The calculation of the self-localization performance metrics only includes the parts with this accurate ground truth data.

6.3.2 Implementation

The factor graph optimization is implemented by leveraging the open-source Georgia Tech Smoothing And Mapping library (GTSAM) [186]. All required factors are already available in this library including the corresponding measurement functions and Lie group optimization techniques. Table 6.4 provides an overview of the utilized factor implementations from the library and the simple structures of the information matrices chosen in this work. Actual numerical values for the important parameters in this study's implementation are listed in Table 6.5.
Due to the incremental nature of the factor graph updates after a new radar measurement cycle is processed, the iSAM2 algorithm is used for efficiency [187]. While for point-shaped landmark associations the corresponding factors are always map-matched and incorporated into the factor graph, line-shaped landmark observations are only considered in every 10^{th} cycle or when the number of point-shaped associations falls short of five. This reduces the overall computational burden with fewer evaluations of the more costly line-shaped landmark matching and a lower number of graph factors and variables. However, the self-localization performance is not impaired as was experimentally validated. While algorithmic feasibility for deploying on an in-vehicle compute unit was taken into account, the focus of the experiments was not on a real-time implementation of the whole self-localization framework. Contrary to the real-time capable GPU-accelerated signal processing (cf. Section 3.1), the self-localization experiments are evaluated offline via Python.

Table 6.4: Factor implementations and information matrices

Factor	GTSAM Implementation	Information Matrix
$\mathbf{f}^{\mathbf{x}}$	`PriorFactorPose2`	$\mathbf{P}^{\mathbf{x}} = \operatorname{diag}\left({\sigma_{\mathbf{x}_\mathrm{T}}}^2, {\sigma_{\mathbf{x}_\mathrm{T}}}^2, {\sigma_{\mathbf{x}_\psi}}^2\right)^{-1}$
$\mathbf{f}^{\mathrm{l^p}}$	`PriorFactorPoint2`	$\mathbf{P}^{\mathrm{l^p}} = \operatorname{diag}\left({\sigma_{\mathrm{l^p}}}^2, {\sigma_{\mathrm{l^p}}}^2\right)^{-1}$
$\mathbf{f}^{\mathrm{l}}$	`PriorFactorPoint2`	$\mathbf{P}_l^{\mathrm{l}} = \left(\mathbf{R}_l \operatorname{diag}\left(\left(\kappa_{\mathrm{l}}\sigma_{\mathrm{l^p}}\right)^2, {\sigma_{\mathrm{l^p}}}^2\right)\mathbf{R}_l^T\right)^{-1}$ rotation $\mathbf{R}_l$ according to Fig. 6.4
$\mathbf{f}^{\mathbf{x},\mathbf{x}}$	`BetweenFactorPose2`	$\mathbf{P}^{\mathbf{x},\mathbf{x}} = \operatorname{diag}\left({\sigma_{\mathbf{x},\mathbf{x}_\mathrm{T}}}^2, {\sigma_{\mathbf{x},\mathbf{x}_\mathrm{T}}}^2, {\sigma_{\mathbf{x},\mathbf{x}_\psi}}^2\right)^{-1}$
$\mathbf{f}^{\mathbf{x},\mathrm{l^p}}$	`BearingRangeFactor2D`	$\mathbf{P}^{\mathbf{x},\mathrm{l^p}} = \operatorname{diag}\left({\sigma_{\mathbf{x},\mathrm{l^p}_\theta}}^2, {\sigma_{\mathbf{x},\mathrm{l^p}_\mathrm{R}}}^2\right)^{-1}$

Table 6.5: Self-localization parameters used for the evaluation

Parameter	Value	Parameter	Value
$d^{\mathrm{lP}}_{\mathrm{thres}}$	0.3 m	$N^{\mathrm{lP}}_{\mathrm{thres}}$	2
$d^{\mathrm{l}}_{\mathrm{ch,thres}}$	0.09 m	$d^{\mathrm{l}}_{\mathrm{prj,thres}}$	1.5 m
$\sigma_{\mathbf{x}_{\mathrm{T}}}$	0.1 m	$\sigma_{\mathbf{x}_\psi}$	0.1 rad
$\sigma_{\mathbf{l}^{\mathrm{P}}}$	0.1 m	$\kappa_{\mathbf{l}^{\mathrm{l}}}$	10
$\sigma_{\mathbf{x},\mathbf{x}_{\mathrm{T}}}$	0.05 m	$\sigma_{\mathbf{x},\mathbf{x}_\psi}$	0.01 rad
$\sigma_{\mathbf{x},\mathbf{l}^{\mathrm{P}}{}_\theta}$	0.03 rad	$\sigma_{\mathbf{x},\mathbf{l}^{\mathrm{P}}{}_{\mathrm{R}}}$	0.5 m
T_{graph}	1 s		

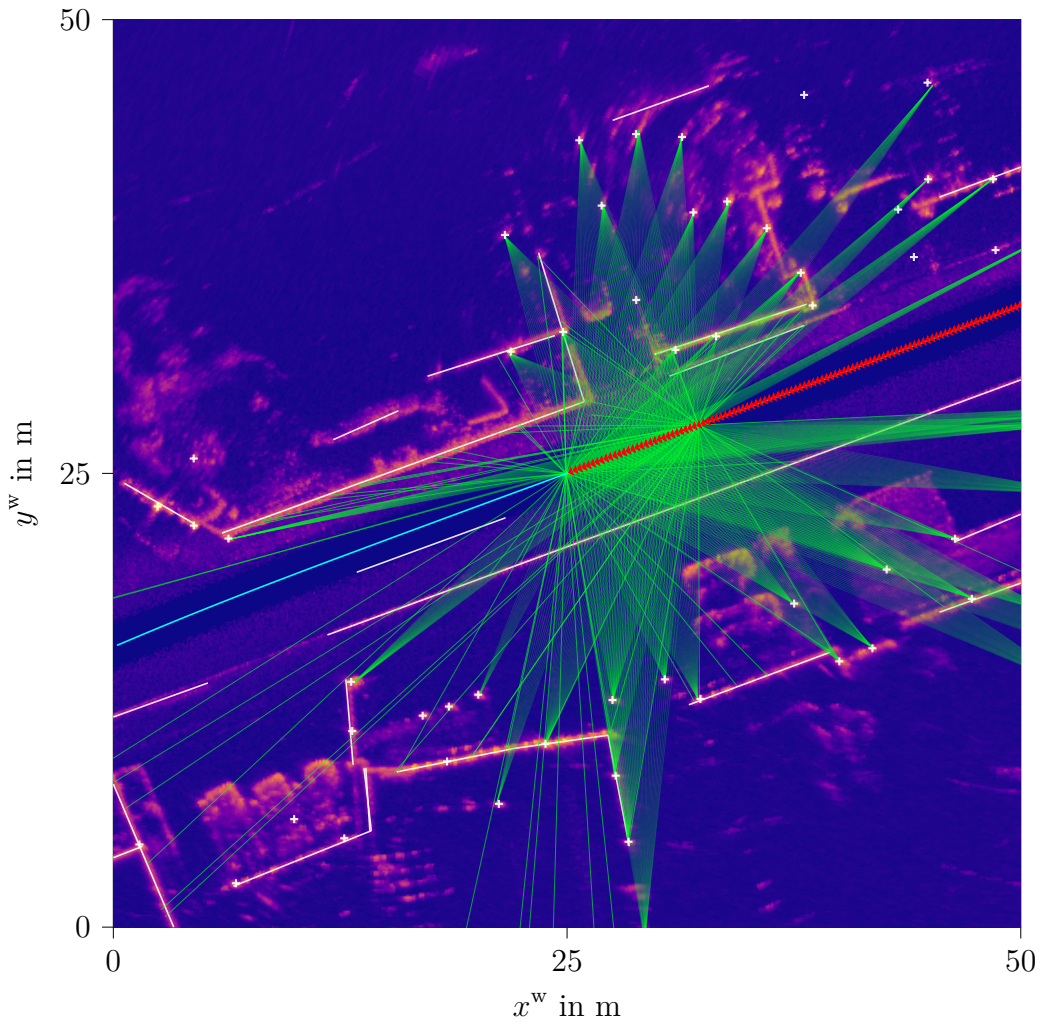


Figure 6.5: The ego-poses (red) are close to the ground truth trajectory (cyan) in this successful self-localization example. Observations of point- and line-shaped landmarks (white) are visualized in green.

An example of how an actual self-localization state looks like is provided by Fig. 6.5. A PreCFAR amplitude gridmap in the background and the point- and line-shaped landmarks (white) allow orienting in the scenario. The ground truth pose of the whole pass is plotted in cyan and serves as a reference. The localization is run up to an ego-vehicle position in the middle of the graph. Red triangles indicate the ego-pose history to this point. Associated observations of the landmarks are connected to the corresponding observing ego-pose. The limited ego-position extent with landmark observations is result of the temporal window of the factor graph.

6.3.3 Fully polarimetric results

The self-localization quality is quantified by absolute trajectory errors in this study. Dropping the pose index for brevity, an arbitrary planar pose $\mathbf{x} \in \mathrm{SE}(2)$ is composed of a rotation $\mathbf{R} \in \mathrm{SU}(2)$ and a translation $\mathbf{t} \in \mathbb{R}^2$ with $\hat{\cdot}$ denoting the estimated and $\cdot_{\mathrm{gt}}$ the ground truth quantities. Then, the three absolute trajectory error components in longitudinal, lateral and rotational directions $\varepsilon_{\mathrm{lon}}$, $\varepsilon_{\mathrm{lat}}$, ε_{ψ} can be derived by

$$\boldsymbol{\varepsilon}_{\mathbf{t}} = \begin{pmatrix} \varepsilon_{\mathrm{lon}} \\ \varepsilon_{\mathrm{lat}} \end{pmatrix} = \mathbf{R}_{\mathrm{gt}}^{-1} \left(\hat{\mathbf{t}} - \mathbf{t}_{\mathrm{gt}} \right) \qquad \text{and} \qquad \varepsilon_{\psi} = \arccos\left(\frac{1}{2} \operatorname{tr}\left(\mathbf{R}_{\mathrm{gt}}^{-1} \hat{\mathbf{R}} \right) \right). \tag{6.4}$$

The error components are calculated for all self-localization cycles, in which high quality carrier phase solutions are available. Other cycles with lower quality ground truth information are left out to avoid considering ground truth errors as localization inaccuracies. Furthermore, a minimum ego-vehicle velocity of $0.5\,\mathrm{m\,s^{-1}}$ is required for inclusion in the error calculation so that standstill phases, e.g., longer stops at traffic lights, do not influence the error statistic disproportionately.

The resulting trajectory errors for all passes in the three environments are provided in Table 6.6. Fully polarimetric information is used for these results. Trajectory errors are summarized by combining the results of all relevant cycles to two performance figures, RMSE and maximum. Moreover, the percentage of cycles with high quality ground truth data per pass is included. Comparing the two translational errors across all passes, significantly lower errors are observed for the lateral direction. The consistency over all passes and environments suggests a generally higher performance in the lateral direction. Such an observation cannot be made in general from the related literature mentioned in Section 6.1. Therefore, one can assume that the effort spent for a high-quality extraction of line-shaped landmarks enabled by exploiting the PreCFAR data level is at least part of the reason for the accurate results. While a sufficient number of point-shaped landmarks might not always be given (discussed below), an automotive environment typically exhibits some form of road boundaries, such as curbstones, guardrails, Jersey barriers or road verges. Thus, the chance of absence of such infrastructure suitable for lateral localization is quite low, which leads to the lower errors compared to the longitudinal direction.

Table 6.6: Localization performance using fully polarimetric information

Route	**Pass**	**High qual. DGNSS**	**longitudinal** (ε_{lon})		**lateral** (ε_{lat})		**rotational** (ε_{ψ})	
			RMSE	max	RMSE	max	RMSE	max
Frankfurt ($\mathcal{R}_{\text{Fra}}$)	#1	76 %	0.12 m	0.84 m	0.06 m	0.45 m	0.44°	2.77°
	#2	84 %	0.11 m	0.74 m	0.06 m	0.37 m	0.45°	2.91°
	#3	87 %	0.15 m	1.29 m	0.06 m	0.49 m	0.48°	3.83°
Ingolstadt ($\mathcal{R}_{\text{Ing}}$)	#1	91 %	0.08 m	0.36 m	0.05 m	0.29 m	0.39°	2.57°
	#2	93 %	0.09 m	0.34 m	0.05 m	0.39 m	0.41°	2.92°
	#3	92 %	0.08 m	0.37 m	0.05 m	0.38 m	0.37°	2.69°
Ulm ($\mathcal{R}_{\text{Ulm}}$)	#1	87 %	0.13 m	0.76 m	0.06 m	0.46 m	0.46°	2.67°
	#2	85 %	0.13 m	0.73 m	0.06 m	0.25 m	0.45°	1.81°
	#3	85 %	0.10 m	0.43 m	0.06 m	0.34 m	0.44°	2.30°

Although the order of routes in Table 6.6 is the same as in Table 6.3, where a sorting according to the average number of landmarks per kilometer route length is present, no direct one to one correlation with the order of trajectory errors can be made. This is due to the fact that the landmarks are not distributed uniformly, as will be shown below. However, all trajectory errors of $\mathcal{R}_{\text{Ing}}$ are repeatedly the lowest. This finding suggests the presence of both a more favorable distribution and a higher density of landmarks in this area compared to the other two.

An analysis of the spatial distribution of the translational trajectory errors allows understanding the cause for some observations. Fig. 6.6 visualizes this for the pass #3 for $\mathcal{R}_{\text{Ulm}}$. Apart from the overall error dominance of the longitudinal component, the areas of increased trajectory errors can be identified. Correlating this observation with the available map landmarks in this area in Fig. 6.7 reveals the cause for the increased longitudinal trajectory error. While a sufficient density of line-shaped landmarks prevents significant errors in the lateral direction, the number of point-shaped landmarks is very low resulting in estimates with higher longitudinal errors.

6.3.4 Impact of polarimetric information

With the recorded data set being fully polarimetric, the analysis of the impact of different polarimetric data levels and representations can be executed in post-processing by a basis transformation and sub-sampling of the polarimetric channels. The basis transformation of polarimetric covariance matrices can be derived from the scattering matrix transformation in Section 2.3.5 and the definition of the covariance [188]. Because quite some polarimetric prototype systems are built based on linear basis antennas (cf. Table 3.1), the circular basis data is transformed to this basis for additional experiments with a subsequent sub-sampling. For the fully polarimetric case, it can be shown that the Wishart distance is identical for the representations in both bases so that only the result in the circular basis is included in the following results for conciseness.

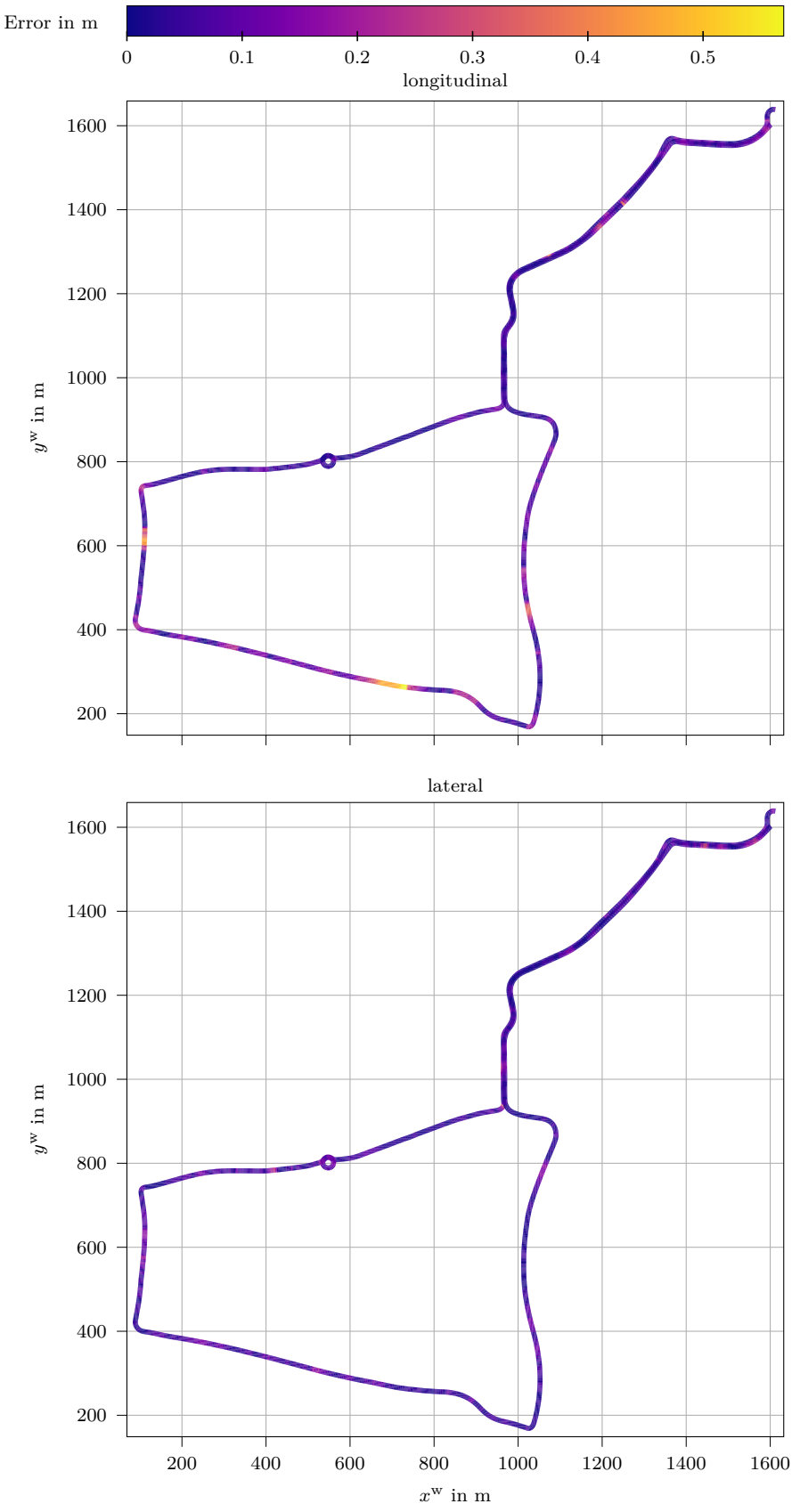


Figure 6.6: The spatial distribution of translational trajectory errors allows identifying areas with increased errors for pass #3 of $\mathcal{R}_{\mathrm{Ulm}}$. Adapted from [**71**], © 2024 IEEE.

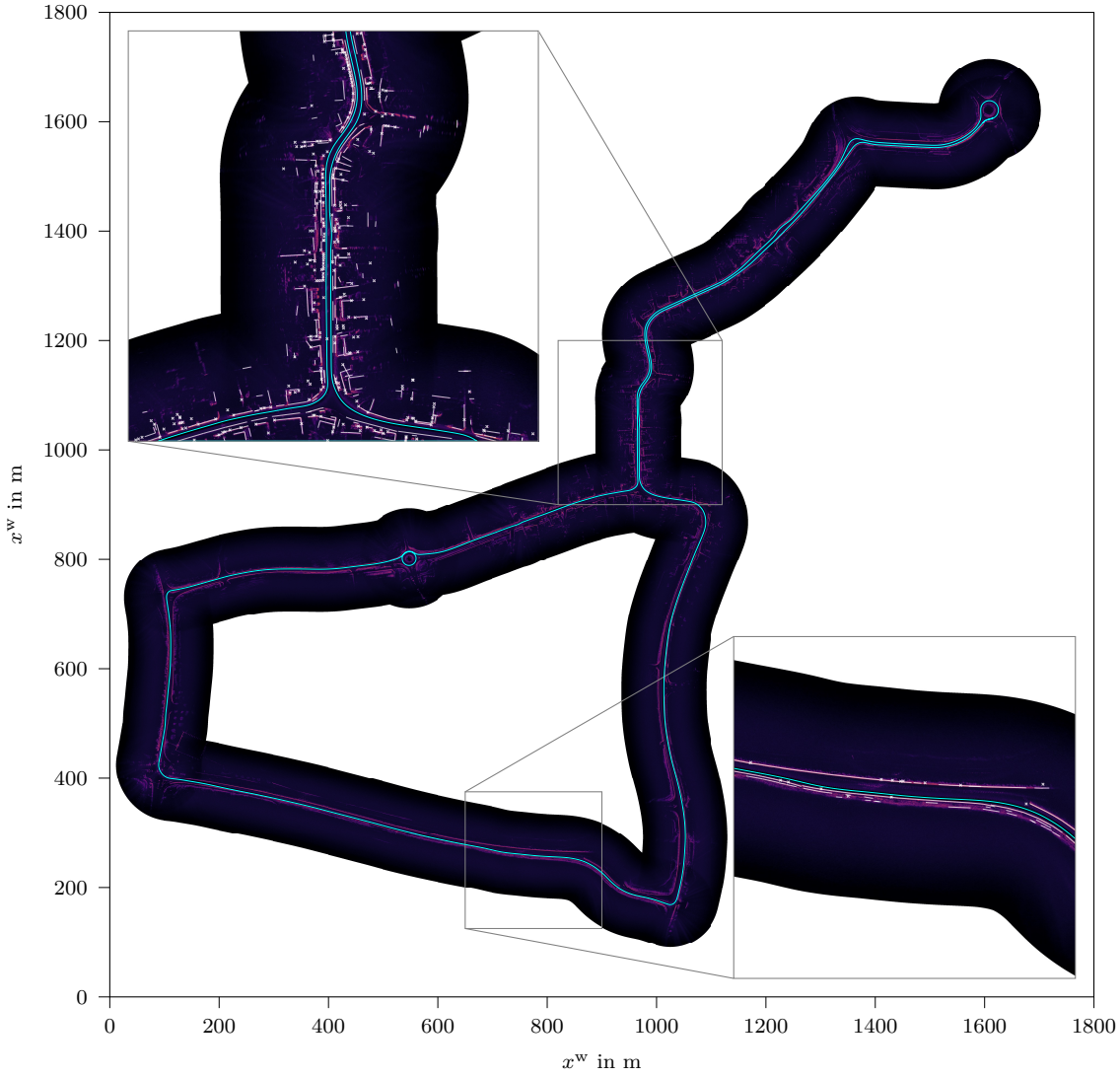


Figure 6.7: The PreCFAR amplitude gridmap shows the distribution of reflectivity from the infrastructure (best viewed on screen, high-resolution imagery allows substantial zooming). For exemplary excerpts, the corresponding map landmarks are visualized in white. A sizeable difference in landmark density depending on the location in the environment can be observed. Adapted from [**71**], © 2024 IEEE.

Sub-sampling to lower levels of polarimetric data is implemented by truncation. The consequence of this sub-sampling is that in comparison to a new recording with the corresponding polarimetric configuration already set for acquisition, one the one hand, a lower unambiguous Doppler domain arises and, on the other hand, a reduced sensitivity results. The polarimetric channels removed by truncation could have been filled with additional samples of the targeted polarimetric channel. However, the effects on the localization performance are assumed to be negligible. With the proposed Nyquist zone augmentation, the ego-motion estimation already works sufficiently well for the small unambiguous Doppler domain in the fully polarimetric experiments. Moreover, point-shaped landmarks, which are at the sensitivity limit, are not robust so that a very limited impact is expected. Due to the distribution of

the scattering centers for line-shaped landmarks, the received power at every grid cell might be rather low so that a reduced sensitivity would potentially have the most impact for them. However, a subsequent analysis of the lateral errors shows no general deterioration for lower polarimetric data levels, so that the validity of the sub-sampling approach can be assumed. Accordingly, only the reduced polarimetric information and dimensionality ν is used in the Wishart distance calculation for both the map creation and landmark candidate extraction during localization. For the single-polarimetric cases, this means the calculations are purely real amplitude-based and no extraction of unique scattering in a similar amplitude neighborhood is possible. The relative phases between the polarimetric channels as part of the features for distinguishing scattering behavior are considered starting with the combinations of at least two channels ($\nu \geq 2$).

Complementary cumulative distribution functions (CCDFs) are the means of choice for comparing the trajectory errors. A CCDF curve gives the probability of how often the trajectory error exceeds a specific value. A logarithmic scaling of the secondary axis is chosen to make the distribution of larger trajectory errors better readable. Furthermore, only some polarimetric combinations are selected to be included in the figures: Quad-polarimetric data, meaningful dual-polarimetric combinations for both bases and reasonable single-polarimetric channels for both bases are shown. For dual-polarimetry, the channel combinations, which allow differentiating between even- and odd-bounce scattering, are chosen. Single-polarimetric experiments of the linear cross-polarized channels (HV and VH) are omitted due to the rarity of such scatterers and consequently bad localization results.

Starting with $\mathcal{R}_{\mathrm{Ing}}$, for which best localization performance was already observed with availability of fully polarimetric data before, the CCDFs of all three passes combined in Fig. 6.8 show no significant variations for the different polarimetric data levels except for the single-polarimetric even-bounce channel RR. This finding suggests that the distribution and number of landmarks in this environment are already sufficient for an accurate self-localization even without more robust landmarks from a scattering-based extraction enabled by more polarimetric information. The occurrence of the RR outlier with noticeably worse longitudinal results can be adequately explained by considering the types of landmarks that are perceptible. Compared to all other polarimetric combinations, the sole RR channel is the only one incapable of perceiving odd-bounce scattering (if you ignore the finite XPD). Recalling the findings in Section 5.3.2, the majority of point-shaped landmarks are scatterers dominated by odd-bounce mechanisms. Consequently, even-bounce-only sensing will not detect many of the landmarks leading to the observed lower localization performance.

While this result shows no advantage of the more robust polarimetry-assisted landmarks for the self-localization performance, the assessment changes for the the more difficult environment of $\mathcal{R}_{\mathrm{Ulm}}$. The joint distribution of trajectory errors for all three passes on this route is shown in Fig. 6.9. Again, ignoring the exceptional RR channel until noted otherwise, a comparison of the lateral and rotational trajectory errors between the different polarimetric combinations reveals comparable results. Because both the lateral and rotational directions are impacted most by line-shaped landmarks parallel to the course of the road, this observation of independence from the level of sub-sampled polarimetric information is evidence for the hypothesis that

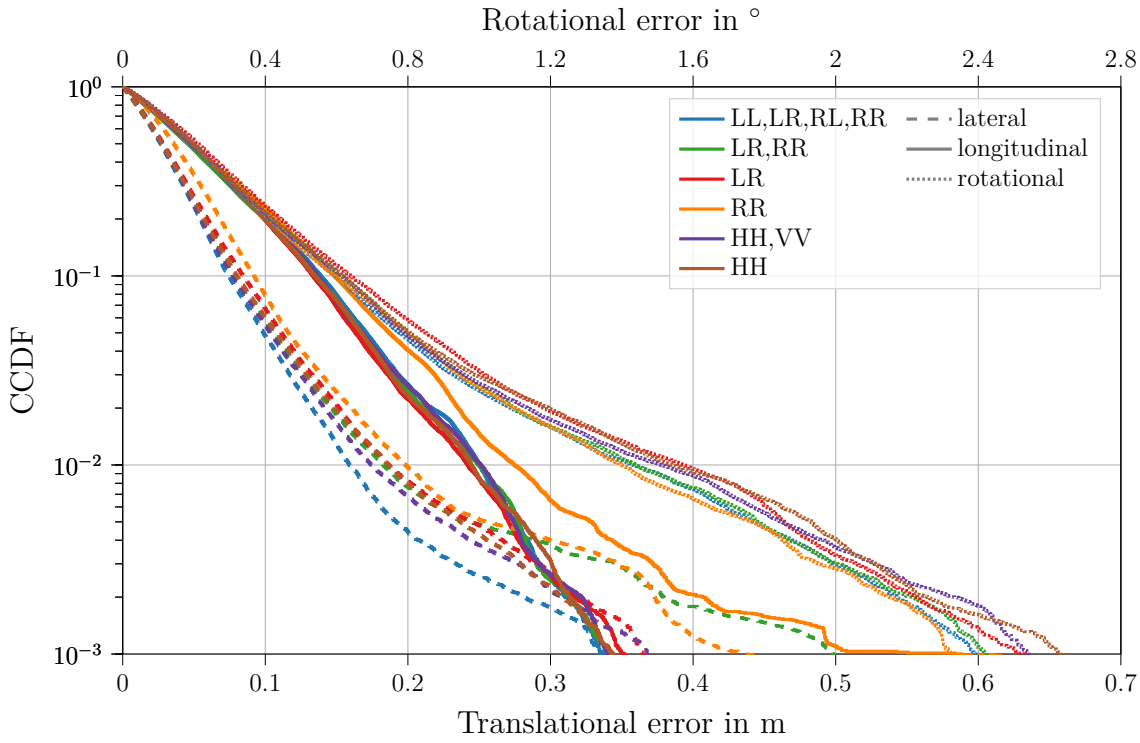


Figure 6.8: The distribution of trajectory errors accumulated over all three passes along $\mathcal{R}_{\text{Ing}}$ shows no significant performance difference depending on the polarimetric data level used, except for the even-bounce channel RR. Adapted from [**71**], © 2024 IEEE.

the extraction of line-shaped landmarks is not primarily limited by sensitivity in the utilized PreCFAR implementation. Thus, the sub-sampling approach by truncation is assumed valid. The crucial differences are observed in the longitudinal trajectory errors. Sorting the polarimetric combinations according to the observed longitudinal errors, which are for example not exceeded in 99 % of cases, one finds a conformity with the order of polarimetric information levels: the fully polarimetric experiment shows best results, followed first by dual-polarimetric and finally single-polarimetric combinations. This finding indicates that, in contrast to $\mathcal{R}_{\text{Ing}}$, there is no longer an abundance of landmarks robustly extracted solely by amplitude. Taking advantage of scattering mechanism discrimination with increasing levels of polarimetric information enables a larger number of correct landmark associations and a consequent reduction of errors. Evidence supporting this scattering-based differentiation advantage as the underlying reason can be further derived from the linear basis results. While the single-polarimetric HH channel can already perceive reflected power from odd- and 0°-even-bounce scattering landmarks, a significantly more accurate result is found by the dual-polarimetric combination, which is not able to perceive additional scatterer types. Thus, it strongly indicates that better landmark associations from more robust extractions are the reason for this. Lastly, the single-polarimetric even-bounce RR experiment results in a lateral error of approximately 2 m in the worst case, which must be considered unsuccessful for a safe navigation in an automotive context. The mismatch of the dominant scattering from the majority of

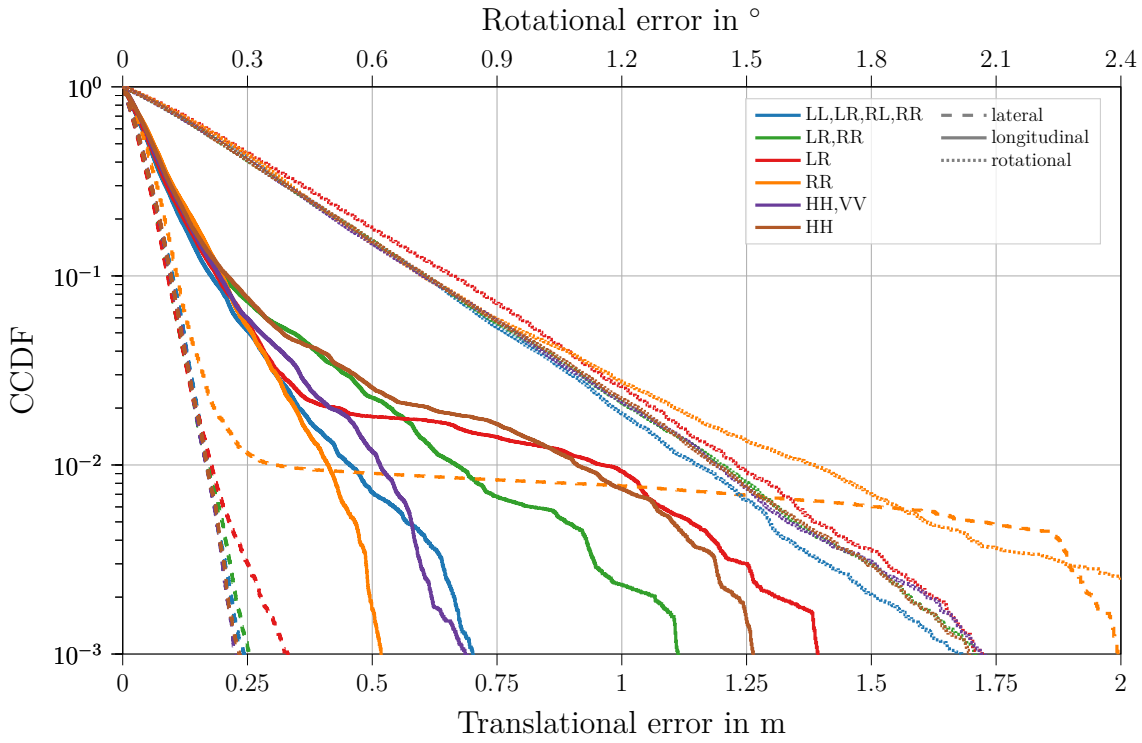


Figure 6.9: The distribution of trajectory errors accumulated over all three passes along $\mathcal{R}_{\text{Ulm}}$ shows a significant performance difference depending on the employed polarization level especially in the longitudinal direction. Adapted from [**71**], © 2024 IEEE.

typical landmarks with the perceptibility of this polarimetric channel was already mentioned as the probable cause. However, in longitudinal direction, the localization performance of this channel is partially even better than the fully polarimetric one. This might be explained by avoiding an ambiguous matching due to the generally lower number of landmarks with a matching polarimetric signature. The overall RR result must still be considered unsuccessful due to the other directions.

6.4 Summary

The remaining building blocks for realizing a radar-only landmark-based self-localization framework were introduced in this chapter. This included the generation of sparse landmark maps from repetitive passes through the areas of interest with a ground truth pose source. Spatial closesness of point- and line-shaped candidates from different passes was chosen as the criterium to create a landmark. The resulting maps served as the basis for the localization experiments. Extensions of known ego-motion estimation and multi-stage map matching approaches were discussed for completing the set of inputs required for the factor graph. This graph-based optimization is used as an efficient and powerful technique for estimating an optimal ego-pose as the result.
The implementation in GTSAM enabled an extensive study of experiments with more than 2.5 h real-world recordings form a variety of public road traffic environments. It was demonstrated that the landmark candidate extraction approaches introduced in the previous chapter are suitable for a precise self-localization. Furthermore, a proof has been provided that exploiting polarimetric information for landmark extraction does not only improve re-observation statistics but also is reflected in the localization accuracy. Especially the analysis of the longitudinal trajectory errors showed that: while some environments already allow a very high localization performance without additional polarimetric information due to an abundance of robust landmarks, the localization quality in more demanding environments, such as $\mathcal{R}_{\mathrm{Ulm}}$, clearly benefits from the more robust landmark extractions due to the polarimetric scattering information.

Chapter 7

Conclusion

Summary of contributions

The aim of this thesis was improving automotive self-localization applications by introducing polarimetry. Therefore, the majority of components in the processing chain were thoroughly considered: starting from the study of scattering mechanisms at potential landmarks, over an experimental vehicle setup with a specifically calibrated sensor set, to a new gridmap representation enabling a more robust landmark extraction and finally a self-localization framework. The initially formulated research objectives are recapitulated based on the contributions by this study in the following.

The first contribution consists of a simple but yet efficient compensation approach for several distortion sources occurring when applying polarimetry in automotive applications. This included techniques for ensuring the smallest possible systematic distortion due to azimuth angle and speed variations among others. Extensive measurements in an automated test facility were used to prove it. Moreover, the evaluation of recordings with an additional series-production radome as a secondary surface showed that standard packaging approaches do not stand in the way of bringing such technology onto the road.

Secondly, a series of measurements and corresponding evaluations were undertaken to better understand the scattering behaviors of typical automotive landmarks. On the one hand, overall reflectivity properties over varying incidence angles revealed that most landmarks exhibit strongly anisotropic behavior. Both reflectivities and observed scattering mechanisms differ significantly for changing angles. On the other hand, the ISAR imaging provided an even deeper insight into the spatial distribution of scattering centers including their corresponding mechanisms, which made an intuitive understanding more tangible.

Based on these findings, it was clear that the static environment representation must be able to handle this anisotropic behavior. The first proposed extension to the well-known gridmapping approach was introduced in form of polarimetric covariance matrix in each grid cell. This second order statistic enabled capturing the superposition of different measurements with potentially distinct scattering resulting from the integration over time and, hence, varying observation angles. Furthermore, the second suggested extension, termed PreCFAR gridmapping, comprised the incorporation of low-level spectral data into the gridmap. Avoiding the masking inherent to any detection-based mapping allowed using all received power from stationary reflectors for an environment representation that is as complete as possible. The resulting polarimetric PreCFAR gridmaps were designed from the beginning with the intention of a robust landmark extraction in the subsequent component in the self-localization stack.

The landmark extraction algorithms are therefore heavily dependent on the proposed gridmap representation. Point-shaped landmark candidates were extracted based on the Wishart distance measure of a cell under test to its spatial neighborhood. Thus, characteristic uniqueness of both the amplitude or the scattering mechanism can be detected. Quantitative evaluations showed higher re-observation rates with an increasing amount of polarimetric information. A correlation with the available HD maps revealed what type of point-shaped landmarks are most suitable for radar. For line-shaped landmarks, a superiority of the PreCFAR-generated map over the common detection-based generation was found: resulting maps as a consensus over multiple passes of the same environment included a more than four times longer set of landmarks for the PreCFAR variant.

A full radar-only self-localization framework was then implemented based on the robust landmark extractors. The radar landmark maps were created by finding spatially close landmark candidates from multiple passes. In a localalization run, the same extraction algorithms were employed in a mono-modal fashion. A well-known radar-based ego-motion estimator was adapted to handle the low unabigous Doppler domain inherent to most fully polarimetric operation modes. Landmark candidates and the ego-motion estimates were input to a multi-stage map matching module for a robust association between map landmarks and online observations. The final pose was result of an efficient factor graph optimization and compared to ground truth pose data for evaluating the self-localization accuracy. A validation based on extensive real-world recordings from public road traffic in diverse environments showed accurate results when fully polarimetric data is used. Due to the high-quality line-shaped landmark extractions and their dominant orientation, the lateral accuracy was always better than 50 cm with an overall RMSE of 6 cm. Longitudinal errors were generally slightly larger with an RMSE of 11 cm and occurred in areas of low point-shaped landmark density. This was also where the main difference between the various polarimetric data levels became apparent: in environments with an abundance of unambiguously associated landmarks, no relevant loss in localization accuracy occurred for an decreasing amount of polarimetric scattering information. However, the more robust landmarks from experiments with higher levels of polarimetric information caused more accurate results in more challenging environments.

Thus, the main research question regarding the potential benefits of polarimetry in self-localization applications of automated vehicles can be answered in the affirmative. As a result, this study's findings contribute to a safer navigation in challenging environments.

Outlook

While this work presented an extensive starting point for leveraging radar polarimetry in self-localization applications, the broad competition of ideas and approaches in this research field is pending due to compact sensor implementations becoming realistic only recently. This thesis leaves a series of obvious subsequent investigations unconsidered that are worth examining in future work. Some promising ones are listed in the following.

One direction for further research is the utilization of cross-modal HD maps. In this study, the types of landmarks in the radar-derived maps were intentionally kept abstract in form of purely geometrical properties so that other modalities for mapping are conceptually close. In this context, it would be particularly interesting to demonstrate whether the map incorporation of specific landmarks, for which the extraction specifically benefits from polarimetry, such as fence posts, improves the localization performance. Proving cross-modal map suitability would pave the way for a quicker large-scale deployment due to simpler mapping efforts.
Another approach for improvements could be the usage of machine learning in different parts of the framework. Proven as indispensable for state of the art performance in classifying other road users, machine learning could also be applied for classification of landmarks. Apart from enriching the information about surroundings semantically for a safe path planning, a less ambiguous association between classified measurements and a semantic map can be expected. Moreover, the map matching itself might benefit from a learning-based implementation as already proposed for lidar among others in literature.
While the limitation to a purely geometry-based landmark information in this study was intentional, a competing approach could additionally use the polarimetric covariance information as a descriptor. Although this would require polarimetric recordings during mapping, a faster convergence from a starting pose with a large uncertainty could result due to an increased probability of correct map matches. For this approach to be effective, however, the stability of the polarimetric descriptors over a longer period of time must be proven first.
Due to the missing elevation measurement capability of the utilized sensors in this thesis, the localization was limited to a two dimensional plane. However, polarimetry could also benefit the real-world elevation estimation due to the capability to distinguish between different multipath responses. Thus, the elevation-distorting impact of the superposition of different propagation paths with the road acting as a mirror can potentially be alleviated. Accordingly, more accurate elevation estimates can potentially result thanks to polarimetry, which in turn could positively impact a three dimensional self-localization.
In summary, the findings and techniques presented in this work lay the solid foundation for applying polarimetry to self-localization of intelligent transportation systems. The gap of a systematic approach to it in public road traffic is closed. Future work can build on this basis to advance this research field.

Appendix A

Approximation of the FMCW signal model for a moving object

In Section 2.1.2, the intermediate frequency signal model for a moving target in case of FMCW modulation is required. Inserting the signal propagation time delay for a moving object $\tilde{\tau}$ from (2.9) into the IF signal $\underline{s}_{\mathrm{IF}}$ (2.5), it results in

$$\underline{s}_{\mathrm{IF}}(t) = \exp\left(\frac{\mathrm{j}4\pi}{c}\left(r_0\left(\frac{\rho r_0}{c} - f_0\right) + \left(\left(\frac{2\rho r_0}{c} - f_0\right)v_{\mathrm{r}} - \rho r_0\right)t + v_{\mathrm{r}}\rho\left(\frac{v_{\mathrm{r}}}{c} - 1\right)t^2\right)\right) \tag{A.1}$$

as derived in Section 2.1.1 in (2.10). The resulting signal consists of a first phase term, a second complex constant frequency term and a third chirp term. With the same approximation as in (2.9) ($v_{\mathrm{r}} \ll c$), the chirp term can be simplified to

$$\exp\left(\frac{\mathrm{j}4\pi}{c}v_{\mathrm{r}}\rho\left(\frac{v_{\mathrm{r}}}{c} - 1\right)t^2\right) \approx \exp\left(-\frac{\mathrm{j}4\pi}{c}v_{\mathrm{r}}\rho t^2\right). \tag{A.2}$$

For the phase and the constant frequency term, the ratio between $\rho r_0/c$ and f_0 offers the potential for another approximation. Considering the ratio

$$\rho = \frac{\frac{\rho r_0}{c}}{f_0} = \rho\frac{r_0}{cf_0} \overset{(2.1)}{=} \frac{B}{T_{\mathrm{chirp}}}\frac{r_0}{cf_0} \tag{A.3}$$

and taking into account that for an automotive radar in the band of interest, there is an absolute maximum bandwidth of 5 GHz starting at 76 GHz available from a regulatory standpoint, it follows

$$\rho \leq \frac{5\,\mathrm{GHz}}{76\,\mathrm{GHz}}\frac{r_0}{cT_{\mathrm{chirp}}} \overset{(2.9)}{=} \frac{5\,\mathrm{GHz}}{76\,\mathrm{GHz}}\frac{\tau_0}{2T_{\mathrm{chirp}}}. \tag{A.4}$$

In order to have a sufficient overlap of the transmitted and received chirp for a feasible sensitivity, even for the largest range, one can assume $\tau_0 \leq 0.1\,T_{\mathrm{chirp}}$. In addition, the limited maximum sample rate of the ADC as well as a limited chirp rate justify this assumption. Then,

$$\rho \leq \frac{5\,\mathrm{GHz}}{76\,\mathrm{GHz}}\frac{0.1\,T_{\mathrm{chirp}}}{2\,T_{\mathrm{chirp}}} = 0.33\,\% \tag{A.5}$$

even in a worst case such that $\rho r_0/c \ll f_0$ is valid. For each of the terms in (A.1), simplifications can be applied as follows leading to the approximation

$$\begin{aligned}\underline{s}_{\mathrm{IF}}(t) = \exp\Bigg(\frac{\mathrm{j}4\pi}{c} \quad & \Bigg(r_0 \underbrace{\left(\frac{\rho r_0}{c} - f_0\right)}_{(\mathrm{A}.5)} + \\ & \underbrace{\left(\left(\frac{2\rho r_0}{c} - f_0\right)}_{(\mathrm{A}.5)} v_{\mathrm{r}} - \rho r_0\Bigg) t + \\ & \underbrace{v_{\mathrm{r}}\rho\left(\frac{v_{\mathrm{r}}}{c} - 1\right) t^2}_{(\mathrm{A}.2)}\Bigg)\Bigg) \\ \approx \exp\left(-\frac{\mathrm{j}4\pi}{c}\left(r_0 f_0 + \left(f_0 v_{\mathrm{r}} + \rho r_0\right) t + v_{\mathrm{r}}\rho t^2\right)\right).\end{aligned} \tag{A.6}$$

This approximation is used in (2.11). With $\lambda_c = \frac{c}{f}$, an alternative expression related to the wavelength results as

$$\underline{s}_{\mathrm{IF}}(t) \approx \exp\left(-\mathrm{j}4\pi\left(\frac{r_0}{\lambda_{c0}} + \left(\frac{v_{\mathrm{r}}}{\lambda_{c0}} + \frac{\rho r_0}{c}\right) t + \frac{v_{\mathrm{r}}\rho}{c} t^2\right)\right). \tag{A.7}$$

Appendix B

Partial ISAR images

By integrating the ISAR measurements over partial apertures only, some previously made assumptions about the scattering origin can be verified. Starting with the speed limit sign in Fig. B.1, the 18 images of 20° incident angle integration resemble the whole set of measurements. First, the anisotropic property of many scatterers can be observed. The sign plates are mainly observable for normal incidence, whereas an actual knife-edge diffraction of the plate's edges is confirmed by correlating the occurrence location with the incident direction. Thus, the mentioned limitation of cross-range separability must be taken into account for interpreting the results. Second, the triple-bounce scattering hypothesis located on the plate side opposite to the pole is further proven: significant scattering power in this area is observed for incidence angles under which such a mechanism is expected.
The stop sign measurement in Fig. B.2 is similar to the previous speed limit sign and is further evidence for the mentioned hypotheses. A minor difference can be observed in the relative power of the plate edge scattering, which is less pronounced for the stop sign. Moreover, the range side-lobes from orthogonal plate incidence are more regular due to a single instead of the two plates for the speed limit sign. Finally, the simulated stop sign data in Fig. B.3 results in the most clean images with a generally matching scattering distribution but without further new insights.

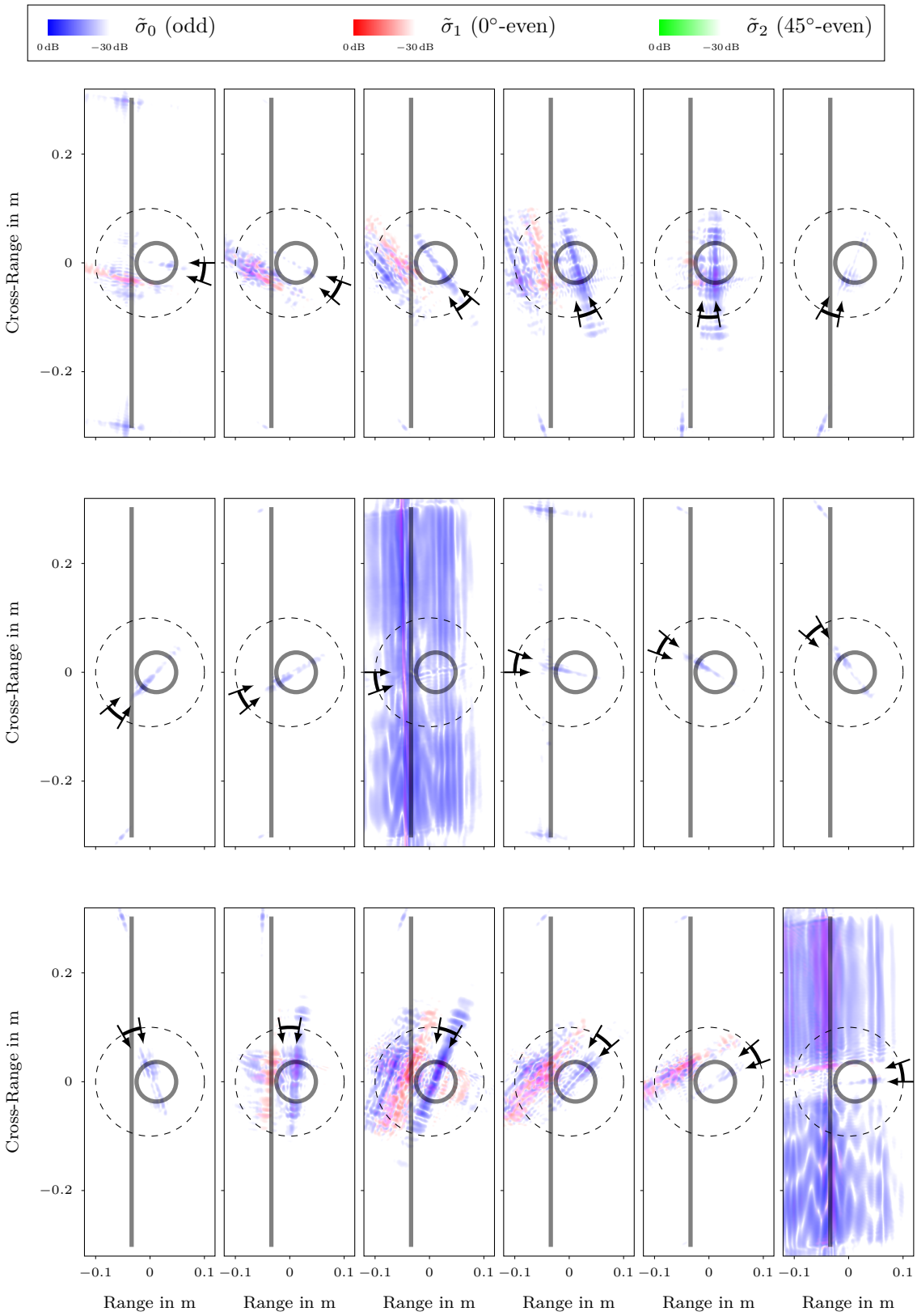


Figure B.1: By performing the ISAR imaging with 20° partial incident angle intervals only (shown by the arcs on the dashed circle), the origin of specific scattering can be related to physical structures in dependence of the incident angle. A Pauli decomposition with a 30 dB dynamic range of the speed limit sign is shown.

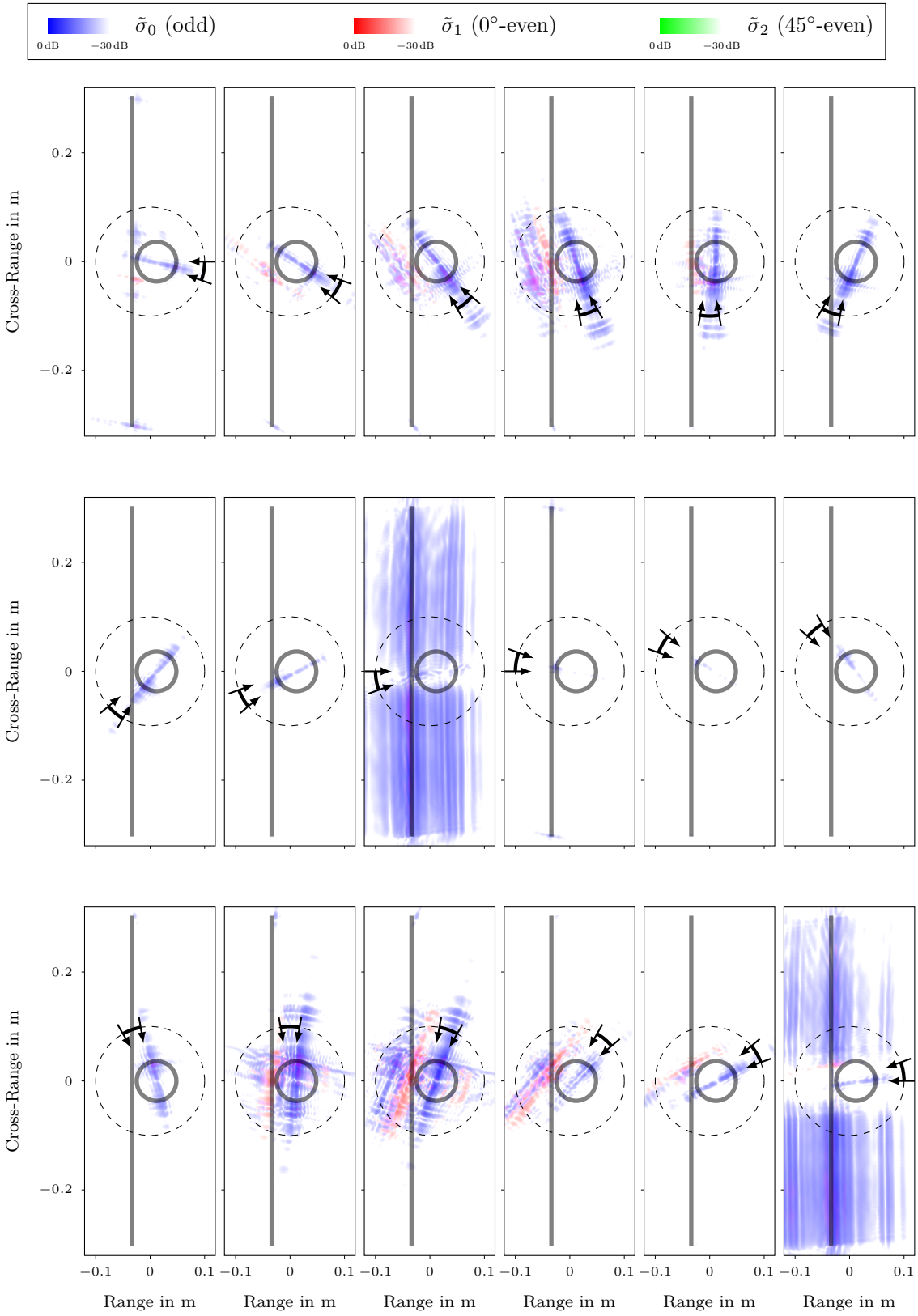


Figure B.2: The partial 20° ISAR imaging results of the stop sign measurement after Pauli decomposition allows associating observed scattering mechanisms to its structural origin.

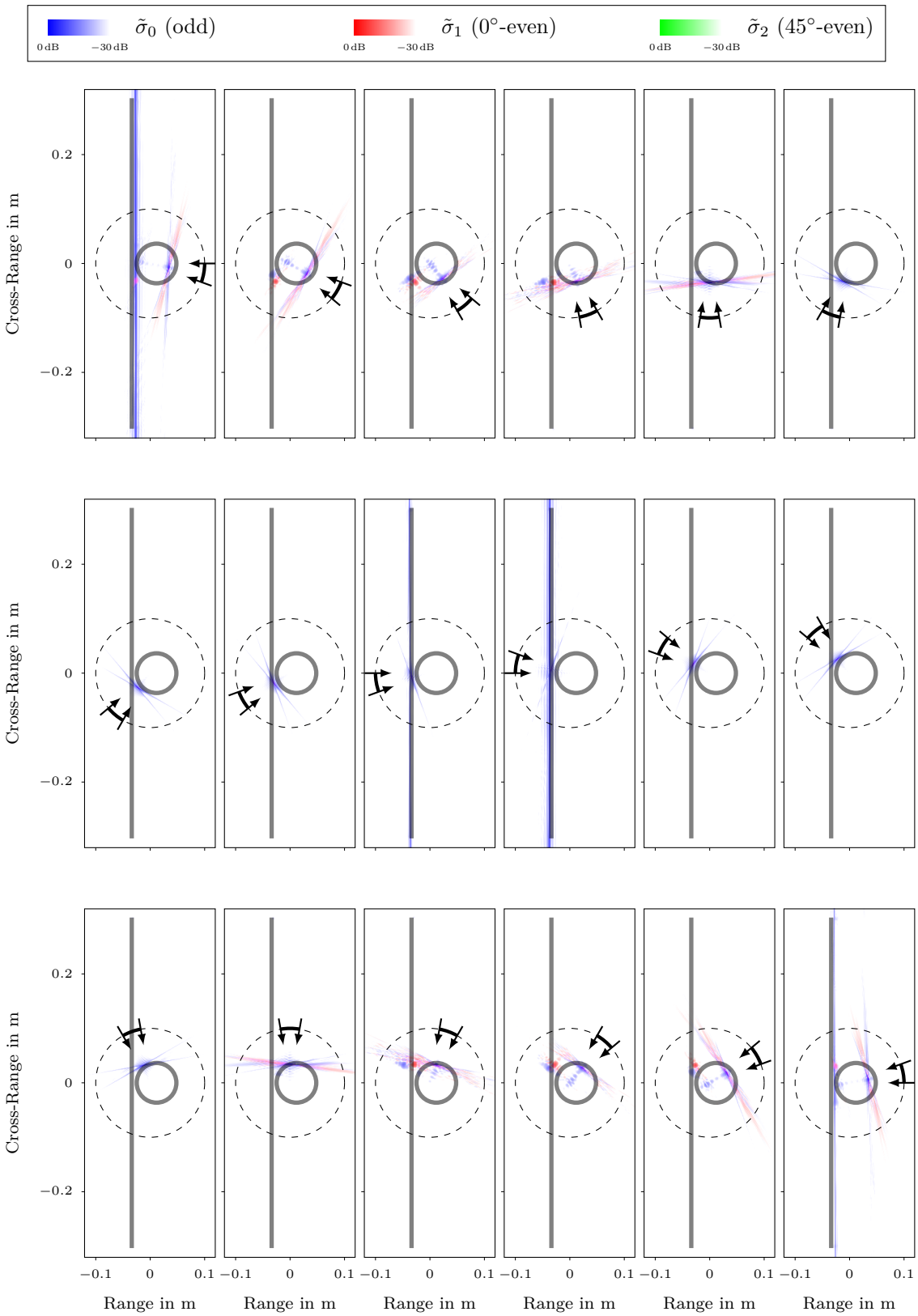


Figure B.3: The Pauli decomposition of partial ISAR images of the stop sign simulation confirm validity of the measurements results.

Appendix C

High turn rate PreCFAR maps

Some SAR approaches assume a specific motion type in order to simplify the computational steps for image formation. However, the proposed PreCFAR mapping approach works independently from a specific underlying motion model. For demonstration, a traversal of a round about with a high turn rate (which typically requires an additional extension in SAR imaging) is recorded and the standard processing is applied. The resulting PreCFAR maps for traversals in both directions are shown in Fig. C.1, where no systematic degradation occurs.

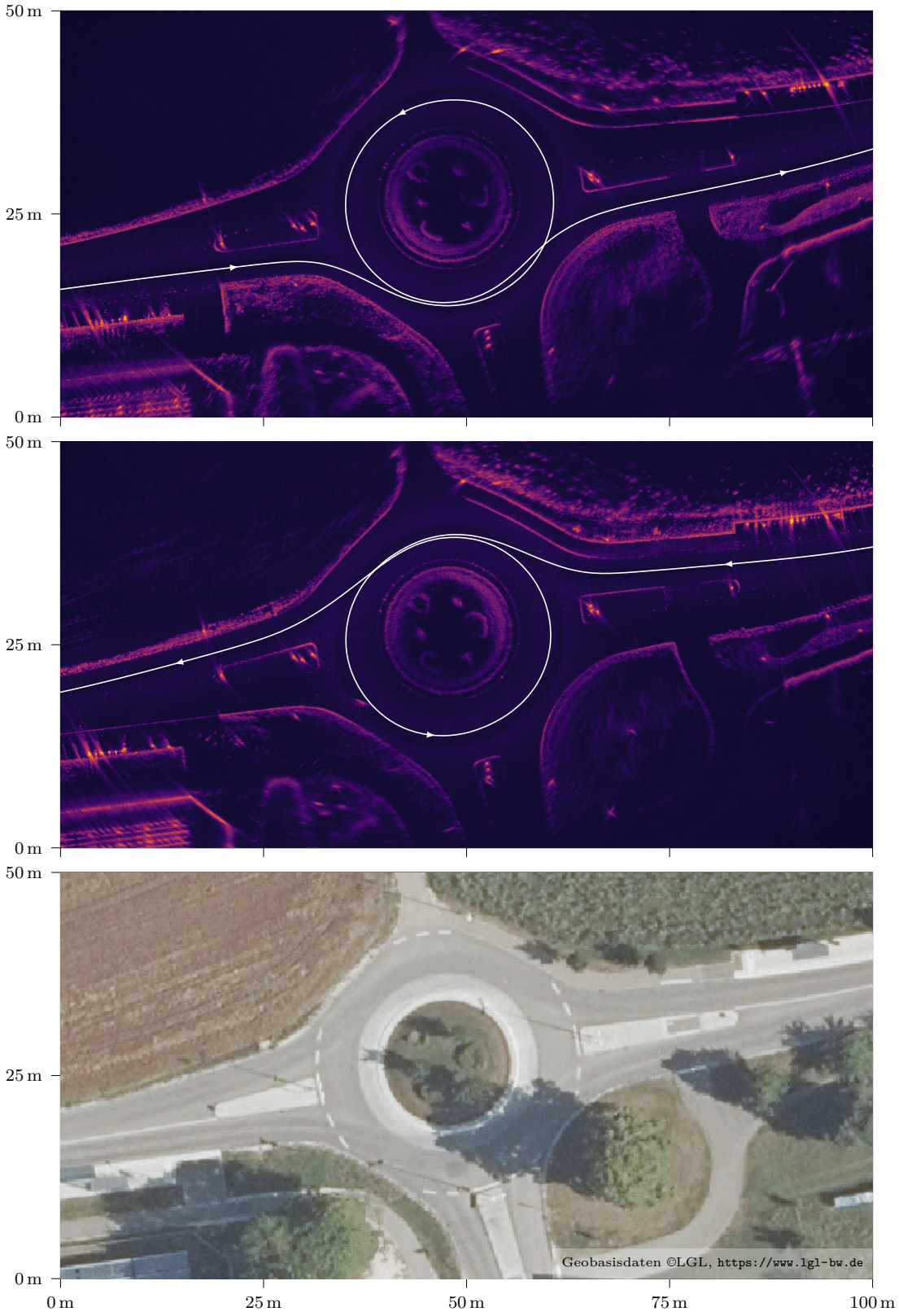


Figure C.1: Compared to SAR, the proposed PreCFAR approach does work without any modification also in high turn rate scenarios. Adapted from [**134**], © 2021 IEEE.

Appendix D

Point-shaped landmark detection in other environments

The evaluation of the quality of landmark candidates detected by the proposed technique and a classification of different landmark types are carried out for $\mathcal{R}_{\text{Ulm}}$ in Section 5.3.2. The self-localization experiments are also performed in other environments, such as the Frankfurt area $\mathcal{R}_{\text{Fra}}$, as detailed in Section 6.3.1.

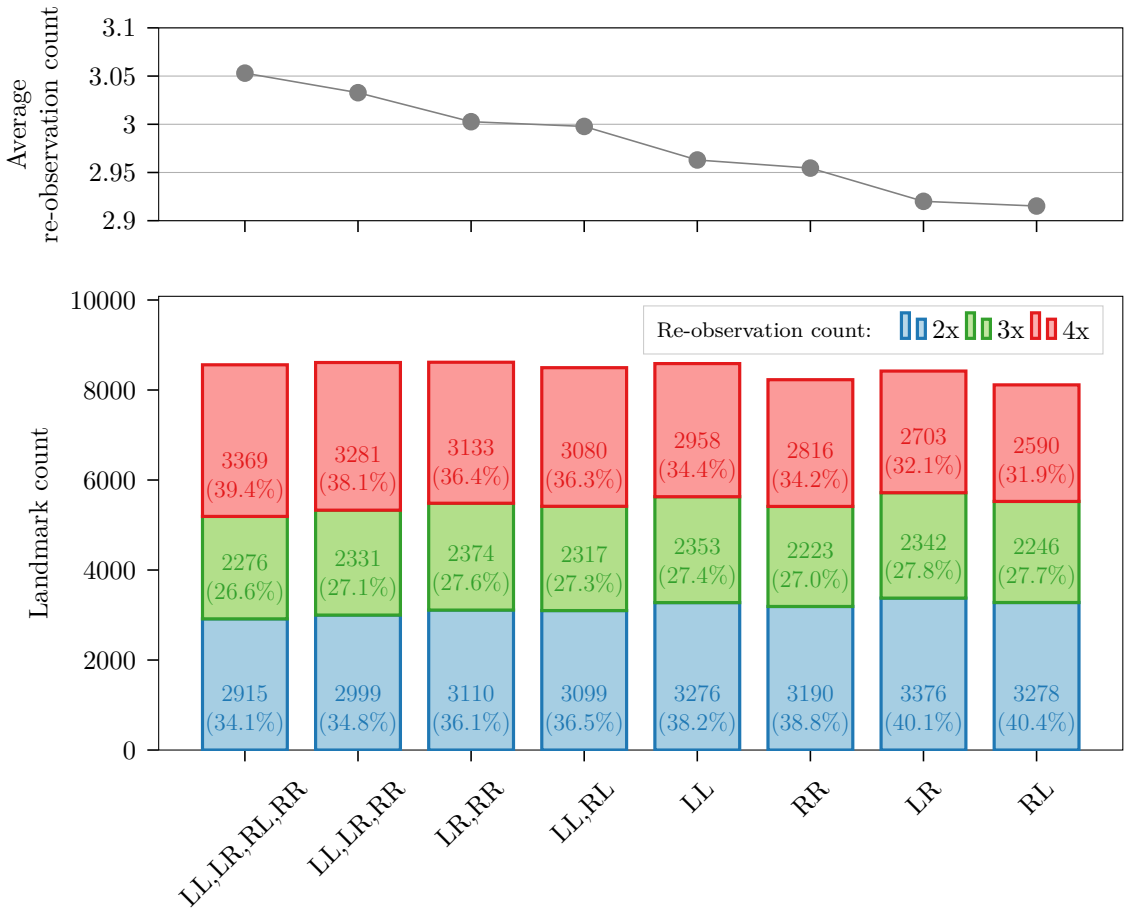


Figure D.1: The distributions of the numbers of re-observation and the average re-observation count for $\mathcal{R}_{\text{Fra}}$ shows similar results to the $\mathcal{R}_{\text{Ulm}}$ evaluation in Fig. 5.23. An increasing amount of polarimetric information results in more re-observations.

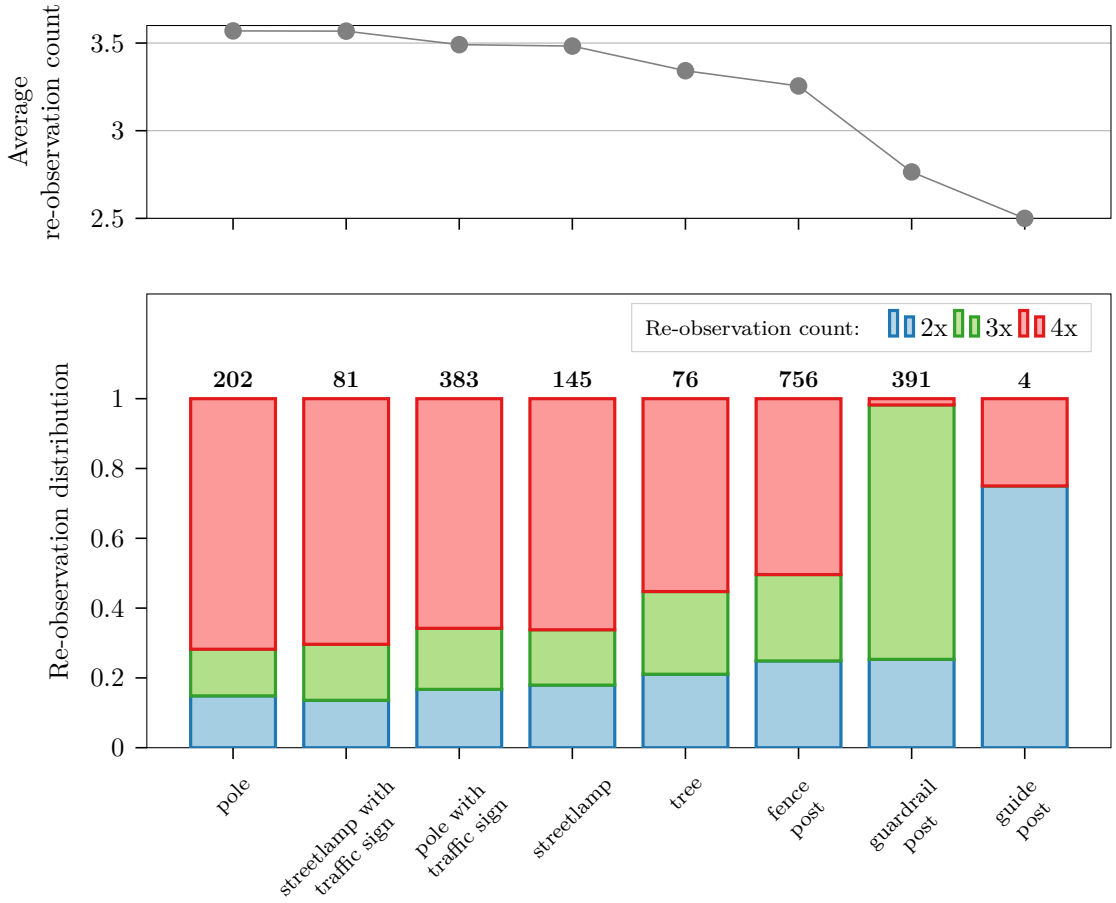


Figure D.2: The different types of landmarks for $\mathcal{R}_{\text{Fra}}$ show different re-observations statistics and, hence, different suitabilities for a self-localization.

Therefore, the same evaluation is executed for this environments. However, as no new insights can be gained and the results are only a confirmation of the observations already made, they are included in this appendix section: the re-observation statistics depending on the polarimetric combination in Fig. D.1 and the distribution per landmark type in Fig. D.2, both for $\mathcal{R}_{\text{Fra}}$.

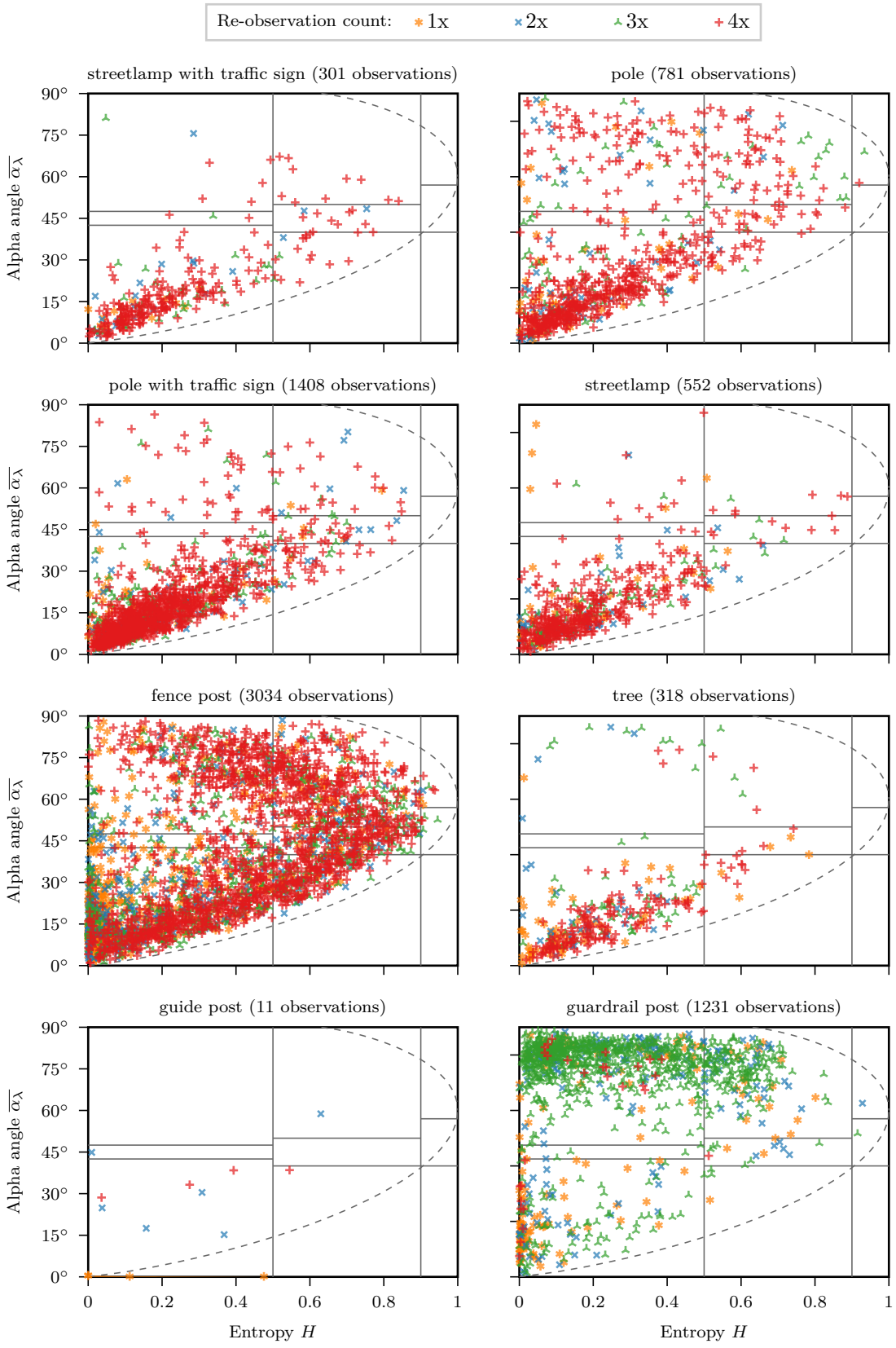


Figure D.3: The Cloude-Pottier approach according to Fig. 2.12 allows classifying the scattering type. $\mathcal{R}_{\text{Fra}}$ serves as the basis for this evaluation.

List of Figures

2.1 Simplified FMCW radar block diagram 8
2.2 CS modulation and data organization principle 13
2.3 Range Doppler processing for CS modulation 14
2.4 ULA beamforming signal model 15
2.5 MIMO principle and virtual elements 17
2.6 Transverse electromagnetic wave 18
2.7 Classical types of polarization 19
2.8 RCS definition 22
2.9 Scattering matrix elements and their scattering paths 25
2.10 Back scatter alignment convention 26
2.11 Canonical scatterers 29
2.12 $H/\overline{\alpha_\lambda}$ classification plane 36
2.13 Phase compensation for dual- and quad-polarimetric virtual elements 37
2.14 TDM schemes for fully polarimetric measurements 39

3.1 Experimental vehicle setup 42
3.2 Experimental vehicle photograph 43
3.3 TDM scheme 46
3.4 Antenna layout 46
3.5 Radar photograph 47

4.1 Calibration test facility 53
4.2 Incidence angle RCS dependency of a dihedral reflector 55
4.3 Signal processing block diagram 56
4.4 Electrical path length equalization 57
4.5 Impact of electrical path length equalization on beamforming 58
4.6 Fine beamforming alignment of the polarimetric channels by ego-motion estimation 60
4.7 Polarimetric relative phase for moving objects 62
4.8 AR model prediction in the virtual array 64
4.9 Polarimetric distortion evaluation in case of AR aperture extension . 65
4.10 Spatial amplitude distribution of target positions 66
4.11 Correction of azimuth-dependent relative polarimetric phases 66
4.12 Spatial errors after calibration 68
4.13 Radome measurements 68
4.14 Radome impact on the relative polarimetric information 69

5.1 Measurement setup for landmark scattering analysis 74
5.2 Landmark measurements in anechoic chamber 75
5.3 Range and phase drift of the local maximum belonging to the reflector 76
5.4 The spatial positions of three distinctive scatterers can be identified in the stop sign measurement power map 77

5.5 Co-polarized channel phase difference of the pole scattering from the stop sign target . . . 78
5.6 Pauli-decomposed relative back-scattered power for the speed limit sign . . . 80
5.7 Pauli-decomposed relative back-scattered power for the stop sign . . . 81
5.8 Pauli-decomposed relative back-scattered power for a simulated stop sign. . . . 82
5.9 Pauli-decomposed relative back-scattered power for the guide post . . 83
5.10 Pauli-decomposed spatial allocation of the relative back-scattered power by ISAR . . . 85
5.11 Pauli-decomposed ISAR images for partial integration of the guide post measurement . . . 87
5.12 Real-world scattering analysis measurement setup . . . 88
5.13 Polarimetric scattering behavior evolution during the approach . . . 89
5.14 Concept of PreCFAR gridmap construction . . . 92
5.15 Coordinate system definition . . . 93
5.16 Qualitative comparison between CFAR and PreCFAR gridmaps . . . 94
5.17 Polarimetric gridmaps are constructed by covariance matrix elements 97
5.18 PreCFAR covariance gridmap calculation scheme . . . 97
5.19 Krogager-decomposed PreCFAR Eigenmaps . . . 99
5.20 Cloude-Pottier-decomposed PreCFAR covariance maps . . . 101
5.21 The proposed Wishart-based point-shaped landmark candidate detector 104
5.22 Advantages of polarimetric information in point-shaped landmark candidate detection . . . 106
5.23 Re-observation distribution of landmarks for $\mathcal{R}_{\text{Ulm}}$ . . . 108
5.24 Distribution of re-observations per landmark type for $\mathcal{R}_{\text{Ulm}}$ . . . 109
5.25 Cloude-Pottier scattering classification of different landmark types for $\mathcal{R}_{\text{Ulm}}$ . . . 110
5.26 Qualitative comparison of line-shaped landmarks based on CFAR and PreCFAR data for $\mathcal{R}_{\text{Ulm}}$ . . . 112

6.1 Self-localization block diagram . . . 119
6.2 Nyquist zone augmentation for ego-motion estimation . . . 121
6.3 Association and factor graphs as results from the map matching . . . 124
6.4 Implementation of line-shaped landmark associations . . . 125
6.5 Exemplary self-localization graph representation . . . 128
6.6 Spatial trajectory error analysis for pass #3 of $\mathcal{R}_{\text{Ulm}}$ . . . 131
6.7 PreCFAR amplitude map of the Ulm environment with partial landmark maps . . . 132
6.8 CCDFs of trajectory errors for $\mathcal{R}_{\text{Ing}}$ . . . 134
6.9 CCDFs of trajectory errors for $\mathcal{R}_{\text{Ulm}}$ . . . 135

B.1 Pauli-decomposed ISAR images for partial integration of the speed limit sign measurement . . . 144
B.2 Pauli-decomposed ISAR images for partial integration of the stop sign measurement . . . 145

B.3 Pauli-decomposed ISAR images for partial integration of the stop sign simulation 146

C.1 PreCFAR gridmaps in high turn rate scenarios 148

D.1 Re-observation distribution of landmarks depending on polarimetric levels for $\mathcal{R}_{\text{Fra}}$ 149
D.2 Re-observation distribution of different landmark types for $\mathcal{R}_{\text{Fra}}$ . . . 150
D.3 Cloude-Pottier scattering classification of different landmark types for $\mathcal{R}_{\text{Fra}}$ 151

List of Tables

2.1 Jones vectors in the two most common bases for typical polarization states 21

3.1 Overview of 77 GHz polarimetric radar sensors for automotive applications 44
3.2 Parameters of the utilized polarimetric radar sensors 47

5.1 Parameters for the landmark scattering analysis 74
5.2 Comparison of gird-based static environment representations 95
5.3 Matched line-shaped landmark lengths for $\mathcal{R}_{\mathrm{Ulm}}$ 113

6.1 Symbolic abbreviations for sensor and map types 117
6.2 Overview of radar-based self-localization approaches 117
6.3 Overview of routes for the self-localization experiments 126
6.4 Factor implementations and information matrices 127
6.5 Self-localization parameters used for the evaluation 128
6.6 Localization performance using fully polarimetric information 130

List of Abbreviations

ACC	adaptive cruise control
ADAS	advanced driver-assistance system
ADC	analog-to-digital converter
BEV	bird's-eye view
BSA	back scatter alignment
CAN	controller area network
CATR	compact antenna test range
CCDF	complementary cumulative distribution function
CFAR	constant false alarm rate
CPU	central processing unit
CS	chirp sequence
CUDA	compute unified device architecture
DBF	digital beamforming
DDM	Doppler-division multiplexing
DGNSS	differential global navigation satellite system
DSP	digital signal processing
FFT	fast Fourier transform
FMCW	frequency-modulated continuous wave
FSA	forward scatter alignment
GNSS	global navigation satellite system
GPU	graphics processing unit
GTSAM	Georgia Tech Smoothing And Mapping library
HD	high-definition
IMU	inertial measurement unit
ISAR	inverse SAR
lidar	**li**ght **d**etection **a**nd **r**anging
LNA	low noise amplifier
MAE	mean absolute error
MIMO	multiple-input multiple-output
MMIC	monolithic microwave integrated circuit
NTP	network time protocol
ODD	operational design domain
PA	power amplifier
PPS	pulse-per-second
radar	**ra**dio **d**etection **a**nd **r**anging
RANSAC	random sample consensus
RCS	radar cross-section
RF	radio frequency
RMSE	root mean square error
ROS	robot operating system
RTCP	real-time control protocol

RTP	real-time transport protocol
SAR	synthetic aperture radar
SFCW	stepped-frequency continuous wave
SIMO	single-input multiple-output
SLAM	simultaneous localization and mapping
SNR	signal-to-noise ratio
TCP	transmission control protocol
TDM	time-division multiplexing
UDP	user datagram protocol
ULA	uniform linear array
VCO	voltage-controlled oscillator
XPD	cross polarization discrimination

List of Symbols

The symbol notation follows the IEEE style, with variables presented in italic font, vectors and matrices in boldface [189]. Complex variables are denoted by underlining the associated symbol.

A	anisotropy parameter of the Cloude-Pottier decomposition
A	anti-diagonally polarized
$\underline{a}$	element of the steering vector $\underline{\mathbf{a}}$ in array processing
$\underline{\mathbf{a}}$	steering vector in array processing
α_{λ_i}	alpha parameter of some eigenvalue-eigenvector pair of the Cloude-Pottier decomposition
α_{λ}	alpha parameter of the Cloude-Pottier decomposition
$\underline{\alpha}$	component of a coherent decomposition
$\underline{\alpha}_0$	plate scattering component of the Pauli decomposition
$\underline{\alpha}_1$	axis-aligned dihedral scattering component of the Pauli decomposition
$\underline{\alpha}_2$	45° dihedral scattering component of the Pauli decomposition
$\underline{\alpha}_3$	anti-symmetric dihedral scattering component of the Pauli decomposition
α_{d}	magnitude of diplane scattering component of the Krogager decomposition
$\underline{\alpha}_{\mathrm{d}}$	diplane scattering component of the Krogager decomposition
α_{h}	magnitude of helix scattering component of the Krogager decomposition
$\underline{\alpha}_{\mathrm{h}}$	helix scattering component of the Krogager decomposition
α_{s}	magnitude of sphere scattering component of the Krogager decomposition
$\underline{\alpha}_{\mathrm{s}}$	sphere scattering component of the Krogager decomposition
$\underline{\boldsymbol{\alpha}}_{\mathrm{Pauli}}$	vector of Pauli decomposition elements
$\sphericalangle$	phase of a complex number, sometimes denoted by $\arg(\cdot)$
AR	autoregressive model
B	bandwidth per chirp
$\mathcal{B}$	polarization basis

β	bistatic angle of a scattering geometry (between incident and scattered direction)
$\mathcal{B}_{\mathrm{HV}}$	vertically polarized, horizontally polarized polarization basis
$\mathcal{B}_{\mathrm{i}}$	incident polarization basis
$\mathcal{B}_{\mathrm{LR}}$	right-hand circular polarized, left-hand circular polarized polarization basis
$\mathcal{B}'$	other polarization basis
$\mathcal{B}_{\mathrm{s}}$	scattered polarization basis
$\mathbb{C}$	complex numbers
$\underline{C}$	element of the polarimetric covariance matrix $\underline{\mathbf{C}}$
$\underline{\mathbf{C}}$	polarimetric covariance matrix
c	superscript for car coordinate system
c	speed of light
$\mathcal{CN}$	complex Gaussian distribution
$\mathcal{D}_{\mathrm{Pauli}}$	Pauli decomposition operator
D	diagonally polarized
D	maximum dimension of an antenna
Δ_f	frequency step size
δ_r	range Rayleigh resolution
Δ_Θ	incident angle step size
δ_θ	azimuth angle Rayleigh resolution
δ_{v_r}	relative radial velocity Rayleigh resolution
Δ_x	grid cell size in x
Δ_y	grid cell size in y
$d^{\mathrm{l}}_{\mathrm{ch,thres}}$	threshold of convex hull distance between line-shaped landmark candidates
$d^{\mathrm{l}}_{\mathrm{prj,thres}}$	threshold of projection distance between line-shaped landmark candidates
$d^{\mathrm{l^p}}_{\mathrm{thres}}$	threshold of Euclidean distance between point-shaped landmark candidates
d_{Rx}	receive channel element spatial distance
d_{Tx}	transmit channel element spatial distance
$d_{\mathrm{wishart,thres}}$	Wishart distance threshold
d_{wishart}	Wishart distance to measure similarity of polarimetric covariances
$\underline{E}$	element of the electric field vector $\underline{\mathbf{E}}$
$\underline{E}_{\mathrm{i,L}}$	left-hand circular polarized, incident element of the electric field vector $\underline{\mathbf{E}}$
$\underline{E}_{\mathrm{i},q}$	arbitrary polarization, incident element of the electric field vector $\underline{\mathbf{E}}$
$\underline{E}_{\mathrm{i,R}}$	right-hand circular polarized, incident element of the electric field vector $\underline{\mathbf{E}}$
$\underline{E}_{\Phi}$	first basis vector of a polarization basis element of the electric field vector $\underline{\mathbf{E}}$

$\underline{E}_{\Psi}$	second basis vector of a polarization basis element of the electric field vector $\underline{\mathbf{E}}$
$\underline{E}_{\mathrm{s,L}}$	left-hand circular polarized, scattered element of the electric field vector $\underline{\mathbf{E}}$
$\underline{E}_{\mathrm{s},p}$	arbitrary polarization, scattered element of the electric field vector $\underline{\mathbf{E}}$
$\underline{E}_{\mathrm{s,R}}$	right-hand circular polarized, scattered element of the electric field vector $\underline{\mathbf{E}}$
$\underline{\boldsymbol{\mathcal{E}}}$	complex version of $\boldsymbol{\mathcal{E}}$
$\boldsymbol{\mathcal{E}}$	electric field vector function including temporal and spatial dependencies
$\underline{\mathbf{E}}$	electric field vector
$\underline{\mathbf{E}}_{\mathcal{B}}$	polarization basis electric field vector
$\underline{\mathbf{E}}_{\mathcal{B},\mathrm{i}}$	incident, polarization basis electric field vector
$\underline{\mathbf{E}}_{\mathcal{B}'}$	other polarization basis electric field vector
$\underline{\mathbf{E}}_{\mathcal{B}',\mathrm{i}}$	incident, other polarization basis electric field vector
$\underline{\mathbf{E}}_{\mathcal{B}',\mathrm{s}}$	scattered, other polarization basis electric field vector
$\underline{\mathbf{E}}_{\mathcal{B},\mathrm{s}}$	scattered, polarization basis electric field vector
$\underline{\hat{\mathbf{E}}}$	normalized electric field vector
$\underline{\hat{\mathbf{E}}}_{\mathcal{B}_{\mathrm{HV}}}$	vertically polarized, horizontally polarized polarization basis normalized electric field vector
$\underline{\hat{\mathbf{E}}}_{\mathcal{B}_{\mathrm{LR}}}$	right-hand circular polarized, left-hand circular polarized polarization basis normalized electric field vector
$\underline{\mathbf{E}}_{\mathrm{i}}$	incident electric field vector
$\underline{\mathbf{E}}_{\mathrm{s}}$	scattered electric field vector
$\varepsilon_{\mathrm{lat}}$	lateral error
$\varepsilon_{\mathrm{lon}}$	longitudinal error
ε_{ψ}	yaw angle error
$\varepsilon_{r,pq}$	per polarimetric channel antenna phase center range error
$\hat{\varepsilon}_{r,pq}$	per polarimetric channel antenna phase center range optimal minimum error
$\mathbf{e}_{\mathrm{H}}$	horizontally polarized unit vector
$\mathbf{e}_{\mathbf{k}}$	wave vector unit vector
$\mathbf{e}_{\mathbf{k},\mathrm{i}}$	incident, wave vector unit vector
$\mathbf{e}_{\mathbf{k},\mathrm{s}}$	scattered, wave vector unit vector
$\mathbf{e}_{\mathrm{L}}$	left-hand circular polarized unit vector
$\mathbf{e}_{\Phi}$	first basis vector of a polarization basis unit vector
$\mathbf{e}_{\Phi,\mathrm{i}}$	incident, first basis vector of a polarization basis unit vector
$\mathbf{e}_{\Phi,\mathrm{s}}$	scattered, first basis vector of a polarization basis unit vector

$\mathbf{e}_\Psi$	second basis vector of a polarization basis unit vector
$\mathbf{e}_{\Psi,\mathrm{i}}$	incident, second basis vector of a polarization basis unit vector
$\mathbf{e}_{\Psi,\mathrm{s}}$	scattered, second basis vector of a polarization basis unit vector
$\mathbf{e}_\mathrm{R}$	right-hand circular polarized unit vector
$\mathbf{e}_\mathrm{V}$	vertically polarized unit vector
$\mathcal{F}$	Fourier transmform
$\underline{\mathbf{F}}$	simplified combined polarimetric distortion matrix
f_c	center frequency of a chirp waveform
f	frequency
$\mathbf{f}$	graph factor
f_0	start frequency of a chirp waveform
f_1	stop frequency of a chirp waveform
f_b	beat frequency
$f_\mathrm{b,max}$	maximum beat frequency
f_cycle	measurement cycle frame rate
f_D	Doppler frequency
$f_\mathrm{D,max}$	maximum unambiguous Doppler frequency
f_s	sampling frequency
$\underline{G}$	element of the polarimetric antenna element gain pattern matrix $\underline{\mathbf{G}}$
$\underline{\mathbf{G}}$	polarimetric antenna element gain pattern matrix
γ	arbitrary amplitude
$\underline{\gamma}$	arbitrary complex amplitude
G_Rx	receive channel antenna gain
G_Tx	transmit channel antenna gain
Γ	gamma function $\Gamma(n) = (n-1)!$
H	entropy parameter of the Cloude-Pottier decomposition
H	horizontally polarized
$\boldsymbol{\mathcal{H}}$	magnetic field vector function including temporal and spatial dependencies
$\mathbf{h}$	measurement function in factor graphs
$\underline{\mathbf{I}}$	isolation matrix
I	energy flux density
I_i	incident energy flux density
I_s	scattered energy flux density
IF	intermediate frequency
i	some index, e.g. in a sum
j	imaginary unit, i.e., $\sqrt{-1}$
k	wavenumber
$\mathbf{k}$	wave vector
κ_l	scaling factor for standard deviation of line-shaped landmarks

κ_r	range calibration scaling factor
$\hat{\kappa}_r$	range optimal calibration scaling factor
κ_θ	azimuth angle calibration scaling factor
$\hat{\kappa}_\theta$	azimuth angle optimal calibration scaling factor
$\mathbf{k}_\mathrm{i}$	incident wave vector
$\mathbf{k}_\mathrm{s}$	scattered wave vector
L	number of landmarks
L	left-hand circular polarized
l	landmark index
$\mathbf{l}$	point- and line-shaped landmarks
$\mathbf{l}^\mathrm{l}$	line-shaped landmarks
$\mathbf{l}^\mathrm{p}$	point-shaped landmarks
Λ_c	scaled wavelength according to array spacing of the utilized sensor
λ_c	wavelength
$\mathbf{\Lambda}$	diagonal matrix of eigenvalues
λ	eigenvalue
$\underline{m}^\mathrm{w}$	complex valued map in a global coordinate frame
n	index of array element
ν	dimensionality of a feature vector $\underline{\mathbf{\Omega}}$
N_fast	fast-time number
$N_\mathrm{thres}^{\mathbf{l}^\mathrm{p}}$	minimum number of point-shaped landmark candidates to establish landmark
N_Rx	receive channel number
n_Rx	receive channel index of array element
N_slow	slow-time number
N_Tx	transmit channel number
n_Tx	transmit channel index of array element
N_VRx	virtual receive channel number
n_VRx	virtual receive channel index of array element
$N_{\underline{\mathbf{Z}}}$	polarimetric sample covariance matrix number
$\underline{\mathbf{\Omega}}$	polarimetric feature vector
ω	angular frequency
$\boldsymbol{\omega}$	angular rate vector
ω	angular rate
$\underline{\mathbf{\Omega}}_\mathcal{B}$	polarization basis polarimetric feature vector
ω_z	yaw rate
$\omega_{z,\mathrm{ego,est}}$	estimated ego-vehicle yaw rate
$\omega_{z,\mathrm{ego,gt}}$	ground truth ego-vehicle yaw rate
$\mathbf{P}$	information matrix
$\mathcal{P}$	propagation path
P_{λ_i}	relative probability of occurrence in eigendecomposition
$\mathbf{p}$	Cartesian coordinate system vector
p	probability density function
Φ	first basis vector of a polarization basis

Φ'	other first basis vector of a polarization basis
$\phi_{\Phi\Phi}$	first basis vector of a polarization basis, first basis vector of a polarization basis phase
$\phi_{\Phi\Psi}$	second basis vector of a polarization basis, first basis vector of a polarization basis phase
$\phi_{\Psi\Psi}$	second basis vector of a polarization basis, second basis vector of a polarization basis phase
ϕ_{s}	relative phase of sphere to diplane scattering component of the Krogager decomposition
$\underline{\Pi}$	ISAR image in Cartesian coordinates
p'	other arbitrary polarization
P_{Rx}	receive channel power
P_{s}	scattered power
ψ	yaw angle
Ψ	second basis vector of a polarization basis
Ψ'	other second basis vector of a polarization basis
P_{Tx}	transmit channel power
$\underline{R}$	element of the polarimetric receive distortion matrix $\underline{\mathbf{R}}$
$\underline{\mathbf{R}}$	polarimetric receive distortion matrix
$\mathbb{R}$	real numbers
R	right-hand circular polarized
$\mathbf{R}$	two-dimensional rotation matrix
$\mathbf{r}$	spatial position in 3D space
r	range
r_0	start range ($t=0$) for a moving object
$\mathfrak{Re}$	real part of the complex argument
$r_{\mathrm{el},n_{\mathrm{VRx}},pq}$	electrical path length difference
r_{FF}	far-field range
ρ	chirp rate
r_m	range for a moving object at the start of ramp m
$r_{\max}$	maximum unambiguous range
$\tilde{r}$	modified range (uncalibrated)
$\mathcal{R}_{\mathrm{Fra}}$	route in Frankfurt area
$\mathcal{R}_{\mathrm{Ing}}$	route in Ingolstadt area
$\mathcal{R}_{\mathrm{Ulm}}$	route in Ulm area
r_{pole}	radius of traffic sign pole
r_{rc}	rotation center distance
r_{Rx}	receive channel range
r_{Tx}	transmit channel range
Rx	receive channel
$\underline{S}$	complex element of the scattering matrix $\underline{\mathbf{S}}$
$\underline{\mathbf{\Sigma}}$	polarimetric covariance matrix desc
σ	radar cross-section
$\underline{\mathbf{S}}$	scattering matrix (Sinclair matrix in this work due to BSA)

$\tilde{\sigma}_0$	pseudo-RCS for plate scattering component of the Pauli decomposition
$\tilde{\sigma}_1$	pseudo-RCS for axis-aligned dihedral scattering component of the Pauli decomposition
$\tilde{\sigma}_2$	pseudo-RCS for 45° dihedral scattering component of the Pauli decomposition
σ^2	variance
$\tilde{\sigma}$	pseudo radar cross-section
$\underline{s}_{\mathrm{IF}}$	intermediate frequency signal in complex notation
$\underline{\mathbf{s}}_{\mathrm{IF}}$	intermediate frequency signal vector in complex notation
$\underline{s}_{\mathrm{IF},pq}$	arbitrary polarimetric channel, intermediate frequency signal in complex notation
$\underline{\tilde{s}}_{\mathrm{IF},pq}$	arbitrary polarimetric channel, intermediate frequency modified signal in complex notation
$\underline{s}_{\mathrm{Rx}}$	receive channel signal in complex notation
$\underline{s}_{\mathrm{Tx}}$	transmit channel signal in complex notation
sc	suffix indicating the center radar sensor
S_{even}	even-bounce scattering element
s_{IF}	intermediate frequency signal
$s_{\mathrm{IF,filt}}$	band-pass filtered intermediate frequency signal
$s_{\mathrm{IF},pq}$	arbitrary polarimetric channel, intermediate frequency signal
$\tilde{\sigma}_{\mathrm{d}}$	pseudo-RCS for diplane scattering component of the Krogager decomposition
$\tilde{\sigma}_{\mathrm{h}}$	pseudo-RCS for helix scattering component of the Krogager decomposition
$\tilde{\sigma}_{\mathrm{s}}$	pseudo-RCS for sphere scattering component of the Krogager decomposition
si	suffix indicating one of the radar sensors
sl	suffix indicating the left radar sensor
$\underline{S}_{\mathrm{LL}}$	left-hand circular polarized, left-hand circular polarized complex element of the scattering matrix $\underline{\mathbf{S}}$
$\underline{S}_{\mathrm{LR}}$	right-hand circular polarized, left-hand circular polarized complex element of the scattering matrix $\underline{\mathbf{S}}$
S_{odd}	odd-bounce scattering element
$\underline{S}_{\Phi'\Phi}$	first basis vector of a polarization basis, other first basis vector of a polarization basis complex element of the scattering matrix $\underline{\mathbf{S}}$
$\underline{S}_{\Phi'\Psi}$	second basis vector of a polarization basis, other first basis vector of a polarization basis complex element of the scattering matrix $\underline{\mathbf{S}}$
$\underline{S}_{\Phi\Phi}$	first basis vector of a polarization basis, first basis vector of a polarization basis complex element of the scattering matrix $\underline{\mathbf{S}}$

$\underline{S}_{\Phi\Psi}$	second basis vector of a polarization basis, first basis vector of a polarization basis complex element of the scattering matrix $\underline{\mathbf{S}}$
$\underline{S}_{p'q}$	arbitrary polarization, other arbitrary polarization complex element of the scattering matrix $\underline{\mathbf{S}}$
$\underline{S}_{pq}$	arbitrary polarization, arbitrary polarization complex element of the scattering matrix $\underline{\mathbf{S}}$
$\underline{S}_{\Psi'\Phi}$	first basis vector of a polarization basis, other second basis vector of a polarization basis complex element of the scattering matrix $\underline{\mathbf{S}}$
$\underline{S}_{\Psi'\Psi}$	second basis vector of a polarization basis, other second basis vector of a polarization basis complex element of the scattering matrix $\underline{\mathbf{S}}$
$\underline{S}_{\Psi\Phi}$	first basis vector of a polarization basis, second basis vector of a polarization basis complex element of the scattering matrix $\underline{\mathbf{S}}$
$\underline{S}_{\Psi\Psi}$	second basis vector of a polarization basis, second basis vector of a polarization basis complex element of the scattering matrix $\underline{\mathbf{S}}$
sr	suffix indicating the right radar sensor
$\underline{S}_{\mathrm{RL}}$	left-hand circular polarized, right-hand circular polarized complex element of the scattering matrix $\underline{\mathbf{S}}$
$\underline{S}_{\mathrm{RR}}$	right-hand circular polarized, right-hand circular polarized complex element of the scattering matrix $\underline{\mathbf{S}}$
s_{Rx}	receive channel signal
s_{Tx}	transmit channel signal
s_{VRx}	virtual receive channel signal
$\underline{T}$	element of the polarimetric transmit distortion matrix $\underline{\mathbf{T}}$
$\underline{\mathbf{T}}$	polarimetric transmit distortion matrix
t	continuous time
$\tilde{\tau}$	signal propagation time delay for a moving object
τ	signal propagation time delay
T_{chirp}	chirp duration
t_{fast}	fast-time continuous time
T_{graph}	temporal history in a sliding window factor graph
Θ	incident angle
$\tilde{\theta}$	modified azimuth angle
θ	azimuth angle
$\boldsymbol{\Theta}$	factor graph variables to be optimized
θ_{s}	scan azimuth angle
θ_{max}	maximum unambiguous azimuth angle
$\theta_{\mathrm{max,cal}}$	calibrated maximum azimuth angle
T_{prf}	ramp repetition duration

t_{slow}	slow-time continuous time
Tx	transmit channel
$\underline{\mathbf{U}}$	basis change matrix
u	some vertex type
$\underline{\mathbf{U}}_{\mathcal{B}\to\mathcal{B}'}$	other polarization basis, polarization basis basis change matrix
$\underline{\mathbf{U}}_{\mathcal{B}_{\text{HV}}\to\mathcal{B}_{\text{LR}}}$	right-hand circular polarized, left-hand circular polarized polarization basis, vertically polarized, horizontally polarized polarization basis basis change matrix
$\underline{\mathbf{U}}_{\mathcal{B}_{\text{LR}}\to\mathcal{B}_{\text{HV}}}$	vertically polarized, horizontally polarized polarization basis, right-hand circular polarized, left-hand circular polarized polarization basis basis change matrix
$\underline{\mathbf{U}}_{\mathcal{B}'\to\mathcal{B}}$	polarization basis, other polarization basis basis change matrix
υ	some other vertex type
V	vertically polarized
$\mathbf{v}$	velocity vector
v	velocity
$v_{\text{ego,est}}$	estimated ego-vehicle forward velocity
$v_{\text{ego,gt}}$	ground truth ego-vehicle forward velocity
v_{r}	relative radial velocity
$v_{\text{r,max}}$	maximum unambiguous relative radial velocity
$v_{\text{r,stat}}$	relative radial velocity of the static surroundings
VRx	virtual receive channel
$\mathbf{v}_{\text{s}}$	sensor velocity vector
$\underline{\mathbf{W}}$	matrix of eigenvector
$\mathcal{CW}$	complex Wishart distribution
$\underline{\mathbf{w}}$	eigenvector
w	superscript for world coordinate system
X	number of poses
x	first component in a Cartesian coordinate system
$\mathbf{x}$	poses
ξ	speed-normalized yaw rate error
y	second component in a Cartesian coordinate system
$\underline{Z}$	element of the polarimetric sample covariance matrix $\underline{\mathbf{Z}}$
z	third component in a Cartesian coordinate system
$\mathbf{z}$	measurement
$\underline{\mathbf{Z}}$	polarimetric sample covariance matrix
Z_0	free space impedance

Bibliography

[1] J.-S. Wang, "Target crash population for crash avoidance technologies in passenger vehicles (Report No. DOT HS 812 653)," 2019. 1

[2] C. Waldschmidt, J. Hasch, and W. Menzel, "Automotive Radar – From First Efforts to Future Systems," *IEEE Journal of Microwaves*, vol. 1, no. 1, pp. 135–148, 2021. 1, 15

[3] J. Vargas, S. Alsweiss, O. Toker, R. Razdan, and J. Santos, "An Overview of Autonomous Vehicles Sensors and Their Vulnerability to Weather Conditions," *Sensors*, vol. 21, no. 16, 2021. [Online]. Available: https://www.mdpi.com/1424-8220/21/16/5397 1

[4] S. Royo and M. Ballesta-Garcia, "An overview of lidar imaging systems for autonomous vehicles," *Applied Sciences*, vol. 9, no. 19, 2019. [Online]. Available: https://www.mdpi.com/2076-3417/9/19/4093 1

[5] P. Boulay and C. Malaquin, "ADAS Sensors and Computing: A 22 Billion Dollar Market in 2025," *PhotonicsViews*, vol. 17, no. 4, pp. 35–37, 2020. [Online]. Available: https://onlinelibrary.wiley.com/doi/abs/10.1002/phvs.202070410 1

[6] Y. Lu, H. Ma, E. Smart, and H. Yu, "Real-Time Performance-Focused Localization Techniques for Autonomous Vehicle: A Review," *IEEE Transactions on Intelligent Transportation Systems*, vol. 23, no. 7, pp. 6082–6100, 2022. 2, 116

[7] K. Werber, J. Klappstein, J. Dickmann, and C. Waldschmidt, "Interesting areas in radar gridmaps for vehicle self-localization," in *2016 IEEE MTT-S International Conference on Microwaves for Intelligent Mobility (ICMIM)*, 2016, pp. 1–4. 2, 90, 103

[8] Wilbers, Daniel, "Graph-based Sliding Window Localization and Map Refinement for Automated Vehicles," Ph.D. dissertation, Rheinische Friedrich-Wilhelms-Universität Bonn, oct 2021. 2, 122, 125, 126

[9] J.-S. Lee and E. Pottier, *Polarimetric radar imaging: from basics to applications*. CRC press, 2017. 3, 20, 22, 23, 26, 27, 28, 29, 30, 31, 32, 33, 34, 35, 96, 98

[10] V. N. Bringi and V. Chandrasekar, *Polarimetric Doppler Weather Radar: Principles and Applications*. Cambridge University Press, 2001. 3, 22, 23

[11] R. Schneider, G. Wanielik, and J. Wenger, "Millimeter-wave imaging of traffic scenarios," in *Proceedings of Conference on Intelligent Vehicles*, 1996, pp. 327–332. 3, 44

[12] K. Sarabandi, E. Li, and A. Nashashibi, "Modeling and measurements of scattering from road surfaces at millimeter-wave frequencies," *IEEE Transactions on Antennas and Propagation*, vol. 45, no. 11, pp. 1679–1688, 1997. 3

[13] R. Finkele, A. Schreck, and G. Wanielik, "Polarimetric road condition classification and data visualisation," in *1995 International Geoscience and Remote Sensing Symposium, IGARSS '95. Quantitative Remote Sensing for Science and Applications*, vol. 3, 1995, pp. 1786–1788 vol.3. 3

[14] J. Wenger, M. Stotz, H. Barth, H. Neef, G. Wanielik, and R. Schneider, "A Polarimetric 76 GHz radar-sensor for automotive applications," in *1997 27th European Microwave Conference*, vol. 2, 1997, pp. 832–837. 3, 44

[15] S. Clark and H. D. Whyte, "The Design of a High Performance MMW Radar System for Autonomous Land Vehicle Navigation," in *Field and Service Robotics*, A. Zelinsky, Ed. London: Springer London, 1998, pp. 281–288. 3, 44

[16] L. Carrea, G. Wanielik, and L. Giubbolini, "The polar decomposition of the scattering matrix applied to the polarimetric image of the guard-rail," in *14th International Conference on Microwaves, Radar and Wireless Communications. MIKON - 2002. Conference Proceedings (IEEE Cat.No.02EX562)*, vol. 2, 2002, pp. 563–566 vol.2. 3

[17] K. Sarabandi and E. Li, "Polarimetric characterization of debris and faults in the highway environment at millimeter-wave frequencies," *IEEE Transactions on Antennas and Propagation*, vol. 48, no. 11, pp. 1756–1768, 2000. 3, 43

[18] E. Li and K. Sarabandi, "Low grazing incidence millimeter-wave scattering models and measurements for various road surfaces," *IEEE Transactions on Antennas and Propagation*, vol. 47, no. 5, pp. 851–861, 1999. 3

[19] S. Trummer, G. F. Hamberger, U. Siart, and T. F. Eibert, "A Polarimetric 76 – 79 GHz Radar-Frontend for Target Classification in Automotive Use," in *2016 European Radar Conference (EuRAD)*, 2016, pp. 346–349. 3, 44, 45, 46, 52

[20] Q. Ren, O. Eriksson, P. Thalya, R. Elezovic, C. Bencivenni, M. Hasselblad, J. Yang, Z. Zang, and A. U. Zaman, "An Automotive Polarimetric Radar Sensor With Circular Polarization Based on Gapwaveguide Technology," *IEEE Transactions on Microwave Theory and Techniques*, pp. 1–13, 2023. 3, 44, 45, 51

[21] T. Visentin, "Polarimetric Radar for Automotive Applications," Ph.D. dissertation, Karlsruhe Institute of Technology (KIT), 2019. 3, 44, 45, 51

[22] A. Tinti, S. T. Alfageme, S. D. Biarge, and N. Pohl, "Full Polarimetric Antenna System for Automotive Radar," in *2023 IEEE Topical Conference on Wireless Sensors and Sensor Networks*, 2023, pp. 39–42. 3, 44, 45

[23] C. Erhart, S. Lutz, M. A. Mutschler, P. A. Scharf, T. Walter, H. Mantz, and R. Weigel, "Compact polarimetry for automotive applications," *International Journal of Microwave and Wireless Technologies*, vol. 11, no. 2, p. 114–120, 2019. 3, 43

[24] J. F. Tilly, O. Schumann, F. Weishaupt, J. Dickmann, and G. Waniliek, "Polarimetric Information Representation for Radar based Road User Detection with Deep Learning," in *2021 IEEE 24th International Conference on Information Fusion (FUSION)*, 2021, pp. 1–6. 3, 41, 44

[25] J. F. Tilly, F. Weishaupt, O. Schumann, J. Dickmann, and G. Wanielik, "Road User Classification with Polarimetric Radars," in *2020 17th European Radar Conference (EuRAD)*, 2021, pp. 112–115. 3, 41, 44

[26] ——, "Road User Detection on Polarimetric Pre-CFAR Radar Data Level," *IEEE Robotics and Automation Letters*, vol. 8, no. 6, pp. 3558–3565, 2023. 3, 41, 44

[27] T. Visentin, J. Hasch, and T. Zwick, "Polarimetric RCS measurements of selected two-wheeled vehicles for automotive radar," in *2017 European Radar Conference (EuRAD)*, 2017, pp. 53–56. 3, 44, 45

[28] S. Trummer, G. F. Hamberger, R. Koerber, U. Siart, and T. F. Eibert, "Autonomous Driving Features based on 79 GHz Polarimetric Radar Data," in *2018 15th European Radar Conference (EuRAD)*, 2018, pp. 18–21. 3, 44, 45

[29] H. Iqbal, C. Knill, M. Z. Khan, T. Chaloun, and C. Waldschmidt, "Polarimetric SAR for automotive applications," in *2018 European Radar Conference (EuRAD)*, 2018, pp. 30–33. 4, 90, 96

[30] J. M. Merlo and J. A. Nanzer, "A C-band fully polarimetric automotive synthetic aperture radar," *IEEE Transactions on Vehicular Technology*, vol. 71, no. 3, pp. 2587–2600, 2022. 4, 44, 90, 96

[31] H. Iqbal, F. Bögelsack, and C. Waldschmidt, "Polarimetric RCS analysis of traffic objects," in *2017 European Radar Conference (EURAD)*, 2017, pp. 49–52. 4, 72, 73, 79, 81

[32] S. Clark and H. Durrant-Whyte, "Autonomous land vehicle navigation using millimeter wave radar," in *1998 IEEE International Conference on Robotics and Automation (ICRA)*, vol. 4, 1998, pp. 3697–3702 vol.4. 4, 44, 117, 118

[33] S. Clark and G. Dissanayake, "Simultaneous localisation and map building using millimetre wave radar to extract natural features," in *1999 IEEE International Conference on Robotics and Automation (ICRA)*, May 1999, pp. 1316–1321. 4, 44, 102

[34] M. A. Richards, *Fundamentals of Radar Signal Processing.* McGraw-Hill Professional, 2005. 9, 10, 11

[35] F. Weishaupt, "Aufbau und Evaluierung eines MIMO-Radarsensornetzwerks sowie signal-theoretische und experimentelle Validierung," Master's thesis, RWTH Aachen University, 2017. 10

[36] A. Stove, "Linear FMCW radar techniques," *IEE Proceedings F (Radar and Signal Processing)*, vol. 139, pp. 343–350(7), October 1992. 11

[37] V. Winkler, "Range Doppler detection for automotive FMCW radars," in *2007 European Microwave Conference*, 2007, pp. 1445–1448. 11

[38] C. A. Balanis, *Antenna theory: analysis and design.* John Wiley & Sons, Inc., 2005. 15

[39] P. Stoica and R. Moses, *Spectral Analysis of Signals.* Pearson Prentice Hall, 2005. 16, 64

[40] J. Li and P. Stoica, *MIMO Radar Signal Processing*, ser. IEEE Press. John Wiley & Sons, Inc., 2009. 17

[41] J. Bechter, F. Roos, and C. Waldschmidt, "Compensation of Motion-Induced Phase Errors in TDM MIMO Radars," *IEEE Microwave and Wireless Components Letters*, vol. 27, no. 12, pp. 1164–1166, 2017. 18, 61

[42] C. M. Schmid, R. Feger, C. Pfeffer, and A. Stelzer, "Motion compensation and efficient array design for TDMA FMCW MIMO radar systems," in *2012 6th European Conference on Antennas and Propagation (EUCAP)*, 2012, pp. 1746–1750. 18, 61

[43] C. Sturm, Y. L. Sit, G. Li, H. A. Vayghan, and U. Lübbert, "Automotive Fast-Chirp MIMO Radar with Simultaneous Transmission in a Doppler-Multiplex," in *2018 19th International Radar Symposium (IRS)*, 2018, pp. 1–6. 18

[44] E. Lüneburg, "Aspects of radar polarimetry," *Turkish Journal of Electrical Engineering and Computer Sciences*, vol. 10, pp. 219–243, 01 2002. 18, 19, 21, 24, 25, 27, 28

[45] T. M. B. Dallmann, "Polarimetric Radar Cross-Section Imaging," Dissertation, RWTH Aachen University, Aachen, 2017, veröffentlicht auf dem Publikationsserver der RWTH Aachen University 2018; Dissertation, RWTH Aachen University, 2017. [Online]. Available: https://publications.rwth-aachen.de/record/709878 18, 32, 33, 34

[46] H. Mott, *Remote Sensing with Polarimetric Radar*. John Wiley & Sons, 2007. 19, 28

[47] "IEEE Standard for Definitions of Terms for Antennas," *IEEE Std 145-2013 (Revision of IEEE Std 145-1993)*, pp. 1–50, 2014. 20

[48] S. R. Cloude, "Special unitary groups in polarimetry theory," in *Polarization Analysis and Measurement II*, D. H. Goldstein and D. B. Chenault, Eds., vol. 2265, International Society for Optics and Photonics. SPIE, 1994, pp. 292 – 303. [Online]. Available: https://doi.org/10.1117/12.186678 20

[49] B. R. Mahafza, *Radar Systems Analysis and Design Using MATLAB ®*. CRC Press, 2013. 23, 24

[50] M. R. Feinstein, *Understanding Reciprocity in Radar Polarimetry*. Dordrecht: Springer Netherlands, 1992, pp. 829–844. [Online]. Available: https://doi.org/10.1007/978-94-010-9243-2_32 25

[51] C. López-Martínez and E. Pottier, *Basic Principles of SAR Polarimetry*. Cham: Springer International Publishing, 2021, pp. 1–58. [Online]. Available: https://doi.org/10.1007/978-3-030-56504-6_1 26, 27, 28

[52] S. Cloude, *Polarisation: Applications in Remote Sensing*. Oxford University Press, 2009. 28, 33, 34, 35, 50

[53] P. Pincus, M. Preiss, A. S. Goh, and D. Gray, "Polarimetric calibration of circularly polarized synthetic aperture radar data," *IEEE Transactions on Geoscience and Remote Sensing*, vol. 55, no. 12, pp. 6824–6839, 2017. 30

[54] Y. Han, P. Lu, X. Liu, W. Hou, Y. Gao, W. Yu, and R. Wang, "On the Method of Circular Polarimetric SAR Calibration Using Distributed Targets," *IEEE Transactions on Geoscience and Remote Sensing*, vol. 61, pp. 1–16, 2023. 31

[55] A. Freeman and S. Durden, "A three-component scattering model for polarimetric SAR data," *IEEE Transactions on Geoscience and Remote Sensing*, vol. 36, no. 3, pp. 963–973, 1998. 33

[56] Y. Yamaguchi, T. Moriyama, M. Ishido, and H. Yamada, "Four-component scattering model for polarimetric SAR image decomposition," *IEEE Transactions on Geoscience and Remote Sensing*, vol. 43, no. 8, pp. 1699–1706, 2005. 33

[57] S. Cloude and E. Pottier, "A review of target decomposition theorems in radar polarimetry," *IEEE Transactions on Geoscience and Remote Sensing*, vol. 34, no. 2, pp. 498–518, 1996. 34

[58] ——, "An entropy based classification scheme for land applications of polarimetric SAR," *IEEE Transactions on Geoscience and Remote Sensing*, vol. 35, no. 1, pp. 68–78, 1997. 34, 35

[59] D. Neudert-Schulz, "A contribution to efficient direction finding using antenna arrays," Ph.D. dissertation, TU Ilmenau, Germany; Ilmenau, Feb 2017. [On-

line]. Available: https://www.db-thueringen.de/receive/dbt_mods_00031763 36

[60] J. F. Tilly, F. Weishaupt, O. Schumann, J. Klappstein, J. Dickmann, and G. Wanielik, "Polarimetric Signatures of a Passenger Car," in *2019 Kleinheubach Conference*, 2019, pp. 1–4. 41, 44

[61] J. F. Tilly, O. Schumann, F. Weishaupt, J. Dickmann, and G. Wanielik, "Reduction of Sidelobe Effects in Automotive Polarimetric Radar Measurements," in *2021 18th European Radar Conference (EuRAD)*, 2022, pp. 169–172. 41

[62] M. Quigley, B. Gerkey, K. Conley, J. Faust, T. Foote, J. Leibs, E. Berger, R. Wheeler, and A. Ng, "ROS: an open-source Robot Operating System," in *Proc. of the IEEE Intl. Conf. on Robotics and Automation (ICRA) Workshop on Open Source Robotics*, Kobe, Japan, May 2009. 41

[63] J. Nickolls, I. Buck, M. Garland, and K. Skadron, "Scalable parallel programming with CUDA," in *ACM SIGGRAPH 2008 Classes*, ser. SIGGRAPH '08. New York, NY, USA: Association for Computing Machinery, 2008. [Online]. Available: https://doi.org/10.1145/1401132.1401152 41

[64] Axis Communications AB. Axis camera system. Accessed: 29th May 2025. [Online]. Available: https://www.axis.com/de-de/products/axis-f44-dual-audio-input/support 41

[65] GeneSys Elektronik GmbH. Automotive Dynamic Motion Analyzer G PRO. Accessed: 29th May 2025. [Online]. Available: https://genesys-offenburg.de/en/adma-g/ 42

[66] AXIO-NET GmbH. AXIO-NET PED. Accessed: 29th May 2025. [Online]. Available: https://axio-net.eu/produkte/axio-net-loesungen/axio-net-ped 42

[67] Landesamt für Geoinformation und Landentwicklung Baden-Württemberg (LGL). SAPOS®. Accessed: 29th May 2025. [Online]. Available: https://gps-web.sapos-bw.de/ 42

[68] gpsd project. (2021) `gpsd` Time Service HOWTO. Accessed: 18th March 2024. [Online]. Available: https://gpsd.io/gpsd-time-service-howto.html 42

[69] ——, "`gpsd`." [Online]. Available: https://gpsd.io/ 42

[70] NTPsec project, "`ntpd`." [Online]. Available: https://www.ntpsec.org/ 42

[71] F. Weishaupt, J. F. Tilly, N. Appenrodt, P. Fischer, J. Dickmann, and D. Heberling, "Landmark-based Vehicle Self-Localization Using Automotive Polarimetric Radars," *IEEE Transactions on Intelligent Transportation Systems*, vol. 25, no. 10, pp. 14 266–14 283, 2024. 43, 47, 96, 97, 106, 115, 119, 121, 124, 125, 131, 132, 134, 135

[72] V. Vassilev, "Road Surface Recognition at mm-Wavelengths Using a Polarimetric Radar," *IEEE Transactions on Intelligent Transportation Systems*, vol. 23, no. 7, pp. 6985–6990, 2022. 43

[73] W. Bouwmeester, F. Fioranelli, and A. G. Yarovoy, "Road Surface Conditions Identification via H α A Decomposition and Its Application to mm-Wave Automotive Radar," *IEEE Transactions on Radar Systems*, vol. 1, pp. 132–145, 2023. 43

[74] T. Freialdenhoven, T. Bertuch, S. Stanko, D. Nötel, D. I. L. Vorst, and T. Dallmann, "Design of a Polarization Rotating SIW-based reflector for polarimetric

radar application," *IEEE Transactions on Antennas and Propagation*, vol. 68, no. 11, pp. 7414–7422, 2020. 43

[75] T. Freialdenhoven, M. Schepers, and T. Dallmann, "Frequency Controlled Polarization Rotating Transmitarray for Polarimetric Radar Applications," in *2022 52nd European Microwave Conference (EuMC)*, 2022, pp. 660–663. 43

[76] T. Freialdenhoven, S. Nair, and T. Dallmann, "Fully Polarimetric Calibration of Ka-Band Radar With Band Separated Twist Reflector," in *2022 23rd International Radar Symposium (IRS)*, 2022, pp. 408–413. 44, 50, 51, 57, 63

[77] A. A. Alaqeel, A. A. Ibrahim, A. Y. Nashashibi, H. N. Shaman, and K. Sarabandi, "Experimental Characterization of Multi-Polarization Radar Backscatter Response of Vehicles at *J*-Band," *IEEE Transactions on Intelligent Transportation Systems*, vol. 20, no. 9, pp. 3337–3350, 2019. 44

[78] G. F. Hamberger, S. Trummer, U. Siart, and T. F. Eibert, "A single layer dual linearly polarized microstrip patch antenna array for automotive applications in the 77 GHz band student submission," in *2016 IEEE International Symposium on Phased Array Systems and Technology (PAST)*, 2016, pp. 1–4. 44

[79] G. F. Hamberger, S. Späth, U. Siart, and T. F. Eibert, "A Mixed Circular/Linear Dual-Polarized Phased Array Concept for Automotive Radar—Planar Antenna Designs and System Evaluation at 78 GHz," *IEEE Transactions on Antennas and Propagation*, vol. 67, no. 3, pp. 1562–1572, 2019. 44

[80] Z. Zang, A. U. Zaman, and J. Yang, "Single Layer Dual Circularly Polarized Antenna Array Based on Ridge Gap Waveguide for 77 GHz Automotive Radar," *IEEE Transactions on Antennas and Propagation*, vol. 70, no. 7, pp. 5977–5982, 2022. 44

[81] G. Wanielik, N. Appenrodt, H. Neef, R. Schneider, and J. Wenger, "Polarimetric millimeter wave imaging radar and traffic scene interpretation," in *IEE Colloquium on Automotive Radar and Navigation Techniques (Ref. No. 1998/230)*, 1998, pp. 4/1–4/7. 44

[82] S. Trummer, G. F. Hamberger, R. Koerber, U. Siart, and T. F. Eibert, "Performance analysis of 79 GHz polarimetric radar sensors for autonomous driving," in *2017 European Radar Conference (EuRAD)*, 2017, pp. 41–44. 44, 45

[83] T. Visentin, J. Hasch, and T. Zwick, "Calibration of a Fully Polarimetric 8×8 MIMO FMCW Radar System at 77 GHz," in *2017 11th European Conference on Antennas and Propagation (EUCAP)*, 2017, pp. 2530–2534. 44, 45, 51

[84] ——, "Analysis of multipath and DOA detection using a fully polarimetric automotive radar," in *2017 European Radar Conference (EURAD)*, 2017, pp. 45–48. 44, 45

[85] ——, "Analysis of multipath and DOA detection using a fully polarimetric automotive radar," *International Journal of Microwave and Wireless Technologies*, vol. 10, no. 5–6, p. 570–577, 2018. 44

[86] A. Y. Nashashibi, M. Kashanianfard, T. J. Douglas, K. Sarabandi, and S. W. Decker, "Fully Polarimetric E-Band Instrumentation Radar in Support of Autonomous Vehicle Research," in *2020 IEEE USNC-CNC-URSI North American Radio Science Meeting (Joint with AP-S Symposium)*, 2020, pp. 97–98. 44, 45

[87] A. Y. Nashashibi, M. Kashanianfard, and K. Sarabandi, "Calibration of Wideband FMCW Polarimetric Radars Operating at Millimeter-Wave Frequencies," *IEEE Transactions on Geoscience and Remote Sensing*, vol. 60, pp. 1–10, 2022. 44, 45, 51

[88] A. Y. Nashashibi, M. Kashanianfard, T. J. Douglas, K. Sarabandi, and S. W. Decker, "High-Resolution Range-Doppler Maps of Moving Targets in Traffic Scene," in *2021 IEEE International Symposium on Antennas and Propagation and USNC-URSI Radio Science Meeting (APS/URSI)*, 2021, pp. 1119–1120. 44, 45

[89] A. Tinti, S. T. Alfageme, S. D. Biarge, and N. Pohl, "±45° Linearly Polarized PCB Antennas for Polarimetric Automotive Radar," in *2023 Photonics & Electromagnetics Research Symposium (PIERS)*, 2023, pp. 571–577. 44, 45

[90] F. Weishaupt, J. F. Tilly, N. Appenrodt, J. Dickmann, and D. Heberling, "Calibration and Signal Processing of Polarimetric Radar Data in Automotive Applications," in *2022 Microwave Mediterranean Symposium (MMS)*, 2022, pp. 1–6. 44, 46, 49, 53, 56, 57, 58, 60, 62, 66, 68, 69

[91] F. Weishaupt, K. Werber, J. Tilly, J. Dickmann, and D. Heberling, "Polarimetric Radar for Automotive Self-Localization," in *2019 20th International Radar Symposium (IRS)*, 2019, pp. 1–8. 44, 55, 72, 88, 89

[92] F. Weishaupt, J. F. Tilly, J. Dickmann, and D. Heberling, "Polarimetric Covariance Gridmaps for Automotive Self-Localization," in *2020 IEEE 23rd International Conference on Information Fusion (FUSION)*, 2020, pp. 1–8. 44, 93, 96, 97, 98

[93] F. Weishaupt, P. S. Will, N. Appenrodt, J. F. Tilly, J. Dickmann, and D. Heberling, "Robust Point-shaped Landmark Detection Using Polarimetric Radar," in *2021 IEEE Intelligent Vehicles Symposium (IV)*, 2021, pp. 859–865. 44, 102, 107

[94] C. Vasanelli, F. Roos, A. Dürr, J. Schlichenmaier, P. Hügler, B. Meinecke, M. Steiner, and C. Waldschmidt, "Calibration and Direction-of-Arrival Estimation of Millimeter-Wave Radars: A Practical Introduction," *IEEE Antennas and Propagation Magazine*, vol. 62, no. 6, pp. 34–45, 2020. 50, 53, 59

[95] M. Harter, J. Hildebrandt, A. Ziroff, and T. Zwick, "Self-Calibration of a 3-D-Digital Beamforming Radar System for Automotive Applications With Installation Behind Automotive Covers," *IEEE Transactions on Microwave Theory and Techniques*, vol. 64, no. 9, pp. 2994–3000, 2016. 50, 59

[96] W. Wiesbeck and D. Kahny, "Single reference, three target calibration and error correction for monostatic, polarimetric free space measurements," *Proceedings of the IEEE*, vol. 79, no. 10, pp. 1551–1558, 1991. 50

[97] I. G. C. David G. Michelson and C. E. Livingstone, "A Calibration Algorithm for Circular Polarimetric Radars," *Journal of Electromagnetic Waves and Applications*, vol. 11, no. 5, pp. 659–674, 1997. 50

[98] K. Sarabandi, F. Ulaby, and M. Tassoudji, "Calibration of polarimetric radar systems with good polarization isolation," *IEEE Transactions on Geoscience and Remote Sensing*, vol. 28, no. 1, pp. 70–75, 1990. 50, 51

[99] T. M. Freialdenhoven, "Frequency-Controlled Polarizers for Polarimetric Radar Applications," Ph.D. dissertation, Rheinisch-Westfälische Technische

Hochschule Aachen, 2023. [Online]. Available: https://publications.rwth-aachen.de/record/971427 51

[100] C. Fulton and W. J. Chappell, "Calibration of a digital phased array for polarimetric radar," in *2010 IEEE MTT-S International Microwave Symposium*, 2010, pp. 161–164. 51, 52

[101] A. E. Fuhs, *Radar cross section lectures.* American Institute of Aeronautics and Astronautics, 1984. 54

[102] A. Dürr, B. Schneele, D. Schwarz, and C. Waldschmidt, "Range-Angle Coupling and Near-Field Effects of Very Large Arrays in mm-Wave Imaging Radars," *IEEE Transactions on Microwave Theory and Techniques*, vol. 69, no. 1, pp. 262–270, 2021. 58

[103] NVIDIA, "NVIDIA® CUDA® Fast Fourier Transform - cuFFT." [Online]. Available: https://docs.nvidia.com/cuda/cufft/index.html 59

[104] D. Kellner, M. Barjenbruch, K. Dietmayer, J. Klappstein, and J. Dickmann, "Joint radar alignment and odometry calibration," in *2015 18th International Conference on Information Fusion (Fusion)*, 2015, pp. 366–374. 60

[105] D. Kellner, "Verfahren zur Bestimmung von Objekt- und Eigenbewegung auf Basis der Dopplerinformation hochauflösender Radarsensoren," Ph.D. dissertation, Ulm University, 2017. 60

[106] J. P. Burg, "Maximum entropy spectral analysis," Ph.D. dissertation, Stanford University, 1975. 64

[107] Barjenbruch, Michael, "Methoden zur Steigerung der Auflösung und Robustheit von Automobilradaren," Ph.D. dissertation, Ulm University, 2019. 64

[108] F. Gerhardes, S. Leuchs, and O. Arpe, "E-Band Based Car Radar Emblem Measurements," *Anritsu Application Note*, 2019. 69

[109] Z. Qamar, N. Aboserwal, and J. L. Salazar-Cerreno, "An Accurate Method for Designing, Characterizing, and Testing a Multi-Layer Radome for mm-Wave Applications," *IEEE Access*, vol. 8, pp. 23 041–23 053, 2020. 69

[110] F. Weishaupt, A. Uzair, R. Moch, H.-L. Bloecher, J. F. Tilly, J. Dickmann, and D. Heberling, "Polarimetric Scattering Mechanism Analysis of Automotive Landmarks," in *2020 21st International Radar Symposium (IRS)*, 2020, pp. 379–384. 72, 75, 76, 77, 80, 81, 83, 84, 85

[111] A. Uzair, "Polarimetric Evaluation of Scattering Mechanisms of Automotive Landmarks," Master's thesis, RWTH Aachen University, 2020. 72

[112] K. Werber, M. Barjenbruch, J. Klappstein, J. Dickmann, and C. Waldschmidt, "How do traffic signs look like in radar?" in *2014 44th European Microwave Conference*, 2014, pp. 135–138. 72, 73, 79, 81

[113] K. Uchiyama, T. Motomura, and A. Kajiwara, "A study on self-vehicle location estimation employing 79GHz UWB radar," in *2018 IEEE Sensors Applications Symposium (SAS)*, 2018, pp. 1–5. 73

[114] U. Chipengo and M. Commens, "A 77 GHz Simulation Study of Roadway Infrastructure Radar Signatures for Smart Roads," in *2019 16th European Radar Conference (EuRAD)*, 2019, pp. 137–140. 73

[115] J. Lin, S. Chien, Y. Chen, C.-C. Chen, and R. Sherony, "24 GHz and 77 GHz Radar Characteristics of Metal Guardrail for the Development of Metal Guardrail Surrogate for Road Departure Mitigation System Testing," in

2019 IEEE Intelligent Transportation Systems Conference (ITSC), 2019, pp. 3340–3346. 73, 111

[116] R. Moch and D. Heberling, "Height Profiles of Typical Automotive Landmarks Using Tomographic Compact-Range Measurements," in *2020 14th European Conference on Antennas and Propagation (EuCAP)*, 2020, pp. 1–5. 73

[117] Institute of High Frequency Technology RWTH Aachen, "Compact Range," https://www.ihf.rwth-aachen.de/en/research/research-topics/antenna-measurement/compact-range [Accessed: 30.03.24]. 73, 74

[118] T. Gemmer, "Generalised test-zone field compensation; 1. Auflage," Dissertation, RWTH Aachen University, Aachen, 2022. [Online]. Available: https://publications.rwth-aachen.de/record/848414 75

[119] M. A. Fischler and R. C. Bolles, "Random sample consensus: a paradigm for model fitting with applications to image analysis and automated cartography," *Commun. ACM*, vol. 24, no. 6, p. 381–395, jun 1981. [Online]. Available: https://doi.org/10.1145/358669.358692 77

[120] F. Hirtenfelder, "Effective Antenna Simulations using CST MICROWAVE STUDIO ®," in *2007 2nd International ITG Conference on Antennas*, 2007, pp. 239–239. 82

[121] C. Özdemir, *Inverse Synthetic Aperture Radar Imaging with MATLAB ® Algorithms*. John Wiley & Sons, Inc., 2012. 84

[122] T. Dallmann and D. Heberling, "Viewpoint correction for polarimetrie turntable inverse synthetic aperture radar," in *2017 11th European Conference on Antennas and Propagation (EUCAP)*, 2017, pp. 2061–2065. 84

[123] H. Moravec and A. Elfes, "High resolution maps from wide angle sonar," in *Proceedings. 1985 IEEE International Conference on Robotics and Automation*, March 1985. 90

[124] D. Nuss, S. Reuter, M. Thom, T. Yuan, G. Krehl, M. Maile, A. Gern, and K. Dietmayer, "A random finite set approach for dynamic occupancy grid maps with real-time application," *The International Journal of Robotics Research*, vol. 37, no. 8, pp. 841–866, 2018. 90

[125] K. Werber, M. Rapp, J. Klappstein, M. Hahn, J. Dickmann, K. Dietmayer, and C. Waldschmidt, "Automotive radar gridmap representations," in *2015 IEEE MTT-S International Conference on Microwaves for Intelligent Mobility (ICMIM)*, 2015, pp. 1–4. 90

[126] P. Fritsche and B. Wagner, "Modeling structure and aerosol concentration with fused radar and LiDAR data in environments with changing visibility," in *2017 IEEE/RSJ International Conference on Intelligent Robots and Systems (IROS)*, 2017, pp. 2685–2690. 90

[127] M. Rapp, K. Dietmayer, M. Hahn, F. Schuster, J. Lombacher, and J. Dickmann, "FSCD and BASD: Robust landmark detection and description on radar-based grids," in *2016 IEEE MTT-S International Conference on Microwaves for Intelligent Mobility (ICMIM)*, 2016, pp. 1–4. 90, 103

[128] Lombacher, Jakob, "Semantische Umgebungserfassung auf Basis von Radar-Merkmalskarten," Ph.D. dissertation, TU Dortmund University, 2021. 90

[129] T. Grebner, A. Grathwohl, P. Schoeder, V. Janoudi, and C. Waldschmidt, "Probabilistic SAR Processing for High-Resolution Mapping Using Millimeter-

Wave Radar Sensors," *IEEE Transactions on Aerospace and Electronic Systems*, vol. 59, no. 5, pp. 4800–4814, 2023. 90

[130] A. Laribi, M. Hahn, J. Dickmann, and C. Waldschmidt, "Performance Investigation of Automotive SAR Imaging," in *2018 IEEE MTT-S International Conference on Microwaves for Intelligent Mobility (ICMIM)*, 2018, pp. 1–4. 90

[131] T. Gisder, M. Meinecke, and E. Biebl, "Synthetic Aperture Radar Towards Automotive Applications," in *2019 20th International Radar Symposium (IRS)*, 2019, pp. 1–10. 90

[132] H. Iqbal, M. Schartel, F. Roos, J. Urban, and C. Waldschmidt, "Implementation of a SAR Demonstrator for Automotive Imaging," in *2018 18th Mediterranean Microwave Symposium (MMS)*, 2018, pp. 240–243. 90

[133] H. Iqbal, A. Löffler, M. N. Mejdoub, and F. Gruson, "Realistic SAR implementation for automotive applications," in *2020 17th European Radar Conference (EuRAD)*, 2021, pp. 306–309. 90

[134] F. Weishaupt, N. Appenrodt, J. F. Tilly, J. Dickmann, and D. Heberling, "PreCFAR gridmaps for automotive radar," in *2021 European Radar Conference (EuRAD)*, 2022, pp. 161–164. 91, 92, 94, 148

[135] J. S. Lee and M. R. Grunes, "Classification of multi-look polarimetric SAR data based on complex Wishart distribution," in *[Proceedings] NTC-92: National Telesystems Conference*, May 1992, pp. 7/21–7/24. 96

[136] S. N. Anfinsen, R. Jenssen, and T. Eltoft, "Spectral clustering of polarimetric SAR data with Wishart-derived distance measures," in *Proc. POLinSAR*, vol. 7, 2007, pp. 1–9. 96, 103

[137] J. van Zyl and Y. Kim, *Synthetic Aperture Radar Polarimetry*. John Wiley & Sons, Ltd, 2011. 98

[138] P. Will, "Investigation of Polarimetric Landmarks for Self-Localization in Automated Driving," Master's thesis, University of Stuttgart, 2021. 102, 104, 107

[139] N. Engel, V. Belagiannis, and K. Dietmayer, "Attention-based Vehicle Self-Localization with HD Feature Maps," in *2021 IEEE International Intelligent Transportation Systems Conference (ITSC)*, 2021, pp. 76–83. 103, 117, 118

[140] M. Lundgren, E. Stenborg, L. Svensson, and L. Hammarstrand, "Vehicle self-localization using off-the-shelf sensors and a detailed map," in *2014 IEEE Intelligent Vehicles Symposium Proceedings*, 2014, pp. 522–528. 103, 117, 118

[141] K. Werber, J. Klappstein, J. Dickmann, and C. Waldschmidt, "Association of Straight Radar Landmarks for Vehicle Self-Localization," in *2019 IEEE Intelligent Vehicles Symposium (IV)*, 2019, pp. 736–743. 103, 120

[142] J.-S. Lee, M. R. Grunes, and R. Kwok, "Classification of multi-look polarimetric SAR imagery based on complex Wishart distribution," *International Journal of Remote Sensing*, vol. 15, no. 11, 1994. 103

[143] J. Wei, P. Li, J. Yang, J. Zhang, and F. Lang, "A New Automatic Ship Detection Method Using *L*-Band Polarimetric SAR Imagery," *IEEE Journal of Selected Topics in Applied Earth Observations and Remote Sensing*, vol. 7, no. 4, pp. 1383–1393, 2014. 103

[144] J.-S. Lee, M. R. Grunes, and E. Pottier, "Quantitative comparison of classification capability: fully polarimetric versus dual and single-polarization SAR,"

IEEE Transactions on Geoscience and Remote Sensing, vol. 39, no. 11, pp. 2343–2351, 2001. 104

[145] K. Conradsen, A. A. Nielsen, J. Schou, and H. Skriver, "A test statistic in the complex Wishart distribution and its application to change detection in polarimetric SAR data," *IEEE Transactions on Geoscience and Remote Sensing*, vol. 41, no. 1, pp. 4–19, 2003. 104

[146] M. Herdin, N. Czink, H. Ozcelik, and E. Bonek, "Correlation matrix distance, a meaningful measure for evaluation of non-stationary MIMO channels," in *2005 IEEE 61st Vehicular Technology Conference*, vol. 1, 2005, pp. 136–140 Vol. 1. 104

[147] F. C. Crow, "Summed-area tables for texture mapping," in *Proceedings of the 11th Annual Conference on Computer Graphics and Interactive Techniques*, ser. SIGGRAPH '84. New York, NY, USA: Association for Computing Machinery, 1984, p. 207–212. 104

[148] P. Chen, M. Wahib, S. Takizawa, R. Takano, and S. Matsuoka, "Efficient Algorithms for the Summed Area Tables Primitive on GPUs," in *2018 IEEE International Conference on Cluster Computing (CLUSTER)*, 2018, pp. 482–493. 104

[149] H. Samet and M. Tamminen, "Efficient component labeling of images of arbitrary dimension represented by linear bintrees," *IEEE Transactions on Pattern Analysis and Machine Intelligence*, vol. 10, no. 4, pp. 579–586, 1988. 105

[150] J. L. Bentley, "Multidimensional binary search trees used for associative searching," *Commun. ACM*, vol. 18, no. 9, p. 509–517, sep 1975. 105, 120

[151] @CITY consortium. Cooperative project "@CITY – Automated Cars and Intelligent Traffic in the City". Accessed: 27th November 2024. [Online]. Available: https://www.atcity-online.de/ 107, 126

[152] T. Lindeberg, "Scale-Space," in *Wiley Encyclopedia of Computer Science and Engineering*, 2009, pp. 2495–2504, qC 20110914. 111

[153] T. Y. Zhang and C. Y. Suen, "A fast parallel algorithm for thinning digital patterns," *Commun. ACM*, vol. 27, no. 3, p. 236–239, Mar. 1984. [Online]. Available: https://doi.org/10.1145/357994.358023 111

[154] R. O. Duda and P. E. Hart, "Use of the Hough transformation to detect lines and curves in pictures," *Commun. ACM*, vol. 15, no. 1, p. 11–15, Jan. 1972. [Online]. Available: https://doi.org/10.1145/361237.361242 111

[155] P. Fischer, "Automotive Self-Localization using Polarimetric Radar," Master's thesis, Goethe University Frankfurt, 2021. 115

[156] Ş. Săftescu, M. Gadd, D. De Martini, D. Barnes, and P. Newman, "Kidnapped Radar: Topological Radar Localisation using Rotationally-Invariant Metric Learning," in *2020 IEEE International Conference on Robotics and Automation (ICRA)*, 2020, pp. 4358–4364. 116

[157] W. Wang, P. P. B. de Gusmão, B. Yang, A. Markham, and N. Trigoni, "RadarLoc: Learning to Relocalize in FMCW radar," in *2021 IEEE International Conference on Robotics and Automation (ICRA)*, 2021, pp. 5809–5815. 116

[158] M. Holder, S. Hellwig, and H. Winner, "Real-Time Pose Graph SLAM based on radar," in *2019 IEEE Intelligent Vehicles Symposium (IV)*, 2019, pp. 1145–1151. 116

[159] Z. Hong, Y. Petillot, and S. Wang, "RadarSLAM: Radar based large-scale SLAM in all weathers," in *2020 IEEE/RSJ International Conference on Intelligent Robots and Systems (IROS)*, 2020, pp. 5164–5170. 116

[160] S. H. Cen and P. Newman, "Precise Ego-Motion Estimation with Millimeter-Wave Radar Under Diverse and Challenging Conditions," in *2018 IEEE International Conference on Robotics and Automation (ICRA)*, 2018, pp. 6045–6052. 116

[161] ——, "Radar-only ego-motion estimation in difficult settings via graph matching," in *2019 IEEE International Conference on Robotics and Automation (ICRA)*, 2019, pp. 298–304. 116

[162] D. Barnes and I. Posner, "Under the Radar: Learning to Predict Robust Keypoints for Odometry Estimation and Metric Localisation in Radar," in *2020 IEEE International Conference on Robotics and Automation (ICRA)*, 2020, pp. 9484–9490. 116

[163] K. Burnett, D. J. Yoon, A. P. Schoellig, and T. D. Barfoot, "Radar odometry combining probabilistic estimation and unsupervised feature learning," *arXiv preprint arXiv:2105.14152*, 2021. 116

[164] D. Kellner, M. Barjenbruch, J. Klappstein, J. Dickmann, and K. Dietmayer, "Instantaneous ego-motion estimation using multiple Doppler radars," in *2014 IEEE International Conference on Robotics and Automation (ICRA)*, 2014, pp. 1592–1597. 116, 120

[165] S. Yuan, S. Zhu, F. Fioranelli, and A. G. Yarovoy, "3-D Ego-Motion Estimation Using Multi-Channel FMCW Radar," *IEEE Transactions on Radar Systems*, vol. 1, pp. 368–381, 2023. 116

[166] M. Cornick, J. Koechling, B. Stanley, and B. Zhang, "Localizing Ground Penetrating RADAR: A Step Toward Robust Autonomous Ground Vehicle Localization," *Journal of Field Robotics*, vol. 33, no. 1, pp. 82–102, 2016. 116, 117, 118

[167] T. Ort, I. Gilitschenski, and D. Rus, "Autonomous Navigation in Inclement Weather Based on a Localizing Ground Penetrating Radar," *IEEE Robotics and Automation Letters*, vol. PP, pp. 1–1, 02 2020. 116, 117, 118

[168] M. Rapp, M. Hahn, M. Thom, J. Dickmann, and K. Dietmayer, "Semi-Markov Process Based Localization Using Radar in Dynamic Environments," in *2015 IEEE International Intelligent Transportation Systems Conference (ITSC)*, 2015, pp. 423–429. 117

[169] F. Schuster, M. Wörner, C. Keller, M. Haueis, and C. Curio, "Robust localization based on radar signal clustering," in *2016 IEEE Intelligent Vehicles Symposium (IV)*, 2016, pp. 839–844. 117, 118

[170] E. Ward and J. Folkesson, "Vehicle localization with low cost radar sensors," in *2016 IEEE Intelligent Vehicles Symposium (IV)*, 2016, pp. 864–870. 117, 118

[171] K. Yoneda, N. Hashimoto, R. Yanase, M. Aldibaja, and N. Suganuma, "Vehicle Localization using 76GHz omnidirectional millimeter-wave radar for winter automated driving," in *2018 IEEE Intelligent Vehicles Symposium (IV)*, 2018, pp. 971–977. 117, 118

[172] M. Li, W. Jia, M. Kunert, R. Henze, and F. Küçükay, "Environment mapping and vehicle localization with a high-resolution radar prototype," in *Proc. 5th*

Int. Symposium on Future Active Safety Technology toward Zero Accidents, 2019. 117

[173] P. A. Iannucci, L. Narula, and T. E. Humphreys, "Cross-Modal Localization: Using automotive radar for absolute geolocation within a map produced with visible-light imagery," in *2020 IEEE/ION Position, Location and Navigation Symposium (PLANS)*, 2020, pp. 285–296. 117, 118

[174] S. Jürgens, N. Koch, and M.-M. Meinecke, "Radar-based Automotive Localization using Landmarks in a Multimodal Sensor Graph-based Approach," in *2020 21st International Radar Symposium (IRS)*, 2020, pp. 373–378. 117, 118, 121

[175] L. Narula, P. A. Iannucci, and T. E. Humphreys, "Automotive-Radar-Based 50-cm Urban Positioning," in *2020 IEEE/ION Position, Location and Navigation Symposium (PLANS)*, 2020, pp. 856–867. 117, 118

[176] A. Pishehvari, M. Stefer, and B. Tibken, "Robust Range-Doppler Registration with HD Maps," in *2020 5th International Conference on Control and Robotics Engineering (ICCRE)*, 2020, pp. 140–147. 117, 118

[177] H. Yin, Y. Wang, L. Tang, and R. Xiong, "Radar-on-Lidar: metric radar localization on prior lidar maps," in *2020 IEEE International Conference on Real-time Computing and Robotics (RCAR)*, 2020, pp. 1–7. 117, 118

[178] B. Otake, "Automotive Radar For Localization In GNSS-Denied Environments," Master's thesis, KTH Royal Institute of Technology, Stockholm, 2021. 117, 118

[179] K. Burnett, Y. Wu, D. J. Yoon, A. P. Schoellig, and T. D. Barfoot, "Are We Ready for Radar to Replace Lidar in All-Weather Mapping and Localization?" *IEEE Robotics and Automation Letters*, pp. 1–8, 2022. 117, 118

[180] R. Yanase, D. Hirano, M. Aldibaja, K. Yoneda, and N. Suganuma, "Lidar- and Radar-Based Robust Vehicle Localization with Confidence Estimation of Matching Results," *Sensors*, vol. 22, no. 9, 2022. 117, 118

[181] H. Yin, R. Chen, Y. Wang, and R. Xiong, "RaLL: End-to-End Radar Localization on Lidar Map Using Differentiable Measurement Model," *IEEE Transactions on Intelligent Transportation Systems*, vol. 23, no. 7, pp. 6737–6750, 2022. 117

[182] U. Ramer, "An iterative procedure for the polygonal approximation of plane curves," *Computer Graphics and Image Processing*, pp. 244–256, 1972. 120

[183] L. Carlone, A. Kim, F. Dellaert, T. Barfoot, and D. Cremers, "SLAM Handbook – From Localization and Mapping to Spatial Intelligence," https://github.com/SLAM-Handbook-contributors/slam-handbook-public-release, 2024. 123

[184] F. Dellaert and M. Kaess, *Factor Graphs for Robot Perception*. Now Foundations and Trends, 2017. 123

[185] D. Wilbers, C. Merfels, and C. Stachniss, "Localization with Sliding Window Factor Graphs on Third-Party Maps for Automated Driving," in *2019 IEEE International Conference on Robotics and Automation (ICRA)*, 2019, pp. 5951–5957. 126

[186] F. Dellaert, R. Roberts, V. Agrawal, A. Cunningham, C. Beall, D.-N. Ta, F. Jiang, lucacarlone, nikai, J. L. Blanco-Claraco, S. Williams, ydjian, J. Lambert, A. Melim, Z. Lv, A. Krishnan, J. Dong, G. Chen, K. Chande, balderdash

devil, DiffDecisionTrees, S. An, mpaluri, E. P. Mendes, M. Bosse, A. Patel, A. Baid, P. Furgale, matthewbroadwaynavenio, and roderick koehle, "borglab/gtsam - Georgia Tech Smoothing and Mapping Library," May 2022. 127

[187] M. Kaess, H. Johannsson, R. Roberts, V. Ila, J. Leonard, and F. Dellaert, "iSAM2: Incremental smoothing and mapping with fluid relinearization and incremental variable reordering," in *2011 IEEE International Conference on Robotics and Automation (ICRA)*, 2011, pp. 3281–3288. 127

[188] D. G. Michelson, I. G. Cumming, and C. E. Livingstone, "Symmetry Properties of the Circular Polarization Covariance Matrix," *Journal of Electromagnetic Waves and Applications*, vol. 11, pp. 719–738, 1997. 130

[189] IEEE Publishing Operations, "IEEE EDITORIAL STYLE MANUAL FOR AUTHORS," 2024, Accessed: 5th May 2024. [Online]. Available: http://journals.ieeeauthorcenter.ieee.org/wp-content/uploads/sites/7/IEEE-Editorial-Style-Manual-for-Authors.pdf 161

[190] J. F. Tilly, S. Haag, O. Schumann, F. Weishaupt, B. Duraisamy, J. Dickmann, and M. Fritzsche, "Detection and Tracking on Automotive Radar Data with Deep Learning," in *2020 IEEE 23rd International Conference on Information Fusion (FUSION)*, 2020, pp. 1–7.

[191] O. Schumann, M. Hahn, N. Scheiner, F. Weishaupt, J. F. Tilly, J. Dickmann, and C. Wöhler, "RadarScenes: A Real-World Radar Point Cloud Data Set for Automotive Applications," in *2021 IEEE 24th International Conference on Information Fusion (FUSION)*, 2021, pp. 1–8.

[192] N. Scheiner, F. Weishaupt, J. F. Tilly, and J. Dickmann, "New Challenges for Deep Neural Networks in Automotive Radar Perception," in *Automatisiertes Fahren 2020*, T. Bertram, Ed. Wiesbaden: Springer Fachmedien Wiesbaden, 2021, pp. 165–182.

List of Publications

The following papers were published as the first author as part of the research conducted for this thesis:

1. F. Weishaupt, K. Werber, J. Tilly, J. Dickmann, and D. Heberling, "Polarimetric Radar for Automotive Self-Localization," in *2019 20th International Radar Symposium (IRS)*, 2019, pp. 1–8
2. F. Weishaupt, J. F. Tilly, J. Dickmann, and D. Heberling, "Polarimetric Covariance Gridmaps for Automotive Self-Localization," in *2020 IEEE 23rd International Conference on Information Fusion (FUSION)*, 2020, pp. 1–8
3. F. Weishaupt, A. Uzair, R. Moch, H.-L. Bloecher, J. F. Tilly, J. Dickmann, and D. Heberling, "Polarimetric Scattering Mechanism Analysis of Automotive Landmarks," in *2020 21st International Radar Symposium (IRS)*, 2020, pp. 379–384
4. F. Weishaupt, P. S. Will, N. Appenrodt, J. F. Tilly, J. Dickmann, and D. Heberling, "Robust Point-shaped Landmark Detection Using Polarimetric Radar," in *2021 IEEE Intelligent Vehicles Symposium (IV)*, 2021, pp. 859–865
5. F. Weishaupt, N. Appenrodt, J. F. Tilly, J. Dickmann, and D. Heberling, "PreCFAR gridmaps for automotive radar," in *2021 European Radar Conference (EuRAD)*, 2022, pp. 161–164
6. F. Weishaupt, J. F. Tilly, N. Appenrodt, J. Dickmann, and D. Heberling, "Calibration and Signal Processing of Polarimetric Radar Data in Automotive Applications," in *2022 Microwave Mediterranean Symposium (MMS)*, 2022, pp. 1–6
7. F. Weishaupt, J. F. Tilly, N. Appenrodt, P. Fischer, J. Dickmann, and D. Heberling, "Landmark-based Vehicle Self-Localization Using Automotive Polarimetric Radars," *IEEE Transactions on Intelligent Transportation Systems*, vol. 25, no. 10, pp. 14 266–14 283, 2024

Furthermore, the following publications were co-authored:

8. J. F. Tilly, F. Weishaupt, O. Schumann, J. Klappstein, J. Dickmann, and G. Wanielik, "Polarimetric Signatures of a Passenger Car," in *2019 Kleinheubach Conference*, 2019, pp. 1–4
9. J. F. Tilly, S. Haag, O. Schumann, F. Weishaupt, B. Duraisamy, J. Dickmann, and M. Fritzsche, "Detection and Tracking on Automotive Radar Data with Deep Learning," in *2020 IEEE 23rd International Conference on Information Fusion (FUSION)*, 2020, pp. 1–7

10. J. F. Tilly, F. Weishaupt, O. Schumann, J. Dickmann, and G. Wanielik, "Road User Classification with Polarimetric Radars," in *2020 17th European Radar Conference (EuRAD)*, 2021, pp. 112–115

11. O. Schumann, M. Hahn, N. Scheiner, F. Weishaupt, J. F. Tilly, J. Dickmann, and C. Wöhler, "RadarScenes: A Real-World Radar Point Cloud Data Set for Automotive Applications," in *2021 IEEE 24th International Conference on Information Fusion (FUSION)*, 2021, pp. 1–8

12. N. Scheiner, F. Weishaupt, J. F. Tilly, and J. Dickmann, "New Challenges for Deep Neural Networks in Automotive Radar Perception," in *Automatisiertes Fahren 2020*, T. Bertram, Ed. Wiesbaden: Springer Fachmedien Wiesbaden, 2021, pp. 165–182

13. J. F. Tilly, O. Schumann, F. Weishaupt, J. Dickmann, and G. Waniliek, "Polarimetric Information Representation for Radar based Road User Detection with Deep Learning," in *2021 IEEE 24th International Conference on Information Fusion (FUSION)*, 2021, pp. 1–6

14. J. F. Tilly, O. Schumann, F. Weishaupt, J. Dickmann, and G. Wanielik, "Reduction of Sidelobe Effects in Automotive Polarimetric Radar Measurements," in *2021 18th European Radar Conference (EuRAD)*, 2022, pp. 169–172

15. ——, "Road User Detection on Polarimetric Pre-CFAR Radar Data Level," *IEEE Robotics and Automation Letters*, vol. 8, no. 6, pp. 3558–3565, 2023

In reference to IEEE copyrighted material which is used with permission in this thesis, the IEEE does not endorse any of RWTH Aachen University's products or services. Internal or personal use of this material is permitted. If interested in reprinting/republishing IEEE copyrighted material for advertising or promotional purposes or for creating new collective works for resale or redistribution, please go to `http://www.ieee.org/publications_standards/publications/rights/rights_link.html` to learn how to obtain a License from RightsLink. If applicable, University Microfilms and/or ProQuest Library, or the Archives of Canada may supply single copies of the dissertation.

Curriculum vitae

Personal details

Name	Fabio Weishaupt
Place of birth	Oberhausen, Germany
Year of birth	1993
Nationality	German

Education

2015 – 2017	Master of Science in Electrical Engineering, Information Technology and Computer Engineering, RWTH Aachen University, Germany Thesis: "Setup and Evaluation of a MIMO Radar Sensor Network together with a Signal-Theoretical and Experimental Validation"
2012 – 2015	Bachelor of Science in Electrical Engineering, Information Technology and Computer Engineering, RWTH Aachen University, Germany Thesis: "Development and Construction of a Multichannel Plethysmography System for Robust Vital Parameter Detection"

Professional Experience

2021 – 2025	Mercedes-Benz AG, Department of Research and Development, Stuttgart, Germany Development Engineer for Radar Sensors
2018 – 2021	Daimler AG (now Mercedes-Benz AG), Department of Research and Development, Ulm, Germany Ph.D. student
2016 – 2017	Fraunhofer Institute for High Frequency Physics and Radar Techniques FHR, Department of Array-based Radar Imaging, Wachtberg, Germany